NIST Special Publication 250-94

Infrared Optical Properties of Materials

Leonard Hanssen
Simon Kaplan
Raju Datla

This publication is available free of charge from:
http://dx.doi.org/10.6028/NIST.SP.250-94

National Institute of
Standards and Technology
U.S. Department of Commerce

NIST Special Publication 250-94

Infrared Optical Properties of Materials

Leonard Hanssen
Simon Kaplan
Raju Datla
Sensor Science Division
Physical Measurement Laboratory

This publication is available free of charge from:
http://dx.doi.org/10.6028/NIST.SP.250-94

February 2015

U.S. Department of Commerce
Penny Pritzker, Secretary

National Institute of Standards and Technology
Willie May, Acting Under Secretary of Commerce for Standards and Technology and Acting Director

National Institute of Standards and Technology Special Publication 250-94
Natl. Inst. Stand. Technol. Spec. Publ. 250-94, 77 pages (February 2015)
CODEN: NSPUE2

This publication is available free of charge from:
http://dx.doi.org/10.6028/NIST.SP.250-94

Abstract

This document describes the Fourier Transform Infrared Spectrophotometry (FTIS) Facility at the Sensor Science Division (SSD) of the National Institute of Standards and Technology (NIST), which provides the infrared optical properties of materials (IROPM) calibration service, 38075 S, over the infrared spectral range of 1 μm to 25 μm. It is organized as follows. Section 1 introduces the FTIS facility for measuring the infrared reflectance, transmittance, absorptance and emittance of materials and the services available. Section 2 describes the physics basis for the measurements. Section 3 describes the setups and measurements. Section 4 describes the measurement assurance process with various publications as appendices on the FTIS measurement uncertainties and intercomparisons. A template for the calibration service report for customers is provided in Sec. 5 and references are added in Sec. 6.

Key Words: diffuse reflectance; directional hemispherical reflectance; reflectance; Fourier Transform Spectrophotometer; integrating sphere; specular reflectance; transmittance; absorptance; emittance.

Table of Contents

1. Introduction

Reflectance, transmittance, and absorptance/emittance are essential optical properties of materials needed for optical science research and industrial applications. The interaction of light with matter is different at different wavelengths and the techniques to measure the optical properties differ based on the spectral region of interest. This document addresses the techniques developed and implemented at NIST for measuring infrared optical properties of materials (IROPM) over the spectral range of 1 μm to 25 μm. The techniques are based on measuring the reflected and transmitted radiation from the sample. Commercial Fourier Transform Infrared (FTIR) spectrophotometer instruments are used to resolve and analyze infrared spectral information. One FTIR is connected to custom built integrating sphere and goniometer setups equipped with state of the art infrared detectors for reflectance and transmittance measurements of samples to meet customer requirements. Also, special cryostats and a modified sample compartment are used for determining the spectral transmittance of filters to meet customer requirements. This specialized instrumentation is part of the Fourier Transform Infrared Spectrophotometry (FTIS) Facility at the Sensor Science Division (SSD). Section 2 provides the physics basis for the measurements. The instrumentation setups and measurements are described in Section 3. In Section 4 the measurement assurance process with uncertainty evaluations and intercomparisons is presented. Section 5 provides a template for the calibration service report for customers. Section 6 contains the references. Appendices at the end provide additional information supporting the main discussion in the document.

NIST strives to provide the best possible measurement services and a research program to support the national requirements for such measurements. NIST maintains trained personnel for realizing and disseminating the absolute scales for the IROPM, and they follow the NIST Quality System for measurement assurance.

2. Reflectance, Transmittance, and Absorptance/Emittance

Reflection is the process by which radiant flux is returned at the boundary between two media (surface reflection) or at the interior of a medium (volume reflection). Transmission is the process of passage of radiant flux through a medium. Both processes can undergo scattering (also called diffusion), which is the deflection of the unidirectional beam of radiation into other directions. When no diffusion occurs the beam of radiation obeys the laws of geometrical optics and the unidirectional beam results in unidirectional beams called specular (or regular) reflection and direct (or regular) transmission. The wavelength of radiation is unchanged in these processes if the medium is stationary. The total reflectance ρ is subdivided into regular reflectance ρ_r, and diffuse reflectance ρ_d. The transmittance τ of a medium is defined by the ratio of transmitted radiant flux to incident radiant flux. The total transmittance τ is subdivided into specular transmittance τ_r and diffuse transmittance τ_d and the terminology for transmittance follows the same definitions as reflectance except the process is transmission and the word reflectance is replaced with transmittance. The absorptance α of a medium is defined by the ratio of absorbed radiant flux to incident radiant flux. By the conservation of energy principle the following relationship holds:

$$\rho + \tau + \alpha = 1 \quad . \tag{1}$$

The emittance (also called emissivity) of a body at temperature T is equal to the absorptance according to Kirchhoff's law:

$$\varepsilon(\lambda, T) = \alpha(\lambda, T) \quad . \tag{2}$$

Therefore, based on Eq. 1 the emittance of a body can be deduced in principle by measuring ρ and τ. For opaque materials no transmission takes place and τ is zero. In such cases the absorptance/emittance can be derived from the measurement of reflectance ρ alone. In this document, Eq. 1 and Eq. 2 are applied to deduce the absorptance/emittance of materials. These quantities are defined using an independent vocabulary to account for the effects of geometry and other parameters such as polarization and temperature of the material, etc. The details of such common vocabulary can be found in Ref. 1.

3. Setups and measurements

The typical setup of equipment for the calibration service 38075S is shown schematically in Fig. 1. In general, the primary spectral source has been a Digilab FTS-7000[1] commercial Fourier transform spectrophotometer, shown in Fig. 2. If necessary, this instrument can be

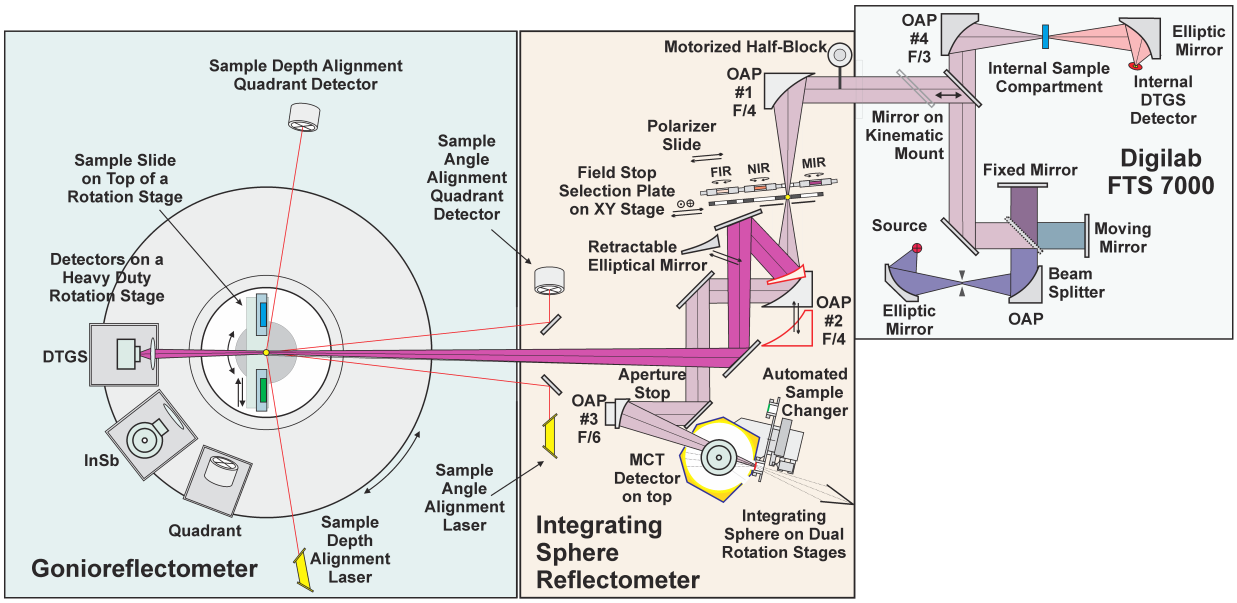

Figure 1: Schematic of the typical equipment setup for the calibration service 38075S. The automatic sample changer in the IRIS setup allows multiple samples to be measured under identical beam alignment. The Mercury Cadmium Telluride (MCT) detector sits on the top port of the integrating sphere and does not interfere with the rotation stages of the integrating sphere. The sample slide on top of the rotation stage of the IGRT allows multiple samples to be measured in identical beam alignment. The sample angle alignment laser and the sample depth alignment laser, and their respective quadrant detectors shown in the IGRT setup allow precise and well defined positioning of the sample in the IGRT setup. The Indium Antimonide (InSb) detector and the DTGS detector located on the heavy duty rotation stage of the goniometer cover the mid IR and the far IR in the IGRT setup.

[1] See NIST disclaimer on the front cover

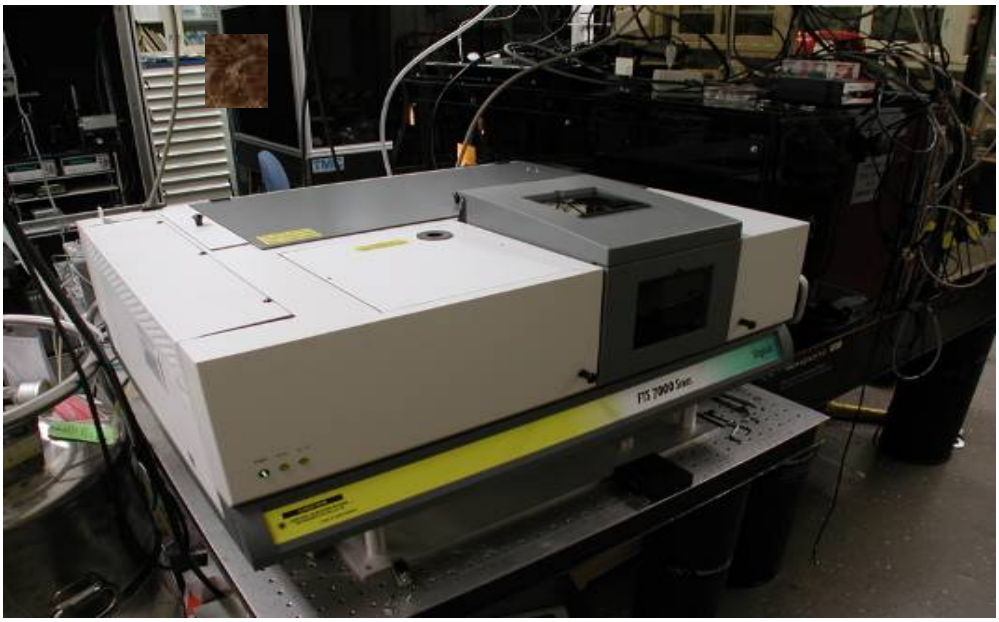

Figure 2: The Digilab FTS 7000 FTIR wavelength range in our setup is 0.8 μm to 50 μm and resolution is ≥ 0.5 cm^{-1}. It is configured for our system with a W–halogen lamp and coated quartz beam splitter for the near-IR spectral region of 1 μm to 3 μm (10,000 cm^{-1} to 3300 cm^{-1}) and a SiC source and coated KBr beam splitter for the mid-IR region of 2 μm to 18 μm (5000 cm^{-1} to 550 cm^{-1}). The available manuals on this instrument are the Digilab FTS-6000 Operating Manual and the Digilab WIN-IR Pro Software Manual, located in the laboratory at Bldg 220, Room B331.

replaced by a similar FTIR, such as the Bruker Vertex 80v, available in the laboratory, without significant modification of the custom external systems described below. The spectrometer with its internal sample testing beam geometry for spectral transmittance measurements is shown in the right box in Fig. 1 labeled Digilab FTS 7000. The mirror on the kinematic mount located in the right box allows the beam to enter the the purged enclosure to the left that houses the Infrared Reference Integrating Sphere (IRIS) and the Infrared Gonio-Reflectometer Transmissometer (IGRT). The equipment is set up on two 122 cm x 183 cm highly stable optical tables.

The interface optics consisting of the field stop selection plate on an x-y stage and polarizer on a slide are commonly available to the IRIS and IGRT with the off-axis paraboloids (OAPs) and an elliptical mirror along with beam steering flat mirrors mounted on translation stages, to select between the instruments. A field stop selection plate shown at the focus of the OAP 1 in the top part of the mid section of the schematic is available to select field stop sizes from 0.25 mm to 2 mm in 0.25 mm intervals, 2 mm to 5 mm at 0.5 mm intervals, and 5 mm to 8 mm at 1 mm intervals. Three polarizers mounted on the polarizer slide and covering the spectral ranges of 0.5 μm to 2.0 μm (NIR), 1.0 μm to 5.0 μm (MIR), and 2 μm to 200 μm (FIR), respectively, are available to provide linear polarization for the incident beam in the measurement. The retractable elliptical mirror allows the beam to be directed to the IGRT section or to the OAP #2 to project to the aperture stop and OAP #3 for the IRIS setup of measurements. The measurement geometry setups for the IRIS and IGRT are described separately in more detail in Section 3.2 and Section 3.3 respectively.

For conventional transmittance measurements other FTIR spectrometers including BOMEM-DA 3, Bruker Vertex 70 and Bruker Vertex 80v are also available at the facility. A liquid He flow-through cryostat is available for measurements at cryogenic sample temperatures. In addition, special filter wheel assemblies have been designed and built to accommodate specific user requirements.

The wavelength scales of the FTIR instruments are set following the methods developed at NIST to provide polystyrene IR wavelength reference standards, SRM 1921 for customers as described in Ref. 2 for high spectral resolution applications and the SRM itself as a secondary standard for low resolution applications.

3.1. "Conventional" transmittance measurements

For transmittance (τ) measurements of fairly thin samples, which do not significantly modify the IR beam geometry, a modified version of the standard sample compartment geometry is used, as shown in Fig. 3. An OAP focuses the input beam at f/3. Half-blocks made of IR absorbing black felt are used to eliminate inter-reflections among the sample, detector and interferometer, while providing an input beam geometry onto the sample equivalent to that of the unblocked case. Neutral density or band pass filters can be placed (tilted, to avoid inter-reflections) before the sample position.Or, they may be used as the reference for the transmittance measurement, in order to provide equivalent levels of flux to the detector and hence minimize any errors due to a detector's non-linear response. Also, a field stop can be placed just before the sample position to limit inclusion of thermal radiation from the source aperture itself. The ratio of IR beam signal measured with the sample-in to sample-out provides the transmittance of the sample.

With the use of appropriate filters and detectors, it is possible to measure transmittance levels as low as 10^{-6} with this configuration [3]. For optically thin (<1 mm) samples with fairly neutral attenuation, the contributions of various error sources to the total uncertainty have been estimated [Appendix A]. Expanded (k = 2) relative uncertainties are in the range of 0.5 % to1 % for samples with optical densities up to 3. These uncertainty estimates have been tested by inter-comparison between two FTIR systems and by inter-comparison with laser measurements on etalon-free samples [4].

Figure 4 shows a comparison between transmittance measurements from 11 to 20 μm on thin metal-coated Si samples with optical densities near 1, 2, and 3 made on the Bio-Rad 60A (predecessor to the Digilab FTS 7000) and DA-3 FTIR spectrometers using the configuration shown in Fig. 3. Both systems were set up with a SiC[2] source and KBr:Ge beamsplitter, and the spectral resolution was 8 cm^{-1}.

[2] Bomem uses the term Globar, a registered tradename. Digilab refers to it as ceramic source.

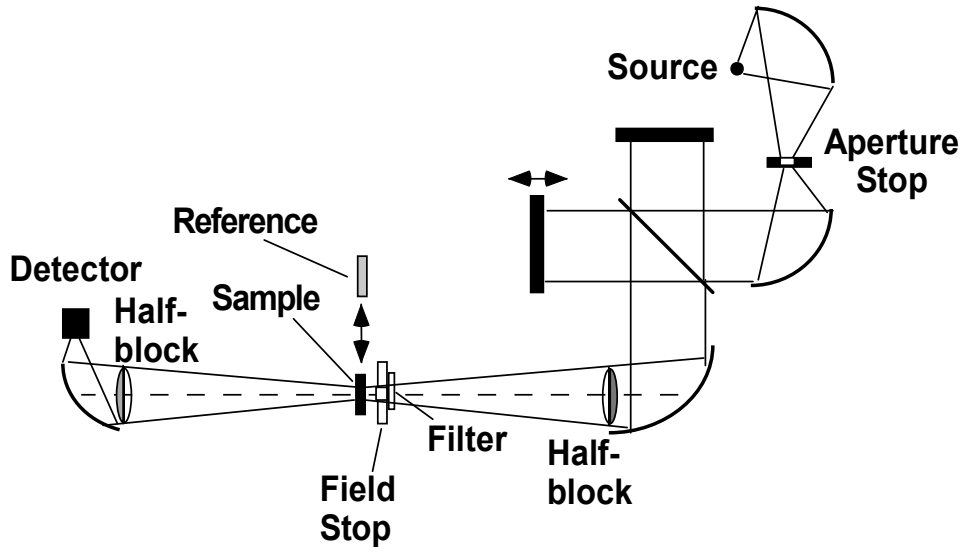

Figure 3: Optical layout for the FTIR transmittance measurements as described in the text.

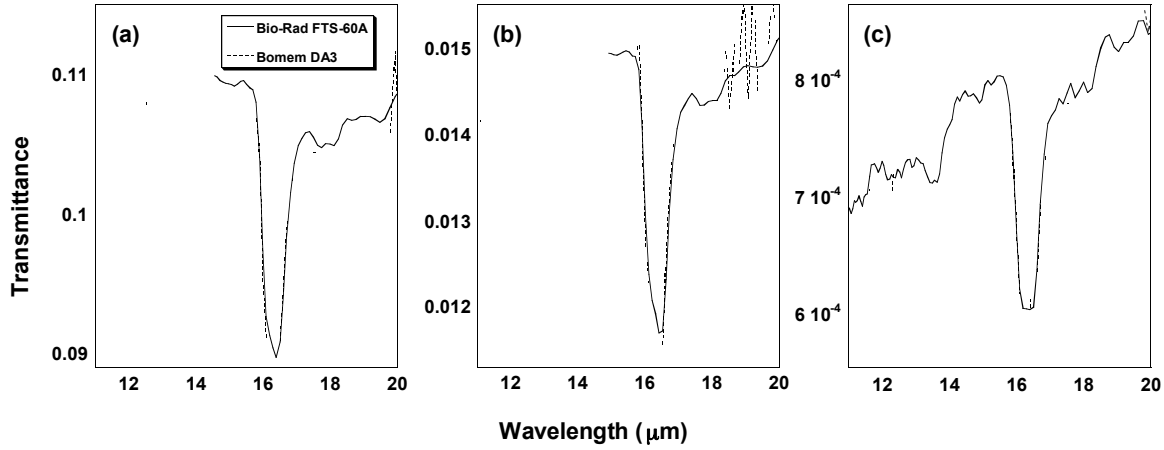

Figure 4: Comparison of measurements of three different metal film/Si neutral density filters performed with two different FTIR systems.

A 2 mm room temperature pyroelectric detector was used with the 60A, while a 1 mm 77 K mercury–cadmium–telluride (MCT) detector was used with the DA-3. The beam geometry at the sample position was *f*/3 in the Bio-Rad and *f*/4 in the DA-3. For the OD 1 (OD = $-\log_{10} T$) sample in frame (a), the two measurement results agree to within 0.5 % over most of the region. For the higher OD samples results shown in (b) and (c), the signal-to-noise ratio is lower, but the measurements still agree to within 1 % to 2 %. The OD 2 measurement was performed with the OD 1 filter as a reference, while the OD 3 measurement was performed with the OD 2 filter as a reference on the DA-3, and the OD 1 filter on the 60A.

3.1.1 Standard reference materials for τ_r

NIST Standard Reference Materials (SRMs) 2053, 2054, 2055, and 2056, for IR transmittance were developed, consisting of thin metallic (Ni:Cr or Cu:Ni) coatings on 0.25 mm thick, 25 mm diameter high-resistivity Si wafer substrates. The coatings were designed to give nominally spectrally neutral attenuation with optical densities near 1, 2, 3, and 4 respectively, over a wavelength range of 2 µm to 25 µm. The thin substrates were chosen to both minimize the Si absorption peaks at 9 µm and 16 µm, and the effects on the geometry of the transmitted beam.

A plot of the optical density of representative samples for the four OD levels is shown in Fig. 5. As is evident in this figure, the OD 1 samples have very neutral attenuation versus wavelength, but the relative spectral variation is larger for the higher OD samples, with the OD 4 filters having a total variation of about 0.6 OD over the measured range. A comparison of the spectra of these filters with previous commercially available Ni:Cr coated filters has been presented [5], and a patent has been issued for the Cu:Ni coatings [6], which provide much more neutral attenuation at the OD 3 and 4 level than do Ni:Cr coatings.

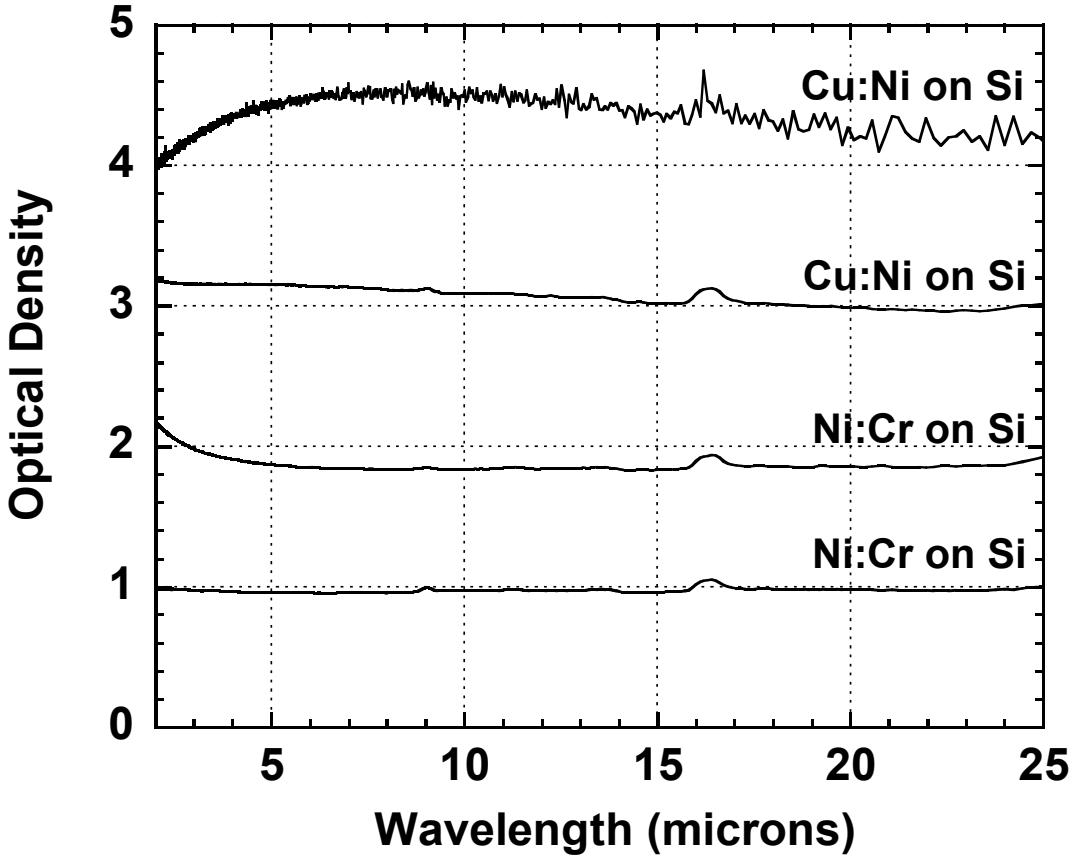

Figure 5: Spectra of neutral density filter SRMs.

A set of 10 samples for each OD level have been produced and the filters have been measured to determine the repeatability and reproducibility of the transmittance over a period of 6 months. The metal coatings have been over-coated with 20 nm of SiO*x* to protect the films from oxidation, and it has been found that the transmittance of the samples is stable within the resolution of the measurements over the 6 month time period. Additional measurements have been performed to determine the spatial uniformity over the central 10 mm diameter circle and temperature dependence of the filters. Table 1 shows estimates for the various uncertainty components in the measured transmittances for the OD 1–4 filters, along with the expanded uncertainties at 10.6 μm wavelength [7]. Some of these filters were sold to customers and the remaining filters were archived by the NIST SRM office. However, such filters can be newly produced and characterized for interested parties through the NIST calibration service 38075 S.

3.1.2 Filter transmission measurements for aerospace applications – GOES -13 filters

Four witness filter samples for the GOES-13 channel 6, 13.3 μm band, were measured as a special calibration test to the researchers at the Satellite Applications Branch (STAR)[3] of the National Oceanic and Atmospheric Administration (NOAA). The requirements were to measure transmittance with an f/6.5 beam geometry at sample temperatures of 296 K and 84 K at resolutions of 0.5 cm^{-1} and 0.2 cm^{-1} and also to compare results with an f/4 geometry at a sample temperature of 296 K. The provided samples were identified with serial numbers (SN) 1, 2, 4, and 28. The samples were all approximately 25 mm in diameter and 2 mm in thickness. They consisted of dielectric coatings on both sides of crystalline Ge substrates.

The measurements performed consisted of three components: (1) measurement of the filter transmittances under conditions that simulated as closely as possible their temperature and incident beam geometry as used in the satellite instrument, (2) dependence of the filter band passes on temperature, and (3) dependence of the filter band passes on incident beam geometry. All four filters were measured at temperatures of 84 K and 296 K, at normal incidence with an f/6.5 geometry and both spectral resolutions of 0.5 cm^{-1} and 2 cm^{-1}. One filter (SN 1) was also

[3] For information on STAR at NOAA, visit http://www.star.nesdis.noaa.gov/star/index.php

Table 1: Uncertainty estimates for ND filter transmittances, in % of measured values

Uncertainty source	**OD 1**	**OD 2**	**OD 3**	**OD 4**
Type B				
Inter-reflections	0.2	0.3	0.3	0.3
Detector non-linearity	0.1	0.1	0.05	0.05
Detector non-equivalence	0.2	0.2	0.1	0.1
Non-source emission	0.15	0.15	0.15	0.15
Beam non-uniformity	0.2	0.2	0.2	0.2
Beam displacement, deviation, focus shift	0.1	0.1	0.1	0.1
Beam-geometry, polarization	0.2	0.2	0.2	0.2
Sample vignetting	0.03	0.03	0.03	0.03
Sample scattering	0.02	0.02	0.02	0.02
Phase errors	0.1	0.1	0.1	0.1
Sample non-uniformity	0.3	0.4	3.5	4.0
Sample temperature	0.05	0.05	0.05	0.05
Sample aging	0.2	0.2	0.2	0.2
Quadrature sum	**0.59**	**0.68**	**3.5**	**4.0**
Type A				
Relative standard uncertainty in mean at 10.6 μm	0.2	0.2	0.5	2.0
Relative expanded uncertainty at 10.6 μm	**1.2**	**1.4**	**8.1**	**9.0**

measured at 81 K and 94 K. A separate set of transmittance measurements at room temperature were performed for all four filters at normal incidence with an f/4 incident beam geometry.

The sample temperatures were controlled by using a liquid-He-cooled cryostat in the schematic setup shown in Fig. 3. The transmittance spectra were measured using a Bomem DA-3 FTIR spectrometer with a Globar source, Ge coated KBr beamsplitter, and Deuterated TriGlycine Sulfate (DTGS) pyroelectric detector.

The sample was aligned to normal incidence by retro-reflecting the incident beam within ± 0.5°. Semi-circular half-blocks were placed in the beam just after the entrance paraboloidal and before the exit ellipsoidal mirrors in order to prevent inter-reflections among the interferometer, sample, and detector. The cryostat windows were tilted relative to the sample to prevent inter-reflections.

For each of the filter transmittance measurements, the filter was moved in and out of the beam to record sample and reference spectra, which were ratioed to produce the transmittance spectrum of the filter. Each sample or reference spectrum consisted of the Fourier transform of a co-addition of 512 or 128 successive interferogram scans of the FTIR, respectively. The process was repeated three times for each transmittance measurement in order to assess the effects of drift in the FTIR and positioning repeatability of the sample. The resulting transmittance spectra were averaged, and the standard deviation was used to produce a type-A uncertainty component for the repeatability of the measurements.

The sample temperature was set and monitored with a microprocessor-based temperature controller with PID (proportional-integral-derivative) control. The set temperature was stable to within ± 0.3 K during a run, after allowing approximately 1 h settling time. A Si diode temperature sensor at the top of the Cu sample holder in the cryostat, rated to ± 0.5 K uncertainty, was used to monitor the sample temperature. The estimated standard uncertainty in sample temperature is ± 0.6 K.

The f/6.5 normal incidence transmittance spectra at 84 K and 296 K for the four filters are shown in Fig. 6 through Fig. 9. In each figure frame (a) shows the transmittance at 0.5 cm^{-1} resolution, while frame (b) shows the transmittance at the reduced resolution of 2 cm^{-1} obtained by truncating the collected interferograms from the data shown in frame (a). Figure 6 also shows

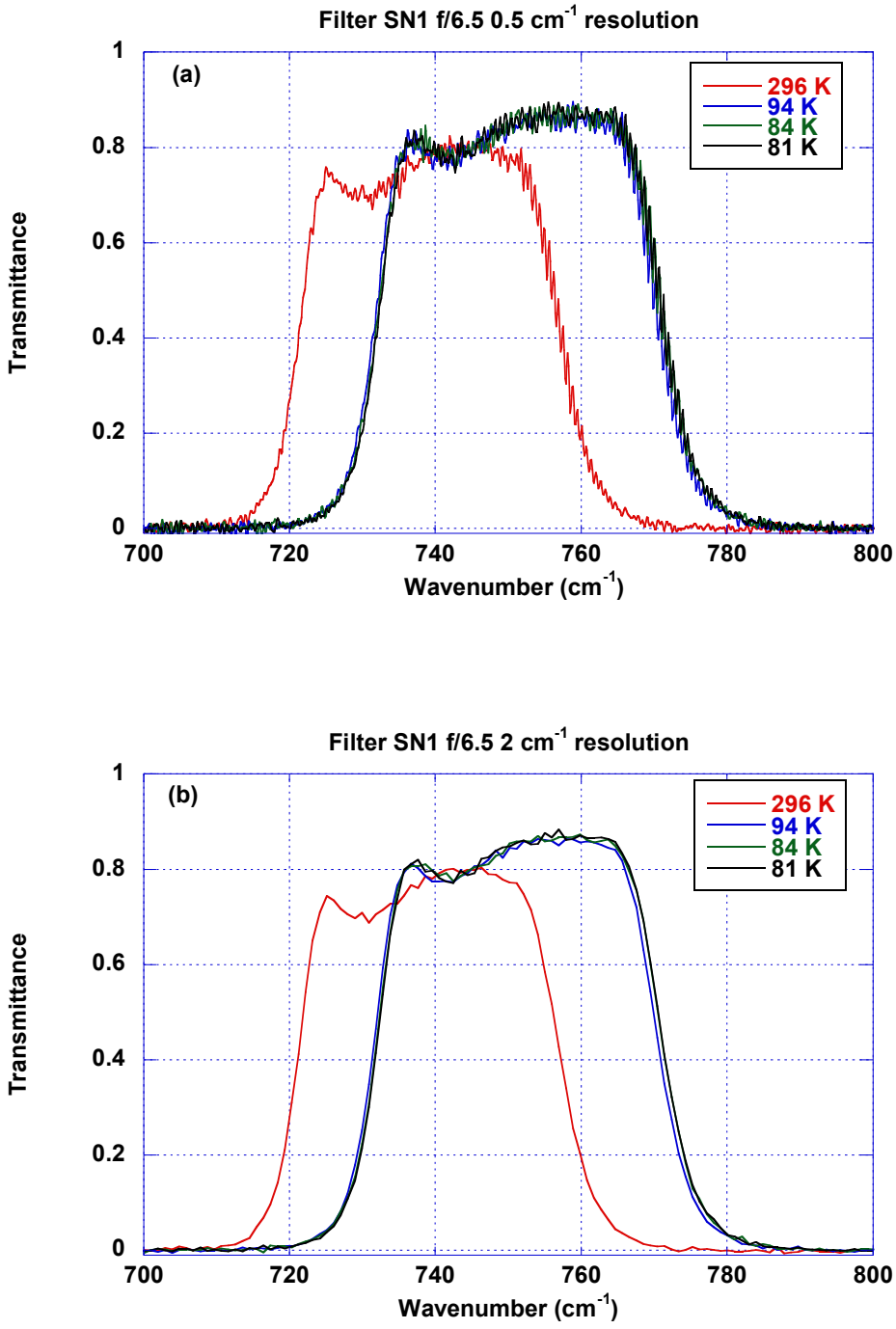

Figure 6: Transmittance of Filter SN 1 versus temperature at (a) 0.5 cm^{-1} and (b) 2 cm^{-1} resolution, f/6.5.

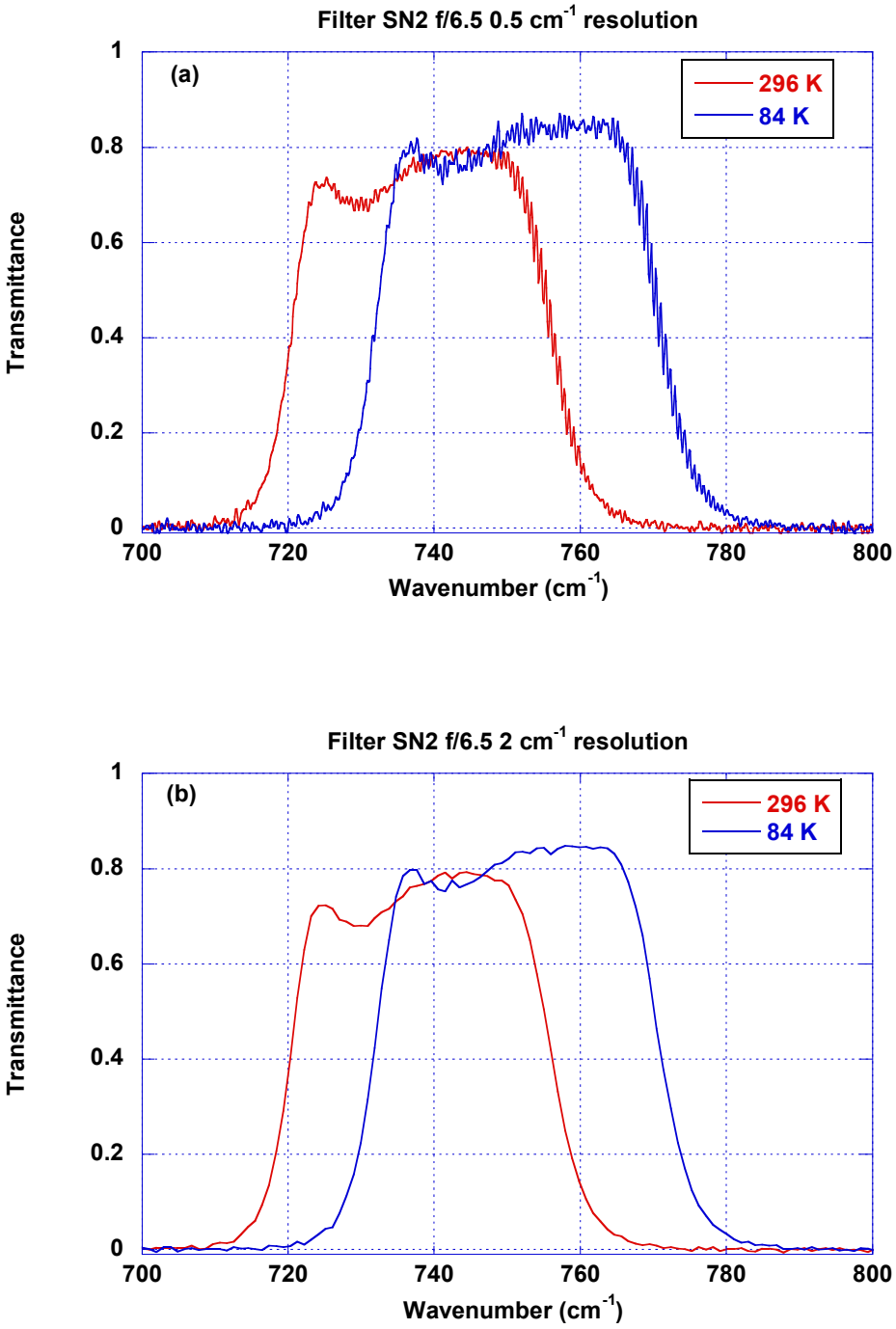

Figure 7: Transmittance of Filter SN 2 versus temperature at (a) 0.5 cm^{-1} and (b) 2 cm^{-1} resolution, f/6.5.

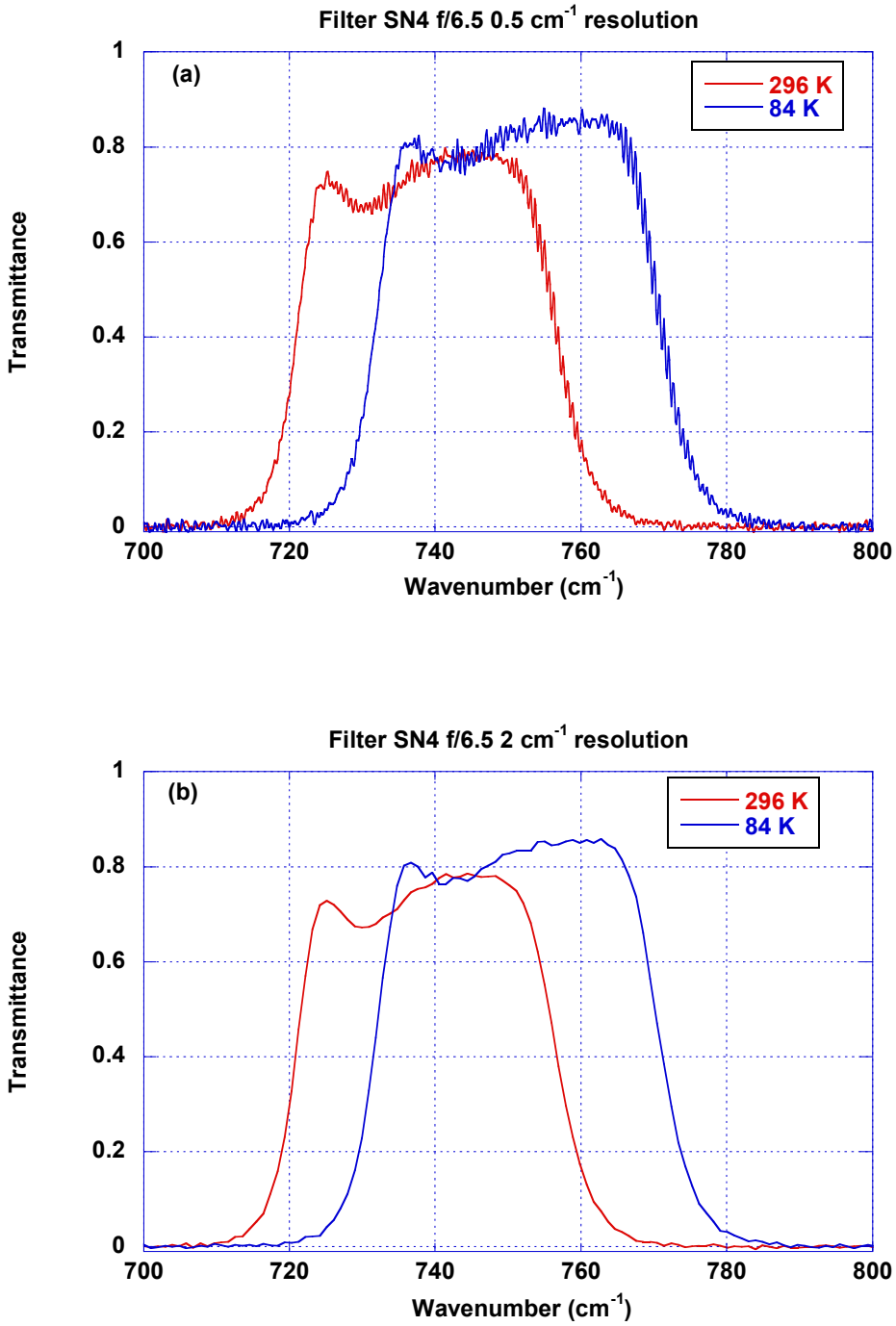

Figure 8: Transmittance of Filter SN 4 versus temperature at (a) 0.5 cm^{-1} and (b) 2 cm^{-1} resolution, f/6.5.

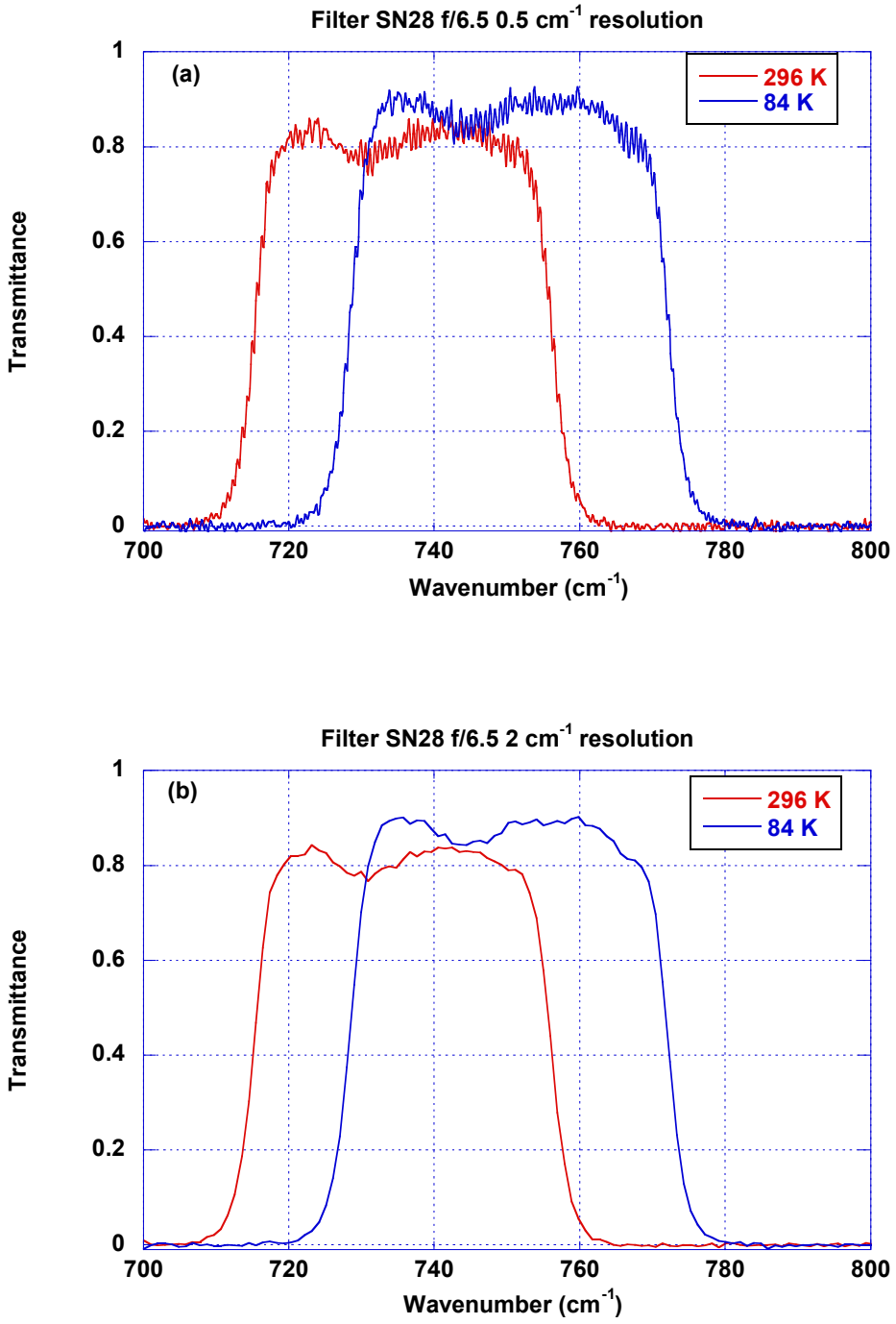

Figure 9: Transmittance of Filter SN 28 versus temperature at (a) 0.5 cm^{-1} and (b) 2 cm^{-1} resolution, f/6.5.

the data taken at 81 K and 94 K for Filter SN 1. The 0.5 cm^{-1} data for these filters show Fabry-Perot fringes due to interference in the Ge substrates. The fringes are eliminated by reducing the spectral resolution to 2 cm^{-1}, and the signal-to-noise ratio is increased as well. There does not appear to be a significant shift in the filter band edge positions between these two resolutions, as the 10 % to 90 % relative transmittance band edges are approximately 7.5 cm^{-1} to 10 cm^{-1} in width. The transmission band shifted to shorter wavelengths as sample temperature was reduced, as expected.

Figures 10 to 13 show the data taken at 296 K on each of the four filters at both f/4 and f/6.5 incident geometry. Shifts of approximately 0.5 cm^{-1} to 1 cm^{-1} are seen in the band edges for filters SN 1, 2, and 4, while almost no shift is seen for filter SN 28. Again, frame (a) in each plot displays the data at 0.5 cm^{-1} resolution and frame (b) at 2 cm^{-1} resolution. These results were presented to National Oceanic and Atmospheric Administration (NOAA) researchers as a calibration report with the data also made available in digital format.

3.1.3 Analysis of uncertainties in the transmittance data

3.1.3.1 Uncertainty in ordinate (transmittance) scale

The largest potential contributors to uncertainty in the ordinate scale for the GOES-13 filter transmittance measurements are errors due to detector nonlinearity, inter-reflections, beam geometry changes produced by the sample, non-source emission, and phase errors in the FTIR. These error sources have been investigated and estimates have been made of their size for IR neutral density filters [3, 4]. The chief difference for these measurements is the optically thick substrate, 2 mm thick Ge. The effects of sample emission are reduced because the filters are nearly non-absorbing in the bands of interest, especially at low temperature. The effects of inter-reflections are somewhat smaller for in-band measurements because of the filter anti-reflective design; the half beam blocks eliminate nearly all of this effect, along with the tilting of the cryostat windows.

Table 2 lists estimated ordinate relative uncertainty components. The various uncertainty components are added in quadrature to produce a combined systematic, type-B uncertainty component [8].

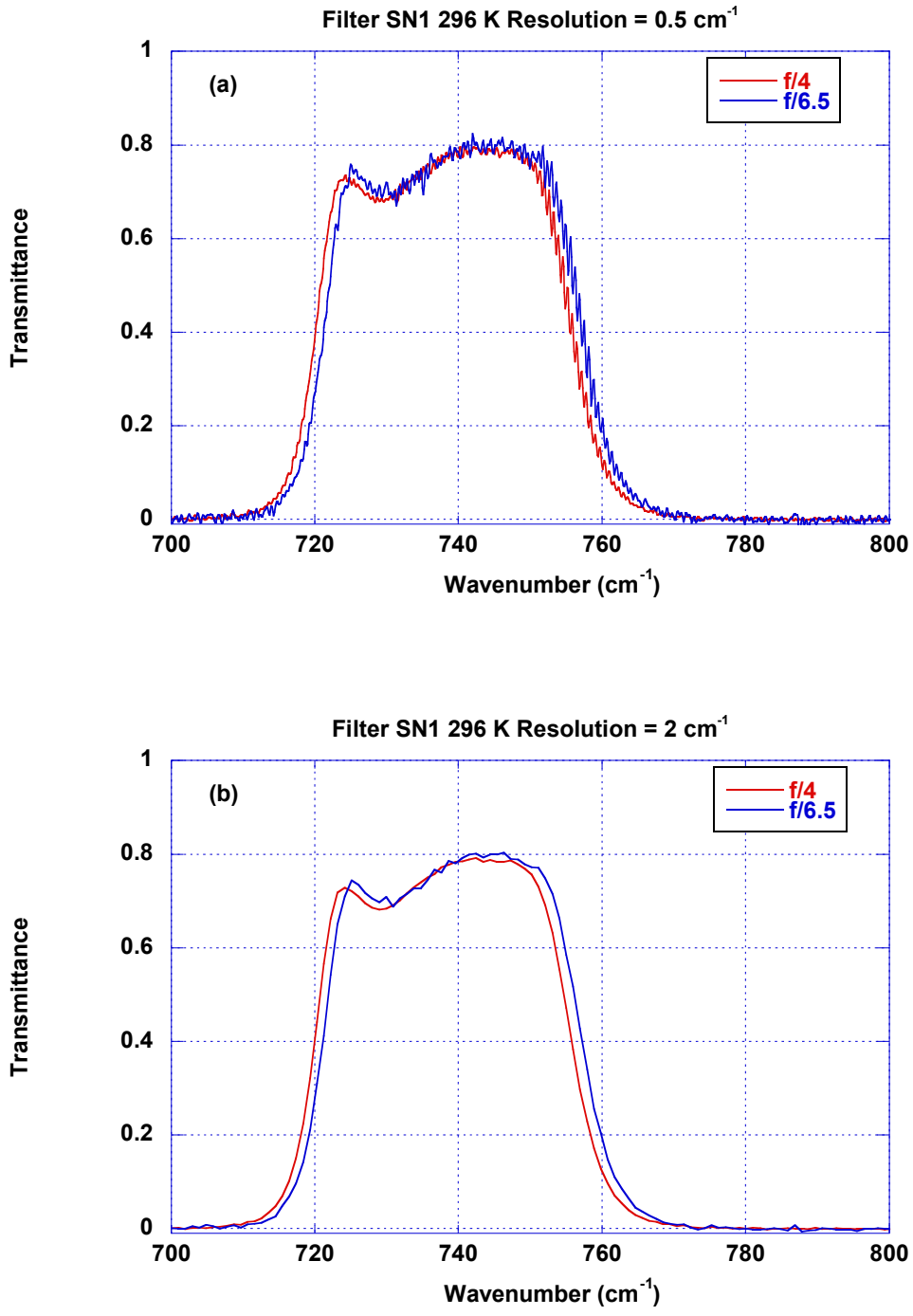

Figure 10: Transmittance of Filter SN 1 at 296 K, comparing f/4 and f/6.5 incident geometry, at (a) 0.5 cm^{-1} and (b) 2 cm^{-1} resolution.

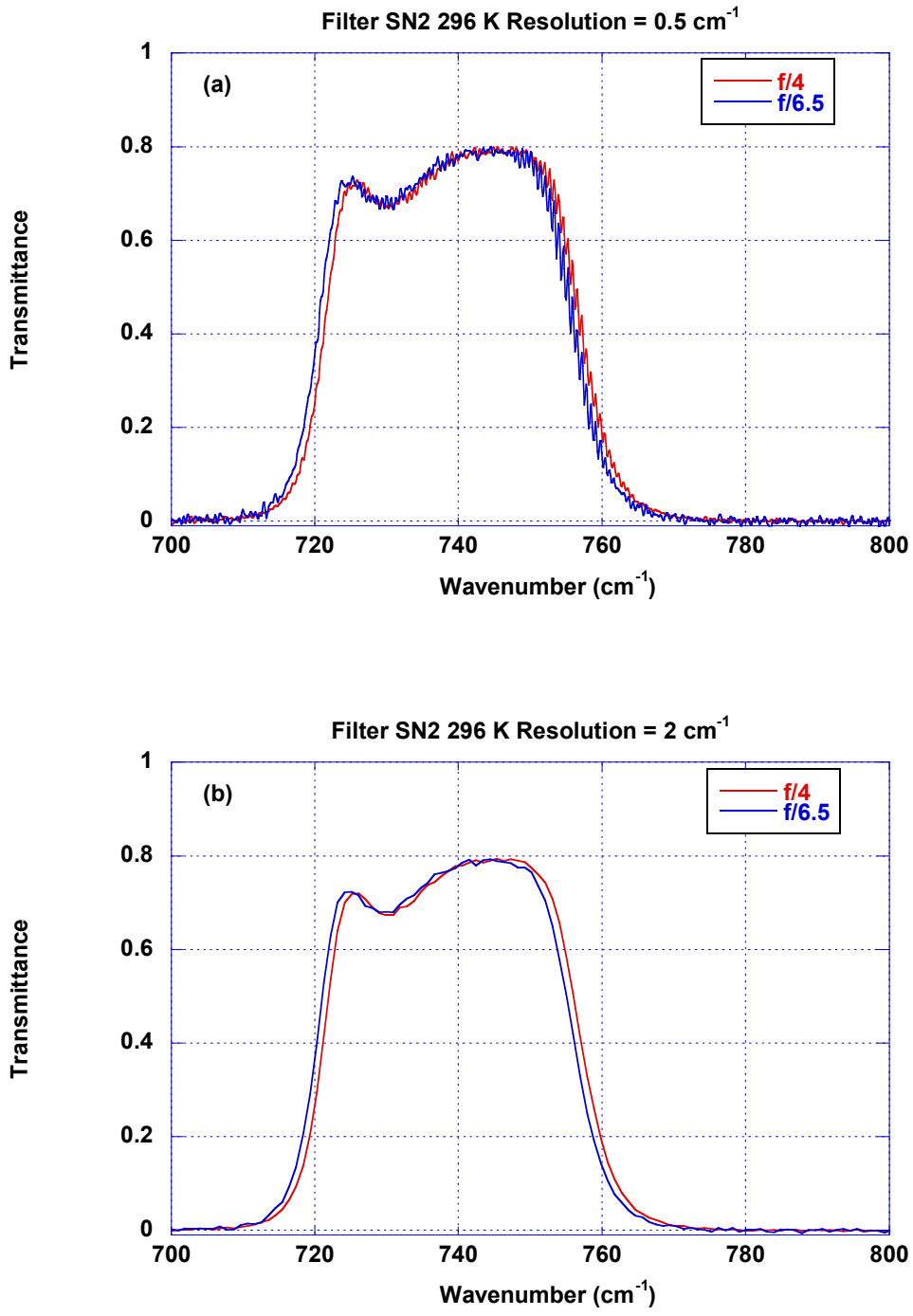

Figure 11: Transmittance of Filter SN 2 at 296 K, comparing f/4 and f/6.5 incident geometry, at (a) 0.5 cm^{-1} and (b) 2 cm^{-1} resolution.

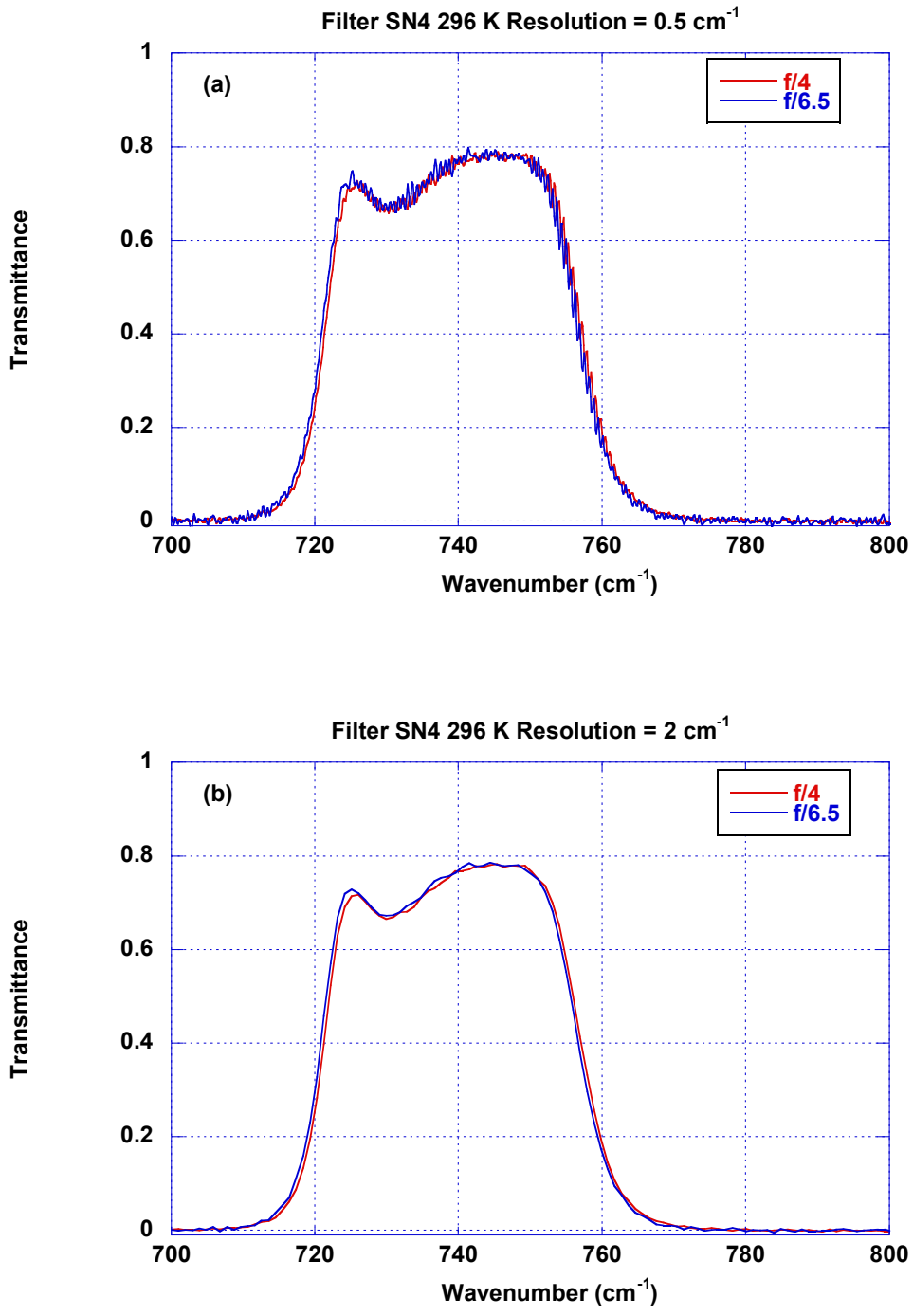

Figure 12: Transmittance of Filter SN 4 at 296 K, comparing f/4 and f/6.5 incident geometry, at (a) 0.5 cm^{-1} and (b) 2 cm^{-1} resolution.

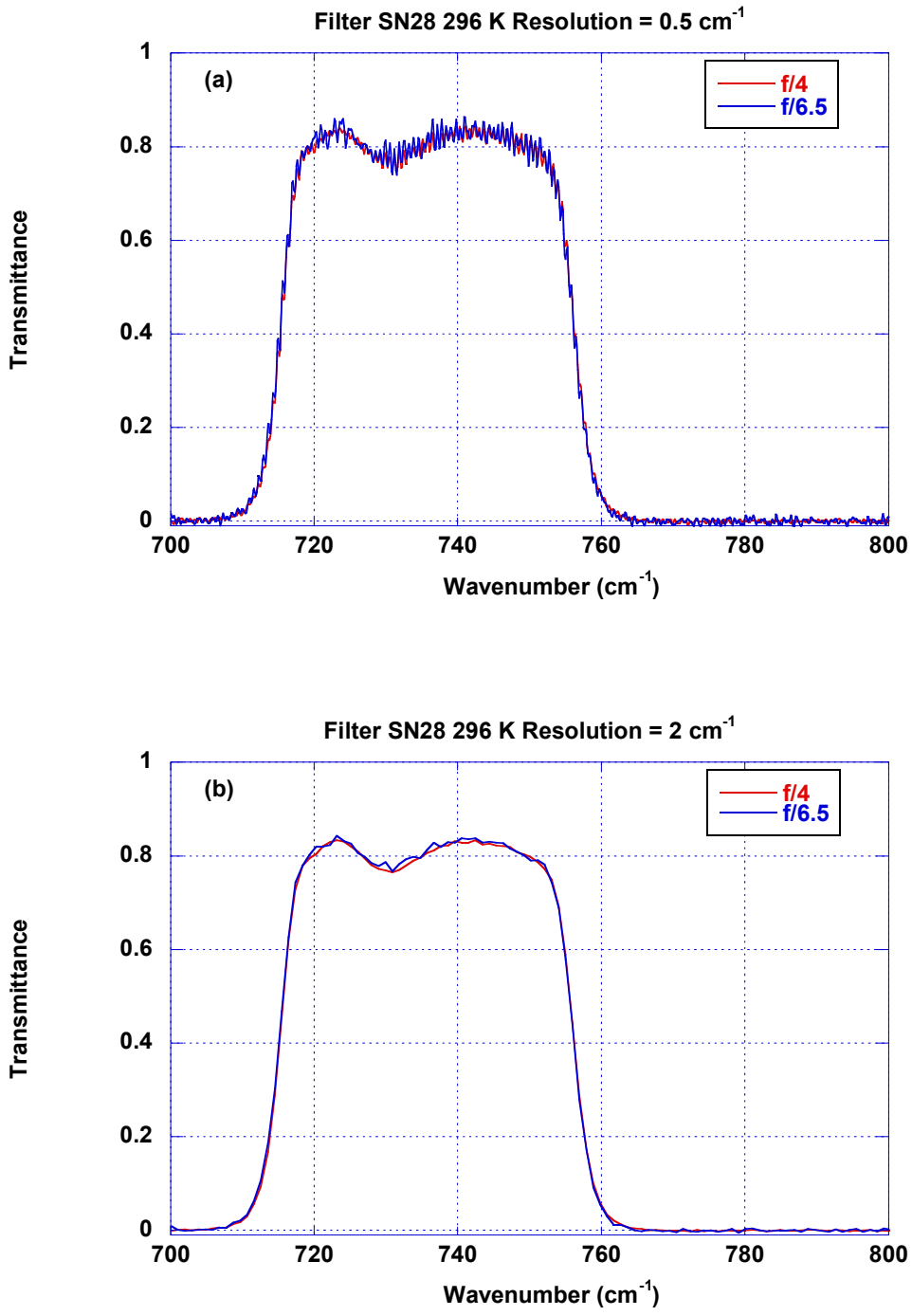

Figure 13: Transmittance of Filter SN 28 at 296 K, comparing f/4 and f/6.5 incident geometry, at (a) 0.5 cm^{-1} and (b) 2 cm^{-1} resolution.

Table 2: Type-B estimated relative uncertainty components for transmittance measurements of the narrow-band filters.

Detector nonlinearity	0.001
Inter-reflections	0.001
Beam-shifting from sample	0.004
Beam geometry/polarization	0.001
Sample emission	0.001
Sample vignetting	0.000
Sample scattering	0.000
FT Phase Error	0.003
Beam/sample/detector nonuniformity	0.001
Quadrature Sum	0.005

The final uncertainties for the in-band transmittance are dominated by beam-shifting from the sample and FT phase error. A type-A component evaluated from the standard deviation of successive measurements of each filter is then added in quadrature to the type-B component at each wavenumber, with the result multiplied by 2 to produce a final expanded uncertainty value with coverage factor k=2, representing a 95 % confidence interval [7].

3.1.3.2 *Uncertainty in abscissa (wavenumber) scale:*

The uncertainties in wavenumber can be divided into two classes: (1) intrinsic wavenumber uncertainty in the FTIR instrument and (2) uncertainty in the filter edge positions propagating from uncertainties in temperature, beam geometry and average angle of incidence, non-uniformity in the coating thickness, and the wavenumber-dependent radiometric error sources listed above [2]. The intrinsic wavenumber uncertainty of the FTIR instrument is small, and is reduced by measuring the positions of H_2O and CO_2 vapor lines and comparing with handbook values. The main component of wavenumber error comes from the difference between the average HeNe laser path and the IR beam path, including the imperfect collimation of the IR beam coming from the finite source size. The error tends to be linear in wavenumber, allowing a constant correction factor to eliminate most of it. We have measured vapor lines and applied appropriate corrections; the residual relative wavenumber errors are estimated to be on the order of 5×10^{-6}. A comprehensive discussion of the wavenumber accuracy in our FTIR measurements can be found in Ref. 2 which is a report of the development of polystyrene films (SRM 1921) for calibrating the wavelength scale of infrared spectrophotometers at the FTIS facility.

More important sources of error in the measured filter edge positions include the geometry and temperature effects listed above. We did not test for the effects of filter non-uniformity. The shift of the filter edge is linear in temperature and quadratic in angle of incidence. For these measurements, uncertainty in the actual incident flux distribution in the nominally f/6.5 beam leads to an appreciable additional component of wavenumber uncertainty. Combined nonlinearity and phase error in the FTIR can affect the sign of the spectrum near the band edge and thus produce a shift in the apparent edge position.

Table 3 lists uncertainty components in cm^{-1} for the filter band edge positions for the four measured filters due to instrument wavenumber error, temperature, angle of incidence, focusing geometry, non-uniformity, phase error, and wavenumber-dependent radiometric (transmittance scale) error. The contributions are added in quadrature and the result multiplied by 2 to give an expanded $k = 2$ uncertainty.

Table 3: Sources of uncertainty in the filter edge positions, along with the quadrature sum and $k = 2$ expanded uncertainty for each filter. The values are given in cm^{-1}.

	Uncertainty component (cm^{-1})
Instrument Wavenumber Error	0.02
Temperature	0.05
Angle of Incidence	0.1
Focusing Geometry	0.1
Phase error	0.2
Ordinate Error	0.03
Quadrature Sum	*0.25*
Expanded Uncertainty	**0.51**

3.2. The Infrared Reference Integrating Sphere (IRIS) setup

The schematic in Fig. 14 shows the integrating sphere measurement geometry at the NIST FTIS facility for diffuse reflectance measurement; for diffuse transmittance measurement with the sphere, the arrow (input beam) comes from below the sample. We can obtain specular (regular) reflectance indirectly by performing specular/diffuse measurement. In addition to those terms defined earlier, the following definitions and symbols are used for describing the measurements.

- *reflectance factor R:* the ratio of flux reflected from a surface to that reflected from a perfect reflecting diffuser under the same incident beam geometry.
- *directional-hemispherical reflectance (DHR)* $\rho_{\gamma,h}$*:* reflectance, where the incident flux is confined (in a narrow range) to a single direction to an input angle γ as, for example 8 degrees off normal and the reflected flux is collected over the complete hemisphere above the surface.
- *hemispherical-directional reflectance factor (HDRF)* $R_{h,d}$*:* reflectance factor, where the incident flux is uniformly distributed over the hemisphere above the surface, and the measured reflected flux is collected (in a narrow range) in a single direction (θ,φ).
- *bidirectional reflectance distribution function* (*BRDF*) $f(\gamma; \theta, \varphi)$: the ratio of reflected radiance from, to incident irradiance on, a surface, where γ represents the input angle geometry, as, for example 8 degrees off normal, and θ, φ the exit angles of the reflected light. This quantity gives a complete description of the manner in which a sample reflects light.
- *integrating sphere throughput* (or simply, *throughput*), $\tau = \Phi_d/\Phi_0$ the efficiency of the integrating sphere system, where Φ_d is the flux incident on the detector, and Φ_0 the input flux. [***Author's Note****: we will use τ for throughput only in this part of section 3.2 and revert to designating transmittance starting again with section 3.2.3*]
- *measurement ratio,* $\rho_0 = V_s/V_r$, , where V_s is the measured signal in the sample reflectance geometry and V_r is the signal in the reference geometry. The signals can be single beam spectra in the FTIR.

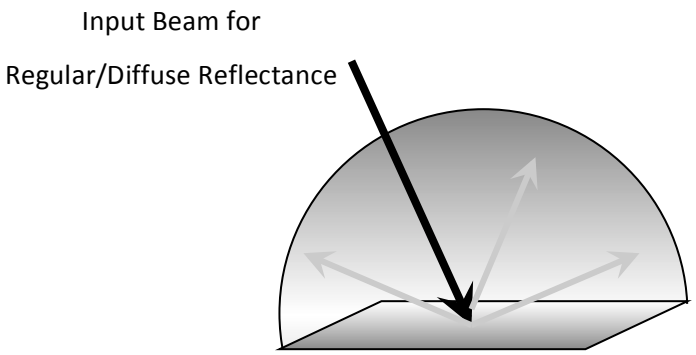

Figure 14: Sphere measurement geometry for directional-hemispherical: single direction input and detection over all angles. The schematic shows the setup for Regular/diffuse measurement. For diffuse transmittance measurement the input beam is from the bottom of the sample.

One of the authors, Leonard Hanssen, developed the absolute DHR method at NIST and designed the integrating sphere that was custom made and implemented the setup for the calibration service 38075 S. The complete details of the method and comparison to other methods can be found in Ref. 9.

The measurement method involves a one-time characterization of the sphere throughput uniformity over the entire sphere, relative to the specular reflection direction. Subsequent characterization of samples involve simply performing the reflectance ratio measurement to produce a DHR value, $\rho_0 = V_s/V_r$. (Details of the sample and reference measurement geometries discussed here are provided in Section 3.2.3). Small corrections to ρ_0 can be performed to reduce the uncertainty. For a sample known to be nearly Lambertian, the correction to ρ_0 is given by Eq. (3):

$$\rho = \frac{\rho_0}{\tau'_{\text{avg}}} \tag{3}$$

$$\tau'_{\text{avg}} = \frac{1}{2\pi} \int_0^{2\pi} \int_0^{\frac{\pi}{2}} \{\tau(\theta,\varphi) / \tau_0\}.\sin(\theta).d\theta.d\varphi \quad , \tag{4}$$

where Eq. (4) is the relative throughput (relative to the throughput (τ_0) in the specular direction) averaged over the sphere surface and (θ,φ) are the output angles of the reflected light leaving the sample. For a sample with arbitrary scattering character, we would use Eq. (5),

$$\rho = \rho_0 \frac{(1+1/\tau'_{\text{avg}})}{2}, \tag{5}$$

and cite a relative expanded uncertainty given by Eq. 6,

$$U = \frac{\{(\frac{1}{\tau'_{\text{avg}}})-1\}}{2}, \tag{6}$$

reasoning that most samples would have the reflected light encounter a sphere throughput somewhere in between the perfectly specular and perfectly diffuse case.

For some samples, such as the DHR standards, a reduction in the uncertainty of the DHR values can be achieved by directly measuring the sample's scattering character, i.e. by measuring its bi-directional reflectance distribution function (BRDF), $f(8°;\theta,\varphi)$ under the sphere measurement condition of 8° incidence angle. After further analysis, Hanssen in Ref. 9 arrives at the following expression where the absolute DHR will be realized by combining four measured quantities: (1) a ratio of sample (V_s) to reference (V_r) measurements with the sphere system, V_s/V_r (or ρ_0) ; (2) a ratio of sample-removed (V_{0s}) to reference (V_{0r}) measurements with the sphere system, V_{0s}/V_{0r}; (3) the relative sphere throughput, as a function of polar (θ) and azimuthal (φ) angles (relative to the sample surface), $\tau(\theta, \varphi)/\tau_0$, where τ_0 is the throughput for the direction corresponding to the sample-removed measurement (generally, the specular direction); and (4) the relative BRDF of the sample for the incidence (8^0) angle of the sphere measurement, $f(8^0; \theta, \varphi)/f_0$, where f_0 is an arbitrary constant.

Then the absolute DHR is given by

$$\rho_{8°,2\pi} = \rho_0 \frac{V_{0r}}{V_{0s}} \left[\frac{\int_0^{2\pi} \int_0^{\frac{\pi}{2}} \left[f(8^0;\theta,\varphi) / f_0 \right] \sin(2\theta) d\theta d\varphi}{\int_0^{2\pi} \int_0^{\frac{\pi}{2}} \left[f(8^0;\theta,\varphi) / f_0 \right] \left[\tau(\theta,\varphi) / \tau_0 \right] \sin(2\theta) d\theta d\varphi} \right]. \quad (7)$$

Effectively, the four measurements that form the term outside the brackets of the right-hand side of Eq. 7 reduce to a ratio of the sample-in signal (V_s) to the sample-out signal (V_r) (properly corrected for sphere throughput change). Measurements of V_{0s}/V_{0r} for an IR sphere with the NIST geometry vary from 1 by only 0.2 % to 0.5 %. In this case the sample removed measurement becomes unnecessary for diffuse samples where the other sources of uncertainty may be significantly larger. For specular samples, the sample removed measurement is useful to obtain the highest accuracy.

By combining BRDF and integrating sphere measurements, the NIST method appears to combine redundant information, since a complete BRDF measurement over a

hemisphere of output angles can also be used to obtain $\rho_{\gamma,h}$. However, it is difficult to obtain sufficiently accurate BRDF over a sufficiently large fraction of the hemisphere (to viewing angles near grazing) to obtain an accurate $\rho_{\gamma,h}$ value. For the method described above, however, only relative BRDF are required. Since Eq. 7 contains a ratio of integrals over the same hemispherical angular range, if the measured data are not complete or require extrapolation, the ratio effectively removes a significant part of the error that would remain in both individual components. Note that if the throughput is perfectly uniform, the relative throughput $\tau(\theta,\varphi)/\tau_0=1$, and Eq. 7 reduces to $\rho_{\gamma,h} = \rho_0$, so that corrections to the directly measured reflectance ratio are only to the extent of the throughput non-uniformity. Note also that there always is one non-uniform feature: the entrance port. For the NIST sphere, for a Lambertian sample, the entrance port loss is ≈1 %.

3.2.1 Description of the integrating sphere

The integrating sphere system has been designed and constructed [11] according to the specifications detailed in the following paragraphs. A photo of the integrating sphere is shown in Fig. 15. The description and analysis of the detector/nonimaging concentrator system of the sphere has been described in Ref. 12. The system consists of a nonimaging compound hyperbolic concentrator (CHC) and a lens in front of 6 mm diameter Hg:Cd:Te (MCT) detector. The CHC was fabricated out of electroplated nickel with a polished stainless steel mandril and was gold coated. The lens material chosen was potassium chloride which has one of the lowest refractive indices of IR lens materials and is the most suitable for reducing the Fresnel effects of the lens. The CHC and the lens restricted the field of view (FOV) of the detector with minimal loss in the throughput of the integrating sphere.

The inside wall of the sphere is coated with a material that is a nearly Lambertian diffuser and at the same time has a high directional hemispherical reflectance (≥ 0.9) for the infrared spectral range: plasma sprayed copper on a brass substrate, electroplated with gold.

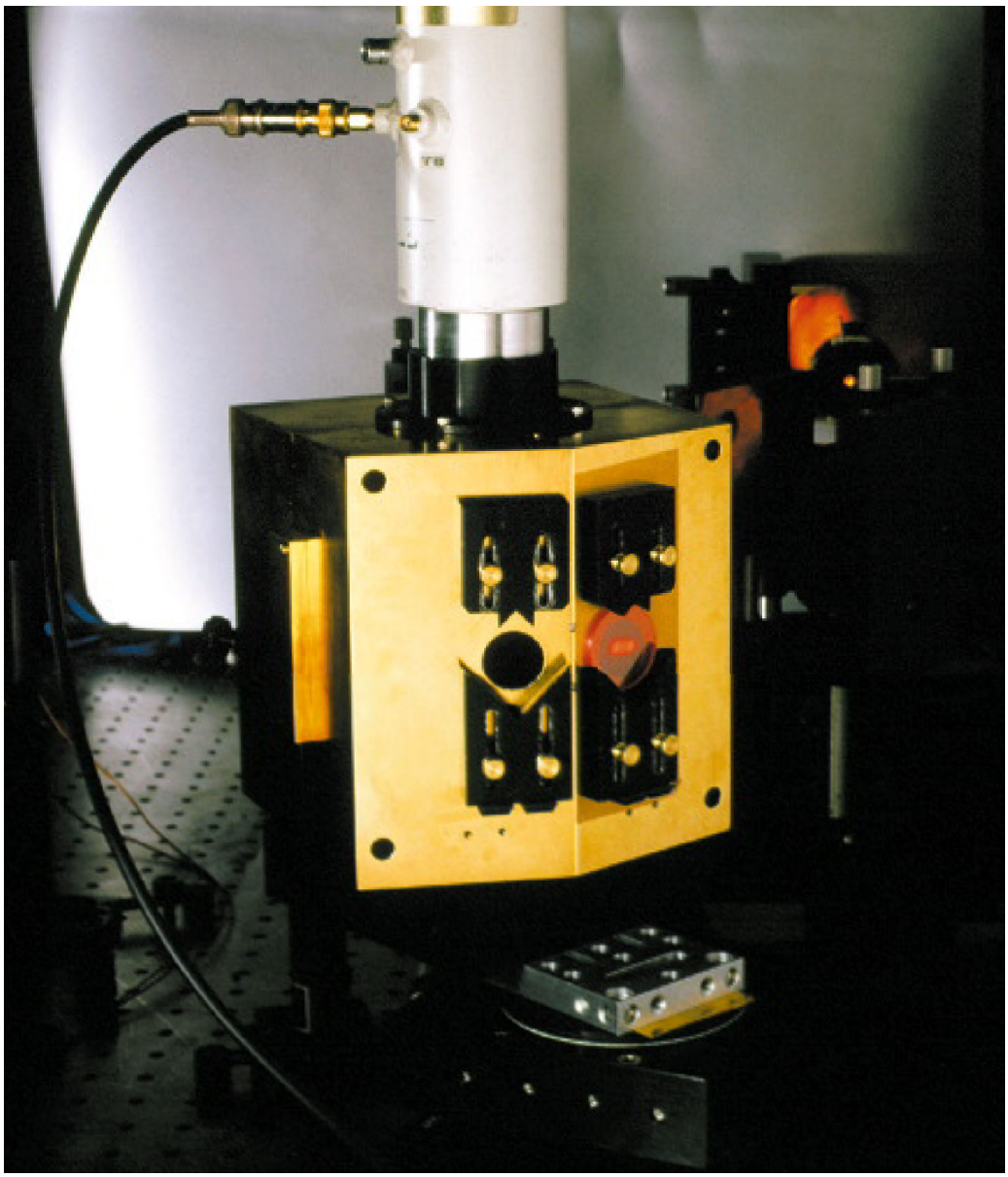

Figure 15: Photograph of the integrating sphere for absolute infrared spectral transmittance and reflectance. On the top is mounted an LN_2 cooled MCT detector with a built-in compound hyperbolic concentrator and lens which views the bottom of the sphere. To the right is some of the FTIR interface optics, which brings the beam into the sphere through the entrance port on the sphere side hidden from view. The reference (empty) and sample (with a KRS-5 window) ports can be seen with adjustable mounts astride them. Due to scattering in the sample, the focused FTIR beam is visible in the center of the sample.

The sphere has entrance, sample, and reference ports all centered on a great circle of the sphere as shown in Fig. 16. There also is a detector port, with its center located along the normal to the great circle. The MCT detector dewar located on the port can be seen mounted on the top of the sphere in Fig.15 and Fig. 16. The detector's field of view is centered on the same normal and corresponds to the bottom region of the sphere. The sample and reference ports are located symmetrically with respect to the entrance port and can be seen in the foreground of Fig. 15 (the sample port has a KRS-5 sample mounted on it).

The exact locations of the sample and reference ports are in general determined by the angle of incidence for which the reflectance and transmittance are to be determined. An arrangement of ports could, in principle, be set up for any angle of incidence from approximately 2° to 28°, and 32° to 75°, depending on the input beam geometry of the source (or spectrophotometer). For this sphere, we have selected port locations for 8°, which is close to normal incidence, yet for which no portion of the f/5 (6° half angle) input beam will be reflected back onto itself. [For incidence angles in the neighborhood of 30°, a variation of the design would be required so that the reflected beam from the sample port does not hit the reference port and vice-versa.] The entrance port is of sufficient size (3.3 cm dia.) to accept the entire input beam, and the sample and reference ports are also sized (2.22 cm dia.) to accept the entire beam (at the focus, in a focused geometry). All the ports are circular in shape, with the sphere inside and outside surfaces forming a knife-edge at the port edge where they meet. In this sphere, as seen in Fig. 16, the measurement of reflectance is designed for an incident angle of 8° (in general θ), the sample and reference ports are located at 16° (in general $+2\theta$) and -16° (in general -2θ), respectively, measured from the center of the sphere and with respect to the line through the sphere center and the sphere wall (at a point directly opposite the entrance port). Baffles separating the detector port and the detector field-of-view region from the sample and the

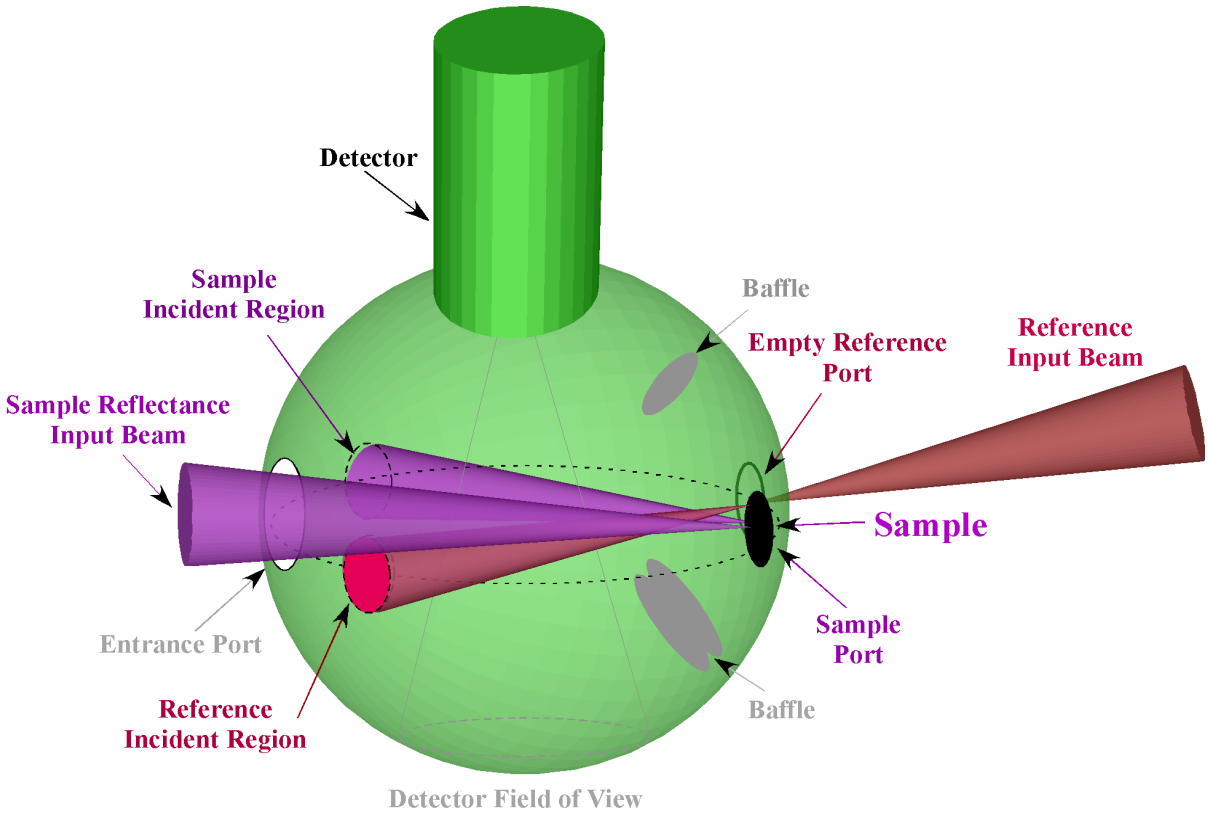

Figure 16: Schematic of the integrating sphere geometry.

reference ports are shown in Fig. 15. The baffles are critical to the sphere performance for characterization of diffuse samples. The spatial non-uniformity of the integrating sphere throughput has been evaluated at 10.6 μm wavelength using a CO_2 laser system [10] using diffuse baffles as well as specular baffles. The relative throughput mapping ($\tau(\theta,\varphi)$ /τ_0) was performed across the entire spectral measurement range of 1 μm to 18 μm using the FTIR beam itself as the source [13]. The specular baffles design showed superior throughput performance. In a raw measurement the diffuse baffle case results were 4.5 % to 9 % below the actual hemispherical reflectance, whereas this is reduced to only 2.5 % for the specular baffles case.

The arrangement of the ports described above will result in the regions of the sphere wall illuminated by the specularly reflected or transmitted light and the reference beam to be centered on the same great circle as the entrance, sample and reference ports. In addition, the regions will be symmetrically positioned around the entrance port. The reflected or transmitted light also will be incident at the same angle on these regions. As a result, the reflected or transmitted light will have nearly identical throughput to the detector. The procedure for orienting the sphere for the reflectance, transmittance and reference measurements is described in Section 3.2.2.

3.2.2. Sphere mounting and manipulation hardware

The sample and reference mounts, a pair of which can be seen on the sphere in Fig. 15, are constructed to hold the sample against and centered on the sample port from the outside of the sphere. During sphere movement, the holders prevent the sample from moving or shifting relative to the sample port. This is done in such a way as to leave the back of the sample free and open, so that the beam centered on the sample can proceed through it (for a transparent sample) without obstruction. This is required to perform either transmittance or reflectance measurements on transparent samples. This arrangement can also be used to check thin-film mirrors for optical opacity. In such a case, after passing through the sample, the beam travels to the purge box enclosure wall, covered by a diffuse black cloth. The reflected light from this black cloth, which returns to the integrating sphere was measured to be less than 0.5×10^{-4}.

The integrating sphere system includes two motorized rotation stages stacked on top of each other. The stages are mounted with their axes of rotation parallel to each other. The rotation axes of the stages are identified in Fig. 17, where each sketch is a top view of the sphere.

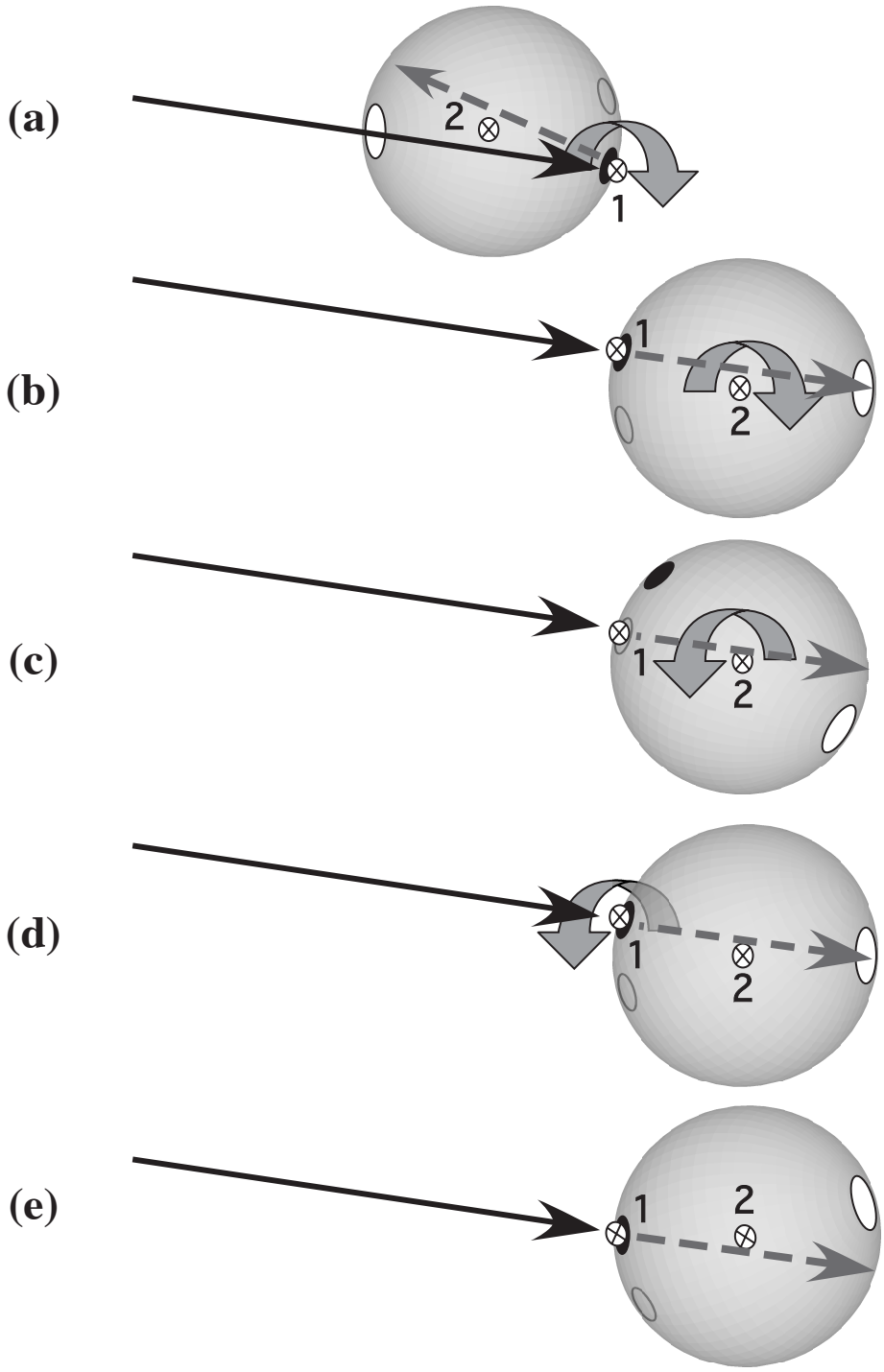

Figure 17: Sphere measurement geometries for reflectance and transmittance and rotation steps used to orient the sphere for each (a) reflectance measurement geometry, (c) reference measurement, and (e) transmittance measurement geometry, (b) and (d) are used for the diffuse component of transmittance.

Stage #1 has its axis of rotation oriented parallel to the normal of the great circle formed by the entrance, sample and reference port centers, as well as passing through the edge of this circle. This base stage remains fixed to the optical table. Its rotation axis is perpendicular to the input beam and passes through the beam focus position. Stage #2 is mounted on the rotation table of the base stage so that its axis of rotation is located a distance away from the base stage axis exactly equal to the sphere radius. The integrating sphere is mounted to the rotation table of stage #2 so that the stage's axis of rotation is along the sphere axis that includes the center of the detector port and the sphere center. Two rotation stages, stage 1 centered at the input-beam focus and sphere wall and stage 2 centered at the sphere center, are used to change geometries.

The function of the base stage (#1) is to vary the angle of incidence of the input beam on the sphere surface and to switch between reflectance and transmittance measurement geometries. The function of the stage #2 is to select between the entrance, sample and reference ports for the beam to be incident upon.

3.2.3. Configuring the Integrating sphere for measuring, ρ, τ, α, and ε

The arrangement of the input beam and the integrating sphere for absolute reflectance and transmittance measurements is shown in Fig. 17. The sample reflectance measurement setup is shown in Fig. 17 (a) (as well as in Fig. 16), the reference measurement in Fig. 17 (c), and the sample transmittance measurement in Fig. 17 (e). In each diagram, the rotation required to reach the following diagram is shown as a curved arrow around the appropriate rotation axis. In the reflectance measurement geometry (a), the input beam passes from the FTIR spectrometer through the sphere entrance port and onto the sample surface facing the sphere. This is the typical reflectance geometry for directional-hemispherical sample reflectance in most sphere systems. The only difference in (a) is the empty reference port (as opposed to one occupied with a standard for a relative measurement). Upon reflection off the sample, the beam transverses the sphere and is incident on a region we will denote as the 'sample specular' region (see Fig. 16). From this point, the reflected flux is distributed throughout the sphere in an even fashion due to the Lambertian coating and 'integrating' nature of the sphere.

In Fig. 17(a) a clockwise rotation about axis #1 turns the back of the sample to the beam in Fig. 17(b). An additional clockwise rotation about axis #2 places the (empty) reference port at the input beam focus in (c) where it continues on to strike the sphere wall at the reference specular region (labeled in Fig. 16), producing the reference measurement. Figure 17(b) further illustrates the beam geometry for the reference measurement. Another counterclockwise rotation about axis #2 results in (d), a repeat of (b). A final counterclockwise rotation about axis #1 positions the sphere in (e) for the transmittance measurement, with the same, as in Fig. 17(a), angle of incidence on the sample and incidence region on the sphere wall (the sample specular region).

For absolute specular reflectance the reference measurement, Fig. 17(c), the input beam is not moved, but enters the sphere through the empty reference port, transverses the sphere, and is incident on a spot denoted as the 'reference specular' region (Fig. 16) This somewhat unusual geometry is chosen in order to achieve the highest degree of symmetry between the reflectance and reference measurements. The sample and reference specular regions are symmetrically located on either side of the entrance port. Because of the symmetry of the sphere design, the throughput is very nearly equal for these two regions. Since the only other difference between the sample reflectance and reference measurements is the initial reflection off the sample, the ratio of sample reflectance and reference measurements is equal to the absolute sample reflectance (for specular samples). Various sources of error, including the difference in the sample and reference specular region throughputs, can be included in the expanded measurement uncertainty, or can be corrected for. The important feature of this measurement technique is there is no need to use a reference reflectance artifact as a standard for reflectance measurement. The integrating sphere itself serves the purpose.

For absolute transmittance, the geometry shown in Fig. 17(e) is similar to the reference measurement geometry, except that the sphere is again reoriented with two rotations so that the input beam is incident on the back side of the sample surface mounted on the sample port. The regularly transmitted beam transverses the sphere and is incident on the same specular region as in the reflectance geometry case, Fig. 17(a). The ratio of the transmittance measurement to the reference measurement, Fig. 17(c) is equal to the absolute sample transmittance (for specular samples).

By conservation of energy, the absolute absorptance is indirectly obtained by subtracting the sum of the absolute reflectance and transmittance from unity. The reflectance and transmittance measurements are made under identical conditions of geometry and wavelength(s). The input beam is incident on opposite surfaces of a sample for the reflectance and transmittance measurements. For a uniform sample with identical front and back surfaces, the side of incidence is immaterial. For samples with some asymmetry, due to for example, a coating on one or both sides, the sample can be reversed to make a pair of reflectance measurements and obtain the corresponding pair of absorptance results. And, by Kirchoff's Law (Eq. 2), this process provides the sample emittance. Due to this equality of absorptance/emittance, we limit further discussion to only absorptance, but with the understanding that "emittance" can be substituted for "absorptance" at all times.

3.2.3.1. Measurement conditions and sphere characterization

The FTIR was configured in two separate modes, a near-infrared mode with a tungsten-halogen lamp and coated quartz beamsplitter for the spectral region of 1 μm to 3 μm (10,000 cm^{-1} to 3,300 cm^{-1}), and a mid-infrared mode with a SiC source and coated KBr beamsplitter for the region of 2 μm to 18 μm (5,000 cm^{-1} to 550 cm^{-1}). The spectral resolution is either 4 cm^{-1} or 8 cm^{-1} for all results shown.

Every plot of transmittance and reflectance is obtained by the following procedure. A number of alternating measurements of reference, sample reflectance, and sample transmittance (where appropriate) single beam spectra, are performed according to Fig. 17, and repeated between 8 and 24 times. For each repetition, the transmittance and reflectance are calculated by taking ratios of the corresponding single beam spectra and a reference single beam spectrum (obtained by interpolation to reduce error due to instrumental drift). From the resulting series of individual transmittance and reflectance spectra, the mean transmittance (τ) and reflectance (ρ), along with the standard deviation and standard error, spectra are calculated. Finally, the absorptance spectrum is obtained from Sec. 2 Eq. 1.

Each single beam spectrum is obtained by coadding 512 or 1024 scans of the FTIR. The total measurement time for most of the results shown is several hours (from 2 to 10). The long measurement times are required to obtain the lowest noise level in the spectra. For less stringent

requirements of 1 % uncertainty, shorter measurement times on the order of 10 min to 20 min will suffice.

In addition to the various potential sources of error due to the Fourier transform spectrometer, [Appendix A] several other sources of error may play a role in the sphere system measurements. These are: (1) spatial non-uniformity of the sphere wall regions directly illuminated by the input beam (reference specular region) or sample first reflection (sample specular region); (2) non-uniformity of the throughput of the sphere wall region directly illuminated by the input beam as compared to the region illuminated by the sample first reflection; (3) overfilling of the entrance port in the sample reflectance measurement; and (4) overfilling of the sample port in any of the measurements.

Regarding error source (1), the spatial non-uniformity of the sphere, the throughput evaluation at the 10.6 μm by use of the CO_2 laser system [9] showed the local spatial variation across the region illuminated directly by the reference beam or indirectly by a specularly reflected or transmitted beam is approximately ± 0.4 % [8]. A translation of the incident light on the sphere wall of 0.5 cm through deflection or deviation (of 2°), should result in a ± 0.1 % relative change in throughput. Thus a transmittance measurement of a sample with an effective wedge of 1° could lead to a 0.1 % relative error in transmittance. Due to the decrease in wall reflectance and corresponding decrease in throughput with decreasing wavelength, the error due to spatial non-uniformity is greater at shorter wavelengths, especially in the near infrared approaching 1 μm [7].

Regarding error sources (2), the difference in throughput between sample and reference port measurement geometries can lead to a small relative error, varying between 0 % and 0.5 %, depending on wavelength. The direct measurement of transmittance or reflectance for specular samples will include this error, but an additional measurement of the transmittance ratio of empty sample and reference ports can be used to correct for the error. This has been done with good reproducibility, and need not be repeated unless the optical input system geometry or alignment is altered. A plot of such a throughput ratio is shown in Fig. 18. Besides the generally featureless spectral curve, a sharp structure occurs at approximately 8.5 μm. This structure occurs at the only wavelength where the incident beam from the FTIR is significantly polarized.

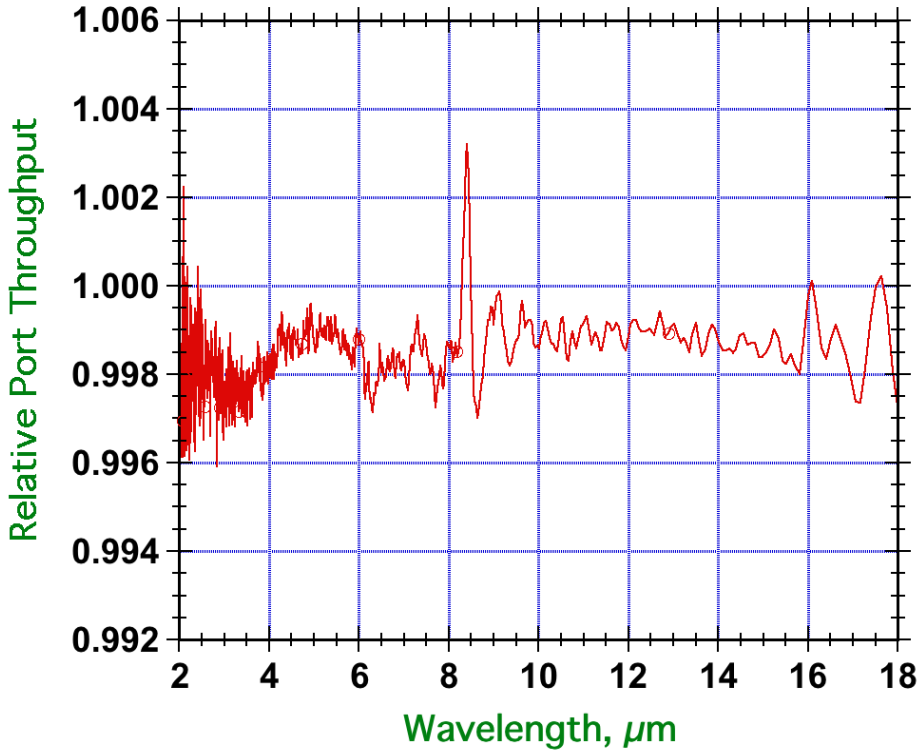

Figure 18: Sample and reference port throughput comparison, the result of an empty sample port transmittance measurement. The curve represents the difference in detector signal for specularly transmitted and reflected light from the sample as compared to light in the reference case. This spectrum can be used in either of two ways: (a) as a component to the systematic uncertainty of the ρ or τ, or (b) as a correction spectrum to divide into the initially obtained spectra of ρ or τ, to eliminate the error.

For specular samples, a correction must be made to the measured transmittance or reflectance values to account for the light from the sphere wall that is back-reflected to the sample (Figs. 17(a) or 17(b)) and lost out of the entrance port of the sphere. In the reference measurement, (Figure 17(c)), the light back-reflected to the sample ends up striking the sphere wall and is not lost. The lost flux has been measured to be 0.25 % of the light reflected from the sample. The measured reflectance or transmittance is thus corrected by multiplying by $1 + 0.0025R$, where R is the sample reflectance. The size of the correction is dependent on the sample reflectance and shown in Fig. 19.

Regarding error sources (3) and (4), the extent of overfilling the entrance, sample and reference ports can be examined by a measurement of an empty sample or reference port in reflectance mode. Any light coming through the entrance port and overfilling the sample (or reference) port will be measured as a reflectance component with nearly unity reflectance of the sphere wall region surrounding the port. In addition, any overfilling of the entrance port in that measurement will result in some light scattering off the rim of the entrance port into the sphere resulting also in a reflectance component with high effective reflectance. A knife-edge design could be used to reduce the result of entrance port overfilling, but it is preferable to be very sensitive to it in order to quantify it (set an upper limit to it). An example of the entrance port overfilling, obtained by measuring the transmittance of a variable aperture matching the diameter and location of the sphere entrance port, is shown in Fig. 20. An example of the sample overfilling error reflectance measurement is shown in Fig. 21. This was obtained after careful alignment of the sphere system and input FTIR beam.

The remaining important sources of error are related to the FTIR spectrometer, detector, electronics and FT processing, which are discussed in Appendix A. The combined measurement error for the transmittance and reflectance measurements will include both FTIR related errors and the integrating sphere system errors. A straightforward method of evaluating the measurement accuracy of the system is in comparison with expected results for the optical properties of common infrared optical materials. Measurements of a few common materials are presented in Sec. 3.2.4 and the results are used to perform this comparison.

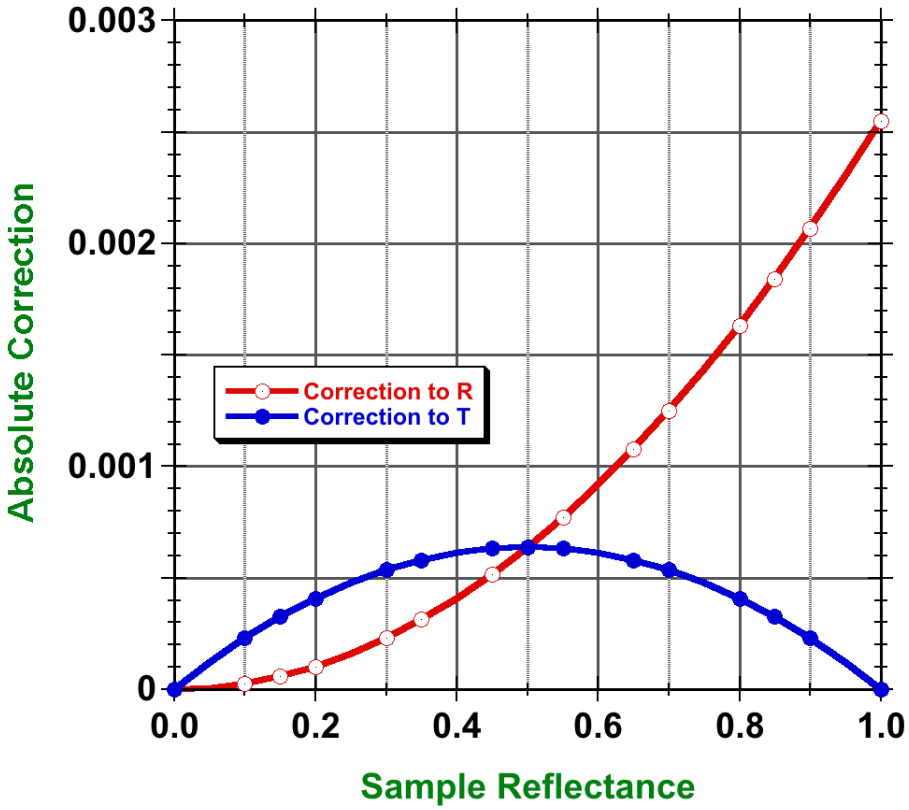

Figure 19: Additive correction for specular samples made when using the IRIS; variation with sample reflectance.

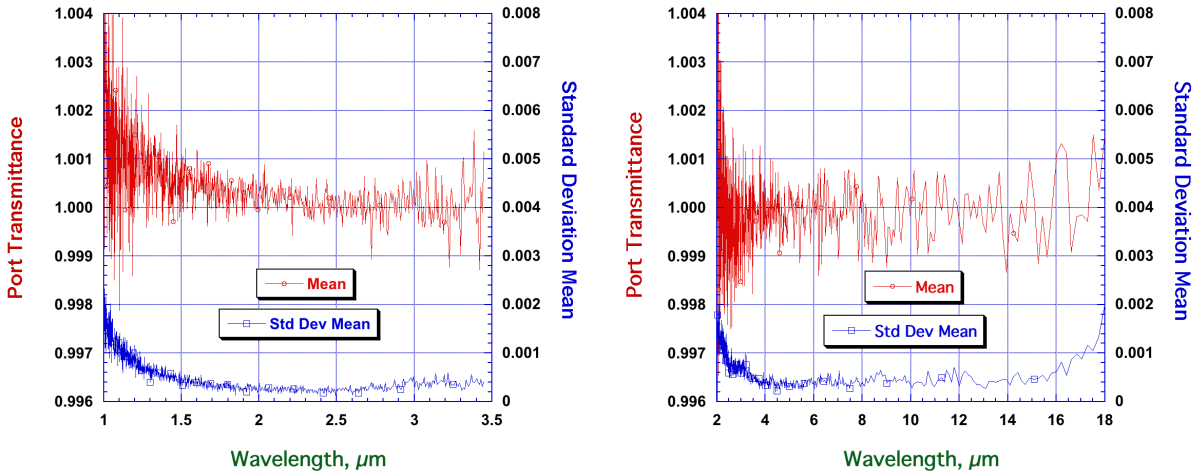

Figure 20: Entrance port overfilling measurements in the near infrared and mid infrared setups.

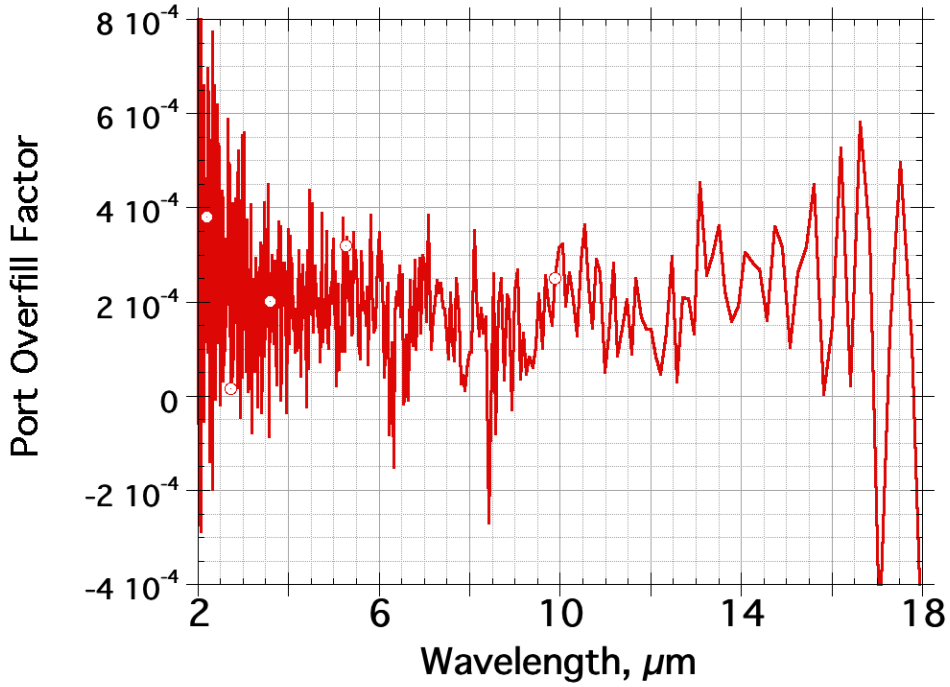

Figure 21: Sample port overfill measurement, the result of an empty sample port reflectance measurement. This is a characterization of the baseline measurement capability of the integrating sphere system. The result can be used to apply corrections to a black sample measurement.

3.2.4. Specular sample measurement results of ρ, τ, and α

A number of samples of optical components have been characterized using the integrating sphere system including windows, filters and mirrors. Several examples of window materials are shown in Fig. 22 to Fig. 29. Both transmittance and reflectance are measured using the same geometry. From these two quantities the absorptance is simply determined by subtracting their sum from 1. Comparisons can be made with calculated values from handbook index of refraction data. This can be done in two ways: (1) a comparison can be made with calculated transmittance and reflectance; and (2) a comparison can be made with calculated absorptance.

The calculated τ and ρ values from the n and k in handbooks will have finite uncertainty values. These will be based on the uncertainties of the original data and the mathematical processes with which, the index values, n and k, were obtained. Other sources of error in this comparison include variations in the material itself, such as the method of growth and processing.

For specific spectral regions for many materials, however, the calculated absorptance can be determined with insignificant ($<10^{-4}$) error to be 0. Because of this, the indirectly measured absorptance in these spectral regions can be used as an accurate evaluation of the total measurement error, not just as an estimate of uncertainty. If, in addition, a number of materials with transmittance and reflectance values spanning a significant fraction of their range (0 to 1) are measured, the measurement error can then be used with reasonable confidence for all transmittance and reflectance results.

Four common infrared window materials were characterized using the sphere system, with results plotted in Fig. 22 to Fig. 25. They are Si (0.5 mm thick), ZnSe (3 mm thick), KRS-5 (5 mm thick), and MgF_2 (5 mm thick), respectively. For each sample, the transmittance, reflectance and absorptance are plotted over a spectral range of 2 μm to 18 μm (1 μm to 18 μm for Figs. 22). Each material has a non-absorbing spectral region over some portion of that range. The reflectance values (in the non-absorbing range) for the selected materials range from 0.05 to 0.45, and the corresponding transmittance values range from 0.55 to 0.95, in the non-absorbing regions. The MgF_2 spectrum exhibits a wide range of values for ρ, τ, and α within the spectral

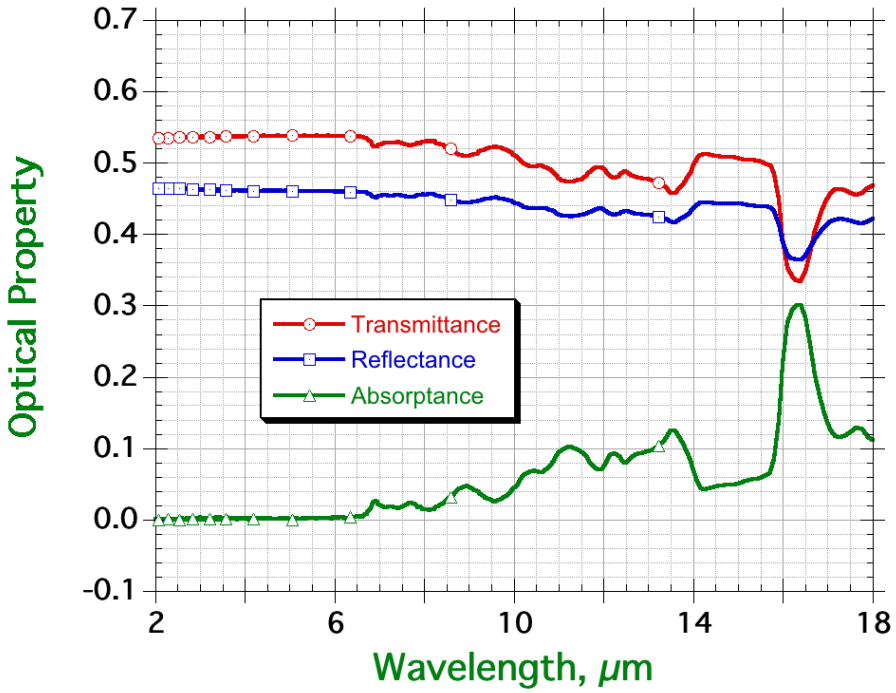

Figure 22: Transmittance, reflectance and absorptance (obtained from 1-ρ-τ) of several common IR window materials, ranging in index from 3.4 to 1.3: Si.

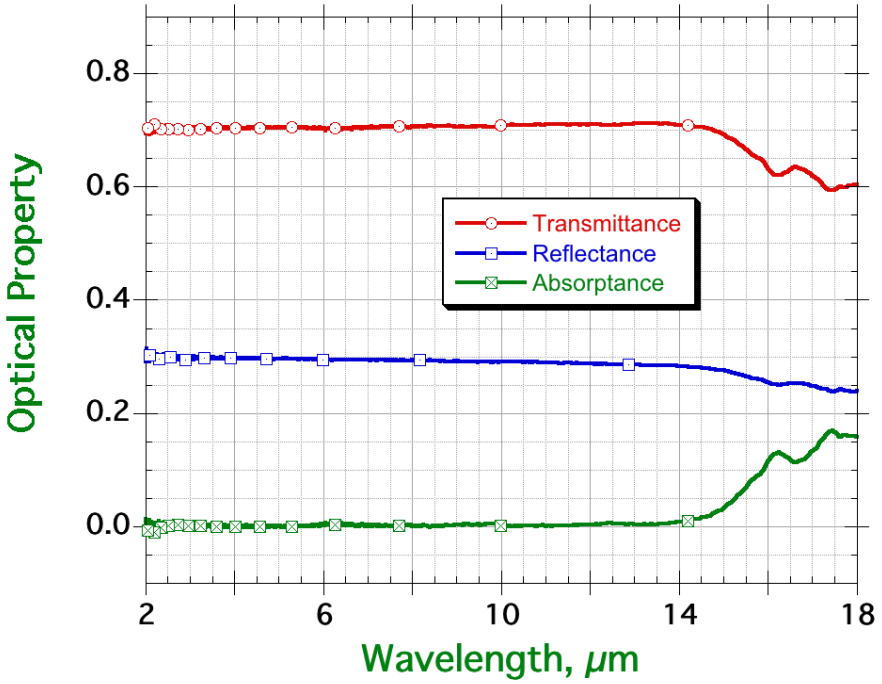

Figure 23: Transmittance, reflectance and absorptance (obtained from 1-ρ-τ) of several common IR window materials, ranging in index from 3.4 to 1.3: ZnSe.

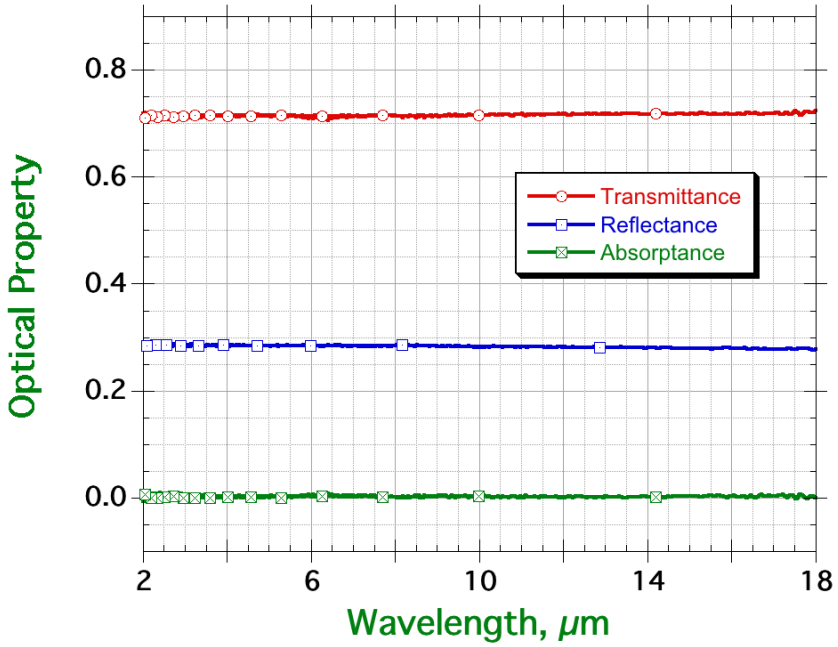

Figure 24: Transmittance, reflectance and absorptance (obtained from 1-ρ-τ) of several common IR window materials, ranging in index from 3.4 to 1.3: KRS-5.

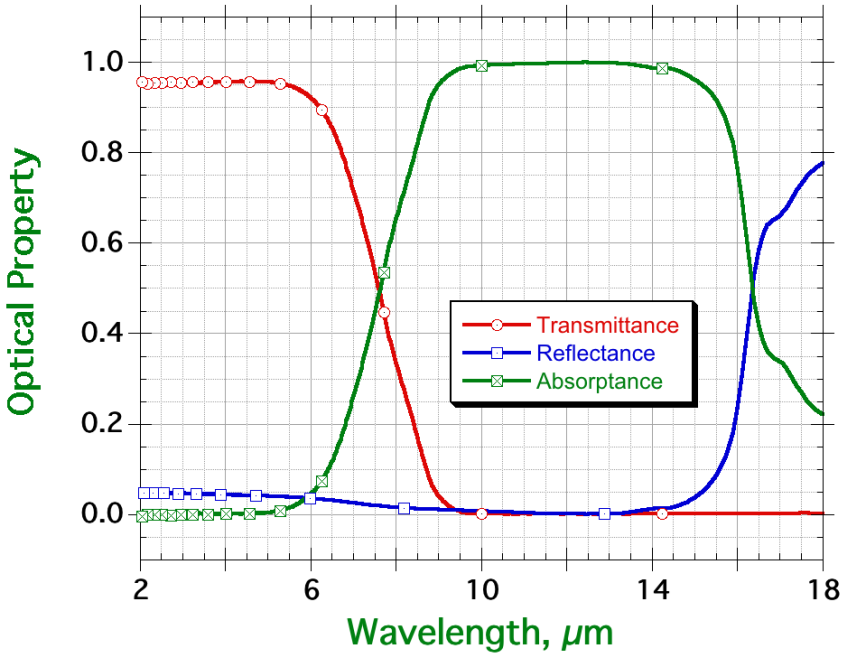

Figure 25: Transmittance, reflectance and absorptance (obtained from 1-ρ-τ) of several common IR window materials, ranging in index from 3.4 to 1.3: MgF_2.

range. At 12.5 μm, both the reflectance and the transmittance are 0, at which the absorption coefficient is substantial ($\tau \rightarrow 0$) and the index is close to 1 ($\rho \rightarrow 0$).

A closer examination of the indirectly measured absorptance in those regions is shown in Fig. 26 to Fig. 29. For each material, an absorptance very close to 0 is observed in the regions with very small *k* value. These are, repectively: 1.2 μm to 5.5 μm, 2 μm to 13.5 μm, 2 μm to 18 μm, and 2 μm to 4.5 μm. In some of the results, some spectral features are seen that can be attributed to contaminants, primarily on the surface, such as water and hydrocarbon modes. Features from 6 μm to 7 μm, and 9 μm to 10 μm, appear in both the ZnSe and KRS-5 spectra. These features could also, in part, be associated with spectral structure seen in the integrating sphere throughput variation mapping, performed for characterization of the sphere for absolute reflectance measurements of non-specular materials.

The indirectly measured absorptance levels in Fig. 26 to Fig. 29 over the spectral ranges cited above, when interpreted as arising from cumulative measurement error, indicate an absolute level of error ranging from 0 to 0.002 for the structureless spectral regions and where structure is observed, up to a maximum of 0.004, at which a structure is observed.

The evaluation of measurement error (using the zero absorptance level) for reflectance of the transparent materials can be transferred with confidence to the opaque sample case (for which a zero absorptance test is not feasible). An example is a gold mirror reflectance measurement shown in Fig. 30. In the opaque sample case, there is only a single reflection, whereas for the transparent sample case, multiple reflections contribute to the reflectance result. The higher order reflected beams will be displaced (due to angle of incidence), enlarged (due to focus shift) and perhaps deviated (due to sample wedge). Hence the effects of spatial non-uniformity of the sphere throughput will be smaller for the opaque mirror measurement, resulting in a correspondingly smaller relative measurement uncertainty for the sample reflectance. This is corroborated by the relative lack of spectral structure in the gold mirror reflectance in Fig. 30.

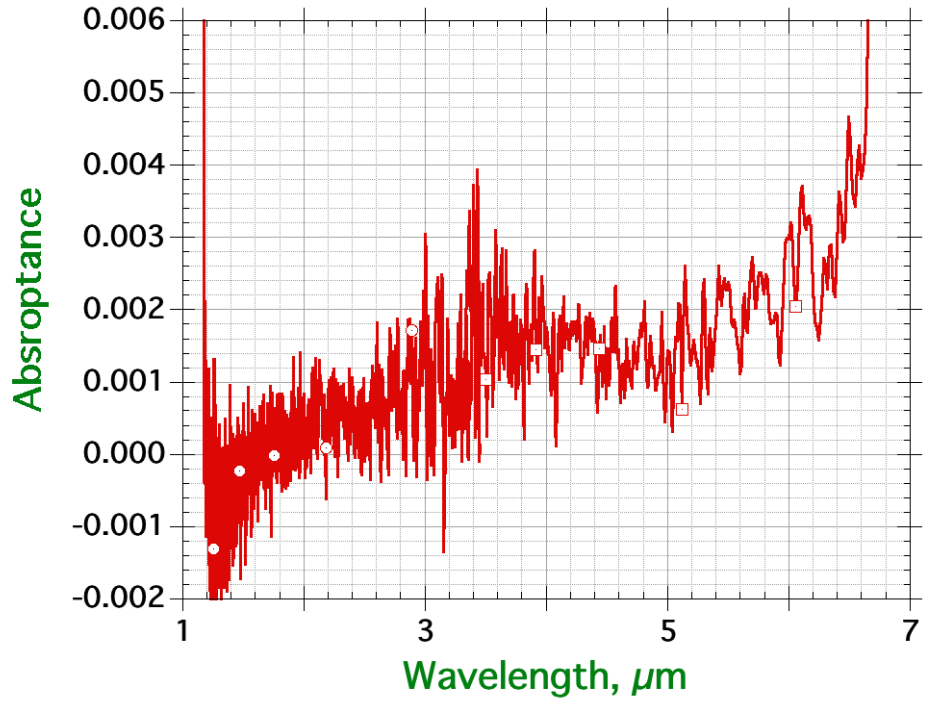

Figure 26: Expanded plot of spectra shown in Fig. 21 highlighting regions with absorptance near zero: Si. The spectra, in regions where *k* should be negligible, [11] result from a combination of (1) cumulative measurement error from all sources in transmittance and reflectance, and (2) additional absorption due to volume or surface contaminants such as hydrocarbons and water.

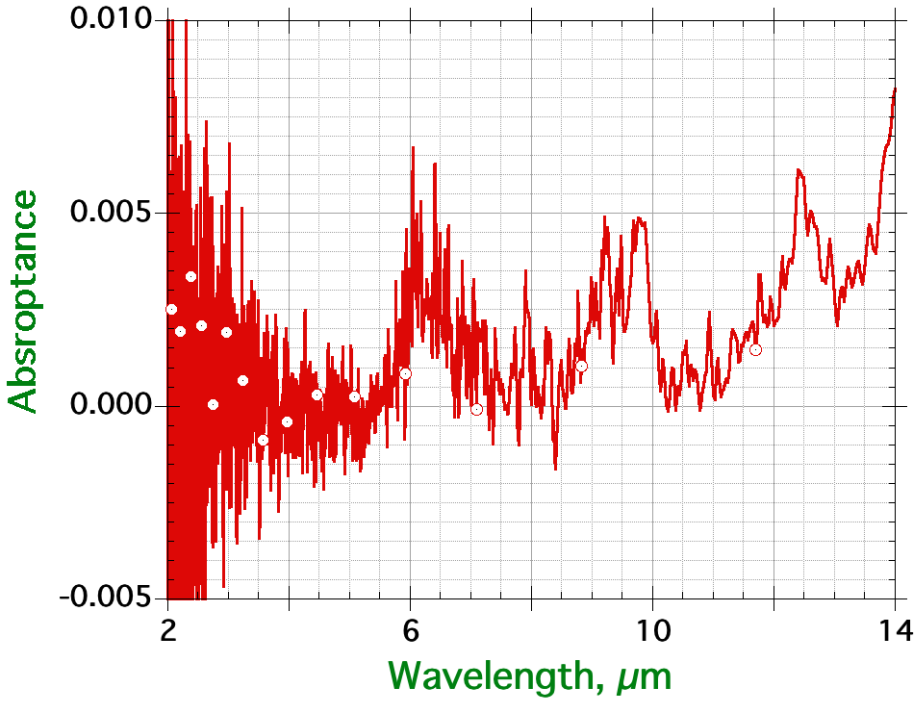

Figure 27: Expanded plot of spectra shown in Fig. 21 highlighting regions with absorptance near zero: ZnSe. The spectra, in regions where *k* should be negligible, [11] result from a combination of (1) cumulative measurement error from all sources in transmittance and reflectance, and (2) additional absorption due to volume or surface contaminants such as hydrocarbons and water.

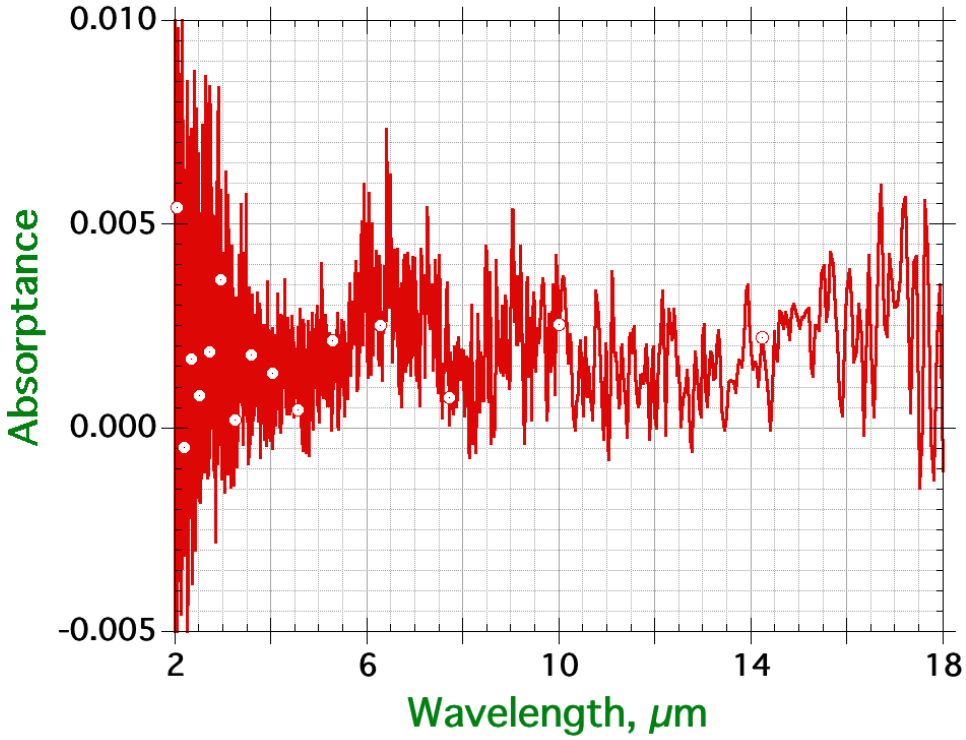

Figure 28: Expanded plot of spectra shown in Fig. 21 highlighting regions with absorptance near zero: KRS-5. The spectra, in regions where k should be negligible, [11] result from a combination of (1) cumulative measurement error from all sources in transmittance and reflectance, and (2) additional absorption due to volume or surface contaminants such as hydrocarbons and water

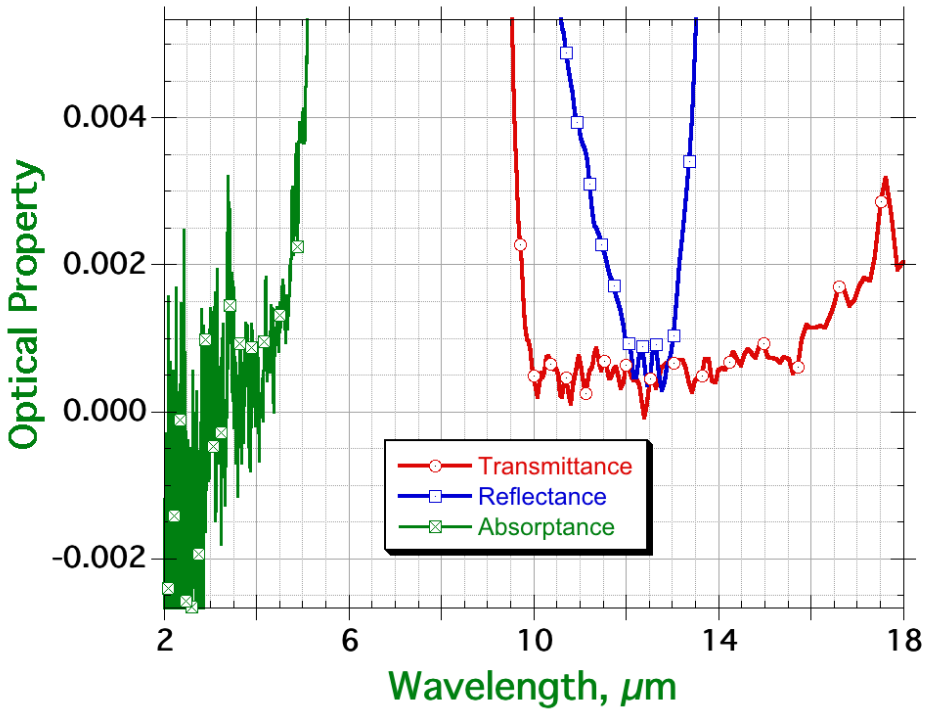

Figure 29: Expanded plot of spectra shown in Fig. 21 highlighting regions with absorptance near zero: MgF_2. The spectra, in regions where *k* should be negligible, [11] result from a combination of (1) cumulative measurement error from all sources in transmittance and reflectance, and (2) additional absorption due to volume or surface contaminants such as hydrocarbons and water. The MgF_2 spectrum also shows regions of near-zero transmittance and reflectance, at longer wavelengths.

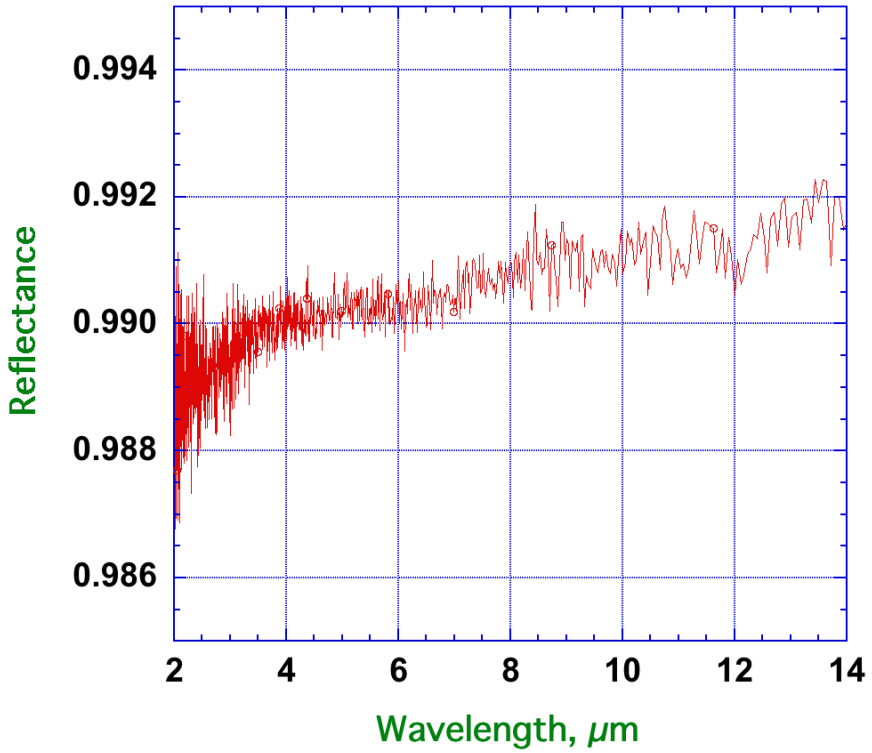

Figure 30: Gold electroplated mirror reflectance.

3.2.4.1. Advantages of using IRIS for measurements of ***ρ, τ and α of specular samples***

The benefits of using the integrating sphere for more accurate detection of light played an important role in the NIST design and development of IRIS for the absolute measurement of ρ, τ and α of samples. The method is demonstrated in the case of infrared windows and mirror characterization. The ability to measure both transmittance τ and reflectance ρ in the same geometry is used to directly quantify the total measurement error for non-absorbing spectral regions, and thereby also obtain reliable uncertainty values for results outside these regions.

Upon careful study and consideration, it can be observed that use of the integrating sphere significantly reduces several important sources of measurement error, enabling the levels of accuracy demonstrated in this paper. These error sources include sample-detector and detector-interferometer inter-reflections, detector non-linearity, detector spatial non-uniformity, and sample-beam geometry interaction (beam deviation, deflection and focus shift) [Appendix A].

The integrating sphere system is not suitable for high sample throughput applications. For these applications other instrumentation designed for fast relative measurements can be used. Such instruments, in turn, can be calibrated with transfer standard samples that are characterized with the sphere system. This approach has allowed us to improve the accuracy of all our FTIR measurement instrumentation, [7] including those designed for variable sample temperature and variable incident angle characterization, not directly feasible with the sphere system.

For accurate characterization of specular samples, direct mounting onto the sphere is not an absolute requirement. Effective systems have been built, especially for the ultraviolet-visible-near-infrared spectral region, that incorporate integrating spheres with detector(s) in the standard "averaging" mode. However, there are at least two important advantages of mounting the sample directly onto the sphere. Both of these relate to the characterization of non-ideal samples. The first is that this design can better handle the worst samples and allow for the greatest amount of beam deflection, deviation, distortion, and focus shift. The second is that one can measure samples that are not perfectly specular, but also exhibit some degree of scatter.

3.2.5 Absolute total scatter (diffuse reflectance, ρ_d; diffuse transmittance, τ_d) measurements.

The IRIS described in Sec. 3.2.3 is an absolute DHR measurement setup and the sphere will collect all or most of the scattered light in addition to the specular component [11]. To enable accurate measurements, the mounting hardware is designed to hold samples from the outside edges. The addition of an 8° compensating wedge enables measurement of normal incidence reflectance and transmittance and to separate each into diffuse and specular components as shown in Fig. 31. The wedge is designed with a port slightly smaller than the sample port, whose sides are polished and gold coated, and tapered to redirect any high angle diffusely reflected light from the samples, onto the sphere wall. Through use of the compensating wedge for achieving normal incidence on the sample, a supplementary measurement is made to determine the scattered component alone as the specular component exits through the entrance window. This measurement, in addition to the standard reflectance or transmittance measurement, which includes both specular and diffuse components, allows separation of the specular and diffuse (scattering) components. For important infrared window materials such as ZnS and CVD diamond, some scatter is unavoidable and typically wavelength dependent. The ability to detect and evaluate scattered light is important to understanding infrared materials, quantifying their behavior and how they can be used appropriately in optical systems. For transmittance, the specular component can be removed without the aid of a wedge. This is accomplished by rotating the sphere to the position for −8° incidence on the sample, for which the specularly transmitted beam will exit the sphere through the entrance port [See Fig. 17 (b) or 17 (d)]. However, with the wedge, normal incidence transmittance can also be measured, using the wedge as shown in Fig. 31 for the diffuse measurement, and with the wedge inverted for the standard transmittance measurement. For scattering[4] measurement, the reflected (or transmitted) light is spread out over the entire sphere and encounters a non-uniform throughput. The ratio of measurements would produce an accurate absolute result if the throughput were perfectly

[4] We assume the scatter is Lambertian. We subtract the total scatter measurement from the DHR measurement, and take the result as the specular component, which requires a minimal correction. Then we multiply the total scatter measurement by the diffuse calibration curve (Fig. 32) to obtain the diffuse component. Then we add the two results to get the corrected DHR result. (See next section)

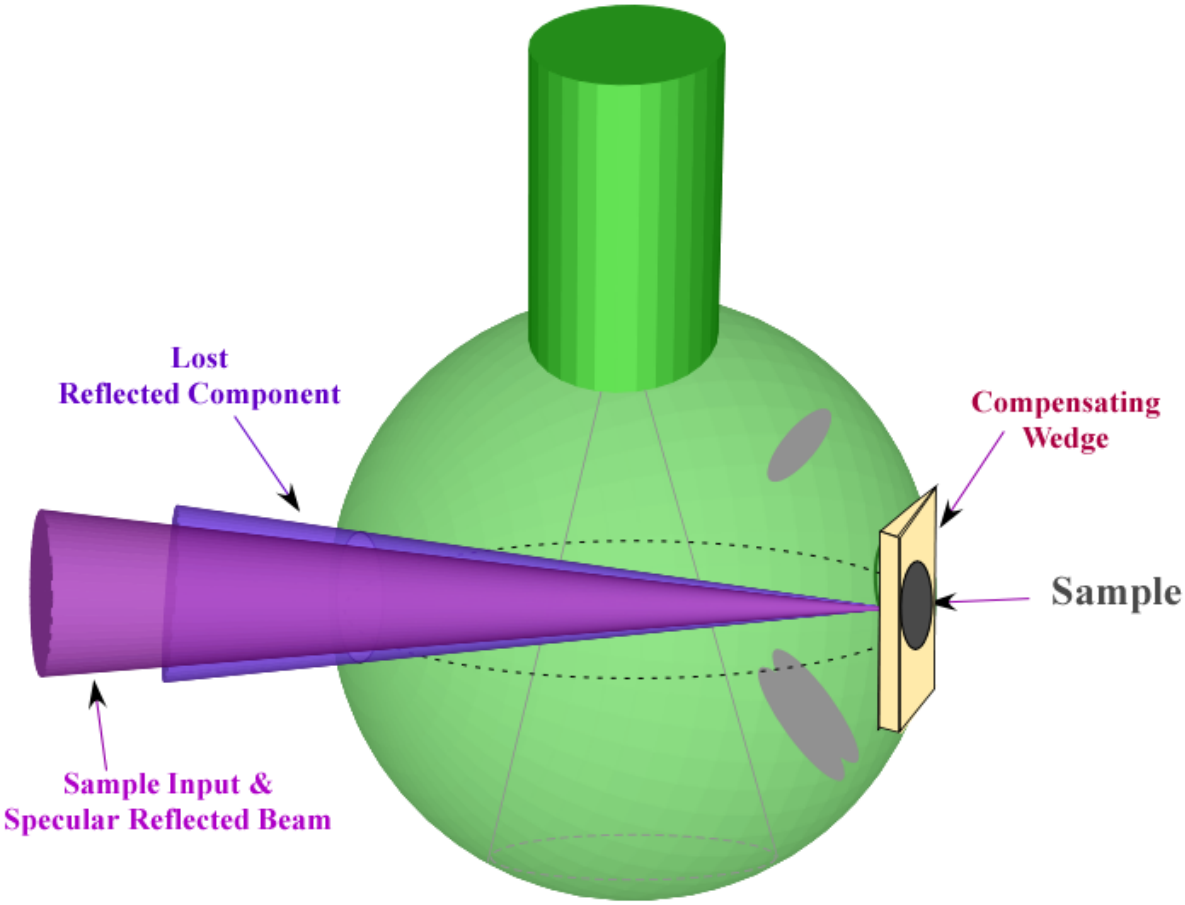

Figure 31: Schematic of the integrating sphere geometry for diffuse component measurement at normal incidence.

uniform. The uncertainty of the DHR result will then depend on the size of the non-uniformity and the extent to which it can be corrected for, which is described in the following section.

result will then depend on the size of the non-uniformity and the extent to which it can be corrected for, which is described in the following section.

3.2.5.1. Calibration methodology for measuring $\rho_{\gamma,h}$ of non-specular samples

Equation 7 and the following discussion in Sec. 3.2 form the basis for the calibration methodology. For samples known as diffuse scatterers the term in the long bracket (the integral ratio) is determined as a correction factor to the ratio of the sample-in signal to the sample-out signal. The calibration factor for the ideal NIST DHR standard is shown in Fig. 32. These curves are obtained by the integral ratio in Eq. 1, where the relative BRDF terms are set to 1. The measured sphere throughput non-uniformity results are used for this evaluation.

Since the integrating sphere coating was selected, we decided to use similar materials for the calibrated internal DHR standards. This material has consisted of an aluminum substrate coated with plasma sprayed copper and then over-coated with electroplated gold. As mentioned earlier, this material reasonably approaches a Lambertian scatterer [10].

Examples of DHR measurements for two other types of diffuse gold samples are shown in Fig. 33 [14]. The simple ratio of sample to reference spectra is shown in Fig. 33 (a). The spectral structure seen is due to a combination of the integrating sphere throughput (which is a function of the coating spectral reflectance) and the reflectance of the sample. Application of the calibration curve for a Lambertian sample [Fig. 32] provides the calibrated value spectra in Fig. 33 (b). The spectral structure in sample Rough Gold 1 is eliminated, whereas Rough Gold 2 retains structure of several percent. This shows the inherent difference between the types of coatings, as well as showing the effectiveness of the calibration procedure as well as the Lambertian character of sample Rough Gold 1.

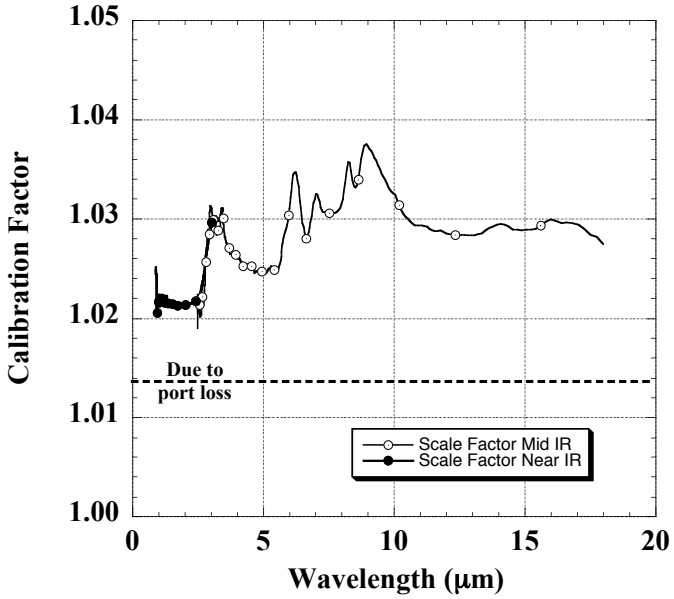

Figure 32: Calibration curves for the near IR and mid IR for a Lambertian (ideal diffuse) sample.

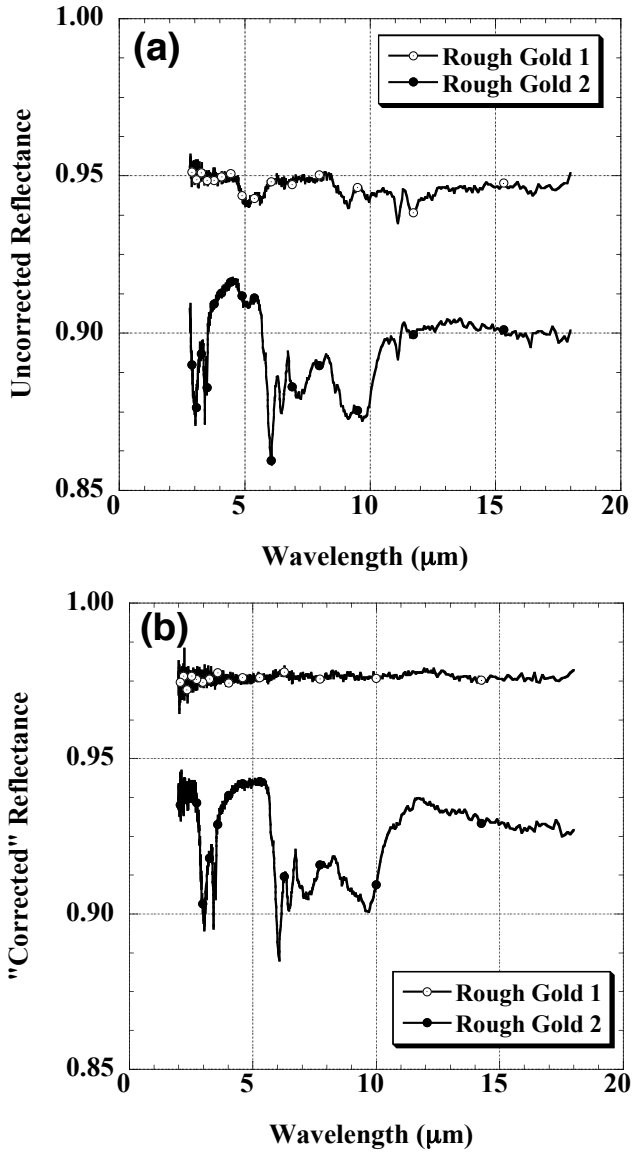

Figure 33: Absolute DHR obtained for two types of diffuse gold samples produced by different methods.

Table 4 shows the uncertainty budget for absolute DHR measurements of a non-specular sample. The dominant component of uncertainty is that due to the spatial non-uniformity of the integrating sphere. This component is reduced for samples with known relative BRDF. Appendix H shows the results of a nationwide inter-laboratory comparison of infrared reflectance. It shows the case of in plane BRDF measured at 1.55 μm and 10.6 μm used to generate a 3 dimensional BRDF data and folded with the integrating sphere uniformity map to produce spectral correction curves for DHR measurement. This procedure is adopted to measure the DHR of Krylon Silver paint (Appendix H).

3.3. Infrared Gonio-Reflectometer-Transmissometer (IGRT)

The optical layout showing the IGRT setup for angle dependent reflectance measurements is shown in Fig. 34 [14]. The 50 mm diameter collimated (≈ f/50) output beam from the FTIR spectrometer is collected by a 90° off-axis paraboloidal (OAP) mirror with a reflected effective focal length of 200 mm and focused at f/4 onto a variable aperture plate. The diverging beam from the aperture is then collected by an insertable (via a translation stage) folding flat mirror and directed onto a 20° off-axis ellipsoidal (OAE) mirror, which sends a slowly converging beam to the sample position at the center of the goniometer. Two flat steering mirrors are used to align the beam to pass through the rotation axis of the goniometer, perpendicular to the plane of the sample surface. The selected plate aperture produces a spot diameter increased by a factor of 10 at the sample surface.

The sample is front-surface mounted on a slotted sample holder designed to allow optical access up to an angle of incidence of 70°. Manual tilt and translation stages are used to bring the surface plane of the sample onto the axis of the motorized sample rotation stage and perpendicular to the incident beam within ± 0.3° to define normal incidence. Precision alignment of the reflectometer is done using the visible output beam of the FTIR spectrometer, making small adjustments in the sample holder tilt and translation along the beam direction to ensure that the reflected spot strikes the detector within ≈ 0.1 mm of the same place as the straight through beam with the sample removed from the path. The relative alignment of the

Table 4: Uncertainty budget for DHR measurement of a non-specular sample

Uncertainty source	**Value** (unit less)
Type B Standard Uncertainty Component	
Inter-reflections	0.0002
Detector nonlinearity	0.0006
Atmospheric absorption variation	0.0001
Beam flip	0.0010
Inequivalent sample/reference beam alignment	0.0005
Retro-reflected light lost out entrance port	0.0040
Spatial variation of throughput	0.0150
Errors in sphere mapping	0.0050
Entrance port overfill	0.0001
Sample port overfill	0.0002
Beam geometry, polarization	0.0002
Phase errors	0.0002
Quadrature sum	**0.016**
Type A Standard Uncertainty Component	0.0010
Expanded Uncertainty (k=2)	**0.033**

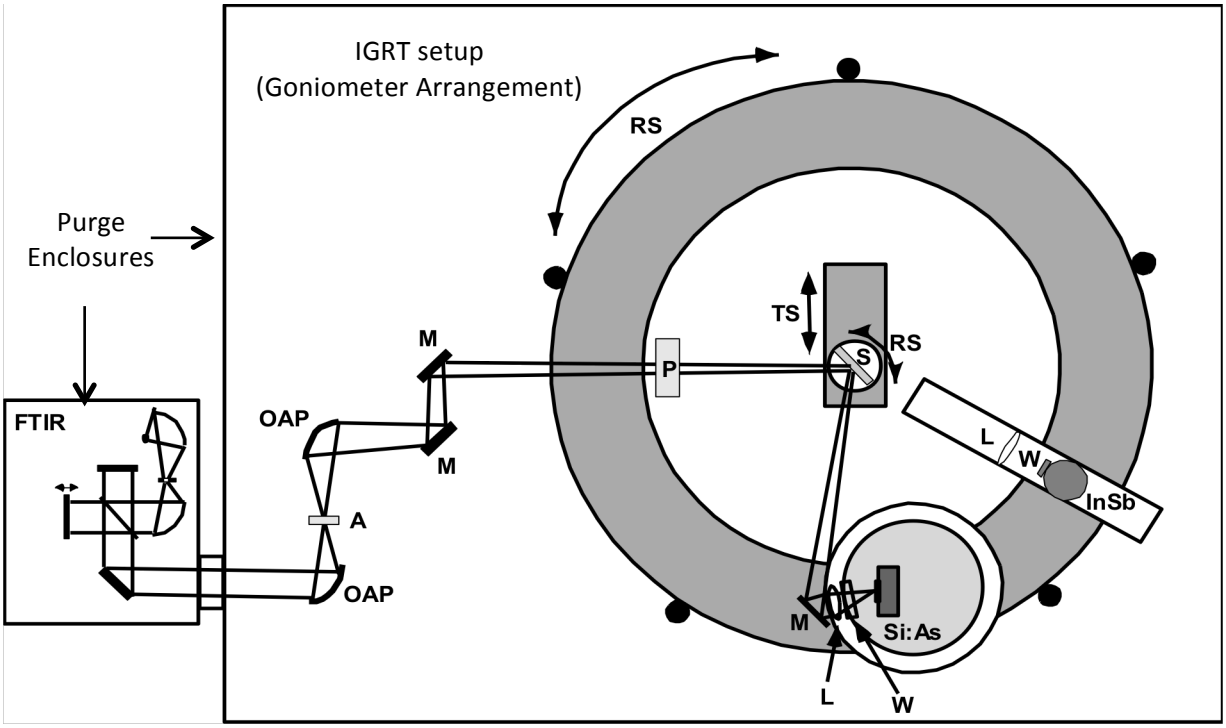

Figure 34: Optical layout of the goniometric reflectometer system described in text. OAP, 90° off-axis paraboloidal mirror; A, variable aperture plate; M, folding mirror; P, polarizer; RS, rotation stage; TS, translation stage; S, sample; L, lens; W, vacuum window. Also shown are the Si:As BIB and InSb photodetectors. The FTIR spectrometer and reflectometer setups are housed in separate sealed enclosures purged with dry, CO_2-free air.

inner and outer goniometer stages is controlled using a small diode laser and quadrant detector system. Once the system is aligned, the sample is held on the axis of rotation of the goniometer on which the detector rotates to intercept and measure the reflected beam (V_s) from the sample. In the reference measurement, the sample is moved out of the incident beam and the detector is rotated to collect the incident beam and measure directly (V_r). The sample reflectance (ρ_o) is thus simply the measurement ratio of the two measured fluxes:

$$\rho_o = {}^{V_s}/_{V_r} \tag{8}$$

This approach has the advantage of allowing the angle of incidence to be varied easily. To vary the sample temperature a cryostat shown in Fig. 35, is used. The cryostat holds the sample within a temperature range of 10 K - 575 K. The cryostat with the sample can be installed at the center of the goniometer circle for measurements of the sample at various temperature settings.

3.3.1. Detectors for the IGRT

For the 1 µm to 5 µm spectral region, the beam passes through a CaF_2 plano-convex lens and CaF_2 window onto a 3.5 mm diameter 77 K photoconductive InSb detector. For the 2 µm to 20 µm spectral region, the beam is reflected through a ZnSe lens and NaCl window onto a 3.1 mm x 3.1 mm photoconductive Si:As BIB detector housed in a liquid helium-cooled cryostat and maintained at a temperature of 12 K. A cooled NiCr-coated Ge neutral density filter with a transmittance of ≈ 0.001 is placed in front of the BIB detector to attenuate the thermal background radiation and keep the response within the linear regime. In each case, the spot diameter on the detector is approximately 2 mm. Both detectors are tilted by 10° relative to the input beam to avoid inter-reflections with the spectrometer. The photoconductor signals are fed through a low-noise current pre-amplifier and back into the FTIR for data collection and Fourier processing.

Figure 36 shows a photograph of the two detector cryostat systems mounted on the motorized outer rotation stage of the goniometer [15]. When filled with cryogens, the InSb and BIB detector cryostats are able to maintain the detector temperatures for approximately 30 h and 48 h, respectively. Also visible in Fig. 36 is the two-axis translation stage and rotary table on

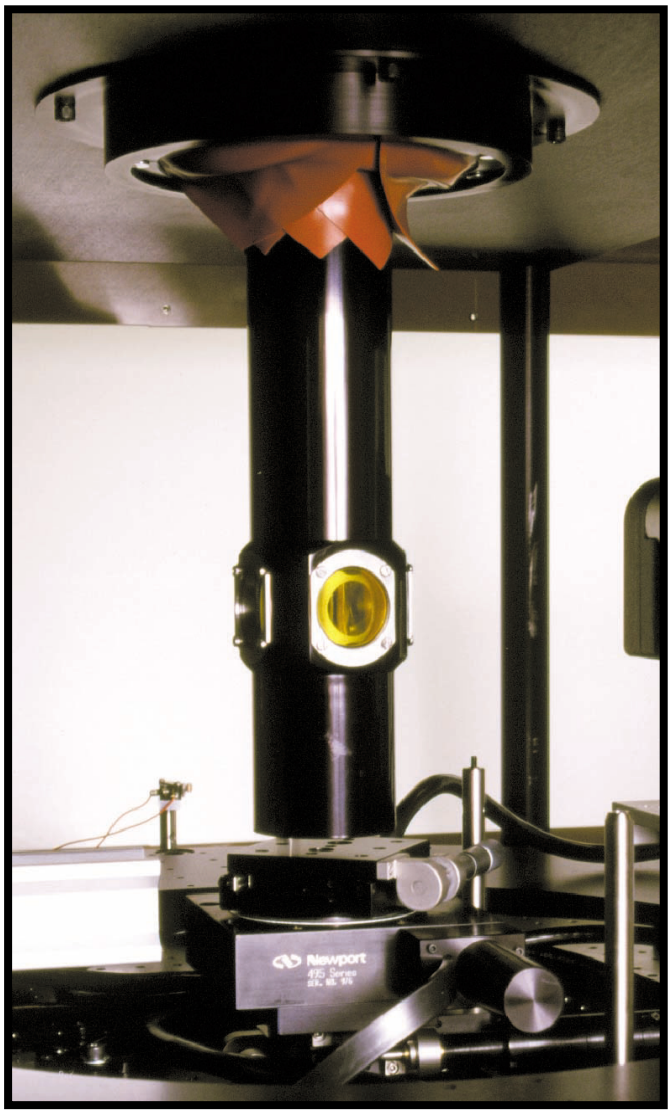

Figure 35: IGRT setup and the cryostat to hold samples at chosen temperature

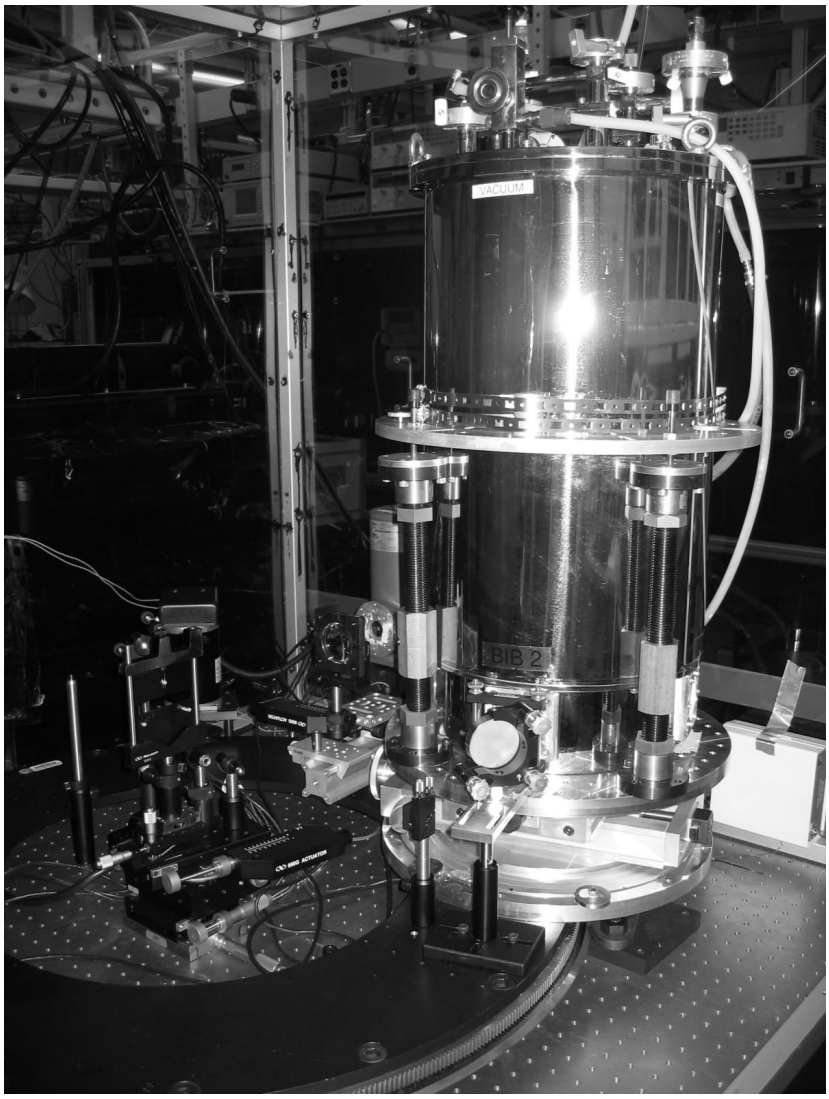

Figure 36: Photograph of goniometer showing the two detector cryostats mounted on the outer rotation stage. The small InSb detector system is visible behind and to the left of the 50 cm tall liquid-He cryostat housing the Si:As BIB detector.

which the BIB detector cryostat is mounted. This is used to manually position the detector relative to the input beam.

3.3.2. Calibration measurement procedure – Example of a gold mirror sample

For the reflectance measurements in this example [14], the FTIR spectrometer was equipped with a SiC source and a Ge-coated KBr beamsplitter. The variable aperture in Fig. 34 was set to 1.25 mm diameter. The spectrometer was scanned with a 20 kHz modulation rate for the reference HeNe laser (15,800 cm^{-1} wavenumber) with a spectral resolution of 16 cm^{-1} and boxcar apodization. 1,500 scans were averaged for each sample or reference spectrum, and the sequence of measurements was repeated to reduce the effects of drift in the modulated FTIR spectra or in the detector responsivity. Data were acquired with both the InSb and Si:As BIB detector systems, for three incident angles from 10° to 65° and both s- and p- polarization. The total averaging time for each angle and polarization was approximately 20 min. The sample temperature was near ambient (22 °C). Figure 37(a) shows the measured reflectance from 2 µm to 5 µm wavelength of a 25.4 mm diameter electroplated gold mirror for three incident angles.

While the reflectance of 0.99 at near-normal incidence is not quite as high as that achieved by protected silver mirrors, there is no apparent H_2O-band absorption in the p-polarized data, with only the weak hydrocarbon absorption near 3.4 µm affecting the smooth variation of reflectance versus wavelength. The optical response of gold films is also very sensitive to deposition and environmental exposure conditions, although good quality films are very stable over time. In Fig. 37(b) and Fig. 37(c) we show calculated reflectance of gold using two different sets of optical constants that can be found in handbooks [15, 16]. The values in Fig. 37(b) are probably closer to typical commercially available gold mirrors, while those in Fig. 37(c) represent the best values obtained from fresh vacuum-deposited gold measured *in-situ* with an ellipsometer. The measured values in Fig. 37(a) fall between these two limits, showing very good results for an electroplated gold mirror. The relative expanded uncertainty (k = 2) for our measurements is 0.5 %. A detailed typical error budget is provided in Appendix D.

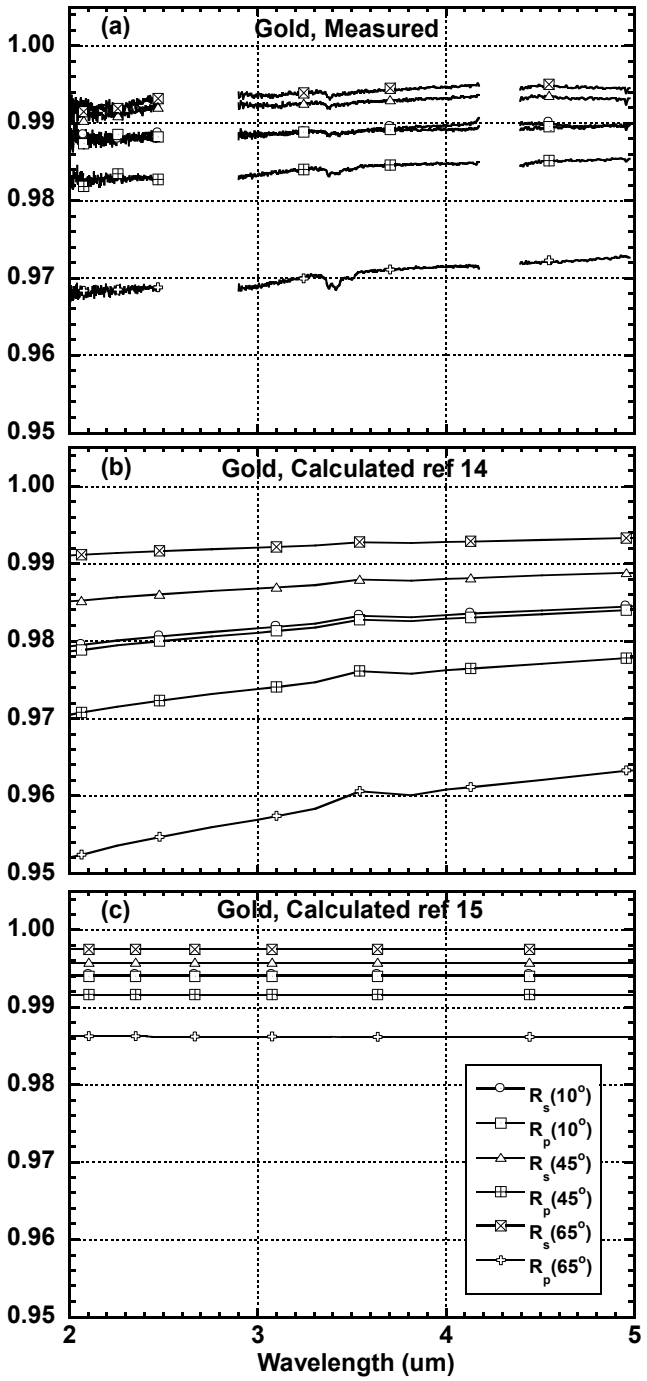

Figure 37: Comparison of measured reflectance values for a gold mirror with predicted values using two different sets of literature values for *n* and *k* of gold. (a) Measurements on a 25.4 mm diameter electroplated gold mirror for three incident angles. (b) and (c) are from calculations using optical constants from two different sources in the literature.

4.0. Measurement Assurance

The measurement assurance for the calibration service 38075S is reviewed as two parts. The first part deals with the work done and published on the sources of error in the measurement procedures. The second part deals with inter-comparisons of measurements with other methods at NIST and other laboratories to assess and validate mutual uncertainties. The latter activity is continued with repeated inter-comparisons internally at NIST and externally with other standard laboratories to maintain measurement assurance.

4.1. Sources of error studies

4.1.1. FTIR errors

Appendix A is the complete description of the FTIR errors. The following errors are addressed and corrections are provided: 1. Inter-reflection; 2. Linearity / Non-equivalence; 3. Aperture heating; Beam Deviation/Deflection/Detector Non-uniformity; 4. Beam Polarization.

4.1.2. Sphere method and associated errors

Appendix B is the complete description of the work done to establish **linearity** in the measurements and any corrections to be applied.

Appendix C describes the following errors due to beam geometry and non-uniformity of the sphere coating: 1. port compensation; 2. sample port overfill; 3. entrance port overfill; 4. spatial uniformity.

4.1.3 Goniometer associated errors

Appendix D describes the alignment errors for the sample and detector on the goniometer and how to use the laser alignment for improving relative accuracy.

4.2 Internal and external intercomparisons

4.2.1 Internal w/ STARR / monochromator/transmittance/reflectance

Appendix E describes the inter-comparison for the regular reflectance and transmittance measurements with the NIST Spectral Tri-Function Automated Reference Reflectometer (STARR) and the monochromator facilities at the overlapping wavelengths. The agreement was within the quoted uncertainties of these facilities. **Appendix D,** Fig. 6 also shows an intercomparison with STARR for a gold mirror and the agreement is within quoted uncertainties.

4.2.2 Internal sapphire disk compared to handbook n & k calculations

Appendix D, Fig. 7 shows the measurements using the goniometer and prediction from theory. The agreement is within the quoted uncertainties.

4.2.3 External w/ National Physical Laboratory (NPL – UK)

Appendix F shows the intercomparison with NPL measurement service that uses monochromator based methodology and the agreement is within the quoted uncertainties of both facilities.

4.2.4 External w/ National Metrology Institute of Japan (NMIJ)

Appendix G describes the intercomparison on the absorptance/emittance scales and the agreement is within quoted uncertainties.

4.2.5 External/Nationwide Intercomparison

Appendix H describes the intercomparison on the IR reflectance scales with NIST as the Pilot Laboratory and the agreement between laboratories is presented.

5.0 Template for Calibration Report

Appendix I shows a template of a calibration report.

6.0 References

[1] J.M. Palmer, "The Measurement of Transmission, Absorption, Emission and Reflection," in Handbook of Optics, second ed., Part II, M. Bass, editor, McGraw-Hill, NY (1994). http://photonics.intec.ugent.be/education/ivpv/res_handbook/v2ch25.pdf

[2] D. Gupta, L. Wang, L. M. Hanssen, J. J. Hsia, and R. U. Datla "Polystyrene films for calibrating the wavelength scale of infrared spectrophotometers - SRM 1921," *NIST Special Pub*. **260-122**, U. S. Dept. of Commerce (1995).

[3] Z. M. Zhang, L. M. Hanssen, R. U. Datla, "High-optical-density out-of-band spectral transmittance measurements of bandpass filters", Opt. Lett. **20** (1995) 1077-1079.

[4] Appendix A

[5] Z. M. Zhang, R. U. Datla, and L. M. Hanssen, "Development of neutral density infrared filters using metallic thin films," Mat. Res. Soc. Symp. Proc. **374**, 117 (1995).

[6] *Z. M.* Zhang, R. U. Datla, *and* L. M. Hanssen**, "**Copper-Nickel Alloy Films for Infrared Neutral Density Filters", *U.S. Patent*, No. **5,726,797**, (1998).

[7] S. G. Kaplan and L. M. Hanssen, "Infrared regular reflectance and transmittance Instrumentation and standards at NIST," Analytica Chimica Acta **380**, 303-310 (1998).

[8] B. N. Taylor and C. E. Kuyatt, "Guidelines for Evaluating and Expressing the Uncertainty of NIST Measurement Results," NIST Technical Note **1297** (1994). (http://physics.nist.gov/cuu/Uncertainty/index.html)

[9] L. M. Hanssen and K. A. Snail, "Integrating Spheres for Mid- and Near Infrared Reflection Spectroscopy", in *Handbook of Vibrational Spectroscopy*, J.M. Chalmers and P.R. Griffiths (Eds), John Wiley & Sons, Ltd, Volume **2**, pp. 1175 - 1192 (2002).

[10] L. M. Hanssen and S. G. Kaplan, "Infrared diffuse reflectance instrumentation and standards at NIST," Analytica Chimica Acta **380**, 289-302 (1998).

[11] L. M. Hanssen, "Integrating-sphere system and method for absolute measurement of transmittance, reflectance, and absorptance of specular samples," Applied Optics **40** (19), 3196-3204 (2001).

[12] D. B. Chenault, K. A. Snail, and L. M. Hanssen, "Improved integrating-sphere throughput with a lens and nonimaging concentrator," Appl. Opt. **34**, 7959-7964 (1995).

[13] L. M. Hanssen, A. V. Prokhorov, V. B. Kromchenko, "Specular baffle for improved infrared integrating sphere performance", Proc. of the SPIE, **5192**, 101-110 (2003).

[14] S. G. Kaplan, E. J. Iglesias, and L. M. Hanssen, "Angle-dependent infrared reflectance measurements in support of VIIRS", Proc. of SPIE, **7082**, (2008)

[15] D. W. Lynch and W. R. Hunter, in *Handbook of Optical Constants of Solids*, ed. E. D. Palik (Academic Press, San Diego 1998), pp. 286-295.

[16] *OPTIMATR 2.1*, Johns Hopkins University/Applied Physics Laboratory and AR Software, Inc., Landover, MD (1993).

Appendix A.

Testing the radiometric accuracy of Fourier transform infrared transmittance measurements

S. G. Kaplan, L. M. Hanssen, and R. U. Datla

We have investigated the ordinate scale accuracy of ambient temperature transmittance measurements made with a Fourier transform infrared (FT-IR) spectrophotometer over the wavelength range of 2–10 μm. Two approaches are used: (1) measurements of Si wafers whose index of refraction are well known from 2 to 5 μm, in which case the FT-IR result is compared with calculated values; (2) comparison of FT-IR and laser transmittance measurements at 3.39 and 10.6 μm on nominally neutral-density filters that are free of etaloning effects. Various schemes are employed to estimate and reduce systematic error sources in both the FT-IR and laser measurements, and quantitative uncertainty analyses are performed.

Key words: Fourier transform infrared spectrophotometer, neutral-density filter, transmittance, photometric accuracy.

1. Introduction

Fourier transform infrared (FT-IR) spectrometers have become the most popular and commonly used instruments for the spectral characterization of materials in the infrared. Their well-known advantages in throughput and signal averaging,[1] combined with advances in high-speed computing for real-time phase correction and Fourier transform processing, and clever engineering of dynamically stabilized moving mirror systems, have led to commercially available systems that are capable of unprecedented speed, signal-to-noise ratio, and stability. These devices have now largely supplanted dispersive instruments for transmittance, reflectance, absorptance, and emittance measurements of solids, liquids, and gases for light with wavelengths greater than 2 μm.

However, some of the same optical design elements that are responsible for the superior performance also lead to more complicated and, in some cases, more severe sources of radiometric error in FT-IR spectra compared with their dispersive counterparts. Extensive theoretical and experimental literature exists on the subjects of detector nonlinearity,[2] interreflection effects,[3,4] ambient thermal emission,[5] and many other error sources.[6] Unfortunately, it is still not uncommon for the high signal-to-noise ratio and good measurement repeatability afforded by FT-IR spectrophotometers to be mistaken for low absolute radiometric uncertainty. While the complete radiometric characterization of even one FT-IR instrument is at present an ambitious long-term goal, it should be possible for users of FT-IR spectrometers to both understand and reduce the various sources of radiometric error through the use of standard and diagnostic samples appropriate to the measurements of interest.

As part of an effort at the National Institute of Standards and Technology (NIST) to develop a set of calibrated neutral-density filters for use as infrared transmittance standards from 2 to 25 μm, we have undertaken a program of testing and improving the radiometric accuracy of simple room-temperature FT-IR transmittance measurements of thin parallel-sided dielectric materials with or without reflective metallic coatings for nominally neutral attenuation. For the uncoated samples the expected transmittance values can be calculated in the wavelength regions where the absorption is negligible by use of the available index of refraction data. These values can be compared to the results of the FT-IR measurements. For higher attenuation values, comparisons of FT-IR and laser measurements at 3.39 μm and 10.6 μm are made for metallic coatings on ultrathin (100 nm) dielectric substrates. The ultrathin samples we have examined had Lexan substrates with a clear aperture of 15-mm diameter and were produced by Luxel Corporation of Friday Harbor, Washington. These samples are discussed further in Subsection 2.C.

The authors are with the National Institute of Standards and Technology, Optical Technology Division, Gaithersburg, Maryland 20899-0001.

Received 31 March 1997; revised manuscript received 23 June 1997.

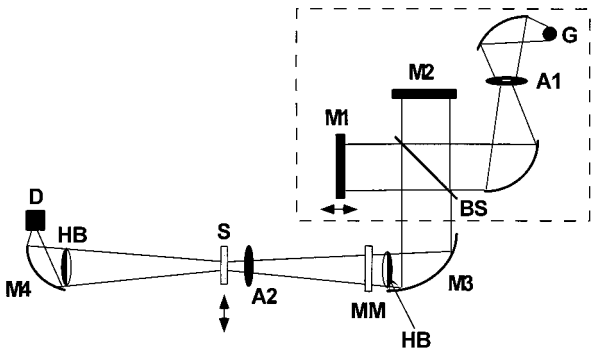

Fig. 1. Schematic optical layout for the FT-IR transmittance measurements: G, globar source; A1, source aperture; BS, beam splitter; M1, moving mirror; M2, fixed mirror; M3, off-axis paraboloidal mirror; HB, half-beam block; MM, metal mesh filter; A2, field stop; S, sample; M4, off-axis ellipsoidal mirror; D, DTGS pyroelectric detector. The transmittance is measured by our switching the sample in and out of the beam and comparing to either an empty path or a reference sample. The half-blocks, metal mesh, and field stop are used to reduce the systematic errors that are due to interreflections, detector nonequivalence, and source aperture radiation, as described in the text.

2. FT-IR Measurements

A. Experimental Setup

Transmittance measurements over the wavelength range from 2 to 25 μm at near-normal incidence were performed with a Bio-Rad FTS-60A scanning FT-IR spectrometer, by use of a ceramic globar source, Ge-coated KBr beam splitter, and a blackened deuterated triglycine sulfide (DTGS) pyroelectric detector with a KBr window. The interferograms were transformed with a zero-filling factor of 2, with boxcar apodization, and the nominal spectral resolution was 8 cm^{-1}.

The sample was placed at the focus (3-mm, 6-mm, or 8-mm spot diameter, selectable by means of a source aperture wheel) of the $f/3$ beam in the instrument sample compartment, which was purged with dry, CO_2-free air. Two samples at a time were held in a movable sample holder that allowed them to be switched vertically in and out of the beam and also provided for rotation with 1′ angular resolution and vertical translation with 5-μm resolution to test for interreflection, beam displacement, and nonuniformity effects as described below. Measurement of the background spectrum was performed before and after each sample measurement, and data were accepted only if the wavelength-averaged signal drift level was less than 0.1% relative change in transmittance over this time interval, which varied from 5 to 60 min depending on the attenuation level of the sample under test.

A schematic of the optical layout of the FT-IR measurements is shown in Fig. 1. The important optical components are labeled and defined in the caption. The half-blocks, attenuators, and field stop are used to test for and reduce several of the major radiometric error sources that are discussed below.

B. Reduction of Major Radiometric Error Sources

1. Errors Due to Interreflections Involving the Sample

Errors in the transmittance spectra can be produced by reflections between the sample and other components in the optical train, chiefly the interferometer and detector. Tests were performed to look for the effects of these interreflections on the measured transmittance spectra. This was done by measuring the ratio of the transmittance of a 0.25 mm thick Si wafer at near-normal incidence to the transmittance at 10° incidence.

The $f/3$ beam of the spectrometer was measured by rotation of a wire grid polarizer at the sample position to have roughly 7% ± 4% vertical polarization (defined in terms of Stokes parameters[7] as s_1). For this degree of polarization, and taking into account the conical beam geometry, the angle of incidence dependence of the transmittance is expected from the Fresnel equations applied to the Si sample to be less than 0.2% between 0° and 10°. Tilting the sample also increases the average optical path length for the transmitted radiation; for the largest absorption feature in the Si sample ($a \sim 20\%$ deep absorption line near 16 μm) the expected change in transmittance between 0° and 10° is 0.02%. Thus any changes larger than 0.2% in the detected flux on tilting the sample should be ascribed to an error source involving the sample, such as interreflection or beam displacement on the detector.

The results of these measurements are shown in Fig. 2(a). Curves A, B, C, and D each represent a ratio of two measurements of a Si sample, one with 0° incidence ratioed to one with 10° incidence. For the $f/3$ beam geometry at the sample, a 10° tilt is sufficient to prevent the beam reflected from the sample from re-entering the interferometer. Curve A was obtained with no additional effort to eliminate the interreflection effects in the normal incidence spectrum. The denominator should represent the transmittance of Si without interreflection from the interferometer, and the relative increase of as much as 4% in measured transmittance at normal incidence can be attributed to the combined effects of sample-interferometer and sample-detector interreflections.

Curve A has a complicated wavelength dependence, qualitatively similar to that observed by previous researchers[4] in the ratio of the apparent transmittances of reflecting and absorbing half-beam blocks placed in the sample position. There is a minimum near the center of the measured spectral range, and prominent structure near 8 μm and 3 μm. The sample-interferometer interreflection should produce contributions of alternating positive and negative signs, respectively, to the apparent transmittance for odd and even multiples of a given frequency component of the spectrum.[3] This behavior is qualitatively borne out in the data, which shows considerable structure of both signs, especially for

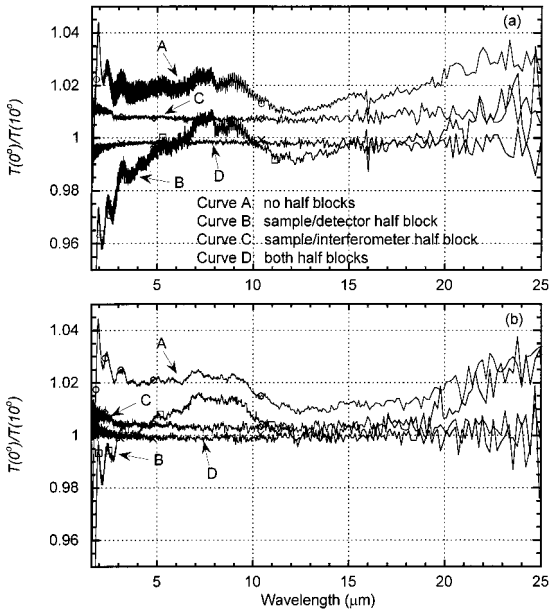

Fig. 2. Effects of sample–interferometer and sample–detector interreflections on the apparent transmittance of (a) a 0.25-mm-thick Si wafer and (b) a 27-nm-thick NiCr film on a 120-nm-thick Lexan substrate, tested by ratioing of the measured transmittance at normal incidence to that at 10° incidence. Curve A, transmittance ratio versus wavelength with no beam blocks; curve B, ratio with a half-block between sample and detector; curve C, ratio with a half-block between the sample and interferometer; curve D, ratio with both half-blocks in place.

wavelengths shorter than 15 μm, half of the cutoff wavelength of the KBr:Ge beam splitter.

For wavelengths shorter than 12 μm, there are apparent Fabry–Perot fringes in the transmittance with an amplitude as high as 0.5% and a spacing of 12.6 cm^{-1}, twice the actual spacing of 6.3 cm^{-1} observed in higher-resolution spectra (not shown in Fig. 2) of the 0.25-mm-thick Si sample. The double-spaced fringes are expected from the first-order sample-interferometer interreflection: each minimum or maximum in the true spectrum shows up again at twice the frequency, so a fringe extending from ν to $\nu + \Delta\nu$ will produce an artifact extending from 2ν to $2\nu + 2\Delta\nu$. Higher-order effects are in principle expected as well[3] but in this measurement are too weak to be discerned.

For curve B, a half-circular beam block made of infrared absorbing black felt was placed near the ellipsoidal focusing mirror for the detector (M4 in Fig. 1) in such a way as to prevent light reflected from the detector from reentering the system, and the tilting test was repeated. The sample-detector and interferometer-detector interreflections should be effectively blocked. The resulting curve for this configuration has a structure similar to curve A, but the change in apparent transmittance between 0° and 10° is smaller, at least for wavelengths greater than 5 μm.

Curve C was obtained by removal of the sample-detector half-beam block with one instead placed near the focusing paraboloidal mirror at the entrance of the sample compartment (M3 in Fig. 1). Thus the sample-interferometer and detector-interferometer interreflections should be substantially reduced,[4] but the sample-detector interreflection remains. In this case an almost wavelength-independent increase of ~1% is seen at normal incidence, of the order of the expected additive contribution of reflections between the ~50% reflecting Si sample and ~8% reflecting KBr detector window.

Finally, curve D, the results of the tilting test with both beam blocks in place are shown. In this case the average change in transmittance is less than 0.5% over the entire wavelength range (2 to 25 μm) that was measured. The remaining difference below 1.0 in the ratio $T(0°)/T(10°)$ is believed to result from beam displacement on the detector from the tilted sample.

To confirm the above analysis, we also performed the tilting tests with a 27-nm-thick NiCr film on a 120-nm-thick Lexan substrate. The results of these tests are shown in Fig. 2(b). They are qualitatively similar to those for the 0.25-mm-thick Si sample shown in Fig. 2(a). The differences can be attributed to the characteristics of the thin coated Lexan sample: the lack of Fabry–Perot fringes in curves A and B (see Subsection 2.C); the lower value in curve C consistent with the lower reflectance of the NiCr–Lexan sample for light incident from the substrate side, which was facing the detector during these measurements; and, last, the smaller residual in curve D, consistent with the negligible beam displacement for such a thin sample.

Use of the half-beam block between the sample and the interferometer is only one way of eliminating interreflections between them. It represents a compromise among (a) minimizing the range of angles on the sample, (b) minimizing the central or average angle on the sample, (c) maximizing the flux throughput to the detector, and (d) minimizing the number and extent of alterations to the standard geometry of the instrument.

The $f/3$ geometry of the Bio-Rad FTS-60A produces a conical beam focused at the sample position with the central ray at normal incidence and the edge ray at approximately 9.5° from the normal. However, the central section of the beam, from 0° to approximately 2°, is blocked inside the interferometer for use by a He–Ne laser beam for alignment and scanning. Thus, the flux-weighted average incident angle in the standard configuration is approximately 6°, with a range of angles from 2° to 9.5°. This geometry is nominally radially symmetric.

In this geometry interreflections between the sample and interferometer can be eliminated in several ways:

(1) The sample can be tilted by at least 10°. The advantages of this method are that (a) the only alteration to the normal configuration is the sample tilt and (b) there is no throughput loss. The disadvantages are (a) a loss of conical symmetry in the incident

geometry and that (b) the maximum incident angle is increased to ~20°, with the weighted average angle increased to ~12°.

(2) A second method (which was used here) is to place a half-beam block near the input focusing mirror. The advantage is that the standard range of incidence angles and sample orientation are maintained. The disadvantages are (a) a reduction in throughput by a factor of 2, (b) loss of radial symmetry (although the conical symmetry is retained in the remaining quadrants), and (c) increased sensitivity to beam wander, as the presence of a knife-edge in the beam can effectively amplify changes in signal level resulting from the beam moving on the detector.

(3) Nearly equivalent to the second method would be a combination of aperturing the beam at the focusing mirror to reduce the cone half-angle from 9.5° to 5° and then tilting the sample by 5°. The disadvantages of this method are a significant loss of throughput due to the empty region of the beam from 0° to 2° and the loss in conical symmetry.

(4) A fourth alternative would be to replace the sample compartment optics and hardware to provide an $f/6$ geometry with the central ray at 5° incidence on the sample. This approach would combine the advantages of the other methods while eliminating their disadvantages (except for the loss of conical symmetry). The disadvantages are (a) the reconstruction or external setup of a new sample compartment and optics and (b) a doubling of the focused spot diameter on the sample (owing to conservation of throughput). Reconstruction would entail replacing the focusing mirrors between the sample and interferometer and between the sample and detector, as well as doubling the path length between the focusing mirrors.

(5) Finally, interreflections can be reduced by placing an attenuator such as a neutral-density filter between the sample and interferometer. The attenuator must itself be tilted by at least 10° to avoid introducing additional interreflection effects and also must be sufficiently large to avoid beam vignetting. For a 10% transmitting attenuator, the sample-interferometer interreflection error should be reduced by a factor of 100. The disadvantages are (a) a major reduction in throughput (a factor of 10 in this example) and (b) alignment changes due to beam deviation or deflection.

For this study the second approach was selected. It is a relatively simple one to implement and does not increase the weighted average angle of incidence or destroy the normal-incidence conical symmetry; thus it does not increase the errors due to angle-dependent effects. Also, as described below, it allows the positioning of a second block after the sample without additional throughput loss. For future research a variation of the third approach is being implemented, which will allow a variation of beam geometry from $f/3$ to nearly collimated.

Interreflection between the sample and the detector takes place in a different geometry. On the input side the sample has light focused onto it by an off-axis paraboloidal or spherical mirror from an input collimated beam. On the output side of the sample, the diverging beam is refocused onto a detector by an off-axis ellipsoidal mirror. The sample center and the detector are generally placed at the two foci of the ellipsoid. This easily leads to multiple interreflections between the sample and detector.

Again, one way to eliminate this problem is (1) to tilt the sample, which has the same advantages and disadvantages as mentioned above. Also, (2) the detector may be tilted. But because the detector collection optics geometry is generally very fast, $f/1$ or even $f/0.5$, the tilt angle required, 30° or 60°, becomes difficult to implement. (3) A third alternative is to use only low reflectance detectors, such as a windowless black-coated detector, or to use a detector with an integrating sphere as a collector. Black-coated windowless detectors are not available for all wavelengths of interest. Use of an integrating sphere significantly reduces the system throughput and requires reconstruction of the hardware. (4) Placement of an intervening attenuator similar to one discussed above will also reduce interreflections but will have similar disadvantages. Finally, (5) an additional half-beam block can be used to prevent light reflected off the detector from reaching the sample.

Method (5) was used here. When combined with the input half-beam block and placed appropriately, the second beam block does not further reduce the throughput to the detector. The disadvantage is an increased sensitivity to beam wander owing to the sample's interaction with the beam (beam deflection and beam deviation). In practice the first beam block is positioned to block slightly more than half of the beam, and the second beam block slightly less, to reduce the sensitivity to sample-induced beam displacement on the detector. Finally, we note that the second half-beam block adopted in this work has the additional advantage of eliminating interreflections between the detector and interferometer, which are present with or without the sample in place and can affect both the reference and sample measurements.

2. *Errors Due to Source Aperture Heating*

Ideally, an image of a portion of the source, defined by the Jacquinot stop in the source compartment of the FT-IR spectrophotometer (A1 in Fig. 1), is transferred to the sample and detector by the optics of the instrument. This is at least approximately the case, as can be observed by examining the visible portion of the beam passing through the instrument. However, the source aperture is heated by the source radiation and itself becomes a source of near-ambient blackbody radiation with a large effective area. Thermal emission from components of the system other than the source is known to produce substantial errors in FT-IR spectra[5] when either the sample or detector temperature is far from ambient. In the present case, where both the sample and detector are near room temperature, the radiation from the slightly

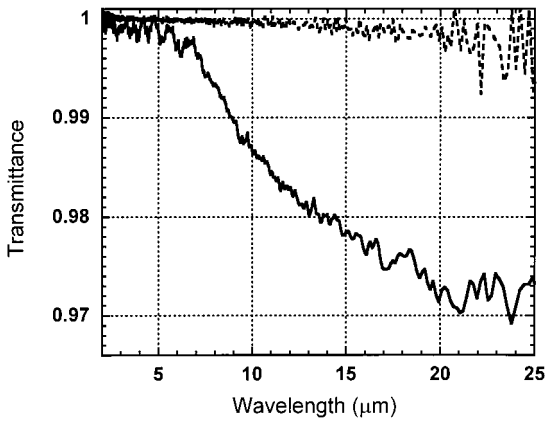

Fig. 3. Transmittance of a 15-mm diameter aperture with a nominal beam diameter of 3 mm at the sample position. The solid curve shows the measured transmittance without field stop A2 (Fig. 1), and the dashed curve shows the results with A2. The reduced transmittance observed at longer wavelengths without A2 is attributed to overfilling of the aperture as a result of thermal radiation from the heated source aperture.

heated source aperture can still overfill the sample area, producing spurious transmittance results.

This effect is demonstrated in Fig. 3, in which measurements of a 15-mm aperture placed at the sample position with a nominal spot diameter of 3 mm are shown. The solid curve shows the measured transmittance, which is close to 1.0 for wavelengths less than 7 μm, but falls off sharply toward longer wavelengths, reaching a value near 0.97 by 25 μm. This behavior is consistent with a wavelength-dependent effective spot size, which overfills the 15-mm aperture at longer wavelengths, where the blackbody radiation from the heated source aperture is a larger fraction of the ~1200-K blackbody spectrum of the globar source. To try to reduce this effect, we placed a second aperture (A2 in Fig. 1) in front of the sample and reduced its size to slightly clip the beam, making it effectively the field stop for the system. This aperture was also tilted by ~45° to avoid additional interreflections. The transmittance of the 15-mm aperture with A2 in place is shown as the dashed curve in Fig. 3. The falloff in transmittance at longer wavelengths is now less than 0.2%.

The use of secondary aperture A2 was adopted for the remaining transmittance experiments described in this paper. Because A2 is not in the image plane, it produces some degree of vignetting, which is also the case with the half-blocks described earlier. This vignetting should be expected to increase the sensitivity of the transmittance measurement to sample nonuniformity. It would be preferable to place the secondary aperture A2 at a focal position, which would be possible with additional focusing mirrors in the beam path. Another possible solution would be to preaperture the source before the Jacquinot stop in the source compartment, thus reducing the temperature rise of this aperture. Finally, nonsource emission effects can be largely removed by chopping the source directly,[5] either using a double-modulation scheme with the rapid-scan FT-IR design, or the more conventional step-scan approach. Of course, chopping the source decreases the throughput by a factor of two.

3. *Errors Due to Detector Nonequivalence*

Another class of important error sources in FT-IR transmittance measurements is detector nonlinearity–nonequivalence effects.[8] In the case of the pyroelectric DTGS detector used in this study, the nonlinearity is a small effect, which can be seen in the signal below the cutoff of the KBr:Ge beam splitter, typically $<10^{-4}$ of the peak single-beam signal. However, the responsivity of DTGS detectors is temperature-dependent near room temperature, so that the change in radiant flux on the detector as the sample is switched in and out of the beam can produce a nonequivalent response and shift the apparent transmittance accordingly.

To test for this effect, we measured the transmittance of the 0.25-mm-thick Si wafer versus the empty beam with increasing amounts of beam attenuation achieved by our placing one or two metal mesh screens before the sample and closing down the field stop A2 (see Fig. 1). Closing down this stop also reduces somewhat the solid angle of the beam, since the stop is not at a focal plane; however, for the nearly unpolarized beam this effect is estimated to produce a relative change of less than 0.05% in measured transmittance. The results of this test are shown in Fig. 4. The measured transmittance of the Si wafer from 2 to 5 μm is shown in Fig. 4(a) for varying degrees of attenuation, denoted by the detector signal at zero path difference (ZPD) with the sample removed from the beam. Apparent in this figure is a nearly wavelength-independent relative increase of 2% in the measured transmittance value as the power level is decreased.

When the incident flux level is decreased by ~1 order of magnitude from the unattenuated beam (which contains only half of the original flux of ~25 mW because of the presence of the half-blocks), the measured transmittance approaches the solid curve. This curve shows the transmissivity calculated for normal incidence, including incoherent addition of multiple reflections, from handbook values[9] of the index of refraction, n, according to the following formula:

$$T = \frac{1 - r}{1 + r}, \tag{1}$$

where $r = (1 - n)^2/(1 + n)^2$ is the single-surface power reflection coefficient. The imaginary part of the index is negligible ($<10^{-7}$) in this spectral range. The spread in the published values for n in the 2- to 5-μm range obtained by two different techniques (minimum deviation in a wedge[10] or observation of channel spectra in an optical flat[11]) is ~0.2%.

In Fig. 4(b) the measured transmittance values at 3.4 μm seem to saturate to an average level within 0.2% of the expected value for ZPD levels of less than

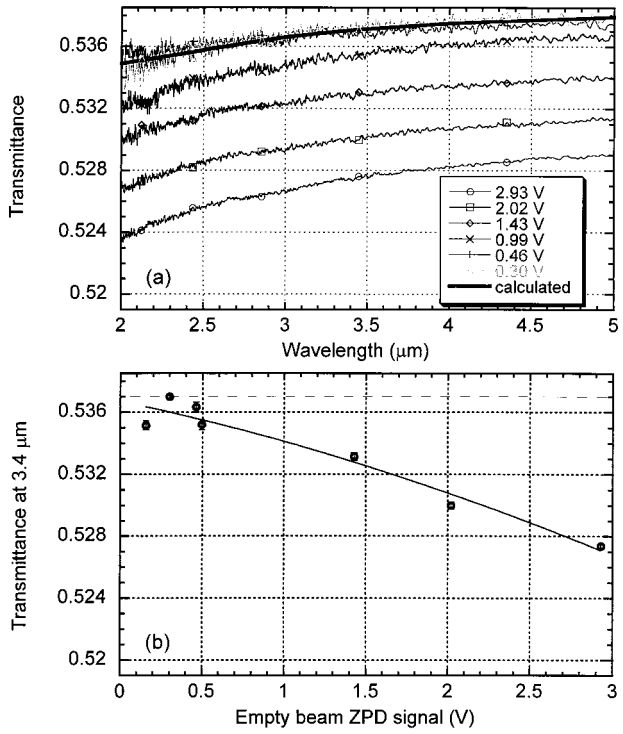

Fig. 4. Measured transmittance of a 0.25-mm-thick Si wafer versus wavelength for different incident power levels. (a) Measured transmittance curves from 2 to 5 μm for different values of the empty beam detector signal at ZPD, compared with the predicted transmittance based on handbook values for the index of refraction. (b) Dependence of the apparent transmittance at 3.4 μm on ZPD signal (open circles, data; solid line, quadratic fit). The measured transmittance approaches the expected value as the incident power level is decreased, reducing the temperature change of the detector.

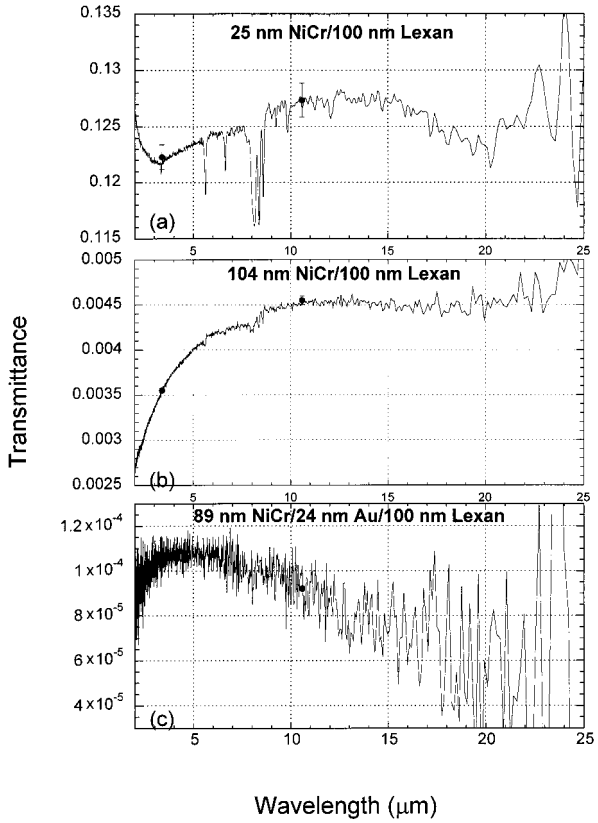

Fig. 5. Comparison of FT-IR and laser transmittance measurements of three metallic thin-film neutral-density filters on 100-nm Lexan substrates: (a) 25-nm NiCr, (b) 104-nm NiCr, and (c) 89-nm NiCr/24-nm Au coatings. Curves, FT-IR data; filled circles, laser data at 3.39 μm and 10.6 μm with expanded uncertainty error bars as described in the text. The laser and FT-IR data appear to agree within the expanded uncertainties.

0.5 V. The scatter (~0.4%) in the four data points at the lowest power levels is reproducible (not the result of random drifts in the interferometer—the error bars show the statistical uncertainty components), but the origin of the differences is not well understood. They are likely related to the small amount of flux scattered by the metal mesh screens or field stop A2 that reaches the detector. In any case the radiometric accuracy of the transmittance measurement is demonstrably improved by attenuating of the beam as we have done here. Transmittance measurements of samples relative to the empty beam were thus performed with empty beam ZPD levels of <0.5 V for the laser intercomparison measurements described in the Subsection 2.C. This represents a large decrease in the signal-to-noise ratio for a given averaging time and thus partially negates the multiplexing advantage of the FT-IR design. Other possible approaches are discussed in Section 5.

C. Measurement of Samples for Intercomparison with Laser Sources

Comparison of broadband low-resolution transmittance spectra of thin parallel-sided dielectric samples with coherent narrow-band laser measurements is in general complicated by Fabry–Perot interference effects. In principle, sufficiently high-resolution measurements could be made with the FT-IR instrument to map out the interference fringes and compare directly with the laser result (assuming the laser wavelength is sufficiently well known). However, in practice, differences in the beam geometry between the two measurements, as well as a slight tilt, wedge, or nonflatness of the sample, make this type of comparison difficult at the 0.1% relative standard uncertainty level that one would like to achieve.

Our approach has been to use samples that are free of interference effects so that the broadband 8-cm^{-1} resolution FT-IR data can be compared easily with the laser measurements. Such samples consist of metallic NiCr or Au coatings on ~100-nm-thick Lexan substrates, which are thin enough that the entire wavelength range of interest (2–25 μm) is contained within the first interference fringe.[12] (The position of the longest wavelength transmittance minimum is given by $\lambda = 4nd \sim 4(1.5)(0.1\ \mu m) = 0.6$ μm, where d is the substrate thickness).

Results of FT-IR transmittance measurements of three metallic film samples on ~100-nm Lexan substrates are shown in Fig. 5. For the 25-nm NiCr

sample shown in Fig. 5(a), the transmittance measurement was made relative to the empty beam with the setup with reduced radiometric errors described in the previous section. This sample shows a fairly flat attenuation, with the transmittance varying between 0.12 and 0.13 over the measured spectral range. A number of absorption features from the Lexan substrate can be seen in the 5–10-μm region. The spectra of the higher-optical-density samples shown in Figs. 5(b) and 5(c) were obtained by removal of the metal mesh filters; for the 104-nm NiCr sample in Fig. 5(b) the sample with the 25-nm NiCr film was used as a reference, and for the 89-nm NiCr/24-nm Au sample in Fig. 5(c) the aperture stop A1 was opened to 8 mm, and the 104-nm NiCr sample was used as a reference. By this method the ZPD signal was kept well under 0.5 V in the reference beam for all three measurements to reduce the detector nonequivalence error.

As is apparent in Fig. 5(b), the transmittance of the 104-nm NiCr coating on Lexan has substantial wavelength dependence for wavelengths shorter than 10 μm. The signal-to-noise ratio is less than that of the laser transmittance measurement (discussed in Section 3). The 89-nm NiCr/24-nm Au sample shown in Fig. 5(c), on the other hand, has a transmittance of less than 10^{-4} at 10.6 μm, so that even with an averaging time of more than 1 h used to obtain this spectrum, the noise level is much larger than that obtained with the laser measurements. The spectral variation is slow enough, however, that a comparison of the average transmission over a 1-μm interval to the laser measurements is still of interest. Lower radiometric uncertainty can probably be achieved for this type of sample by use of a photoconductive detector.

3. Laser Measurements

Two laser sources were used to make transmittance measurements on the samples described in the previous section: a He–Ne laser at 3.39 μm and a CO_2 laser at 10.6 μm. The CO_2 laser system in the Optical Technology Division at NIST is set up to be used in either heterodyne mode or direct mode and has been described previously.[13] The He–Ne system was a direct transmittance setup, employing a beam splitter and reference detector to improve the signal stability by ratioing the signal of the two detectors. In each laser system the sample was swapped repeatedly in and out of the beam to yield statistics on the transmittance value as well as to cancel out residual drift and improve the signal-to-noise ratio.

In the 10.6-μm system the sample was placed either in one arm of the interferometer (heterodyne mode) or after the second beam splitter (direct mode), and the data from both sets of measurements were found to agree to within the statistical uncertainty. The 3.39-μm transmittance measurements were performed with a pyroelectric detector for the 25-nm and 104-nm NiCr film samples, measured relative to the empty beam, and a photovoltaic InSb detector for the 89-nm NiCr/24-nm Au film sample, which was measured relative to the 104-nm NiCr film sample. The results of the laser transmittance measurements are shown as filled circles in Fig. 5, and the error bars represent the expanded uncertainties, which are explained in Section 4.

4. Uncertainty Analysis

The following subsections list sources of ordinate scale error in the FT-IR[6] and laser transmittance measurements that we believe may be important in the present study. In each case we have either performed a test to estimate the size of the uncertainty in the measured transmittance that results from the given effect or estimated it on the basis of geometrical or other arguments. Many of the uncertainty sources are difficult to isolate from one another, and we indicate where more rigorous tests are planned. Tables 1–3 list our estimated type B (systematic) relative standard uncertainty components,[14] evaluated by various means (given relative to the measured transmittance value, unless noted), and then the relative standard uncertainty based on statistical analysis of the repeatability of the measurements, for each of the three samples that were used for intercomparison with the laser measurements.

The type B uncertainties, although in general not orthogonal, are added in quadrature because their detailed interdependencies are not well understood. Then the type A uncertainty is added in quadrature to this sum, and the final uncertainty is multiplied by 2, so that the quoted relative expanded uncertainties in Tables 1–3 represent approximate 95% confidence intervals. For the case of the 89-nm NiCr/24-nm Au sample, the uncertainty is added in quadrature to that of the 104-nm NiCr sample, which was used as the reference sample for this measurement. The final results for the transmittance values at the intercomparison wavelengths for the FT-IR and laser measurements, with the expanded uncertainties, are listed in Table 4.

A. FT-IR Measurements

The following is a discussion of the relative standard uncertainty estimates for the FT-IR transmittance values, which are summarized in Table 1.

1. 0% Transmittance Level Offset

FT-IR instruments are intrinsically ac-coupled devices, since the FT process naturally removes the unmodulated portion of the flux incident on the detector. However, it is still possible for false modulated signals to be present because of coherent electrical noise sources in the local environment or because of flaws in the amplification, digitization electronics, or software, leading to an apparent transmittance signal even when no modulated flux is reaching the detector. This possibility was tested by placing an opaque metal disk in the place of the sample. No signal was found above the noise floor of 10^{-5} transmittance for the one hour averaging time and the DTGS detector used in the current experiment. Based on other measurements

Table 1. FT-IR Transmittance Relative Standard Uncertainty Components (% Measured Value)

Uncertainty Source	25-nm NiCr/100-nm Lexan	104-nm NiCr/100-nm Lexan	89-nm NiCr/24-nm Au/100-nm Lexan
Type B			
0% offset	0.00	0.00	0.00
Interreflections	0.20	0.35	0.40
Detector nonlinearity	0.10	0.10	0.10
Detector nonequivalence	0.20	0.20	0.20
Nonsource emission	0.15	0.15	0.15
Sample nonuniformity	0.20	0.20	0.20
Beam, sample, detector nonuniformity	0.20	0.20	0.20
Beam displacement, deviation, focus shift	0.00	0.00	0.00
Beam geometry, polarization	0.15	0.15	0.15
Sample vignetting	0.03	0.03	0.03
Sample scattering, diffraction[a]	0.00	0.00	0.00
Apodization errors	0.00	0.00	0.00
Phase errors[a]	0.00	0.00	0.00
Sample temperature change[a]	0.00	0.00	0.00
Sample aging	0.30	0.00	0.00
Quadrature sum	0.55	0.55	0.58
Type A			
Relative standard uncertainty of mean at 3.39 μm	0.14	0.32	3.30
Relative standard uncertainty of mean at 10.6 μm	0.22	0.27	5.00
Relative expanded uncertainty at 3.39 μm	1.14	1.27	6.82
Relative expanded uncertainty at 10.6 μm	1.19	1.22	10.14

[a]Not tested; assumed negligible.

on this and similar FT-IR instruments with more sensitive photoconductive detectors, we believe the intrinsic offset to be less than 10^{-7} in transmittance,[15] so we choose not to include it in the uncertainty budget.

2. Interreflections

Interreflection effects are a large source of radiometric error, as was discussed in Subsection 2.B.1, where we described our efforts to minimize interreflections involving the sample. Interreflections involving

Table 2. 3.39-μm He–Ne Laser Transmittance Relative Standard Uncertainty Components (% Measured Value)

Uncertainty Source	25-nm NiCr/100-nm Lexan	104-nm NiCr/100-nm Lexan	89-nm NiCr/24-nm Au/100-nm Lexan
Type B			
0% offset	0.01	0.01	0.01
Interreflections	0.10	0.10	0.10
Detector nonlinearity	0.10	0.10	0.20
Nonsource emission	0.00	0.00	0.00
Sample nonuniformity	0.20	0.20	0.20
Beam, sample, detector nonuniformity	0.20	0.20	0.20
Beam displacement, deviation, focus shift	0.00	0.00	0.00
Beam geometry, polarization	0.03	0.03	0.03
Sample vignetting	0.01	0.01	0.01
Sample scattering, diffraction[a]	0.00	0.00	0.00
Sample temperature change[a]	0.00	0.00	0.00
Sample aging	0.30	0.00	0.00
Quadrature sum	0.44	0.32	0.36
Type A			
Relative standard uncertainty of mean	0.01	0.01	0.01
Relative expanded uncertainty	0.87	0.64	0.96

[a]Not tested; assumed negligible.

Table 3. 10.6-μm CO_2 Laser Transmittance Relative Standard Uncertainty Components (% Measured Value)

Uncertainty Source	25-nm NiCr/100-nm Lexan	104-nm NiCr/100-nm Lexan	89-nm NiCr/24-nm Au/100-nm Lexan
Type B			
0% offset	0.00	0.00	0.00
Interreflections	0.00	0.00	0.00
Detector nonlinearity	0.03	0.03	0.03
Nonsource emission	0.00	0.00	0.00
Sample nonuniformity	0.20	0.20	0.20
Beam, sample, detector nonuniformity	0.20	0.20	0.20
Beam displacement, deviation, focus shift	0.00	0.00	0.00
Beam geometry, polarization	0.03	0.03	0.03
Sample vignetting	0.01	0.01	0.01
Sample scattering, diffraction[a]	0.00	0.00	0.00
Sample temperature change[a]	0.00	0.00	0.00
Sample aging	0.30	0.00	0.00
Quadrature sum	0.41	0.29	0.29
Type A			
Relative standard uncertainty of mean	0.40	0.45	0.47
Relative expanded uncertainty	1.15	1.07	1.10

[a]Not tested; assumed negligible.

multiple passes through the interferometer result in false signals of alternating sign at harmonics of the actual (physical) wave number of a particular spectral component.[3,4] Other interreflections, if they involve the sample, merely add to the apparent transmittance of the sample. Errors as great as 10% were noted for reflective neutral-density filter samples without the beam blocks, but with the beam blocks the change in apparent transmittance of a NiCr/Lexan sample was less than 0.2%. Other interreflections involving the interferometer but not the sample, such as reflections between the interferometer and source aperture, also can lead to spurious spectral components, which we have not tested for. We assign a value from 0.2% to 0.4% to the relative standard uncertainty that is due to interreflections for the metallic film samples (because of the varying reflectance levels).

3. *Nonlinearity in Detector/Electronics*

Distortion of the transmittance spectrum owing to nonlinearity is most apparent in spurious signals at wave numbers below which the beam splitter is opaque. In the present case, with the signal always attenuated by at least a factor of 20, the below-cutoff signal was never observed to be larger than 1×10^{-4} of the peak single-beam signal. Also, as shown in Fig. 4, the shape of the Si transmittance spectrum between 2 and 5 μm is nearly unaffected by the changes in flux on the detector of at least a factor of 10. Measurements of narrow-band filters under similar conditions revealed some nonlinearity error (showing up as false transmittance at twice the main band wave number) at the 0.1% level. We assign a value of 0.1% to the relative standard uncertainty in transmittance that is due to detector nonlinearity.

4. *Nonequivalence in Detector Response*

A large nonequivalence effect of as great as 3% in relative transmittance level was observed when the unattenuated beam was used as a reference for sample measurement. Reducing the incident flux by a factor of 20 was found to yield transmittance values for Si from 2 to 5 μm that vary by less than 0.3% from the expected values. Based on the apparent slope in the transmittance level at 3.4 μm versus ZPD voltage level shown in Fig. 4(b), we estimate the relative standard uncertainty component that is due to residual nonequivalence error to be 0.2%.

Table 4. Comparison of the FT-IR and Laser Transmittance Values for the Three Samples Discussed in the Text[a]

Sample	3.39-μm FT-IR	3.39-μm Laser	10.6-μm FT-IR	10.6-μm Laser
25-nm NiCr	0.1217 ± 0.0014	0.1223 ± 0.0011	0.1272 ± 0.0015	0.1274 ± 0.0015
104-nm NiCr	$0.00354 \pm 4.5 \times 10^{-5}$	$0.003551 \pm 2.2 \times 10^{-5}$	$0.00452 \pm 5.5 \times 10^{-5}$	$0.00455 \pm 4.8 \times 10^{-5}$
89-nm NiCr/24-nm Au	$1.05 \times 10^{-5} \pm 7.2 \times 10^{-6}$	$1.06 \times 10^{-4} \pm 1.0 \times 10^{-6}$	$9.8 \times 10^{-5} \pm 9.9 \times 10^{-6}$	$9.2 \times 10^{-5} \pm 1.0 \times 10^{-6}$

[a]The expanded uncertainties in transmittance derived from the values in Tables 1–3 are also listed.

5. Nonsource Emission Errors

Errors due to source-aperture emission's overfilling the sample were substantially reduced on the placement of field stop A2 (Fig. 1) before the sample. Figure 3 shows that there may be a 0.1%–0.2% residual effect for wavelengths greater than 10 μm even with A2 in place. Emission from the sample or detector[5] is not expected to cause significant error because both are near room temperature. A test was performed with the source blocked, and no interferogram was detected above the $\sim 10^{-5}$ noise level. We estimate the relative standard uncertainty that is due to nonsource emission errors to be 0.15%.

6. Sample Nonuniformity

The uniformity of the Lexan neutral-density filter samples was tested with a 3-mm diameter spot moved on the sample by 3 mm in two orthogonal directions perpendicular to the sample normal. The maximum spatial variation was found to be 0.4% in the 9-mm-diameter circle centered at the center of the film. In principle this need not be a source of error if the sample is mapped completely and the beam and detector uniformities are known as well (see Subsection 4.A.7). The transmittance can then be defined as the appropriate spatial average. However, the absolute position of the sample relative to the beam was known only to within 1 mm. Since the transmittance measurements to compare with the lasers were performed with a 6-mm aperture, and the laser measurements had different spot sizes, we assign a relative standard uncertainty of 0.2% to sample nonuniformity for the metal film/Lexan samples.

7. Interaction of Sample, Beam, and Detector Nonuniformity

Even if the position of the spot on the sample is well defined and the uniformity map of the sample is known, nonuniformity in the beam and detector can produce errors in the transmittance spectrum owing to nonuniform averaging over the sample area. This effect was tested for by our flipping the sample by 180° without moving it relative to the beam; the estimated relative standard uncertainty is 0.2% for the Lexan samples.

8. Beam Displacement, Deviation, or Focus Shifting

Error introduced by beam displacement, deviation, or focus shifting is negligibly small for the thin metal-coated Lexan samples. Tests are planned of the general size of these effects for different types of sample by measurement of the transmittance of variable thickness and variable wedge-angle Si wafers.

9. Beam Geometry, Polarization Effects

Because the beam geometry and polarization states are different for the laser and the FT-IR measurements, the measured transmittance values would not in general agree even in the absence of other sources of error. The laser geometry is nearly collimated, normal incidence, and highly polarized. In contrast, the half-angle of the beam in the sample compartment of the Bio-Rad FTS-60A spectrophotometer is nominally 9.5°, and the central portion (~2°) of the beam is blocked for use by the alignment He–Ne laser. With the half-beam blocks in place, the geometry at the sample position is a half cone with an average angle of incidence of 6°, but with the axis of the cone aligned perpendicular to the sample to within 0.5°. Because of the conical geometry, the polarization of the beam is unimportant as long as the cone is normal to the sample surface,[16] and the transmittance is calculated to be of the order of 0.05%–0.2% lower than the collimated normal incidence value. The difference is wavelength and thickness dependent, being greatest for the shortest wavelengths and thickest samples.

In principle, one could account for the deviation from normal-incidence, collimated incident radiation in the FT-IR measurement when comparing with the laser measurements. However, there is sufficient uncertainty in the actual flux distribution of the FT-IR beam that we include the differences between the two geometries as part of the uncertainty in the measured transmittance.

10. Sample Vignetting

We tested vignetting by placing a blank aperture of the same size as the sample in the beam and measuring its transmittance. Other than the possible residual effects from the source aperture radiation for wavelengths longer than 6 μm already discussed (Subsection 4.A.4), no effects of sample vignetting have been observed, and the relative standard uncertainty is estimated to be less than 0.03%.

11. Scattering or Diffraction by the Sample

Scattering or diffraction by the sample can cause the measured transmittance of the sample to depend on the geometry of the collection optics of the detector system. It can in principle be tested by placing a series of baffles after the sample and looking for any change in the detector signal. This test has not been performed. Backscattering into the beam by the baffles could complicate this analysis. Another possible test is to measure the transmittance with an integrating sphere. At this time we estimate this error source to be negligible.

12. Apodization Effects

The interferograms for the background and sample spectra were transformed with either boxcar or triangular apodization, and no differences were noted in the spectra to within the minimum noise level. Self-apodization due to the finite source size and imperfections in the optical components of the interferometer may degrade the resolution from the nominal 8 cm^{-1} value and result in wave-number errors of at most 0.2 cm^{-1} for the largest (8 mm) spot diameter. Since the spectra are not strongly wavelength dependent near the laser intercomparison

points, this error source is not expected to be important in our analysis.

13. Interferometer Phase Errors/Phase Drift

Improper phase correction of the interferogram can cause a number of errors, including a false slope of the transmittance curves. This effect was not tested directly but is folded into the repeatability estimate given below. Wavelength errors due to drift in the FT-IR He–Ne laser wavelength are estimated to be less than 0.05 cm^{-1} and are considered unimportant for these samples, which are free from spectral structure at the points where the laser–FT-IR intercomparisons are made.

14. Sample Temperature Change or Drift

Sample temperature effects were also not tested for directly; we plan to measure the temperature dependence of the samples near room temperature to provide an estimate for this error source. This source of error is not expected to be significant for the metal films, whose electronic relaxation rates are dominated by impurity scattering, which is fairly independent of temperature.

15. Sample Aging

All the samples were measured more than once over a 10-month period, and no observable time dependence was found except for the 25-μm NiCr/100-nm Lexan sample, which may have oxidized somewhat over time and become more transparent by as much as 2%. However, the last measurements of this sample were performed both with the laser and the FT-IR systems within 2 months of each other, and changes observed over this amount of time were no more than 0.3%. We take this as the relative standard uncertainty for this sample.

16. Type A Uncertainty (Random Noise/Drift/Repeatability)

All the spectra shown in Fig. 5 exhibit apparently random fluctuations from one data point to another, which are believed to result from noise in the DTGS detector. In addition, drifts in the temperature or position of optical components in the FT-IR spectrophotometer, or in the atmosphere inside the instrument, can cause shifts in the spectra on a time scale longer than that of an individual scan. Both of these effects can be reduced by averaging of spectra taken at different times. The uncertainties from these random effects were estimated by performance of several successive measurement runs with the interferometer and evaluation of the standard deviations at each wave number. For comparison with the laser measurements, the transmittance was averaged over a 16-cm^{-1} interval. The values of the relative standard uncertainty taken as the standard deviation of the mean are listed in Table 1.

B. Laser Measurements

Below is a description of uncertainty sources for the laser measurements. These estimates are summarized in Table 2 (3.39 μm) and Table 3 (10.6 μm).

1. 0% Transmittance Level Offset

The 0% transmittance level effect was measured by our blocking the laser beam; and where need be, it was subtracted from both sample and reference measurements. It was found to be significant only in the case of the 3.39-μm laser measurement, where there was a slight zero offset in the lock-in amplifier. In the 10.6-μm measurement the offset was below the noise floor of the detector–amplifier system.

2. Interreflections

The effect of interreflections was tested by our rotating the sample about an axis perpendicular to the beam for both *s* and *p* polarized light and checking to see how well the angle-of-incidence dependence followed the expected behavior from the Fresnel equations. The transmittance was found to follow the expected curves with no evidence of a central bump in the transmittance versus angle curve at the level of 0.1% relative to the transmittance at normal incidence. The relative standard uncertainty that is due to this error source is estimated to be less than 0.1%. Backreflections from the sample into the laser can affect the laser output, but this effect was not observed in the reference detector measurement with the 3.39-μm system or in the 10.6-μm system, where statistically indistinguishable values for transmittance were obtained with either the heterodyne or direct method.

3. Nonlinearity in Detector or Electronics

The power level dependence of the transmittance values were tested, and the beam was attenuated to the point at which the transmittance changed by less than 0.1% versus power level. In the case of the 3.39-μm system a power level of less than 1 mW was used with a pyroelectric detector, and less than 10 μW with a photovoltaic detector. In the 10.6-μm system the power level was approximately 5 mW. The electronics were calibrated against known standards. The relative standard uncertainty that is due to the combined effects of these errors is estimated at 0.1%.

4. Nonsource Emission

In the 3.39-μm system, unwanted light from the laser was filtered out to at least the 10^{-5} level. The laser beam was chopped to reduce stray light effects. Blocking the beam with an opaque object always yielded just the noise floor of the electronics and detector. In the 10.6-μm system the modulation of the two beams at a relative difference frequency of 30 MHz is extremely effective at eliminating background (thermal) radiation.[13] This error source is considered unimportant on the scale of this intercomparison test.

5. Sample Nonuniformity

We tested the uniformity of the samples by moving the samples relative to the incident beam to several different positions and estimating a standard deviation in the resulting transmittance values. In each case the spot diameter at the sample position was approximately 5 mm. The variation was found to be of the order of 0.2% as in the FT-IR measurements, and we take this value for the relative standard uncertainty.

6. Beam Displacement, Deviation, or Focus Shifting

For these ultrathin samples, the effect on the beam geometry of the sample is negligible for beam displacement, deviation, or focus shifting.

7. Beam Geometry or Polarization

The beam geometry for the laser measurements was at least $f/80$ or even more collimated. In both systems the beam was highly polarized. Rotating the polarization with the beam at normal incidence on the sample did not produce any effect above the 0.1% level on the measured transmittance. Residual strains in the Lexan substrate could have produced some change in the transmitted polarization state through the sample, possibly affecting the measured transmittance because of the polarization sensitivity of the detector; however, this effect was not observed. The angle of incidence was less than 0.5°, at which angle the transmittance could be different from the normal-incidence value by 0.03%. This is our estimate for the relative standard uncertainty of the measured transmittance from the ideal normal-incidence value for the laser measurements that is due to beam geometry and polarization effects.

8. Sample Vignetting

The beam diameter at the sample position in each of the laser measurements was approximately ⅓ of the sample diameter. In each case the sample was replaced by an empty ring with the same clear aperture, which was found to have a transmittance of 1 within the statistical significance of the measurements. Thus vignetting is considered to be negligible as an error source for these measurements.

9. Scattering or Diffraction by Sample

Sample diffraction or scattering was not tested for directly but for the given wavelengths and spot diameters is not expected to produce significant errors in the measurements.

10. Type A (Statistical) Uncertainty

The samples were repeatedly moved in and out of the beam to permit us to collect statistics and correct for drift in the lasers and detectors. The mean value and the standard deviation of the mean were calculated, and the components of relative standard uncertainty are shown in Tables 2 and 3.

5. Conclusions

We have made FT-IR and laser transmittance measurements of several thin-film samples with optical densities in the range from 1 to 4 and found at best 0.5% relative differences between the two types of measurement. We obtained these results by reducing as much as possible the known sources of radiometric error in the FT-IR system, with the largest errors found to come from interreflection and detector nonequivalence effects. In all cases the laser and FT-IR measurements agree to within the estimated expanded uncertainty levels, although for the highest-optical-density metallic film sample the comparison is less meaningful because of the noise in the FT-IR measurement.

Commonly available optical detectors for this spectral range exhibit poor linearity. Our approach has been to attenuate the beam to the point at which the response becomes linear, thus trading dynamic range for improved linearity (and losing much of the multiplexing FT advantage). This limits the major benefit of the present comparison, with the DTGS detector, to measurements of samples with optical densities less than 2.5. Clearly a better approach would be to use a more sensitive photoconductive detector and directly measure its response curve by comparison, ultimately, to the NIST High Accuracy Cryogenic Radiometer. Preliminary results obtained by comparison of HgCdTe photoconductor and Si bolometer detectors at 1.32 μm to a Ge photoconductor calibrated against the High Accuracy Cryogenic Radiometer have shown that the effects of the nonlinear and nonequivalent detector response can be largely removed,[17] at least over part of the spectral range of each detector. These comparisons can be made at only a few laser lines, so broad absolute calibration remains difficult to perform at the high-optical-power levels (~50 mW) typical of FT-IR instruments.

In addition, intercomparison tests are planned with dispersive instruments, as well as with additional laser wavelengths including 5.3 μm and with diode lasers for wavelengths greater than 11 μm. Further work on differentiating the various error sources is planned by methodical study of samples of varying thickness, wedge angle, and reflectance. With the use of more sensitive, calibrated detectors, it is expected that the radiometric accuracy can be significantly improved, especially for higher-optical-density samples.

We thank Alan Migdall and Alan Pine for help with the laser transmittance measurements at 10.6 μm and 3.39 μm, respectively. Also, we thank Claude Roy of Bomem, Inc., for suggesting the circular half-beam block method of reducing interreflection errors.

References

1. P. R. Griffiths and J. A. de Haseth, *Fourier Transform Infrared Spectroscopy* (Wiley-Interscience, New York, 1986); D. R. Mattson, "Sensitivity of a Fourier transform infrared spectrometer," Appl. Spectrosc. **32,** 335–338 (1978); D. A. C. Comp-

ton, J. Drab, and H. S. Barr, "Accurate infrared transmittance measurements on optical filters using an FT-IR spectrometer," Appl. Opt. **29,** 2908–2912 (1980).
2. D. B. Chase, "Nonlinear detector response in FT-IR," Appl. Spectrosc. **38,** 491–494 (1984).
3. H. W. H. M. Jongbloets, M. J. H. Van de Steeg, E. J. C. M. Van der Werf, J. H. M. Stoelinga, and P. Wyder, "Spectrum distortion in far-infrared Fourier spectroscopy by multiple reflections between sample and Michelson interferometer," Infrared Phys. **20,** 185–192 (1980).
4. M. A. Ford, "Dispersive vs. FTIR photometric accuracy—can it be measured?" in *Advances in Standards and Methodology in Spectrophotometry*, C. Burgess and K. D. Mielenz, eds. (Elsevier, Amsterdam, 1987), pp. 359–366.
5. J. R. Birch and E. A. Nicol, "The removal of detector port radiation effects in power transmission or reflection Fourier transform spectroscopy," Infrared Phys. **27,** 159–165 (1987); D. B. Tanner and R. P. McCall, "Source of a problem with Fourier transform spectroscopy," Appl. Opt. **23,** 2363–2368 (1984).
6. J. R. Birch and F. J. J. Clarke, "Fifty categories of ordinate error in Fourier transform spectroscopy," Spectrosc. Europe **7,** 16–22 (1995).
7. J. D. Jackson, *Classical Electrodynamics* (Wiley, New York, 1975), p. 277.
8. M. I. Flik and Z. M. Zhang, "Influence of nonequivalent detector responsivity on FT-IR photometric accuracy," J. Quant. Spectrosc. Radiat. Transfer **47,** 293–303 (1992).
9. E. D. Palik, *Handbook of Optical Constants of Solids* (Academic, Orlando, Fla., 1985), p. 566.
10. H. W. Icenogle, B. C. Platt, and W. L. Wolfe, "Refractive indexes and temperature coefficients of germanium and silicon," Appl. Opt. **15,** 2348–2351 (1976); W. Primak, "Refractive index of silicon," Appl. Opt. **10,** 759–763 (1971); C. D. Salzberg and J. J. Villa, "Infrared refractive indices of silicon, germanium, and modified selenium glass," J. Opt. Soc. Am. **47,** 244–246 (1957).
11. D. F. Edwards and E. Ochoa, "Infrared refractive index of silicon," Appl. Opt. **19,** 4130–4131 (1980).
12. A. Frenkel and Z. M. Zhang, "Broadband high-optical-density filters in the infrared," Opt. Lett. **19,** 1495–1497 (1994).
13. A. L. Migdall, B. Roop, Y. C. Zheng, J. E. Hardis, and G. J. Xia, "Use of heterodyne detection to measure optical transmittance over a wide range," Appl. Opt. **29,** 5136–5144 (1990).
14. B. N. Taylor and C. E. Kuyatt, "Guidelines for evaluating and expressing the uncertainty of NIST measurement results," NIST Tech. Note 1297 (U.S. GPO, Washington, DC, 1994).
15. Z. M. Zhang, L. M. Hanssen, and R. U. Datla, "High-optical-density out-of-band spectral transmittance measurements of bandpass filters," Opt. Lett. **20,** 1077–1079 (1995).
16. K. D. Mielenz, "Physical parameters in high-accuracy spectrophotometry," Natl. Bur. Stand. (U.S.) Spec. Publ. 378 (U.S. GPO, Washington, DC, 1973).
17. Z. M. Zhang, C. J. Zhu, and L. M. Hanssen, "Methods for correcting nonlinearity errors in Fourier transform infrared spectrometers," Appl. Spectrosc. **51,** 576–579 (1997).

Appendix B.

Linearity characterization of NIST's infrared spectral regular transmittance and reflectance scales

Leonard Hanssen and Simon Kaplan
Optical Technology Division, NIST
Gaithersburg, MD, USA 20899-8442

ABSTRACT

In the past decade, scales for infrared spectral regular (specular) transmittance and reflectance have been established at the National Institute of Standards and Technology (NIST). Recently, we have developed an error budget based on direct evaluation of the sources of error in the measurement process. These include the detection system non-linearity, spatial non-uniformity of the detector, misalignment of components, inter-reflection between components, asymmetry of sample and reference measurements, and source polarization effects. Here we describe the evaluation of the linearity of our measurement system that includes a Fourier transform spectrophotometer, integrating sphere and MCT detector. From the linearity results, relative responsivity curves are also established.
Keywords: Transmittance, reflectance, infrared, scale, linearity, Fourier transform infrared, FTIR, integrating, sphere.

1. INTRODUCTION

Calibration of the photometric scale of Fourier transform infrared spectrometers (FT-IRs) is an important characterization for numerous applications, but especially for a calibration facility or standards laboratory. The National Institute of Standards and Technology (NIST) has developed infrared spectral reflectance (ρ) and transmittance (τ) capabilities around FT-IRs for characterization of solid samples. It has produced spectrally neutral infrared transmittance standard reference materials SRMs 2053, 4, 5, and 6, with respective nominal optical densities (OD) of 1, 2, 3, and 4, for calibration of the photometric scale. Currently the primary system for ρ and τ with the highest accuracy uses an integrating sphere. Although designed for diffuse sample characterization, specular samples can be measured with high accuracy. Many sources of error have been investigated and characterized.[1,2] Assessment of the linearity of the scale is perhaps the most important part of the scale calibration, and is addressed in this paper for our FT-IR-sphere system. Uncertainties for these scales were originally determined by a method that provides a direct determination of the combined (transmittance and reflectance) absolute error.

Although linearity calibration of spectrophotometers is of first order importance, the classical methods used with dispersive instruments, namely the double aperture and sector wheel methods, do not work well for rapid scan FT-IRs.[3] Alternative methods include the use of transmittance standards that span the scale of interest such as those from the National Physical Laboratory (NPL) and NIST. For primary standards, however, another technique must be used. We present such an alternative method for the linearity evaluation of our FT system. This method combines filter transmittance measurements with a means of changing flux level in a way that does not introduce other significant errors into the process. No prior knowledge of the filter transmittance is required other than to assume that it is spatially uniform.

2. DESCRIPTION OF LINEARITY EVALUATION METHOD

The method of linearity evaluation for the FT-IR-sphere system involves the repeated measurement of the spectral transmittance of a Si sample (or other relatively neutral filter) at different levels of input flux ranging over approximately two decades. (A variation of this method has been employed in the past for linearity evaluation in the calibration of

Fourth Oxford Conference on Spectroscopy, Art Springsteen, Michael Pointer, Editors, SPIE Vol. 4826 (2003) © 2003 SPIE · 0277-786X/03/$15.00

standard detectors at NIST.) We achieve the variation of input flux level by use of an aperture plate shown in Figure 1, using 14 apertures ranging in diameter from 1 to 8 mm. The aperture plate is located at an intermediate focus of the external beam coming from the FT-IR. For the measurements performed in this study, the size of the illuminated region of the Si sample ranges from 1.7 to 14 mm as the aperture size is increased. The method requires neither an exact knowledge of the aperture size, nor an absolute measurement of the modulated input flux. It requires the Si (or other filter) transmittance measurement in order to measure the ratio of the responsivities of the system between the sample and reference measurements. (It can also be taken as a measure of the relative responsivity at the midpoint flux level between sample and reference measurements.)

When the transmittance measurements are performed over all the available aperture settings, the flux input ranges (between sample and reference measurement) overlap. This means that (a) if the measured transmittance values are constant, the system is linear to within the variation, and (b) a relative system responsivity curve can be constructed. Both the change in aperture and the Si wafer insertion provide relatively (spectrally) neutral changes to the input flux, which is preferable for linearity evaluation.

3. EXPERIMENTAL SETUP

The FT-IR used in the system is a Bio-Rad 60A/896 with KBr & quartz beamsplitters, Globar & W-halogen sources, and an external measurement setup shown in Figure 1.[4] The external optics arrangement is used to define the beam geometry for several custom accessories, including a gold integrating sphere used for transmittance and reflectance measurements of both specular and diffuse samples. The detector, located on the sphere, is a medium band MCT

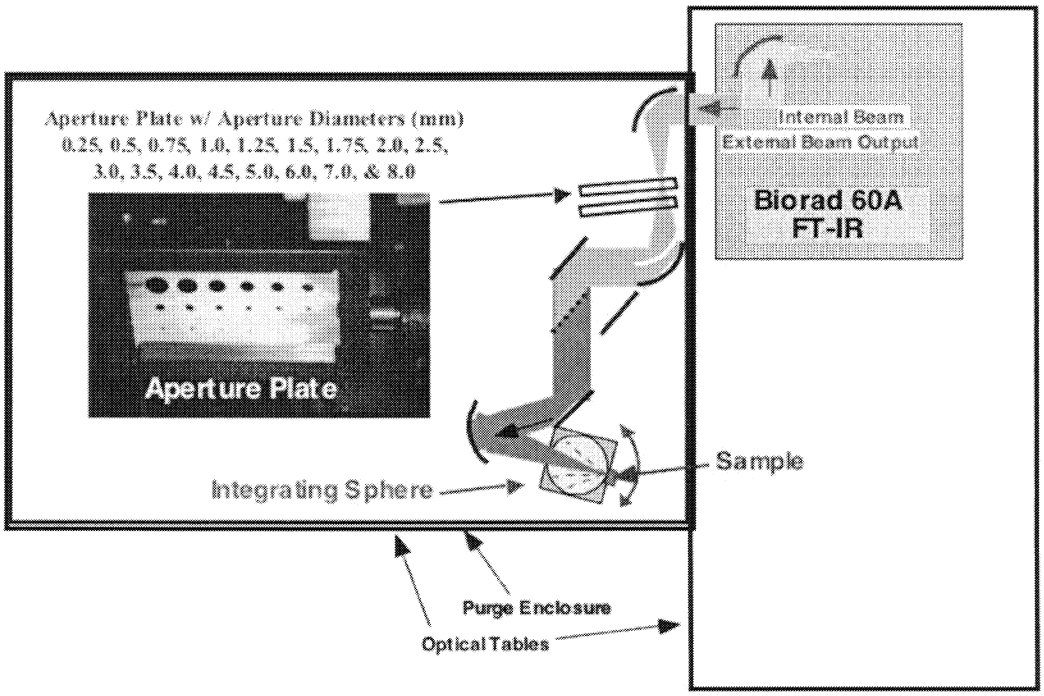

Figure 1. Layout of experimental setup, showing the FT source, external optics including the aperture plate with photo, integrating sphere, and sample in reflectance mode position. For transmittance, the sphere is rotated so that the beam is incident on the sample from behind.

(HgCdTe) with non-imaging optics designed for high throughput. In particular, ρ and τ of specular samples can be measured with an uncertainty of ~0.25%.[2] A pair of off-axis paraboloidal mirrors (OAPs) is used to provide an adjustable focus arrangement, with an intermediate focus where an aperture plate and filter wheel are located. For the integrating sphere measurements the beam remains collimated prior to a third OAP that provides an f/6 input to the sample. The spot size on the sample is determined by the setting of the aperture plate, as described above.

4. LINEARITY CHARACTERIZATION PROCESS AND RESULTS

Measurements were made of the silicon sample τ in both the near-infrared (NIR) and mid-infrared (MIR) configurations of the FT-IR. This was repeated for all available apertures from 1.0 mm through 8.0 mm. All transmittance results are shown overlayed in Figure 2: NIR τ in (a) and MIR τ in (b). As can be expected, the data for small apertures are rather noisy. However, on the scale of the plots, no systematic deviations are evident, indicating good linearity.

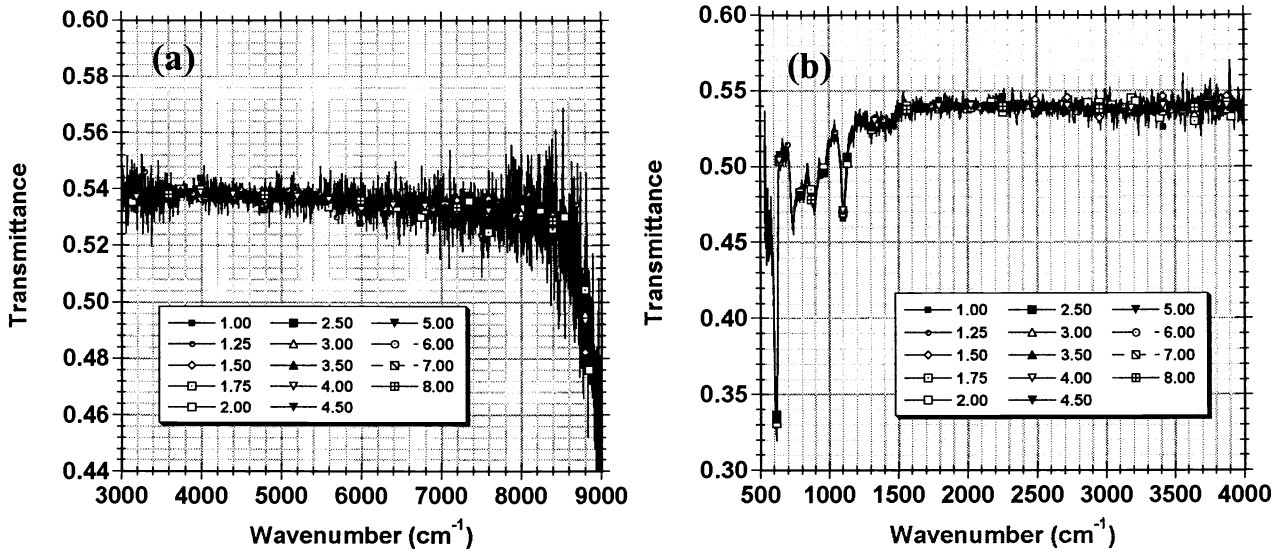

Figure 2. Measured transmittance of a Si sample for the (a) near-infrared and (b) mid-infrared system configurations. Each plot contains 14 curves overlaid, corresponding to different source apertures used from 1 mm through 8 mm in diameter.

The spectra shown in Figure 2 were obtained for input flux levels ranging over two decades as shown in Figure 3. Figure 3 contains plots of the relative signal level for all silicon sample and reference measurements for all apertures. Both NIR and MIR results are shown. Each curve represents the maximum signal in each spectrum as a function of source aperture diameter. Alternatively, other characteristics of the measurement data (such as the spectrally integrated flux, or the maximum of the measured interferograms) could also be used, without any change in the outcome of the results. In Figure 3, each point is also projected onto the right or left axis to demonstrate the number and density of flux levels obtained for determination of the system linearity and responsivity.

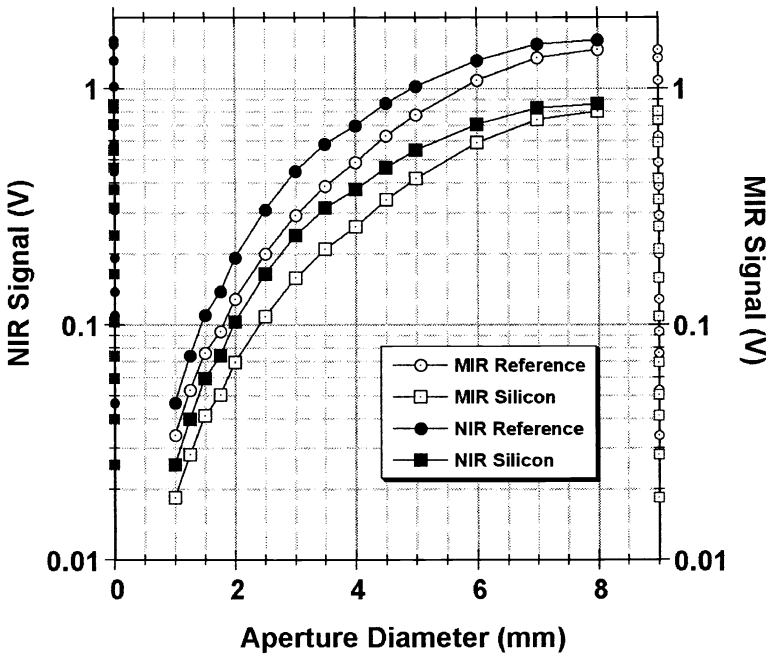

Figure 3. Relative input flux obtained for the sample and reference spectra used to determine the Silicon transmittance. The four curves denote the maximum signal values in the spectra for both the MIR and NIR configurations, as a function of source aperture diameter. Each point is also projected onto the right or left axis to emphasize the number and density of flux levels obtained for determination of the system linearity and responsivity.

Further processing of the spectra shown in Figure 2, included normalizing each spectrum to the mean τ. Then to reduce the effect of noise, for comparison purposes the data were smoothed. After this process, the spectral normalized τ showed a maximum variation of ± 0.002 (0.2%) for both NIR and MIR results. The smallest aperture data produced the maximum variation, which appear to be primarily noise related. To reduce the effect of the noise, a further step of averaging the normalized spectra over the ranges of 3000 cm^{-1} to 7000 cm^{-1}, and 600 cm^{-1} to 4000 cm^{-1}, for the NIR and MIR ranges, respectively, was taken. (For this step the initial smoothing is superfluous.) This revealed a variation of only ± 0.0006 (0.06%) for both the NIR and MIR cases. These results are shown in Figure 4. The mean normalized transmittance is plotted versus the maximum signal of the corresponding reference spectrum. The error bars represent two standard deviations obtained from averaging over each τ spectrum.

Since the curves shown in Figure 4 are bound within ± 0.001, the FT-integrating sphere spectral transmittance / reflectance measurement system is demonstrated to be linear to at least $\pm 0.1\%$. This is true despite the ease with which in general, MCT detectors can be operated in a nonlinear regime in FT spectrometers. In the special case of use of an integrating sphere, the flux levels are reduced by over two orders of magnitude, so that all measurements can be performed in the linear regime of both detector and amplifier electronics.

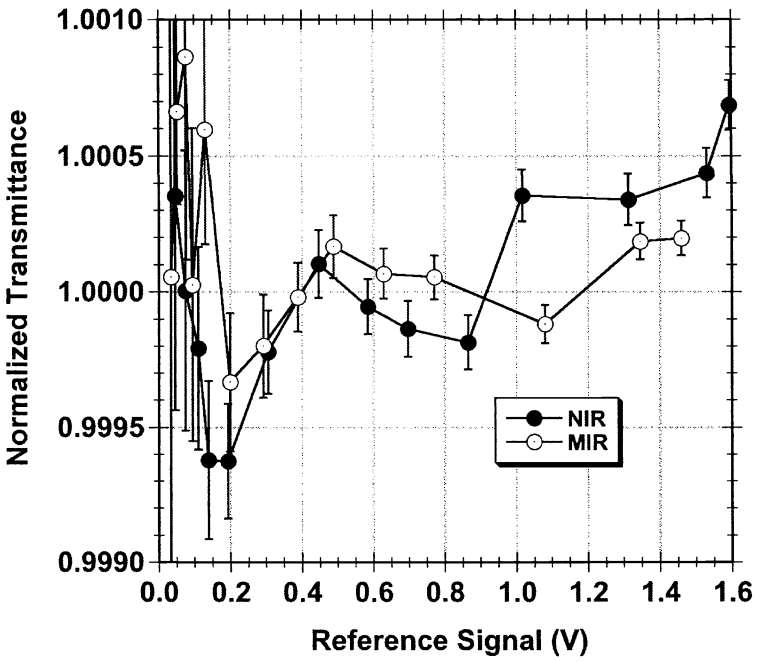

Figure 4. The mean normalized transmittance as a function of maximum signal in the reference measurement (for all values of source aperture diameter) for both the MIR and NIR configurations. The transmittance is averaged over the spectral ranges of 600 cm^{-1} to 4000 cm^{-1} for the MIR, and 3000 cm^{-1} to 7000 cm^{-1} for the NIR. The error bars represent two standard deviations obtained from averaging the spectral data.

5. RESPONSIVITY DETERMINATION

The linearity results can be used to reconstruct a relative responsivity curve for the FT-IR-Sphere system over the input flux range of the complete set of measurements. Since the input flux level is proportional to the single beam spectrum signal, a relative flux level can be obtained for every sample and reference measurement. This was done to convert the aperture diameter axis to a relative flux level axis. The normalized transmittance value for each aperture setting is also a ratio of the system responsivities for the sample and reference input flux levels. The relationship between the responsivity ratios for the various apertures is determined by the reasonable assumption that the relative system responsivity curve is a slowly changing and continuous function along which both sample and reference measurement relative responsivities must lie. System responsivity curves shown in Figure 5 are obtained by plotting sample and reference data points in pairs, whose ratio remains fixed, but whose responsivity values are adjusted by the requirement that all points lie on a relatively smooth curve. This process is made feasible by the overlap of the sample flux levels with reference levels from other apertures as seen in Figure 3. The system relative responsivity in Figure 5 is constant to within ±0.06%. (And hence the linearity of the system is also within ±0.06%.) The error bars represent two standard deviations obtained from averaging over the spectral range. The remaining variations in the curve could be due to any of a number of possible sources of error including noise, instrument drift, purge variation, etc.

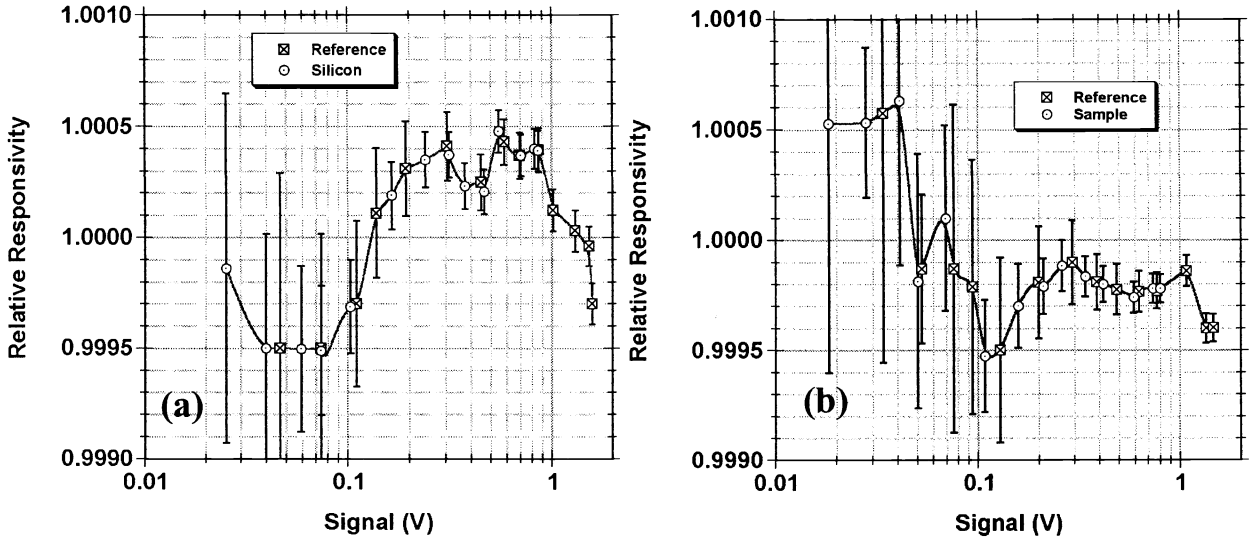

Figure 5. Relative responsivity for the FT-IR-sphere system for the (a) near-infrared and (b) mid-infrared configurations. Error bars indicate twice the standard deviation from averaging across the 600 cm^{-1} to 4000 cm^{-1} spectral range.

6. REMARKS AND CONCLUSIONS

A number of traditional methods for linearity evaluation of spectrophotometers pose difficulties for similar characterization of rapid scan FT-IRs and the application of other techniques can be thwarted by sources of error such as beam and detector non-uniformities. However, for an FT-IR-integrating-sphere system such as the one described herein, the method of filter transmittance combined with input flux variation by means of aperturing can work well. As demonstrated for both NIR and MIR configurations, the deviations from linearity for our FT-IR-Sphere system are less than ±0.06%. Due to the low throughput of the integrating sphere, the flux level at the MCT detector is sufficiently low to be in its linear response regime. Also, other sphere characteristics such as very good local spatial uniformity and the absence of inter-reflections, as well as measurement system features such as automatic repetition of measurements for drift compensation, enable very accurate and repeatable results.[2] These factors enable us to resolve small variations less than 0.1% and to establish linearity to a level even better than that. Although the spectral results showed a greater deviation in linearity, this was seen for the smallest apertures with the lowest flux level and greatest noise in the results. We anticipate with further measurements and reduced noise levels, the deviations from linearity spectrally will show similar behavior to the averaged results described here.

REFERENCES

1. S.G. Kaplan, R.U. Datla, and L.M. Hanssen, Applied Optics **36**, 8896-8908 (1997).
2. L. M. Hanssen, Appl. Opt. **40**, 3196-3204 (2001).
3. F. J. J. Clarke, Anal. Chim. Act. **380**, 127-141 (1999).
4. The use of a trade name or manufacturer in this publication is for identification purposes only and does not imply endorsement of the product by NIST.

Appendix C.

Integrating-sphere system and method for absolute measurement of transmittance, reflectance, and absorptance of specular samples

Leonard Hanssen

An integrating-sphere system has been designed and constructed for multiple optical properties measurement in the IR spectral range. In particular, for specular samples, the absolute transmittance and reflectance can be measured directly with high accuracy and the absorptance can be obtained from these by simple calculation. These properties are measured with a Fourier transform spectrophotometer for several samples of both opaque and transmitting materials. The expanded uncertainties of the measurements are shown to be less than 0.003 (absolute) over most of the detector-limited working spectral range of 2 to 18 μm. The sphere is manipulated by means of two rotation stages that enable the ports on the sphere to be rearranged in any orientation relative to the input beam. Although the sphere system is used for infrared spectral measurements, the measurement method, design principles, and features are generally applicable to other wavelengths as well.

OCIS codes: 120.0120, 120.3150, 120.5700, 120.7000, 120.3940, 120.4570.

1. Introduction

Integrating spheres have long been used for the measurement of diffuse reflectance and transmittance of materials in the UV, visible, and near-IR spectral regions, as well as somewhat more recently (since the 1970's) in the mid- to far-IR regions. However, integrating spheres have been used infrequently for specifically measuring specular materials. This is true despite the fact that, according to integrating-sphere theory, for an ideal sphere, a simple ratio of two measurements should result in the absolute reflectance of a specular sample. The reason for the lack of use of integrating spheres for specular measurements of reflectance is that real integrating spheres are not ideal. The sphere-wall coating is never a perfect Lambertian diffuser, baffles perturb the light distribution within the sphere, and all detectors exhibit some angular dependence. These and other deviations from an ideal sphere can drastically affect the accuracy of the sphere equations.[1]

Because of the deviations, all spheres have some degree of nonuniformity of throughput. This means that the detector signal will vary as the direction of the reflected or the transmitted light (and the regions upon which the light is incident) within the sphere is varied. The result may be errors in the quantities derived from the measurements. For this reason, measurements of reflectance of specular materials are usually performed relative to a known specular standard. When this is done, the regions of the sphere wall upon which the reflected light of the sample and the reference falls usually have similar throughputs.

For absolute regular (specular) reflectance measurements, various methods, including, V–W, V–N, and goniometer-based methods, are typically used.[2,3] These methods typically do not involve an integrating sphere. They involve an input beam, several directing mirrors, and the detector. Some subsets of the mirrors, the sample, and the detector are rotated and translated between sample and reference measurements. For the V–N and the goniometer methods, a simple ratio of the two results produces the absolute sample reflectance, whereas for the V–W method, the square root is taken.

The primary sources of error in the methods just mentioned are the result of alignment problems and the spatial nonuniformity of the detector. These problems can easily lead to errors of several percent

L. Hanssen (hanssen@nist.gov) is with the Optical Technology Division, National Institute of Standards and Technology, Gaithersburg, Maryland 20899.

Received 17 October 2000; revised manuscript received 20 March 2001.

0003-6935/01/193196-09$15.00/0

or more.[4] With considerable effort to achieve accurate alignment, excellent results can be achieved for standards quality samples. However, even in these cases, characteristics of the sample surface can limit ultimate measurement accuracy.[5,6] For transparent materials, dealing properly with the transmitted light and measuring the backsurface reflection accurately pose additional difficulties.

An important application of integrating spheres is their use as an averaging device for detectors. Because of the useful properties of the sphere, an averaging sphere's entrance port can be both significantly larger and much more spatially uniform than a bare detector. The trade-off made for these improvements is a degradation of the signal-to-noise ratio. The benefits of using the integrating sphere for more accurate detection of light are used in the design of the system and development of the method presented in this paper. The measurement of absolute transmittance (τ), reflectance (ρ), and absorptance (α) of specular samples is described and demonstrated. The inherent problems of sphere spatial nonuniformity are overcome through judicious use of the symmetries of the sphere design to establish symmetries in the measurement geometry. After describing the specifics of the integrating sphere in Section 2, the other components of the sphere system in Section 3, and the absolute measurement method in Section 4, we present the sphere characterization measurement results for error analysis in Section 5. The achievement of measurement uncertainties of 0.002 to 0.004 are demonstrated in Section 6 for several common IR materials. Finally, Section 7 contains the discussion of the results with conclusions about the usefulness of the sphere method for specular materials.

2. Description of the Integrating Sphere

The integrating-sphere system has been designed and constructed according to the specifications detailed in the following paragraphs. Figure 1 is a photograph of the integrating sphere. Specific parameters of the sphere, including a description and analysis of the detector–nonimaging-concentrator system, have been described previously.[7] The inside wall of the sphere is coated with a material that is nearly a Lambertian diffuser and at the same time has a high directional hemispherical (diffuse) reflectance ($\geq$0.9) for the IR spectral range: plasma-sprayed Cu on a brass substrate, electroplated with Au.

The sphere has entrance, sample, and reference ports, all centered on a great circle of the sphere, as shown in Fig. 2. There also is a detector port, with its center located along the normal to the great circle. The white Hg:Cd:Te (MCT) detector Dewar located on the port can be seen mounted on the top of the sphere in Figs. 1 and 2. The detector's field of view is centered on the same normal and corresponds to the bottom region of the sphere. The sample and the reference ports are located symmetrically with respect to the entrance port and can be seen in the foreground of Fig. 1 (the sample port has a KRS-5 sample mounted on it). The exact location of the sample and the reference ports is in general determined by the angle of incidence for which the reflectance and the transmittance are to be determined. An arrangement of ports could, in principle, be set up for any angle of incidence from approximately 2° to 28° and from 32° to 75°, depending on the input-beam geometry of the source (or spectrophotometer). For this sphere, port locations have been selected for 8°, which is close to normal incidence, yet for which no portion of the $f/5$ (6° half-angle) input beam will be reflected back onto itself. (For incidence angles in the neighborhood of 30°, a variation of the design would be required so that the reflected beam from the sample port does not hit the reference port and vice versa). The entrance port is of sufficient size (3.3-cm diameter) to accept the entire input beam, and the sample and the reference ports are also sized (2.22-cm diameter) to accept the entire beam (at the focus, in a focused geometry). All the ports are circular in shape, with the sphere's inside and outside surfaces forming a knife edge at the port edge where they meet. In this sphere, as seen in Fig. 2, the measurement of reflectance is designed for an incidence angle of 8° (in general θ); the sample and the reference ports are located at 16° (in general $+2\theta$) and $-16°$ (in general -2θ), respectively, measured from the center of the sphere and with respect to the line through the sphere center and the sphere wall (at

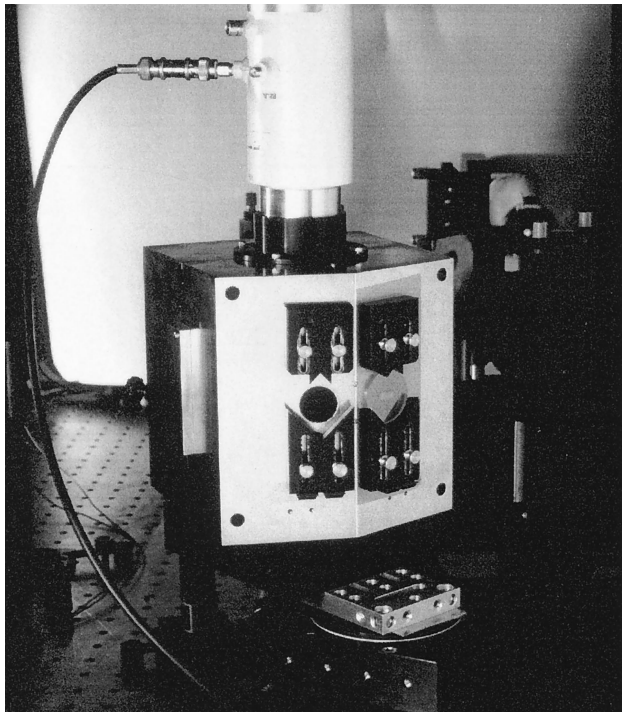

Fig. 1. Photograph of the integrating sphere for absolute IR spectral transmittance and reflectance. The Hg:Cd:Te (MCT) detector Dewar (white) is mounted on the top of the sphere. We view the back side of the sphere that includes reference (empty) and sample (with a KRS-5 window) ports. A pair of rotation stages underneath the sphere is used to move the sphere into positions for both reflectance and transmittance measurements.

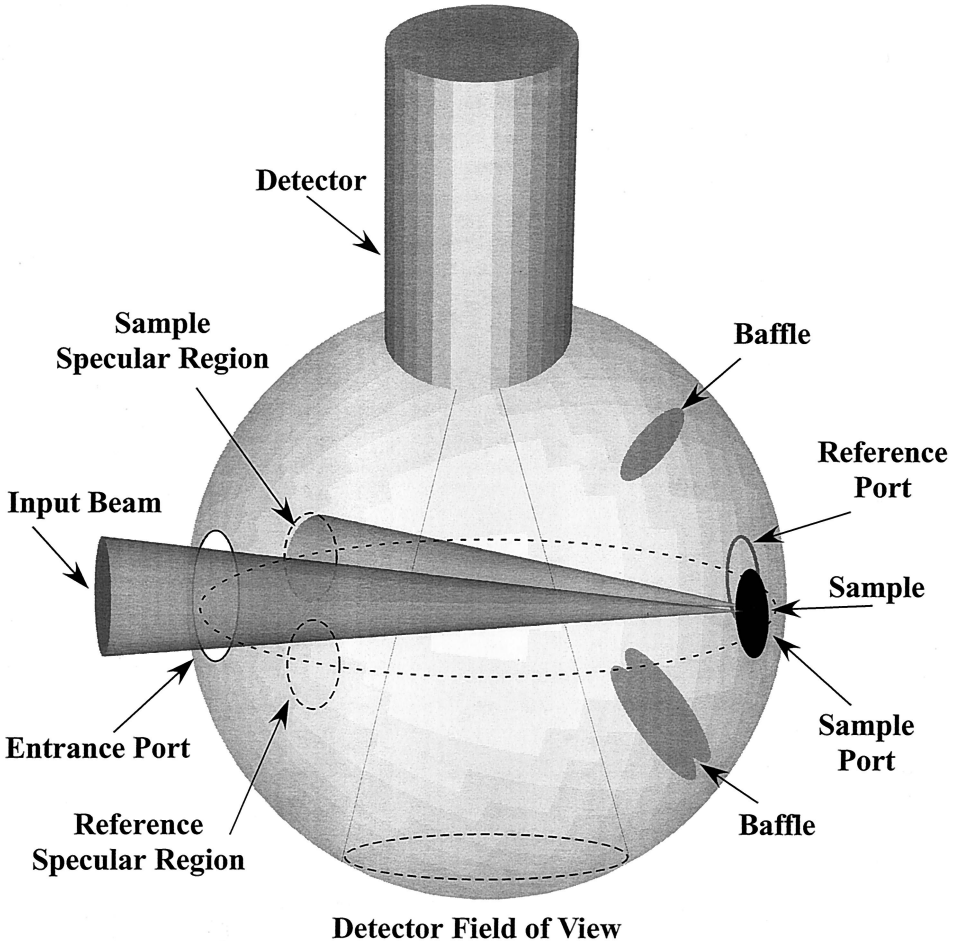

Fig. 2. Diagram of sphere interior and arrangement of its elements. Input and reflected beams are shown for a specular sample in the reflectance measurement geometry. The sample and the reference specular regions of the sphere wall are the first to be illuminated in the sample and the reference measurements, respectively. The baffles are positioned for measurement of diffuse samples and are not critical for specular sample measurement.

a point directly opposite the entrance port). Baffles separating the detector port and the detector field-of-view region from the sample and the reference ports are shown in Fig. 2. The baffles are critical to the sphere performance for characterization of diffuse samples,[8] but do not play a significant role for the specular-sample case.

The arrangement of the ports described above results in the regions of the sphere wall illuminated by the specularly reflected or transmitted light and the reference beam being centered on the same great circle as the entrance, sample, and reference ports. In addition, the regions are symmetrically positioned around the entrance port. The reflected or the transmitted light also will be incident at the same angle on these regions. As a result, the reflected or the transmitted light will have throughput to the detector that is nearly identical. The procedure for orienting the sphere for the reflectance, transmittance, and reference measurements is described in Section 3.

3. Sphere Mounting and Manipulation Hardware

The sample and the reference mounts, a pair of which can be seen on the sphere in Fig. 1, are constructed to hold the sample against and centered on the sample port from outside of the sphere. During sphere movement, the holders prevent the sample from moving or shifting relative to the sample port. This is done in such a way as to leave the back of the sample free and open, so that the beam centered on the sample can proceed through it (for a transparent sample) without obstruction. This is required for performing either transmittance or reflectance measurements on transparent samples. This arrangement can also be used to check thin-film mirrors for optical opacity.

The integrating-sphere system includes two motorized rotation stages stacked on top of each other. The stages are mounted with their axes of rotation parallel to each other. The rotation axes of the stages are identified in Fig. 3. Stage 1 has its axis of rotation oriented parallel to the normal of the great circle formed by the entrance-, sample-, and detector-port centers, as well as passing through the edge of this circle. This base stage remains fixed to the optical table. Its rotation axis is perpendicular to the input beam and passes through the beam-focus position. Stage 2 is mounted on the rotation table of the base stage so that its axis of rotation is located a distance

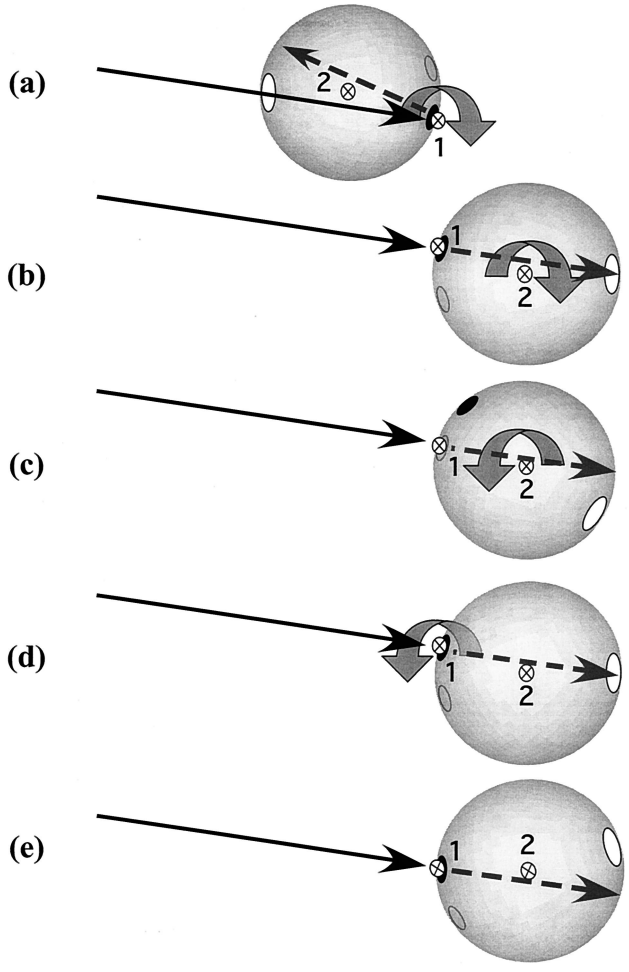

Fig. 3. Sphere measurement geometries for reflectance and transmittance and rotation steps used to orient the sphere for each (a) reflectance measurement geometry, (c) reference measurement, and (e) transmittance measurement geometry. (b) and (d) are intermediate steps. Two rotation stages, stage 1 centered at the input-beam focus and sphere wall and stage 2 centered at the sphere center, are used to change geometries.

away from the base-stage axis exactly equal to the sphere radius. The integrating sphere is mounted to the rotation table of stage 2 so that the stage's axis of rotation is along the sphere axis that includes the center of the detector port and the sphere center.

The function of base stage 1 is to vary the angle of incidence of the input beam on the sphere surface and to switch between reflectance and transmittance measurement geometries. The function of stage 2 is to select upon which port, the entrance, the sample, or the reference port, the beam will be incident.

4. Measurement Geometry and Method for Reflectance and Transmittance

The arrangement of the input beam and the integrating sphere for absolute transmittance and reflectance measurements is shown in Fig. 3. The sample reflectance measurement setup is shown in Fig. 3(a) (as well as in Fig. 2), the reference measurement in Fig. 3(c), and the sample transmittance measurement in Fig. 3(e). In each diagram, the rotation required for reaching the following diagram is shown as a curved arrow around the appropriate rotation axis. In the reflectance measurement geometry of Fig. 3(a), the input beam passes from the spectrometer through the sphere entrance port and onto the sample surface facing the sphere. This is the typical reflectance geometry for directional-hemispherical sample reflectance in most sphere systems. The only difference in Fig. 3(a) is the empty reference port (as opposed to one occupied with a standard for a relative measurement). On reflection off the sample, the beam transverses the sphere and is incident upon a region we denote as the sample specular region (see Fig. 2). From this point, the reflected flux is distributed throughout the sphere in an even fashion because of the Lambertian coating and the integrating nature of the sphere. In Fig. 3(a) a clockwise rotation about axis 1 turns the back of the sample to the beam in Fig. 3(b). An additional clockwise rotation about axis 2 places the (empty) reference port at the input beam focus in Fig. 3(c), where it continues on to strike the sphere wall at the reference specular region (labeled in Fig. 2), producing the reference measurement. Another counterclockwise rotation about axis 2 results in Fig. 3(d), a repeat of Fig. 3(b). A final counterclockwise rotation about axis 1 positions the sphere in Fig. 3(e) for the transmittance measurement, with the same angle of incidence as that of Fig. 3(a) on the sample and incidence region on the sphere wall (the sample specular region).

The somewhat unusual geometry for the reference measurement [Fig. 3(c)] is chosen in order to achieve the highest degree of symmetry between the reflectance and the reference measurements. The sample and the reference specular regions are symmetrically located on either side of the entrance port. Because of the symmetry of the sphere design, the throughput is nearly equal for these two regions. Because the only other difference between the sample reflectance and reference measurements is the initial reflection off the sample, the ratio of sample reflectance and reference measurements is equal to the absolute sample reflectance (for specular samples). Various sources of error, including the difference in the sample and the reference specular region throughputs, can be included in the expanded measurement uncertainty or can be corrected for.

The ratio of the sample reflectance measurement of Fig. 3(a) to the reference measurement of Fig. 3(c) is equal to the absolute sample reflectance (for specular samples). The ratio of the transmittance measurement of Fig. 3(e) to the reference measurement of Fig. 3(c) is equal to the absolute sample transmittance (for specular samples).

The absolute absorptance is indirectly obtained when the sum of the absolute reflectance and transmittance is subtracted from unity. Kirchoff's law applies because the reflectance and the transmittance measurements are made under identical conditions of geometry and wavelength(s). The input beam is incident upon opposite surfaces of a sample

for the reflectance and the transmittance measurements. For a uniform sample with identical front and back surfaces, the side of incidence is immaterial. For samples with some asymmetry that is due to, for example, a coating on one or both sides, the sample can be reversed to make a pair of reflectance measurements and to obtain the corresponding pair of absorptance results.

5. Measurement Conditions and Sphere Characterization

The integrating-sphere system is a measurement component of a larger Fourier transform (FT) spectrophotometer (FTS) system described in more detail elsewhere.[9] The incident-beam geometry for all measurements described in Sections 5 and 6 is an $f/5$ cone with an 8° central angle of incidence. The FTS was configured with a W–halogen lamp and coated-quartz beam splitter for the near-IR spectral region of 1 to 3 μm (10,000 to 3300 cm^{-1}), and a SiC source and coated-KBr beam splitter for the mid-IR region of 2 to 18 μm (5000 to 550 cm^{-1}). The spectral resolution is either 4 or 8 cm^{-1} for all results shown.

Every plot of transmittance and reflectance is obtained by the following procedure. A number of alternating measurements of reference, sample reflectance, and sample transmittance (where appropriate) single-beam spectra are performed according to Fig. 3 and are repeated between 8 and 24 times. For each repetition, we calculate the transmittance and the reflectance by taking ratios of the corresponding single-beam spectra and a reference single-beam spectrum (obtained by interpolation to reduce the error that is due to instrumental drift). From the resulting series of individual transmittance and reflectance spectra, the mean transmittance (τ) and reflectance (ρ), along with the standard deviation and standard error, spectra are calculated. Finally, the absorptance spectrum is obtained from $1 - \tau - \rho$.

We obtain each single-beam spectrum by coadding 512 or 1024 scans of the FTS. The total measurement time for most of the results shown is several hours (from 2 to 10). The long measurement times are required for obtaining the lowest noise level in the spectra. For less stringent requirements of 1% uncertainty, shorter measurement times of the order of 10 to 20 min will suffice.

In addition to the various potential sources of error that are due to the FT spectrometer,[10,11] several other sources of error may play a role in the sphere system measurements. These are (1) spatial nonuniformity of the sphere-wall regions directly illuminated by the input beam (reference specular region) or sample first reflection (sample specular region), (2) nonuniformity of the throughput of the sphere-wall region directly illuminated by the input beam compared with that of the region illuminated by the sample first reflection; (3) overfilling the entrance port in the sample reflectance measurement, and (4) overfilling the sample port in any of the measurements.

The spatial nonuniformity of the integrating-sphere throughput has been evaluated at the 10.6-μm wavelength by use of a CO_2 laser system. The local spatial variation across the region illuminated directly by the reference beam or indirectly by a specularly reflected or transmitted beam is approximately ±0.4%.[8] A translation of the light incident upon the sphere wall of 0.5 cm through deflection or deviation (of 2°) should result in a ±0.1% relative change in throughput. Thus a transmittance measurement of a sample with an effective wedge of 1° could lead to a 0.1% relative error in transmittance. Because of the decrease in wall reflectance and corresponding decrease in throughput with decreasing wavelength, the error that is due to spatial nonuniformity is greater at shorter wavelengths, especially in the near-IR region, approaching 1 μm.[9] Spectral evaluation of this error is currently in progress.

The difference in throughput between sample- and reference-port measurement geometries can lead to a small relative error, varying between 0% and 0.5%, depending on wavelength. The direct measurement of transmittance or reflectance for specular samples will include this error, but an additional measurement of the transmittance ratio of empty sample and reference ports can be used to correct for the error. This has been done with good reproducibility and need not be repeated unless the optical-input-system geometry or alignment is altered. A plot of such a throughput ratio is shown in Fig. 4.

Besides the generally featureless spectral curve, a sharp structure occurs at approximately 8.5 μm. This structure occurs at the only wavelength at which the incident beam from the FTIR beam is significantly polarized. It is anticipated that a future test of the sphere in which polarized light is used will show increased throughput variation with polarization. At the same time, averaging *s*- and *p*-polarized beam measurements is expected to eliminate the structure seen at 8.5 μm.

The extent of overfilling the entrance, sample, and reference ports can be examined by a measurement of an empty sample or reference port in the reflectance mode. Any light coming through the entrance port and overfilling the sample (or reference) port will be measured as a reflectance component with near-unity reflectance of the sphere-wall region surrounding the port. In addition, any overfilling of the entrance port in that measurement will result in some light scattering off the rim of the entrance port into the sphere, resulting also in a reflectance component with high effective reflectance. A knife-edge design could be used to reduce the result of entrance-port overfilling, but it is preferable to be sensitive to it in order to quantify it (set an upper limit to it). An example of the combined overfilling-error reflectance measurement is shown in Fig. 5. This was obtained after careful alignment of the sphere system and the input FTIR beam. The level of this measurement is lower than has been reported previously.[9] The previous empty-port measurement was in error because of a subtlety of the FT processing that produced a rectification of the noise in the measurement. This error was eliminated when the phase-error spectrum

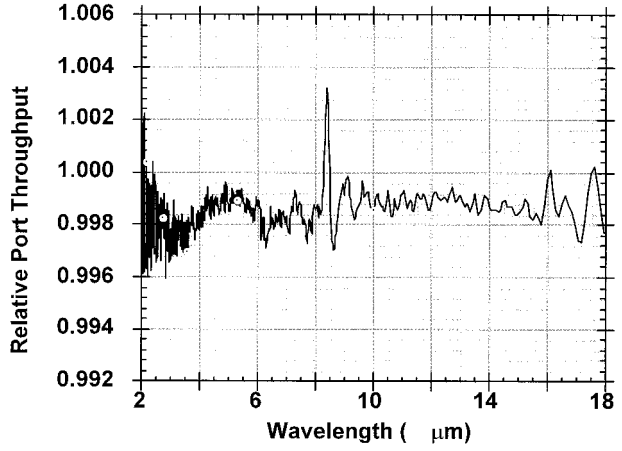

Fig. 4. Sample- and reference-port throughput comparison, the result of an empty-sample-port transmittance measurement. The curve represents the difference in detector signal for specularly transmitted and reflected light from the sample compared with light in the reference case. This spectrum can be used in either of two ways: (1) as a component to the systematic uncertainty of ρ or τ, or (2) as a correction spectrum to divide into the initially obtained spectra of ρ or τ to eliminate the error.

obtained in the reference measurement was used for correction of the sample empty-port measurement.

The remaining important sources of error are related to the FTIR spectrometer, detector, electronics, and FT processing, which are not discussed in detail here. The combined measurement error for the transmittance and the reflectance measurements include both FTIR-related errors and the integrating-sphere system errors. A straightforward method of evaluating the measurement accuracy of the system is to compare measurement results with calculated results for the optical properties of common IR optical materials. Measurements of a few common materials are presented in Section 6, and the results are used to perform this comparison.

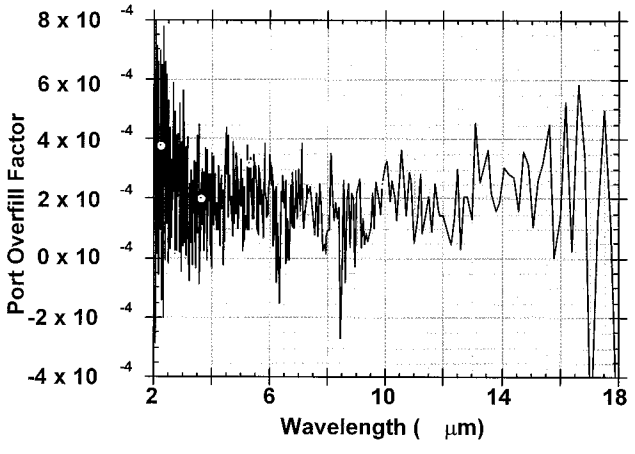

Fig. 5. Sample-port overfill measurement, the result of an empty-sample-port reflectance measurement. This is a characterization of the baseline measurement capability of the integrating-sphere system. The result can be used to apply corrections to a black sample measurement.

6. Transmittance, Reflectance, and Absorptance Results

A number of optical components have been characterized by the integrating-sphere system, including windows, filters, and mirrors. Several examples of window materials are shown in Figs. 6 and 7. Both transmittance and reflectance are measured with the same geometry. From these two quantities the absorptance is simply determined by subtraction of their sum from 1. Comparisons can be made with calculated values from handbook indexes of refraction data.[12,13] This can be done in two ways: (1) A comparison can be made with calculated transmittance and reflectance, and (2) a comparison can be made with calculated absorptance.

The calculated τ and ρ values from the n and k values in handbooks have finite uncertainty values. These are based on the uncertainties of the original data and the mathematical processes with which the index values n and k were obtained. Other sources of error in this comparison include variations in the material itself, such as the method of growth and processing.

For specific spectral regions for many materials, however, the calculated absorptance can be determined, with insignificant ($<10^{-4}$) error, to be 0. Because of this, the indirectly measured absorptance in these spectral regions can be used as an accurate evaluation of the total measurement error, not just as an estimate of uncertainty. If, in addition, a number of materials with transmittance and reflectance values spanning a significant fraction of their range (0 to 1) are measured, the measurement error can then be used with reasonable confidence for all transmittance and reflectance results.

Four common IR window materials were characterized with the sphere system, with the results plotted in Figs. 6(a)–6(d). They are Si (0.5 mm thick) [Fig. 6(a)], ZnSe (3 mm thick) [Fig. 6(b)], KRS-5 (5 mm thick) [Fig. 6(c)], and MgF_2 (5 mm thick) [Fig. 6(d)]. For each sample, the transmittance, reflectance, and absorptance are plotted over a spectral range of 2–18 μm [1–18 μm for Fig. 6(a)]. Each material has a nonabsorbing spectral region over some portion of that range. The reflectance values (in the nonabsorbing range) for the selected materials range from 0.05 to 0.45, and the corresponding transmittance values range from 0.55 to 0.95, in the nonabsorbing regions. The MgF_2 spectrum exhibits a wide range of values for ρ, τ, and α within the spectral range. At 12.5 μm, both the reflectance and the transmittance are 0, at which the absorption coefficient is substantial ($\tau \rightarrow 0$) and the index n is close to 1 ($\rho \rightarrow 0$).

A closer examination of the indirectly measured absorptance in the nonabsorbing regions is shown in Figs. 7(a)–7(d). For each material, an absorptance close to 0 is observed in the spectral regions with a nearly 0 k value. These are 1.2–5.5 μm [Fig. 7(a)], 2–13.5 μm [Fig. 7(b)], 2–18 μm [Fig. 7(c)], and 2–4.5 μm [Fig. 7(d)]. In the results,

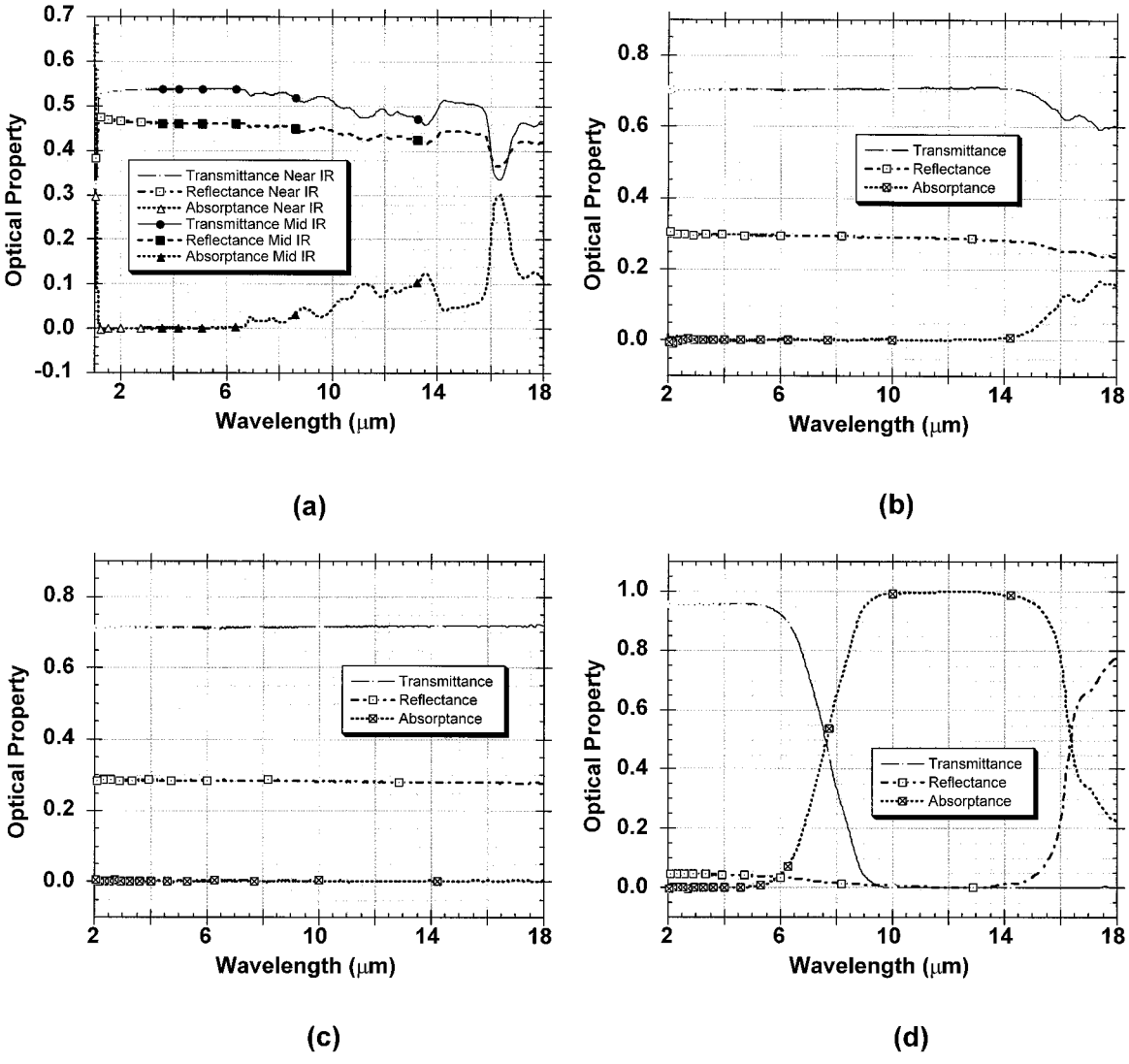

Fig. 6. Transmittance, reflectance, and absorptance (obtained from $1 - \rho - \tau$) of several common IR window materials, ranging in index from 3.4 to 1.3: (a) Si, (b) ZnSe, (c) KRS-5, (d) MgF_2.

spectral features are seen that can be attributed to contaminants, primarily on the surface, such as water and hydrocarbon modes. Features from 6 to 7 μm, 9 to 10 μm, and 12.5 μm appear in the ZnSe and the KRS-5 spectra. These features could also, in part, be associated with the input-beam nonuniformity's interacting with residual sphere spatial nonuniformity. In this way, the spectral structure that is due to the beam splitter and the detector can be observed in the results, thus comprising a component of measurement error. Conclusive results will require further characterization.

The indirectly measured absorptance levels in Figs. 7(a)–7(d) over the spectral ranges cited above can be interpreted as arising from cumulative measurement error. The results exhibit an absolute level of error ranging from 0 to 0.002 for the structureless spectral regions up to a maximum of 0.004, at which a structure is observed.

The evaluation of measurement error (by use of the zero-absorptance level) for reflectance of the transparent materials can be transferred with confidence to the opaque sample case (for which a zero-absorptance test is not feasible). An example is a Au mirror reflectance measurement, shown in Fig. 8. In the opaque sample case, there is only a single reflection, whereas for the transparent sample case, multiple reflections contribute to the reflectance result. The higher-order reflected beams will be displaced (because of the angle of incidence), enlarged (because of focus shift), and perhaps deviated (because of sample wedge). Hence the effects of spatial nonuniformity of the sphere throughput will be smaller for the opaque mirror measurement, resulting in a smaller relative measurement uncertainty for the sample reflectance. This is corroborated by the relative lack of spectral structure below 16 μm in the Au mirror reflectance in Fig. 8 (the structure above 16 μm is due to the increased noise level at the extreme end of the detector's spectral range).

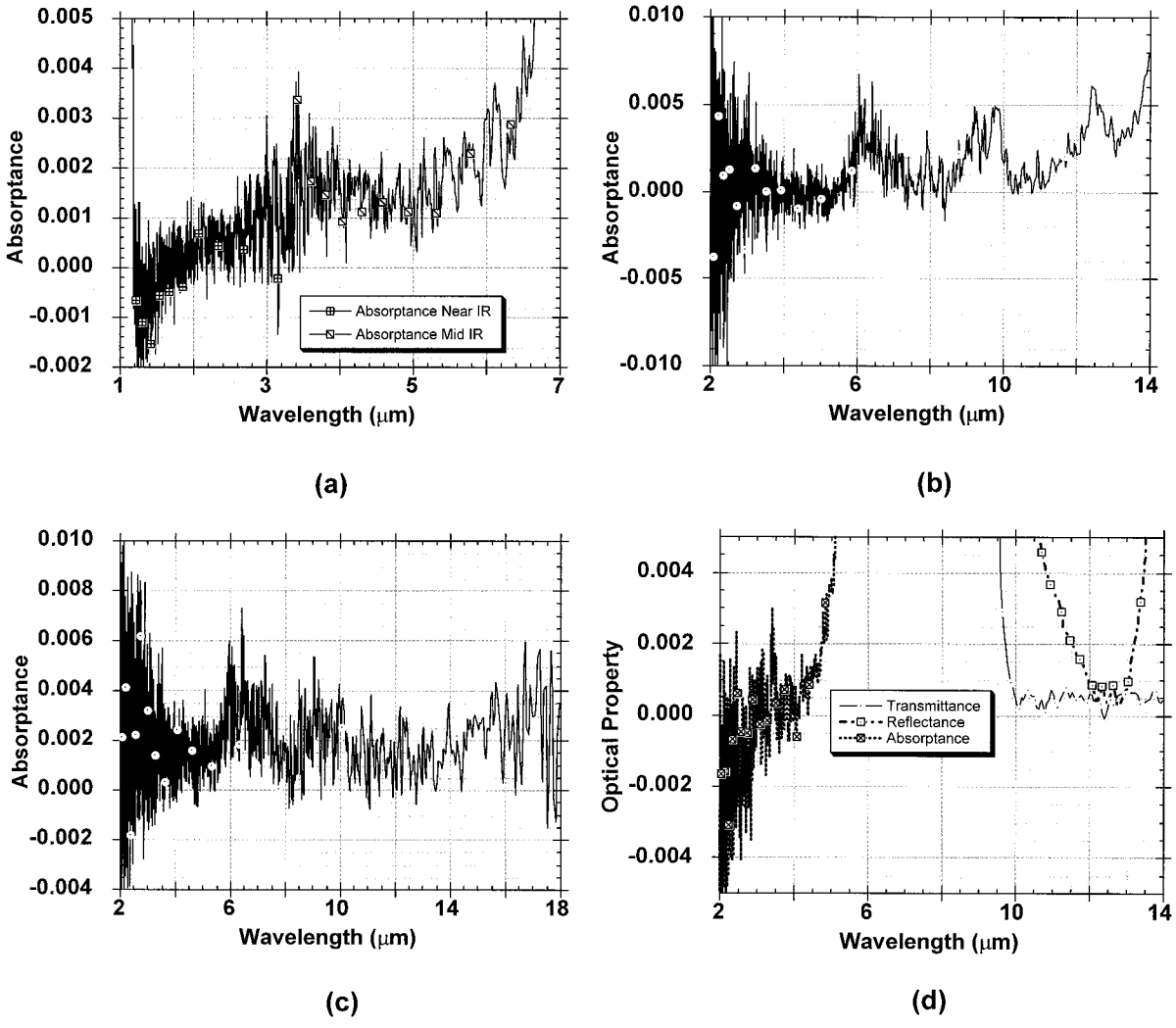

Fig. 7. Expanded plot of spectra shown in Fig. 6, highlighting regions with absorptance near zero: (a) Si, (b) ZnSe, (c) KRS-5, (d) MgF_2. The spectra, in regions where k should be negligible,[12] result from a combination of (1) cumulative measurement error from all sources in transmittance and reflectance, and (2) additional absorption that is due to volume or surface contaminants such as hydrocarbons and water. The MgF_2 spectrum also shows regions of near-zero transmittance and reflectance at longer wavelengths.

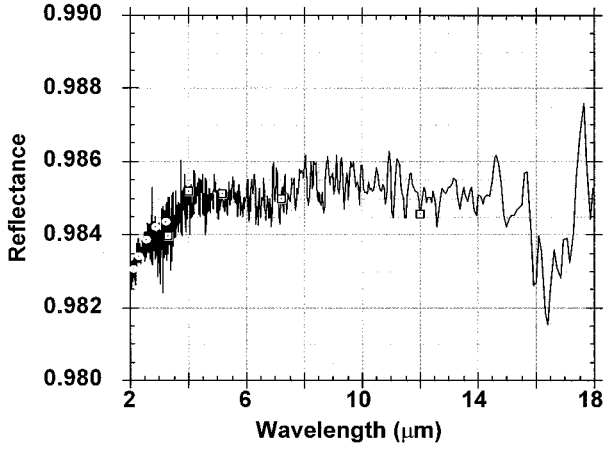

Fig. 8. Au electroplated mirror reflectance. The spectrum is a combination of near-IR (2–3.5 μm, circles) and mid-IR (3.5–18 μm, squares) spectra taken with different source–beam-splitter combinations of the FTIR. This accounts for the reduced noise near 2 μm in comparison with Fig. 6.

7. Discussion and Conclusions

The benefits of using the integrating sphere for more accurate detection of light are used in the design and the development of a device for absolute measurement of transmittance, reflectance, and absorptance of specular samples. The method is demonstrated in the case of IR windows and mirror characterization. The ability to measure both transmittance and reflectance in the same geometry is used to quantify directly the total measurement error for nonabsorbing spectral regions, thereby also obtaining reliable uncertainty values for results outside these regions.

On careful study and consideration, it can be observed that use of the integrating sphere significantly reduces several important sources of measurement error, enabling the levels of accuracy demonstrated in this paper. These error sources include sample–detector and detector–interferometer interreflections, detector nonlinearity, detector spatial nonuniformity, and sample–

beam geometry interaction (beam deviation, deflection, and focus shift).[11]

The integrating-sphere system is not suitable for high-sample-throughput applications. For these applications other instrumentation designed for fast relative measurements can be used. Such instruments, in turn, can be calibrated with transfer standard samples that are characterized with the sphere system. This approach has allowed us to improve the accuracy of measurements made on all our FTS instrumentation,[9] including those designed for variable sample temperature and variable incidence-angle characterization, not directly feasible with the sphere system.

For accurate characterization of specular samples, direct mounting onto the sphere is not an absolute requirement. Effective systems have been built, especially for the UV–visible–near-IR spectral region, that incorporate integrating spheres with detector(s) in the standard averaging mode. However, there are at least two important advantages of mounting the sample directly onto the sphere as shown in this paper. Both of these relate to the characterization of nonideal samples. The first is that this design can better handle the worst samples and allow for the greatest amount of beam deflection, deviation, distortion, and focus shift. The second is that one can measure samples that are not perfectly specular, but that also exhibit some degree of scatter. The sphere measurement is a hemispherical measurement and will collect all or most of the scattered light in addition to the specular component.[14] Through use of a compensating wedge to achieve normal incidence on the sample, for reflectance, and the sphere oriented in the position of Fig. 3(b) for transmittance, supplementary measurements can be made to sort out the scattered component from the specular. For important IR window materials, such as ZnS and chemical-vapor-deposited diamond, some scatter is unavoidable and typically is wavelength dependent. The ability to detect and evaluate scattered light is important in understanding IR materials, in quantifying their behavior, and in determining how they can be used appropriately in optical systems.

The sphere system and method presented in this paper is one that can be reasonably easily reproduced and implemented on, or adapted to, most FTIR spectrophotometers in near- to far-IR regions. In addition, the method can be readily implemented in the UV–visible–near-IR regions for use with monochromator instrumentation. A duplicate system of the one described herein would entail a moderate cost. A less expensive version with a simpler rotation stage mechanism and detector arrangement, smaller sphere, etc., although perhaps not yielding the highest accuracy results (approaching 0.1–0.3%), should, if well designed, be expected to produce consistently measurements with uncertainties of the order of 1%. This expectation is reasonable because many of the inherent benefits of using the sphere would remain, even for a simpler version. Such uncertainty levels would compare favorably with most, if not all, commercial accessories currently available. At the same time, improvements to the current sphere system, including the development and the application of a more spatially uniform coating, should result in better performance and potentially higher-accuracy data.

References

1. D. Sheffer, U. P. Oppenheim, and A. D. Devir, "Absolute reflectometer in the mid-infrared region," Appl. Opt. **29,** 129–132 (1990).
2. "Absolute methods for reflection measurement," CIE Tech. Rep. 44 (CIE, Vienna, 1979).
3. J. M. Palmer, "The measurement of transmission, absorption, emission, and reflection," in *Handbook of Optics* (American Institute of Physics, New York, 1997), Vol. II.
4. K. A. Snail, A. A. Morrish, and L. M. Hanssen, "Absolute specular reflectance measurements in the infrared," in *Materials and Optics for Solar Energy Conversion and Advanced Lighting Technology*, S. Holly and C. M. Lampert, eds., Proc. SPIE **692,** 143–150 (1986).
5. T. M. Wang, K. L. Eckerle, and J. J. Hsia, "Absolute specular reflectometer with an autocollimator telescope and auxiliary mirrors," NIST Tech. Note 1280 (U.S. Government Printing Office, Washington, D.C., 1990).
6. F. J. J. Clarke, "Infrared regular reflectance standards from NPL," in *Developments in Optical Coatings*, I. Ried, ed., Proc. SPIE **2776,** 184–195 (1996).
7. D. B. Chenault, K. A. Snail, and L. M. Hanssen, "Improved integrating-sphere throughput with a lens and nonimaging concentrator," Appl. Opt. **34,** 7959–7964 (1995).
8. L. M. Hanssen and S. G. Kaplan, "Infrared diffuse reflectance instrumentation and standards at NIST," Anal. Chim. Acta **380,** 289–302 (1999).
9. S. G. Kaplan and L. M. Hanssen, "Infrared regular reflectance and transmittance instrumentation and standards at NIST," Anal. Chim. Acta **380,** 303–310 (1999).
10. J. R. Birch and F. J. J. Clarke, "Fifty sources of error in Fourier transform spectroscopy," Spectrosc. Eur. **7,** 16–22 (1995).
11. S. Kaplan, R. U. Datla, and L. M. Hanssen, "Testing the radiometric accuracy of Fourier transform transmittance measurements," Appl. Opt. **36,** 8896–8908 (1997).
12. E. O. Palik, *Handbook of Optical Constants of Solids* (Academic, San Diego, Calif., 1985).
13. P. Klocek, *Handbook of Infrared Optical Materials* (Wiley, New York, 1991).
14. L. M. Hanssen and S. G. Kaplan, "Problems posed by scattering transmissive materials for accurate transmittance and reflectance measurements," in *Optical Diagnostic Methods for Inorganic Transmissive Materials*, R. U. Datla and L. M. Hanssen, eds., Proc. SPIE **3425,** 28–36 (1998).

Appendix D.

ELSEVIER

Analytica Chimica Acta 380 (1999) 303–310

ANALYTICA CHIMICA ACTA

Infrared regular reflectance and transmittance instrumentation and standards at NIST

S.G. Kaplan*, L.M. Hanssen

Optical Technology Division, NIST, Gaithersburg, MD 20899, USA

Received 17 June 1998; accepted 25 August 1998

Abstract

Instrumentation is described that has been constructed at the National Institute of Standards and Technology (NIST) for the measurement of regular reflectance and transmittance over the 2–25 μm wavelength region. This includes both specialized accessories used with Fourier-transform infrared (FT-IR) spectrometers and laser-based systems for high optical density transmittance measurements. The FT-IR systems have been used to develop standard reference materials for IR regular transmittance.

Keywords: Infrared regular reflectance; Transmittance; FT-IR measurements; Beam geometry

1. Introduction

The Optical Technology Division at NIST has developed Fourier-transform infrared (FT-IR) based instrumentation for accurate measurement of regular spectral transmittance (T) and reflectance (R) in the mid-IR wavelength region. Two commercial FT-IR spectrometers, a Bio-Rad FTS-60A and a Bomem DA3[1], have been fitted with specialized accessories for T and R measurements. The Bio-Rad system, shown in Fig. 1, can be used to perform transmittance measurements in the standard $f/3$ sample compartment geometry, or T and R measurements with one of two external arrangements. A 6 in. diameter side-mount integrating sphere system can be used to perform absolute regular R and T measurements at 8° incidence on specular samples, with an $f/4$ incident beam geometry [1]. A goniometer system has been constructed for polarized, angle-dependent measurements, and an optical access cryostat for 10–600 K operation can be used to control the sample temperature.

The Bomem DA3 is configured with an 8 in. center-mount integrating sphere, a high-temperature blackbody source, and an additional cryostat [2] for T/R measurements from 10 to 77 K. A collimated beam transmittance accessory has also been added, and used to perform high-resolution measurements on etalon samples to measure the mid-IR index of refraction to 10^{-4} uncertainty. In this paper we describe the investigation and reduction of radiometric error sources in the FT-IR measurements, results of inter-comparisons

*Corresponding author. Tel.: +1-301-975-2366; fax: +1-301-869-5700; e-mail: simon.kaplan@nist.gov

[1]The use of certain trade names in this paper is for informational purposes only and does not constitute an endorsement by NIST that this equipment is necessarily the best suited for the task.

0003-2670/99/$ – see front matter
PII: S0003-2670(98)00670-9

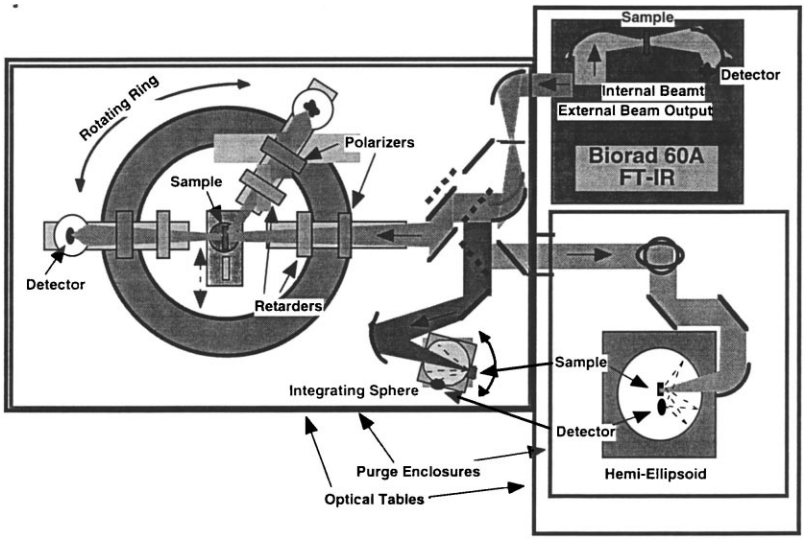

Fig. 1. Goniometer and integrating sphere systems with Bio-Rad FT-IR.

among FT-IR, grating monochromator, and laser-based systems, and the development of standard reference materials for regular IR transmittance.

FT-IR spectrometers are the most widely used instruments for routine IR *T* and *R* analysis of solid samples. Although they provide advantages in signal-to-noise ratio and wavelength accuracy over dispersive instruments, FT measurements are more prone to errors [3] due to inter-reflections [4,5], detector non-linearity and non-equivalence [6,7], and background thermal radiation [8,9]. We have found that it is possible to perform measurements of *T* and *R* with FT-IR instruments to within 0.2–1% relative uncertainties, depending upon the sample and type of measurement [10].

2. Experimental

2.1. "Conventional" transmittance measurements

T and *R* measurements are performed in several different configurations. For *T* measurements of fairly thin samples, which have a small effect on the beam geometry, a modified version of the standard sample compartment geometry is used [10], as shown in Fig. 2. Half-blocks made of IR absorbing black felt

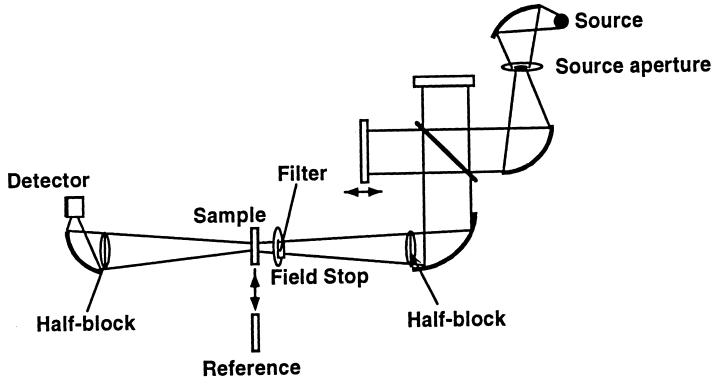

Fig. 2. Optical layout for FT-IR transmittance measurements as described in the text.

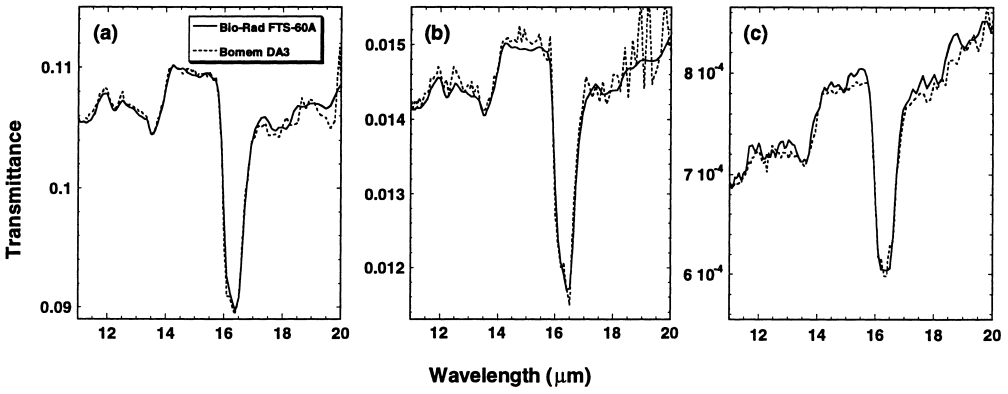

Fig. 3. Comparison between measurements of three different metal film/Si neutral density filters performed with two different FT-IR systems.

are used to eliminate inter-reflections among the sample, detector and interferometer. Neutral-density or band pass filters are placed (tilted, to avoid inter-reflections) before the sample position, or used as the reference for the transmittance calculation, in order to keep the detector response linear and equivalent between sample and reference. A field stop is placed just before the sample position to limit diffuse thermal radiation from the source aperture.

With the use of appropriate filters and detectors, it is possible to measure transmittances as low as 10^{-6} with this configuration [11]. For optically thin (<1 mm) samples with fairly neutral attenuation, the contributions of various error sources to the total radiometric uncertainty have been estimated [10]. Expanded (2σ) relative uncertainties are in the range of 0.5–1% for samples with optical densities up to 3. These uncertainty estimates have been tested by inter-comparison between the two FT-IR systems and by inter-comparison with laser measurements on etalon-free samples.

Fig. 3 shows a comparison between transmittance measurements from 11 to 20 μm on thin metal-coated Si samples with optical densities near 1, 2, and 3 made on the Bio-Rad and Bomem FT-IR spectrometers using the configuration shown in Fig. 2. Both systems were set up with a ceramic global source and KBr:Ge beamsplitter, and the spectral resolution was 8 cm^{-1}. A 2 mm room temperature pyroelectric detector was used with the Bio-Rad, while a 1 mm 77 K mercury–cadmium–telluride (MCT) detector was used with the Bomem. The beam geometry at the sample position is *f*/3 in the Bio-Rad and *f*/4 in the Bomem. For the OD 1 ($OD=-\log_{10} T$) sample in frame (a), the two measurements agree to within 0.5% over most of the region. For the higher OD samples shown in (b) and (c), the signal-to-noise ratio is lower, but the measurements still agree to within 1–2%. The OD 2 measurement was done with the OD 1 filter as a reference, while the OD 3 measurement was done with the OD 2 filter as a reference on the Bomem, and the OD 1 filter on the Bio-Rad.

Fig. 4 shows the results of an inter-comparison between two laser transmittance measurements at 3.39 μm and 10.6 μm and the FT-IR system on two metal film/Lexan filters [10]. The Lexan substrates are only 100 nm thick, allowing a direct comparison between the laser and FT-IR results without the complication of Fabry–Perot fringes in the spectra. In this case it can be seen that the two sets of measurements agree to within 0.5–1%, within the expanded uncertainty of the laser measurements.

2.2. *T/R measurements with integrating sphere*

For the measurement of absolute specular reflectance, there are two external arrangements, as shown in Fig. 1. The integrating sphere system, described in the preceding paper [12], can be used to perform either *T* or *R* measurements at 8° incidence. By rotating the sphere about both the center and the sample position, it is possible to make either a sample or reference measurement in such a way that the incident beam

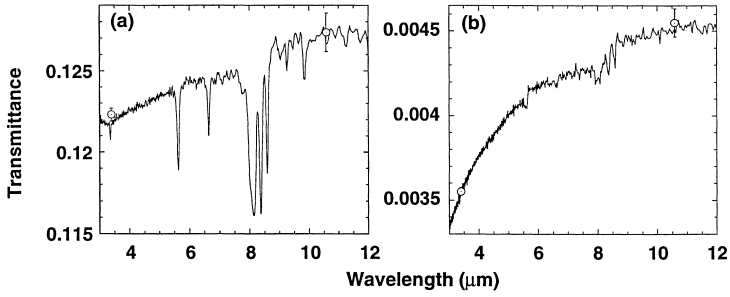

Fig. 4. Comparison between transmittances of two thin metal film/Lexan neutral density filters measured with an FT-IR system (lines) and laser systems at 3.39 μm and 10.6 μm (circles).

in the reference measurement strikes the surface of the sphere in an optically equivalent position to that of the specular beam from the sample. Thus the ratio of the two measurements provides an absolute measurement [1], independent of sphere throughput.

The high degree of unformity of the sphere, combined with its averaging properties, greatly reduces the effects of the sample on the beam geometry at the position of the 6 mm MCT detector. The 8° incidence on the sample, with *f*/4 geometry, eliminates interreflections with the interferometer, while the field stop at the focal position of the 90° off-axis paraboloids limits diffuse source aperture radiation. The low throughput (∼0.5%) of the sphere tends to keep the detector response nearly linear for mid-IR measurements. Other sources of error in the measurement include

1. a small (ca. 0.1–0.2%) non-equivalence between the specular positions on the sphere wall opposite the sample and reference ports,
2. small (<1°) vertical misalignment between the transmittance and reflectance measurements,
3. light diffusely scattered by the sample,
4. light emitted from the sample and modulated by the interferometer before reaching the detector, and
5. overfilling of the sample/reference ports by scattered or diffracted incident light.

These effects can be characterized and approximately accounted for in the results [1].

Several measurements have been performed to test the accuracy of T and R values obtained with this integrating sphere system. Fig. 5 shows T and R measured for parallel-sided samples of ZnSe (thickness 3 mm) and Si (thickness 2 mm). In each case, there is a wavelength region in which the absorption coefficient is negligibly small ($<10^{-3}$ cm^{-1}) [13], so that the measured absorptance, 1-T–R, should be zero within the reproducibility of the experiment in the absence of the various errors listed above. As can be seen in this figure, the measured residual absorptance is typically less than 0.3% in these regions. Also shown are T and R curves calculated from tabulated values for the index of refraction of each material [14]. These calculations treat the multiple reflections in the sample incoherently, and include the measured degree of linear polarization of the incident beam, which is generally small ($|s_1|<0.07$) except near 8 μm, where the p-polarized absorption in the SiO_x overcoating [15,16] on several of the Al mirrors gives $s_1 \sim 0.5$ (these mirrors have since been replaced with Au-coated ones). The calculations are done for collimated light at 8° incidence; proper averaging over the range of incidence angles is expected to yield differences of less than 0.03%.

The good agreement between the expected values and the measured values tends to confirm that the T and R measurements with the sphere are accurate to within 0.3% for these samples, even with none of the corrections 1–5 listed above having been applied. The structure near 6 μm in frames (a) and (c) is due to H_2O adsorbed in the sphere wall coating, which causes some variation in throughput as a function of input geometry. Dielectric samples such as these actually provide a more stringent test of the sphere uniformity than opaque front-surface reflectance samples, because the multiple reflections within the material

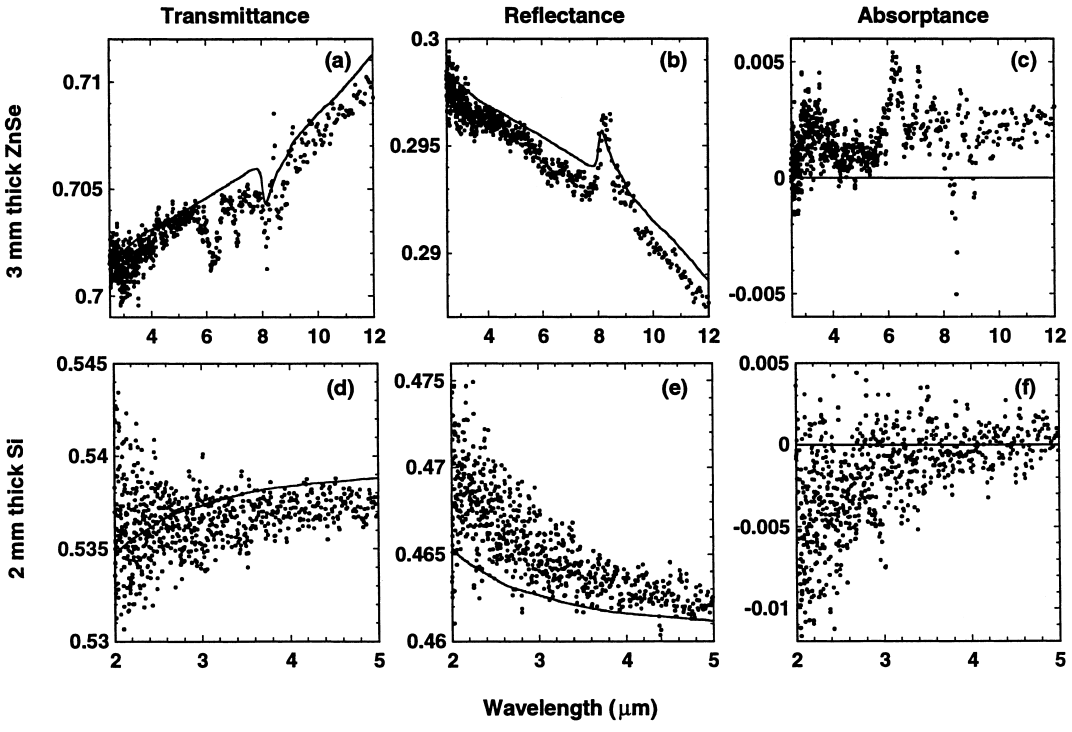

Fig. 5. Transmittance, reflectance and absorptance measured with an integrating sphere for a 3 mm thick piece of ZnSe (a,b,c) and a 2 mm thick piece of Si (d,e,f). In each frame the circles show the measured signal and the lines show the calculated signal using tabulated values for the index of refraction, as described in the text.

increase the size of the transmitted or reflected spot on the sphere wall compared to the reference spot. To test the accuracy for lower signal levels, an intercomparison with a "conventional" measurement was performed on the transmittance of an OD 2 filter such as that shown in Fig. 3(b), and the relative differences were found to be less than 1%.

An inter-comparison was made between the reflectance values of a gold mirror standard reference material measured on this sphere system and the NIST spectral tri-function absolute reference reflectometer (STARR) [17], which uses a grating monochromator and has a long-wavelength limit of 2.5 μm. This comparison is shown in Fig. 6. In the region of overlap of the two sets of data (1.5–2.5 μm) the differences are less than 0.1%, which is within the estimated uncertainty (±0.3%) of the STARR data. The structure near 8 μm is again related to *s*-polarization of the beam coming from SiO_x overcoatings on some of the mirrors, and the 6 μm structure from H_2O in the sphere wall. These Au mirror standard reference materials (SRMs) may possibly be extended for use as mid-IR reflectance standards.

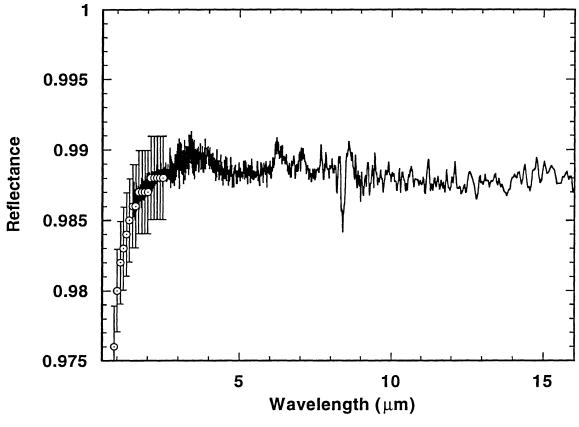

Fig. 6. Comparison of reflectance of Au SRM mirror measured on the integrating sphere with FT-IR (solid line) and the NIST STARR monochromator facility (circles).

2.3. T/R measurements with goniometer

Another method for measuring absolute reflectance is the goniometer arrangement shown in Fig. 1. In this set up, the beam is reflected from the sample directly onto the detector. Then, the sample is moved out of the beam and the detector is rotated to collect the undeflected beam. The ratio of these two measurements yields the sample reflectance. In this configuration, the angle of incidence on the sample can be varied from 7.5° to nearly grazing incidence (depending on the size of the sample), with a roughly *f*/20 beam geometry.

We have performed absolute reflectance measurements with this device and have found that the difficulty in aligning the reflected beam and reference beam onto the detector (1–2 mm pyroelectric or photoconductive element) limits the relative uncertainty that can be achieved to ca. 3–5%. The use of larger, more uniform detectors should greatly decrease the alignment sensitivity and make more accurate measurements possible.

By using a HeNe alignment laser, it is possible to perform fairly accurate *relative* reflectance measurements by aligning the sample front surface and a reference mirror to within ca. 0.5 mrad of each other. The reference mirror reflectance is measured on the integrating sphere as described in Section 2.2. Using this configuration, we are able to make reflectance measurements to within 0.5–1% relative uncertainty. The advantages of the goniometer system even for near-normal T and R measurements include complete control of the beam polarization state, greater flexibility in sample handling, and control of the sample temperature with the optical access cryostat.

Fig. 7 shows measurements of T and R for a 2 mm thick z-cut Al_2O_3 disk at 296 K and 582 K, in the region of the multiphonon absorption edge for this material [18]. The measured values are compared to calculated T and R values using the OPTIMATR code [14] for the Al_2O_3 dielectric function. The measured and calculated values agree quite closely except in the 6–6.5 μm region, where the data show an absorption feature believed to be due to a 2-phonon process which is not included in the model. The relative expanded uncertainty in the measured values is estimated to be ±1%.

The goniometer system incorporates high-quality Brewster's angle polarizers on the input and output arms. These polarizers have an extinction ratio of less than 10^{-5} over the entire IR region [19] and can be used for highly accurate polarimetric or ellipsometric measurements, as well as the calibration of other polarizers. Fig. 8 shows the measured extinction ratios (defined as the ratio of minor to major principal transmittances) of three different IR wire grid polarizers on ZnSe substrates. The extremely low extinction ratio of the Ge chevron polarizers allows measurements such as these to be performed directly, by simply rotating the polarizer under test. This method is simpler and less prone to error than the conventional method of measuring three or more polarizers in pairs and solving a system of equations to derive the extinction ratios of the individual

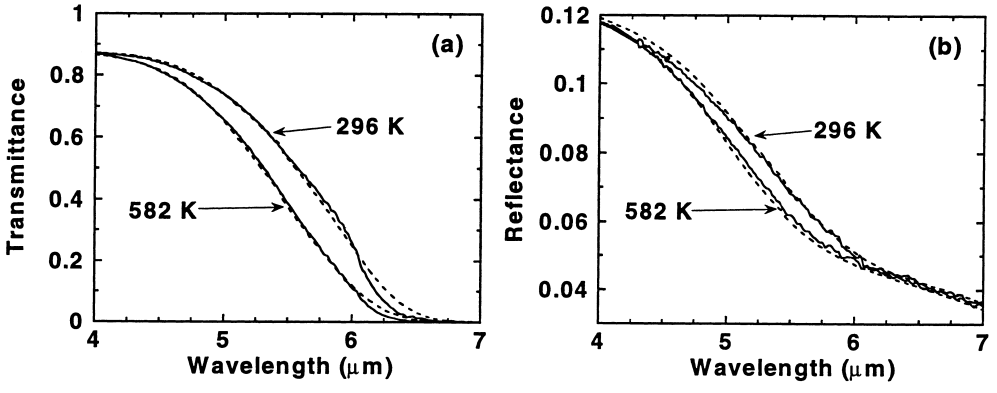

Fig. 7. Transmittance and reflectance of a 2 mm thick Al_2O_3 sample measured with the goniometer system at 296 K and 582 K. The solid curves show the experimental data and the dashed curves the predicted T and R using a multiphonon model for Al_2O_3.

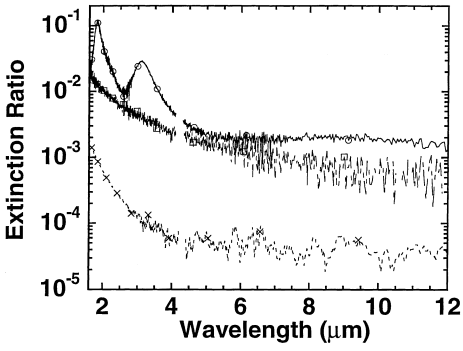

Fig. 8. Extinction ratios of three different wire grid/ZnSe polarizers measured with the goniometer system and Ge chevron polarizer.

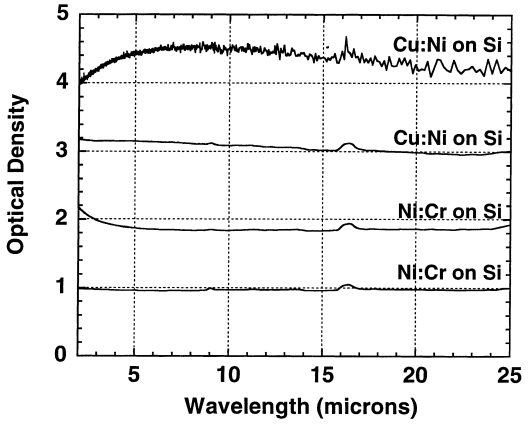

Fig. 9. Spectra for neutral density filter SRMs.

polarizers. As shown in Fig. 1, MgF_2 pseudo-zero-order waveplates can also be placed in the optical train to realize a rotating-retarder polarimeter [20], which has been used to measure the complete Mueller matrix of wire-grid polarizers in the near IR (1–2 μm), where these polarizers have significant retardance.

3. Standard reference materials for regular infrared transmittance

Standard reference materials (SRMs) for IR transmittance have been developed, consisting of thin metallic (Ni:Cr or Cu:Ni) coatings on 0.25 mm thick, 25 mm diameter high-resistivity Si wafers. The coatings were designed to give nominally neutral attenuation with optical densities near 1, 2, 3, and 4 over a wavelength range of 2–25 μm. The thin substrates were chosen to both minimize the Si absorption peaks at 9 and 16 μm, and the effects on the geometry of the transmitted beam.

A plot of the optical density of representative samples for the four OD levels is shown in Fig. 9. As is evident in this figure, the OD 1 samples have very neutral attenuation versus wavelength, but the spectral variation is larger for the higher OD samples, with the OD 4 filters having a total variation of about 0.6 over the measured range. A comparison of the spectra of these filters with previous commercially available filters has been presented [21], and a patent has been issued for the Cu:Ni coatings [22], which provide much more neutral attenuation at the OD 3 and 4 level than do Ni:Cr coatings.

A set of 10 samples for each OD level has been produced and the filters have been measured to determine the repeatability and reproducibility of the transmittance over a period of 6 months. The metal coatings have been overcoated with 20 nm of SiO_x to protect the films from oxidation, and it has been found that the transmittance of the samples is stable within the resolution of the measurements over the 6 month time period. Additional measurements have been performed to determine the spatial uniformity over the central 10 mm diameter circle and temperature dependence of the filters. Table 1 shows estimates for the various uncertainty components in the measured transmittances for the OD 1–4 filters, along with the expanded uncertainties at 10.6 μm wavelength.

4. Conclusions

Facilities have been developed in the Optical Technology Division at NIST for measuring regular IR transmittance and reflectance with high accuracy, using specialized accessories in conjunction with commercial FT-IR spectrometers, as well as laser systems at specific wavelengths. Transmittances as low as 10^{-6} can be measured with the FT-IR systems. The most accurate T and R measurements are performed with an integrating sphere, with which specular samples having T and R in range of 1–100% can be measured with relative uncertainties of 0.2–0.3%

Table 1
Uncertainty estimates for ND filter transmittances, in % of measured values

Uncertainty source	OD 1	OD 2	OD 3	OD 4
Type B				
Inter-reflections	0.2	0.3	0.3	0.3
Detector non-linearity	0.1	0.1	0.05	0.05
Detector non-equivalence	0.2	0.2	0.1	0.1
Non-source emission	0.15	0.15	0.15	0.15
Beam non-uniformity	0.2	0.2	0.2	0.2
Beam displacement, deviation, focus shift	0.1	0.1	0.1	0.1
Beam-geometry, polarization	0.2	0.2	0.2	0.2
Sample vignetting	0.03	0.03	0.03	0.03
Sample scattering	0.02	0.02	0.02	0.02
Phase errors	0.1	0.1	0.1	0.1
Sample non-uniformity	0.3	0.4	3.5	4.0
Sample temperature	0.05	0.05	0.05	0.05
Sample aging	0.2	0.2	0.2	0.2
Quadrature sum	0.59	0.68	3.5	4.0
Type A				
Relative standard uncertainty in mean at 10.6 μm	0.2	0.2	0.5	2.0
Relative expanded uncertainty at 10.6 μm	1.2	1.4	8.1	9.0

depending on the type of the sample. A goniometer system has also been constructed and used for angle, polarization, and temperature dependent measurements. A set of neutral density filters has been produced to serve as regular transmittance standards for 2–25 μm.

References

[1] L.M. Hanssen, Appl. Opt. (1998), submitted.
[2] Z.M. Zhang, L.M. Hanssen, R.U. Datla, H.D. Drew, Int. J. Thermophys. 17 (1996) 1441.
[3] J.R. Birch, F.J.J. Clarke, Spectrosc. Eur. 7 (1995) 16–22.
[4] H.W.H.M. Jongbloets, M.J.H. Van de Steeg, E.J.C.M. Van der Werf, J.H.M. Stoelinga, P. Wyder, Infrared Phys. 20 (1980) 185–192.
[5] M. A. Ford, in: C. Burgess, K.D. Mielenz (Eds.), Advances in Standards and Methodology in Spectrophotometry, Elsevier, Amsterdam, 1987, pp. 359–366.
[6] D.B. Chase, Appl. Spectrosc. 38 (1984) 491–494.
[7] M.I. Flik, Z.M. Zhang, J. Quant. Spectrosc. Radiat. Transfer 47 (1992) 293–303.
[8] J.R. Birch, E.A. Nicol, Infrared Phys. 27 (1987) 159–165.
[9] D.B. Tanner, R.P. McCall, Appl. Opt. 23 (1984) 2363–2368.
[10] S.G. Kaplan, L.M. Hanssen, R.U. Datla, Appl. Opt. 36 (1997) 8896.
[11] Z.M. Zhang, L.M. Hanssen, R.U. Datla, Opt. Lett. 20 (1995) 1077–1079.
[12] L.M. Hanssen, S.G. Kaplan, Microch. Acta., accompanying article.
[13] E.D. Palik, Handbook of Optical Constants of Solids, Academic Press, Orlando, FL, 1985.
[14] OPTIMATR 2.1, Johns Hopkins University, Applied Physics Laboratory and ARSoftware, Landover, 1993.
[15] J.T. Cox, G. Hass, W.R. Hunter, Appl. Opt. 14 (1975) 1247.
[16] J.J. Clarke, SPIE 2776, (1996) 184.
[17] P.Y. Barnes, E.A. Early, A.C. Parr, Spectral Reflectance, NIST Special Publication 250-48, US Government Printing Office, Washington, DC, 1998.
[18] S.G. Kaplan, L.M. Hanssen, Emittance of coated sapphire windows, in: Proceedings of the Seventh DOD Electromagnetic Windows Symposium, 1998.
[19] D.J. Dummer, S.G. Kaplan, L.M. Hanssen, A.S. Pine, Y. Zong, Appl. Opt. 37 (1998) 1194.
[20] R. Chipman, Polarimetry, in: M. Bass (Ed.), Handbook of Optics 2, Chapter 22, McGraw-Hill, New York, 1995.
[21] Z.M. Zhang, R.U. Datla, L.M. Hanssen, Mat. Res. Soc. Symp. Proc. 374 (1995) 117.
[22] Z.M. Zhang, R.U. Datla, L.M. Hanssen, US Patent 5 726 797 (1998).

Appendix E.

Comparison of near-infrared transmittance and reflectance measurements using dispersive and Fourier transform spectrophotometers

S. G. Kaplan, L. M. Hanssen, E. A. Early, M. E. Nadal and D. Allen

Abstract. A spectrophotometer based on an integrating sphere coupled to a commercial Fourier Transform Infrared (FTIR) instrument has been constructed for regular spectral transmittance and reflectance measurements over the 1 μm to 18 μm wavelength region. Despite the large number of sources of error that often limit the radiometric accuracy of FTIR measurements, we demonstrate uncertainties similar to established dispersive instrumentation. We performed near-normal-incidence reflectance and transmittance measurements on a series of samples over the 1 μm to 2.5 μm wavelength range using both FTIR and dispersive spectrophotometers. The results are compared, taking into account any differences in measurement geometry among the various systems and the combined measurement uncertainty. We find agreement within the combined uncertainties over most of the measured spectral region.

1. Introduction

Although there is extensive literature on the accuracy of regular (i.e. equivalent input and output geometry) spectral transmittance and reflectance measurements with both dispersive and FTIR spectrophotometers, there has been little direct comparison of data from the two types of system. In the ultraviolet, visible and near-infrared spectral regions, dispersive instruments will probably remain favoured for the highest-accuracy measurements at national standards laboratories. However, FTIR spectrometers have replaced dispersive instruments for thermal infrared measurements in many applications.

Despite the growing use of FTIR spectrophotometry in quantitative infrared measurements, where radiometric accuracy is very important, relatively little work has been done to quantify all the sources of uncertainty that contribute to a particular measurement result. Some effort has been made to catalogue and quantify the various sources of error in FTIR measurements [1, 2]. Comparisons have also been made of FTIR and laser-based transmittance measurements of neutral-density filters at 3.39 μm and 10.6 μm. However, these comparisons were limited to ultra-thin (approx. 100 nm thick) samples [2] in order to avoid etalon effects in the laser measurements.

S. G. Kaplan, L. M. Hanssen, E. A. Early, M. E. Nadal and D. Allen: Physics Laboratory, National Institute of Standards and Technology, Gaithersburg, MD 20899, USA.

A comparison of a more representative set of samples is needed to test the accuracy of the FTIR measurements on filters, mirrors or other optical components and materials that require calibration for use in radiometric applications. There are two dispersive instruments in the Optical Technology Division (OTD) at the National Institute of Standards and Technology (NIST) available for such comparisons: the Spectral Tri-Function Automated Reference Reflectometer (STARR), which performs specular, directional-directional, and directional-hemispherical reflectance measurements for the ultraviolet to near-infrared spectral regions [3], and the NIST Reference Spectrophotometer for Regular Spectral Transmittance [4], another monochromator-based system, which performs regular spectral transmittance measurements for the same spectral region. Both of these systems overlap with the FTIR-based system in the 1 μm to 2.5 μm wavelength region. Although this covers only a small region of the infrared, many of the sources of error in the measurements vary only gradually with wavelength. Thus the comparison can provide some indication of the accuracy of the FTIR system at longer wavelengths.

In this paper we present the results of transmittance measurements on four samples: a 5 mm thick silica-glass plate, a 2 mm thick absorbing glass filter, a 0.5 mm thick crystalline Si wafer, and a 0.25 mm thick Si wafer coated with NiCr. In addition, we measured the reflectance of a first-surface aluminium mirror and a black-glass sample. The differences between the dispersive and FTIR results are examined to see

whether or not they fall within the combined expanded uncertainty of the two measurements. We also consider any differences in beam geometry, polarization and spectral resolution among the various systems and estimate any differences in measured values that might result from these effects.

2. Experimental details

2.1 FTIR transmittance and reflectance measurements

The FTIR-based system uses a Bio-Rad FTS-60A FTIR spectrophotometer with external beam output as a source. For near-infrared measurements, the FTIR is configured with a quartz-tungsten-halogen (QTH) lamp and a TiO_2-coated quartz beam splitter. The nearly collimated output beam (approx. 50 mm diameter) from the FTIR is focused (f/4) on to an external variable aperture wheel, re-collimated, and directed into an integrating sphere with approximately f/6 focusing geometry. The entire system, including the integrating sphere, is housed in a sealed enclosure continuously purged with dry, CO_2-free air. The design and operation of the integrating sphere for transmittance and reflectance measurements has been described previously [5, 6]. Figure 1 shows the basic geometry of these measurements.

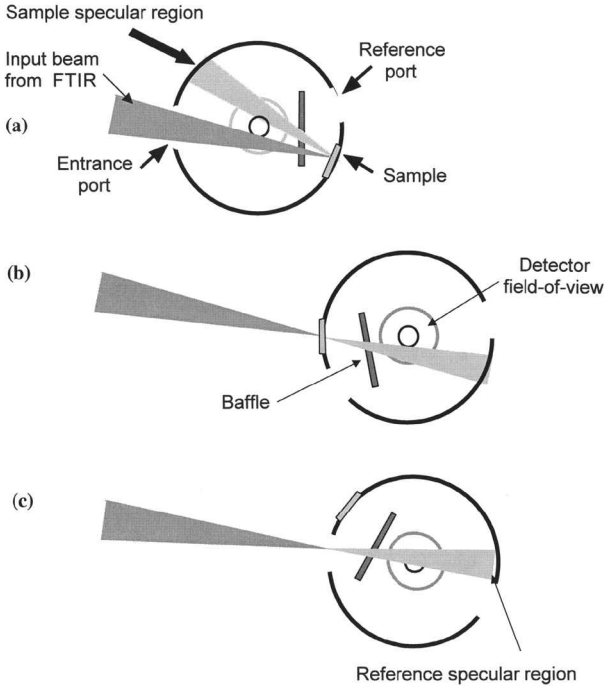

Figure 1. Geometry of integrating-sphere transmittance and reflectance measurements using an input beam from an FTIR spectrophotometer. (a) reflectance configuration: input beam reflects from sample at 8° and strikes sphere wall near entrance port; (b) transmittance configuration: beam passes through sample and strikes sphere wall in the same place as (a); (c) reference configuration: beam passes through reference port and strikes sphere wall on other side of entrance port.

The sample is mounted on the side of the sphere, and the detector (a liquid-nitrogen-cooled HgCdTe photoconductor) is mounted on the top, with its field-of-view restricted to a portion of the bottom of the sphere. The incident beam is focused at the sample position, and the sphere is rotated about both its centre and the entrance port to allow the beam to reflect from the sample front surface (Figure 1a), transmit through the sample (1b), or pass through the reference port (1c). In both the reflectance (a) and transmittance (b) configurations, the beam leaving the sample strikes a portion of the sphere wall next to the entrance port, which we designate the sample specular region, and is then scattered into the sphere volume. In the reference measurement (c), the incident beam strikes the sphere wall at a position on the other side of the entrance port to the sample specular region, known as the reference specular region. In an ideally manufactured sphere system, light incident on either the sample or reference specular regions would yield the same irradiance on the rest of the sphere wall. The ratio of the detected flux in the transmittance or reflectance position to that in the reference position yields an absolute transmittance or reflectance measurement of the sample. In practice, a small correction (approx. 0.2 %) is applied for throughput non-uniformity between the specular and reference regions, or the sample is measured in both the sample and reference ports and the results are averaged.

The advantages of the sphere for accurate transmittance and reflectance measurements have been discussed elsewhere [5]. The main feature is a reduced sensitivity to sample-induced geometrical changes in the beam incident on the detector. Although the sphere throughput is small (approx. 0.5 %), the multiplexing advantage of the FTIR allows data with adequate signal-to-noise and 8 cm^{-1} or 16 cm^{-1} resolution to be acquired in approximately 1 h to 3 h for samples with transmittance or reflectance between 0.01 and 0.99. The spectrometer and sphere positioning are computer-controlled. Typically, sample or reference spectra are acquired for several minutes each, and the process is repeated 20 to 30 times in order to average over drift in the FTIR signal level and estimate the repeatability component of the final measurement uncertainty.

The incident geometry at the sample position is nominally an f/5 or f/6 cone with its central axis at 8° to the sample normal; however, the central portion of the FTIR beam is blocked for use by the He-Ne alignment and position-sensing laser system in the interferometer. Thus, the range of incident angles excludes the central 1.5° or so (half-angle) of the cone. It is also possible to mount the sample on a compensating wedge to achieve normal incidence for the central (missing) rays; in this case a half-block is placed in the incident beam to remove interreflections between the sample and the FTIR. This was done for the absorbing glass filter described below to match more closely

the average absorption path length in the dispersive measurement. The spot diameter at the sample position is approximately 5 mm. The beam polarization has been checked using wire-grid polarizers and found to be quite small (Stokes components $s_2 \approx 0.03$ and $s_3 < 0.01$). Because of the 2π collection geometry of the side-mount sphere design, any scattered light from the exit side of the sample will be collected, unlike the two dispersive measurement systems described below. The diffuse component can be measured separately and subtracted if necessary, but all the samples used in this study are quite specular so that the diffuse component is negligible (less than 0.01 %).

For specular samples, a correction must be made to the measured transmittance or reflectance values to account for the light from the sphere wall that is back-reflected to the sample (Figures 1a or 1b) and lost out of the entrance port of the sphere. In the reference measurement (Figure 1c), the light back-reflected to the sample ends up striking the sphere wall and is not lost. The lost flux has been measured to be 0.25 % of the light reflected from the sample. The measured reflectance or transmittance is thus corrected by multiplying by $1 + 0.0025\ \boldsymbol{R}$, where $\boldsymbol{R}$ is the sample reflectance.

In addition to the repeatability (Type A) uncertainty component mentioned above, there are systematic (Type B) standard uncertainty components in the transmittance and reflectance measurements whose quadrature sum we have estimated to be approximately 0.1 % of the measured value at a given wavenumber. These estimates are based on analysis of the results of measurements on high-reflectance mirrors and transparent infrared materials [6], as well as an analysis of the sensitivity of the sphere throughput to system and sample alignment errors. The wavenumber scale of the instrument has been tested with high-resolution measurements of residual CO_2 and H_20 absorption lines in the purge gas and corrected to within 5 parts in 10^6. The linearity of the system response has been tested by using a series of apertures which vary the flux level reaching the sphere, without affecting the irradiation pattern on the detector, which is determined by its field-of-view limiting fore-optics. No evidence of non-linearity was found in the measured transmittance of a Si wafer over nearly two decades of flux level [7]. However, we have found small offset errors at short wavelength that may be related to interreflections or sampling errors within the FTIR spectrometer adding spurious features to the modulated signal. They are reduced by filtering out longer-wavelength light ($\lambda > 1.5$ μm) where necessary, but still may contribute an additional absolute Type B standard uncertainty component of 5 parts in 10^5. The expanded uncertainties in the FTIR measurements are calculated using the Type B relative uncertainty added in quadrature to the Type A component, which depends on the sample and averaging time, and multiplying the result by the coverage factor, $\boldsymbol{k = 2}$, for 95 % confidence intervals.

2.2 Dispersive transmittance measurements

Monochromator-based transmittance measurements were performed with the NIST Reference Spectrophotometer for Regular Spectral Transmittance. This instrument has undergone significant modifications for automation, but the optical design is similar to the one described previously [4]. Figure 2 shows the optical layout of this instrument.

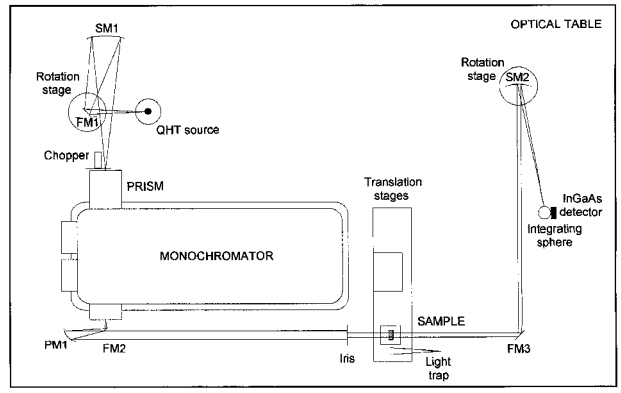

Figure 2. Optical layout of the NIST Reference Spectrophotometer for Regular Spectral Transmittance. For these measurements the source is a quartz-tungsten-halogen lamp and the detector is an extended-range InGaAs photoconductor. A translation stage sequentially places the open, sample, or light-trap position in the beam. The entire assembly is housed in a light-tight enclosure.

The instrument measures the transmittance of a sample using collimated, monochromatic radiant flux incident from the normal direction to the front surface of the sample. A spherical mirror focuses radiant flux from a QTH incandescent lamp through an optical chopper and on to the entrance slit of a prism-grating monochromator. The beam emerging from the exit slit of the monochromator is collimated by an off-axis parabolic mirror to within 0.1° and is incident on an iris to provide a circular incident beam. The beam passes through the sample carriage, is collected over a solid angle of 0.01 sr, and is focused by a spherical mirror into an averaging sphere. A signal proportional to the radiant flux of the beam is measured by an optical detector attached to the averaging sphere. The sample carriage consists of three incident positions for the beam: open, sample, and light trap. At each wavelength, signals are measured from the open, trap, sample, trap and open positions, in that order. Signals from the open and sample positions are proportional to the incident and transmitted fluxes, respectively. Net signals for the open and sample positions are obtained by subtracting the signals from the light trap position. The regular spectral transmittance of the test item is

given by the net sample signal divided by the average net open signal.

Individual samples were cleaned with an air bulb and mounted in a commercial lens holder with the beam centred on the front surface of the test item at normal incidence. This was achieved by adjusting tilts and translations of the sample holder and carriage until a laser beam at a wavelength of 632.8 nm, propagating collinear to the beam from the monochromator, was centred on the front of the test item and retroreflected.

The diameter of the incident beam was 10 mm. All samples were measured at wavelengths from 1000 nm to 2400 nm at increments between 10 nm and 25 nm with a 3 nm spectral bandwidth. The grating had 600 lines/mm and was blazed at 1250 nm; the detector was an InGaAs extended-range photodiode.

The three major components of uncertainty in measured transmittance values are the effects of wavelength error and detector non-linearity (Type B), and non-repeatability due to noise or drift (Type A). The wavelength uncertainty is 0.1 nm, which only contributes significantly to uncertainty on the transmittance scale near sharp attenuation features in the spectra, where the standard component can be as large as 0.0003 in some of the measurements reported here. The non-linearity uncertainty is a quadratic function of transmittance, with zero contribution at 0 or 1 on the transmittance scale, and a maximum of 0.000 25 at a transmittance of 0.5. The repeatability component is evaluated from the standard deviation of successive measurements. These three standard uncertainty components are added in quadrature over each wavelength band, and the result multiplied by a coverage factor of $k = 2$ to produce expanded uncertainty values for the dispersive transmittance measurements.

2.3 Dispersive reflectance measurements

Monochromator-based reflectance measurements were performed using STARR, which is designed to perform absolute spectral measurements of bidirectional, specular and directional-hemispherical reflectance [3]. Figure 3 shows the optical layout of this instrument. The source of radiant flux for STARR is a filter/grating-based monochromator, shown in the upper right of Figure 3a. For visible/near-infrared measurements, a QTH lamp was focused through a filter wheel and on to the entrance slit of the 0.25 m, f/3.9 monochromator, with a 600 line/mm grating blazed for 1000 nm. The entrance slit width was 2 mm, yielding a spectral resolution of 10 nm. Light exits the monochromator through a 1 mm diameter circular aperture, is collimated by a 51 mm diameter, 15° off-axis parabolic mirror, and directed to the rest of the system with a 51 mm flat mirror. The collimated beam has a diameter of approximately 14 mm and an angular divergence of less than 1°. For these measurements the incident angle at

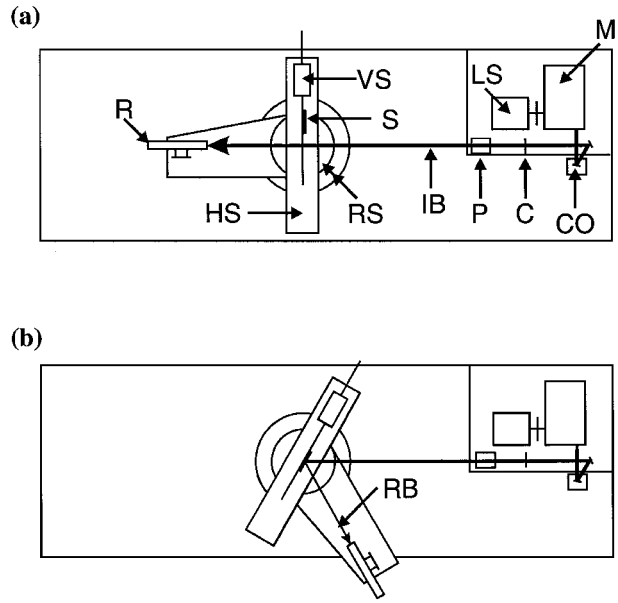

Figure 3. Schematic diagram of STARR showing the configuration for measuring (a) flux of incident beam and (b) flux of reflected beam. LS: light source; M: monochromator; CO: collimating optics; C: chopper; P: polarizer; IB: incident beam; S: sample; RS: rotation stages; VS: vertical stage; HS: horizontal stage; R: receiver; RB: reflected beam.

the sample position was 6° and the beam was nominally unpolarized.

Three detectors are manually interchangeable on the end of the receiver assembly mounted on the goniometer. For these measurements, a thermoelectrically cooled InGaAs photodiode mounted on a 38 mm diameter polytetrafluoroethylene (PTFE) integrating sphere was used. The incident beam was chopped and the detector signal measured with a phase-sensitive amplifier. Measured values of the reflected flux from the sample and straight-through flux from the source are ratioed to produce specular reflectance values at a series of wavelength settings of the monochromator, and the measurements are repeated to allow a statistical analysis. The entire system is located in a light-tight room with black walls, and computer-controlled from an adjoining room.

A detailed uncertainty analysis for measurements with this system is available [3]. In the measurements reported here, the dominant sources of uncertainty are incident angle, sample uniformity and detector noise, and the expanded uncertainty is approximately 0.0012 on the reflectance scale.

2.4 Samples

For this comparison, four samples were selected for transmittance and two for reflectance measurements. The chief criteria were uniformity, specularity and relative insensitivity to incident beam geometry, in order to minimize the need for correction factors due

to different incident angles and optical path lengths in the materials. We also wanted to test both large (near 1) and small (<0.1) values on the radiometric scale to assess linearity. All six samples were measured on the FTIR system described in Section 2.1, while the monochromator-based measurements were performed on one of the systems in Sections 2.2 and 2.3. All three facilities are kept in rooms fitted with air-filtration units to reduce particulate accumulation. The room temperatures did not vary outside the range 22 °C to 24 °C.

The transmittance samples were a 5 mm thick 25 mm diameter fused-silica plate from VLOC Corporation (actually an uncoated etalon), a 2 mm thick 25 mm diameter absorbing glass filter from Reynard Corporation, designed as a 10 % neutral-density filter for visible wavelengths, a <100>-oriented 0.5 mm thick 25 mm diameter high-resistivity (>20 Ω cm) Si wafer from Virginia Semiconductor, and a nominally 1 % neutral density NiCr coating for 2 μm to 4 μm from Spectrogon, Inc., on a 0.25 mm thick Si substrate. For the reflectance measurements, the samples were 51 mm diameter mirrors: a first-surface aluminium mirror (NIST Standard Reference Material (SRM) 2003), and a black-glass sample similar to SRM 2026. Neither of these samples has a significant contribution from the back-surface reflection.

3. Results and discussion

3.1 Transmittance

Figure 4a shows the measured regular spectral transmittance for the fused-silica plate with the FTIR and monochromator-based systems, while the difference between the two measurement results is shown in Figure 4b. Over most of the spectral region, the difference between the two measurements is less than the combined uncertainty (calculated as the quadrature sum of the $k = 2$ expanded uncertainties of each measurement result) shown by the solid curves. The differences are largest near the fused-silica absorption features at 1.4 μm and 2.2 μm, with one outlier point on the steep edge of the absorption line at 2.2 μm probably due to a difference between the effective spectral resolutions of the two systems. The difference of 0.008 is more than an order of magnitude larger than would be expected from the combined wavelength uncertainties in the two instruments. Increased noise is seen in the H_2O vapour absorption region around 1.85 μm. The uncertainty in the FTIR data grows at shorter wavelengths due to the reduction in modulated signal level and interferometric stability.

For this measurement, the FTIR data were taken with an average angle of incidence of 8° and an f/5 cone, while the monochromator data were taken at near normal incidence and collimated. In the transparent spectral regions of fused silica, the difference between

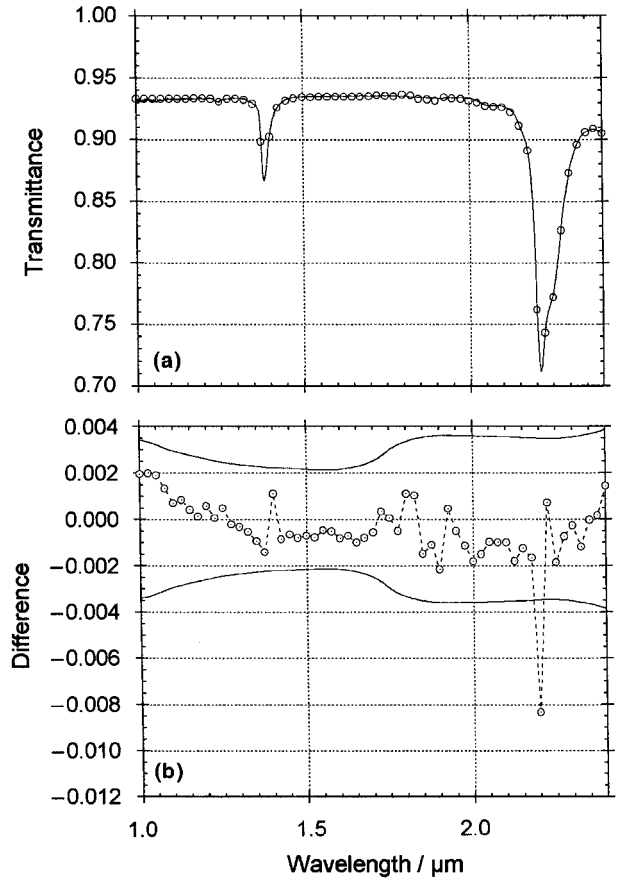

Figure 4. Comparison of FTIR and monochromator measurements of 5 mm thick fused-silica transmittance. (a) measured transmittances, with open circles showing monochromator data and solid curve showing FTIR data; (b) difference $(T_{\mathrm{mono}} - T_{\mathrm{FTIR}})$ between the two measurement results (open circles) and combined uncertainty $(k = 2)$ in the two measurements (solid curves).

the measured values in these two geometries for unpolarized light is expected to be less than 0.0001. At the minimum transmittance value of about 0.71 near 2.2 μm, the FTIR data are expected to be roughly 0.001 lower than the monochromator results because of the increased absorption path length in the material. This effect is not resolvable in the data shown in Figure 4b.

The second sample that was compared in transmittance was the 2 mm thick absorbing-glass filter. The results of these measurements are shown in Figure 5a, while Figure 5b shows the difference between the two sets of data. This sample has much lower transmittance than the fused silica and thus provides a test of the linearity of both systems. Over the 1.3 μm to 2.4 μm wavelength range, the differences between the two sets of data are mostly within the combined expanded uncertainty $(k = 2)$ of the two measurements. At shorter wavelengths (less than 1.3 μm), the differences grow systematically larger outside the expected statistical fluctuations, with the FTIR data consistently higher than the monochromator data. Near the minimum in transmittance of about 0.08

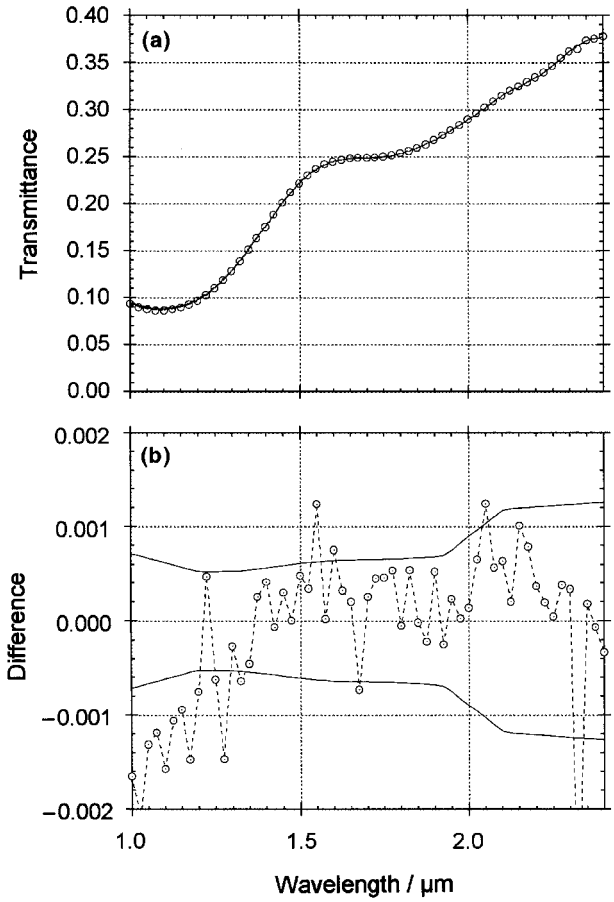

Figure 5. Comparison of FTIR and monochromator measurements of a 2 mm thick absorbing-glass filter. (a) measured transmittances, with open circles showing monochromator data and solid curve showing FTIR data; (b) difference $(T_{\mathrm{mono}} - T_{\mathrm{FTIR}})$ between the two measurement results (open circles) and combined uncertainty $(k = 2)$ in the two measurements (solid curves).

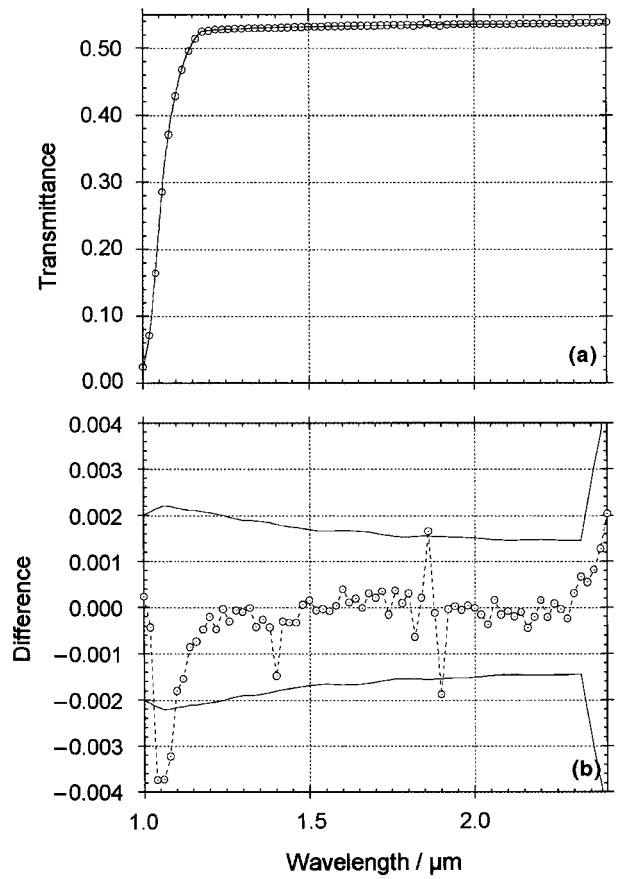

Figure 6. Comparison of FTIR and monochromator measurements of a 0.5 mm thick Si wafer. (a) measured transmittances, with open circles showing monochromator data and solid curve showing FTIR data; (b) difference $(T_{\mathrm{mono}} - T_{\mathrm{FTIR}})$ between the two measurement results (open circles) and combined uncertainty $(k = 2)$ in the two measurements (solid curves).

at 1.1 μm, the FTIR value would be expected to be 0.0024 lower than the monochromator value due to the increased path length of the converging beam. However, the observed difference is less than 0.002 and has the opposite sign to what is expected. The differences between the two sets of data at these short wavelengths could be caused by spurious harmonic signals in the FTIR spectrum, which need to be investigated more closely.

Figure 6a shows the transmittance comparison for a 0.5 mm thick Si wafer, with the difference between the monochromator and FTIR data shown in Figure 6b. Over most of the spectral region, the differences are less than 0.001 and thus smaller than the combined uncertainty of the two measurements. The difference in measured values due to variation in beam geometry between the two systems is expected to be smaller than the combined measurement uncertainty. In the transparent spectral region for Si ($\lambda > 1.5$ μm) the difference due to the 8° incident, f/6 geometry of the sphere is at most expected to be 0.0001 for the nearly unpolarized beam. Near the cutoff wavelength at 1 μm, the expected decrease in transmittance due to the increased path length in the sphere geometry is only 4×10^{-5}, significantly smaller than the combined measurement uncertainty.

The sharp structures apparent at 1.4 μm and 1.85 μm in Figure 6b may result from H_2O vapour absorption. They appear mostly in the monochromator data, which were not acquired under purged conditions. The difference grows systematically larger, reaching –0.004 at the Si absorption edge near 1.1 μm. The possibility was considered that this discrepancy arises from an error in wavelength in one or both instruments, but the differences are too large and the average amplitude cannot be made any smaller by shifting the abscissa scale of one data set relative to the other. At the short-wavelength limit of the data, the FTIR data were measured using a 8000 cm^{-1} to 12 000 cm^{-1} bandpass filter in order to reduce any effect of false harmonic signals from interreflections or sampling errors, which can be significant for high-frequency measurements at low levels of signal. Some of the discrepancy between

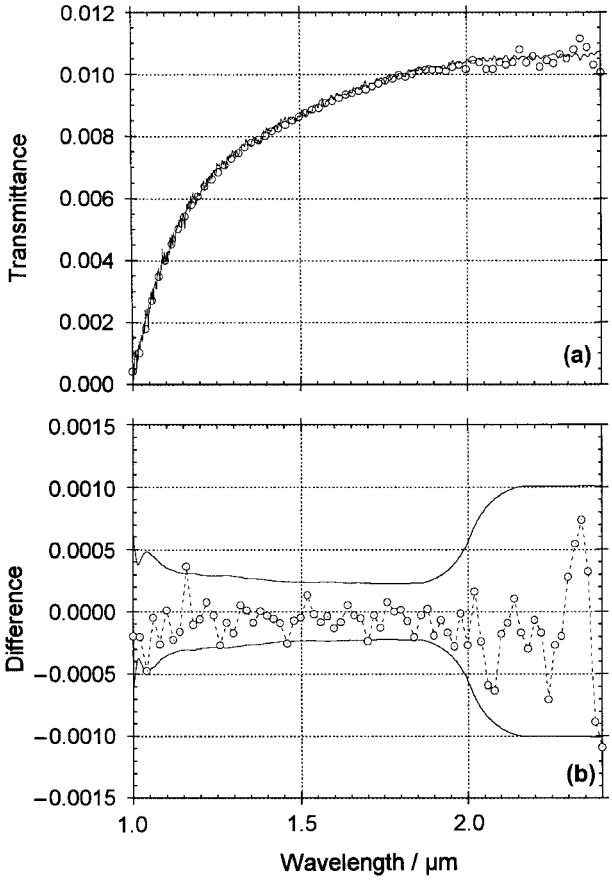

Figure 7. Comparison of FTIR and monochromator measurements of a 0.25 mm thick Si wafer with a NiCr coating. (a) measured transmittances, with open circles showing monochromator data and solid curve showing FTIR data; (b) difference $(T_{\mathrm{mono}} - T_{\mathrm{FTIR}})$ between the two measurement results (open circles) and combined uncertainty $(k = 2)$ in the two measurements (solid curves).

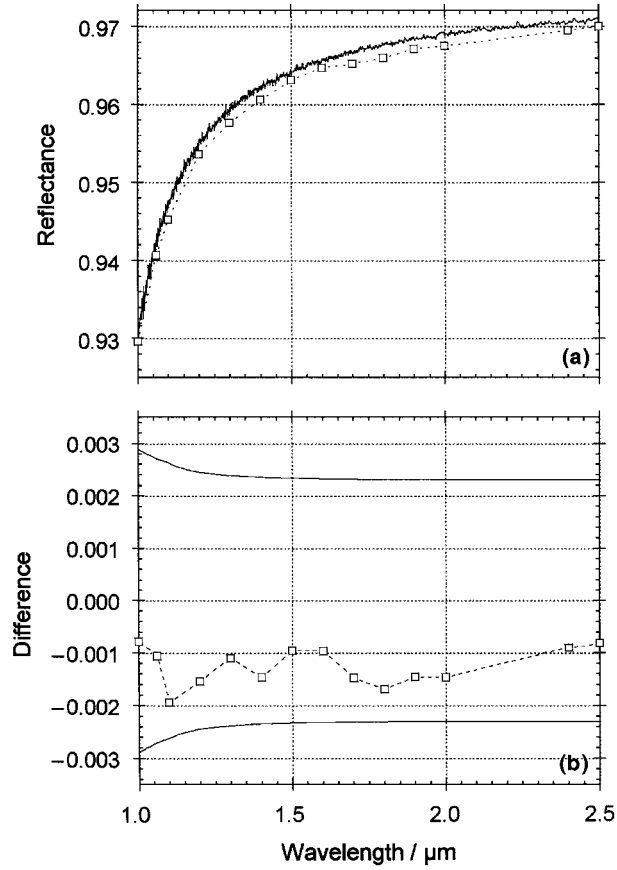

Figure 8. Comparison of FTIR and STARR reflectance measurements of an SRM 2003 aluminium mirror. (a) measured reflectances with STARR as open squares and FTIR as solid line; (b) difference $(R_{\mathrm{STARR}} - R_{\mathrm{FTIR}})$ between the two measurements (squares) and combined uncertainty $(k = 2$, solid lines).

the FTIR and monochromator results may be attributed to residual harmonics in the FTIR measurement, but some may also result from differences in effective resolution between the two systems. These differences need to be investigated more closely.

The final sample to be compared in transmittance was the 0.25 mm thick Si with NiCr coating, shown in Figure 7. The difference between the transmittances measured at normal incidence and 8° f/6 geometry for this sample, consisting of an absorbing metallic film on an absorbing substrate, is expected to be of order 1×10^{-5} or smaller, much less than the combined measurement uncertainty. The difference between the two measurement results, shown in Figure 7b, is on average about 1×10^{-4}, with the FTIR measurement being higher than the monochromator result. However, the observed differences are less than the combined uncertainty for most of the wavelengths measured.

3.2 Reflectance

Figure 8 shows a comparison of reflectance measurements at 8° (FTIR) and 6° (STARR) on an SRM 2003 Al mirror. As may be seen, the agreement at all wavelengths is well within the combined uncertainty for the two measurements, with the FTIR values consistently about 0.001 higher than the STARR values. We do not believe that this difference results from non-uniformity of the sample, although the spot diameters on the sample were quite different (5 mm versus 14 mm). Because both beams are nearly unpolarized, the difference due to incident angle should be negligible (approx. 3×10^{-5}). Further comparisons of high-reflectance mirrors may reveal a systematic difference between the two systems that would be interesting to investigate.

Finally, Figure 9 shows a comparison of the FTIR and STARR measurements on the black-glass sample. This sample has a reflectance of approximately 0.04 over the measured spectral range, and again the two measurements agree within the combined uncertainty. Much of the uncertainty comes from non-uniformity

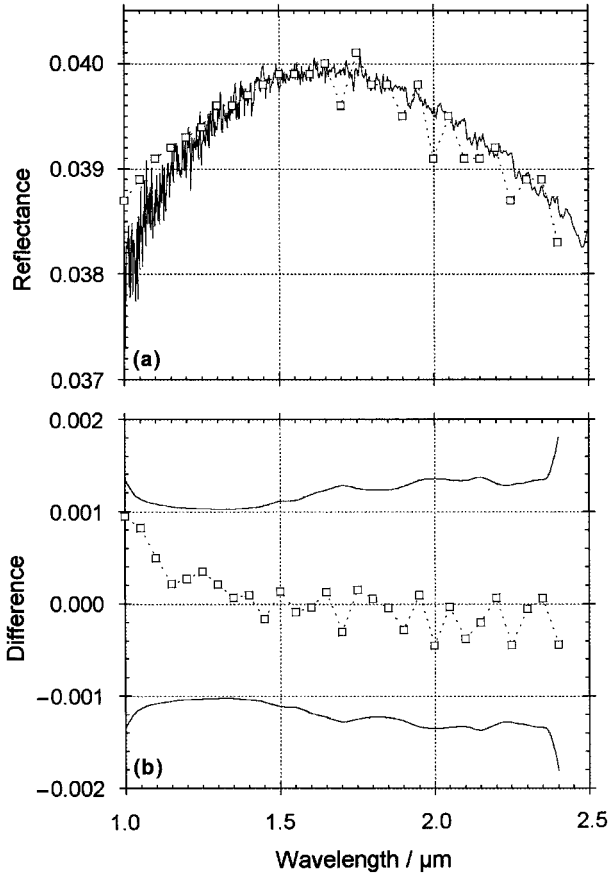

Figure 9. Comparison of FTIR and STARR reflectance measurements of a black-glass mirror. (a) measured reflectances with STARR as open squares and FTIR as solid line; (b) difference $(R_{\mathrm{STARR}} - R_{\mathrm{FTIR}})$ between the two measurements (squares) and combined uncertainty ($k = 2$, solid lines).

in the black glass. The average difference is much less than the expanded uncertainty $(k = 2)$, indicating that the uniformity near the centre of the sample may be somewhat better. An apparently systematic difference between the two measurements can be seen between 1 μm and 1.3 μm. This is the same region where the differences in transmittance were noted in the absorbing-glass filter (Figure 5b). The discrepancy again points to the possibility of small spurious modulation errors in the FTIR measurement that become significant in the spectral regions where the level of flux is small compared with the peak value.

4. Conclusions

A comparison has been made of near-normal regular transmittance and specular reflectance measurements of a series of samples on FTIR and monochromator-based spectrophotometers. We find agreement within the combined expanded uncertainty of about 0.002 $(k = 2)$ over most of the measured spectral range, and an ordinate scale range of nearly three decades. The only indication of systematic differences outside the combined uncertainties is found at the short-wavelength limit of the data, most prominently in Figures 5 and 6. We are currently investigating the possibility of interreflection or sampling errors in the FTIR spectrometer affecting the measurement results near the short-wavelength cutoff of 1 μm, where the overall signal is low compared with that at longer wavelengths, and residual false harmonic features could be significant sources of error in the sample/reference ratios. We will also be adding an InSb detector to the sphere system to increase the signal-to-noise ratio in the near-infrared region and improve our evaluation of the measurement uncertainties in this spectral region.

Note. The mention of certain trade names in this manuscript is for information only and not meant to imply an endorsement by the National Institute of Standards and Technology or that the equipment mentioned is necessarily the best suited for the task.

References

1. Birch J. R., Clarke F. J. J., *Spectroscopy Europe*, 1995, **7**, 16-22.
2. Kaplan S. G., Hanssen L. M., Datla R. U., *Appl. Opt.*, 1997, **36**, 8896-8908.
3. Barnes P. Y., Early E. A., Parr A. C., *Natl. Inst. Stand. Technol. Spec. Publ. 250-48*, Washington, D.C., U.S. Government Printing Office, 1998.
4. Eckerle K. L., Hsia J. J., Mielenz K. D., Weidner V. R., *Natl. Bur. Stand. Spec. Publ. 250-6*, Washington, D.C., U.S. Government Printing Office, 1987.
5. Hanssen L., Kaplan S., *Proc. SPIE*, 1998, **3425**, 16-27.
6. Hanssen L. M., *Appl. Opt.*, 2001, **40**, 3196.
7. Hanssen L. M., Kaplan S. G., *Vibr. Spect.*, 2001, in press.

Received on 5 December 2001 and in revised form on 31 January 2002.

Appendix F.

INSTITUTE OF PHYSICS PUBLISHING METROLOGIA
Metrologia **40** (2003) S55–S59 PII: S0026-1394(03)57649-6

NIST–NPL comparison of mid-infrared regular transmittance and reflectance

C J Chunnilall[1], F J J Clarke[1], M P Smart[1], L M Hanssen[2] and S G Kaplan[2]

[1] National Physical Laboratory (NPL), Teddington, Middlesex TW11 0LW, UK
[2] National Institute of Standards and Technology (NIST), Gaithersburg, MD 20899, USA

E-mail: chris.chunnilall@npl.co.uk

Published 7 February 2003
Online at stacks.iop.org/Met/40/S55

Abstract
The National Institute of Standards and Technology (NIST) and the National Physical Laboratory (NPL) realize independent scales for regular transmittance and near-normal regular reflectance in the mid-infrared part of the spectrum. Comparisons of these scales have recently been completed and the results are reported here. The agreement was excellent, lying within the quadrature combined uncertainties for the great majority of values measured and within the simple sum of uncertainties in all cases, demonstrating the level of equivalence of the NIST and NPL scales.

1. Introduction

The mutual recognition arrangement (MRA) requires that the metrological equivalence of national measurement standards be based on the results of comparisons which follow the guidelines established by the BIPM [1]. Comparisons of regular transmittance and regular reflectance in the mid-infrared part of the spectrum satisfying these guidelines have recently been completed between the National Institute of Standards and Technology (NIST) and the National Physical Laboratory (NPL). These comparisons are the first of their kind in the mid-infrared and the results are reported here.

2. Measurement techniques

Major differences exist between the techniques used at NIST and NPL to realize these scales [2]. NIST uses Fourier transform (FT) spectrometers, whereas NPL has so far used grating spectrometers. Secondly, NIST uses an improved integrating sphere system [3, 4] for both transmittance and reflectance measurements, whereas NPL uses focusing optical systems with no diffusing components [5, 6].

The comparisons addressed the standard manner in which NIST and NPL disseminate their scales. The NIST technique is a direct absolute technique, and therefore each artefact is independently calibrated. NPL calibrates an artefact relative to in-house reference standards that have been previously calibrated absolutely. There is a very small degradation in uncertainty, but since the reference standards are similar to the artefacts, a like-with-like measurement is carried out which relaxes most of the stringent experimental conditions required for absolute calibrations.

The NIST primary scales and measurement facility is based on a Bio-Rad[3] FTS-60A FT-IR spectrometer with a custom-built external integrating sphere assembly where corrections are applied for sphere non-ideality [3, 4].

The NPL primary scales are established using modified Perkin–Elmer PE580B and PE983G grating IR spectrometers. These instruments are also used to calibrate the NPL reference standards as well as customer artefacts. For regular reflectance, a VW reflectometer technique is used to establish an absolute calibration, and relative calibrations are made using a V-only substitution technique [5, 6].

3. The comparison

The measurement sequence was NPL–NIST–NPL. Measurements were carried out between 2.5 μm (4000 cm^{-1}) and 18 μm (550 cm^{-1}), the spectral range common to both laboratories. The comparison of regular reflectance was limited to near-normal incidence, as large angles introduce further complications which may be addressed in future.

3.1. Description of artefacts

3.1.1. Transmittance artefact. An NPL transmittance transfer and QA standard was used. This consists of an optically worked filter of Schott NG11 optical glass, a material

[3] The identification of any commercial product or trade name does not imply endorsement or recommendation by NIST.

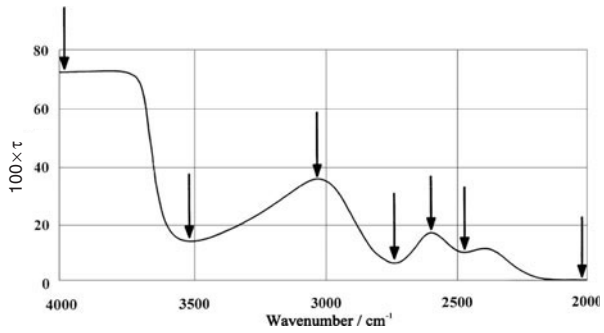

Figure 1. Typical transmittance spectrum of 1 mm of Schott NG11 glass.

known from some 50 years' work in visible region standards to be very stable for transmittance, provided that it is not cleaned repeatedly using fluids. (These can slowly leach out the metal oxide constituents, leaving a silica-rich residual surface layer of reduced refractive index.) The thickness is nominally 1 mm, which gives a very useful selection of transmittance levels at portions of the spectrum with zero gradient and low enough second derivative to eliminate significant influence from wavenumber error or inadequate resolution. As a consequence stray light (grating) or apodization fall-off (FT) are not likely to be critical or even need correction. These levels are at about 73%, 36%, 17%, 14%, 10%, 6% and just above 0% as shown in figure 1. The standard therefore samples enough values to reveal any problems with non-linearity of response, zero-offset error or scaling error due to imperfect substitution with respect to the reference readings. The 1 mm thickness is thin enough, in conjunction with the refractive index of only 1.45, to minimize problems of beam shift, beam size or focal shift, yet it is thick enough to eliminate problems of interference fringing at all but the highest resolutions possible on normal analytical instruments. In addition, it has the useful property of being insensitive to multiple modulation effects in FT instruments caused by interreflections between sample and interferometer.

3.1.2. Reflectance artefacts. Three flat samples were used—a non-overcoated aluminized glass mirror, a NiCr coating on a glass substrate and an uncoated plate of 6 mm thick Schott BK7 optical glass. The first sample has a very high reflectance (about 98% to 99%), the second has a progressive change of reflectance from about 84% to about 92%, while the third has a more complex spectrum including a long flat low-reflectance region with a narrow peak of about 40% and variable values at the low-wavenumber end. These three samples therefore cover a large range of reflectance values, as shown in figure 2. They also have zero or very low transmittance, and therefore no reflected component from the back surface. BK7 does suffer from this drawback from 4000 cm^{-1} to 3600 cm^{-1}, so while measurements were generally made from 4000 cm^{-1} to 550 cm^{-1} at intervals of 10 cm^{-1}, measurements for BK7 were only made from 3600 cm^{-1}.

3.2. Results for transmittance comparison

3.2.1. Results. The NIST measurements were carried out at $f/6$ with 8° incidence at 23.5 °C, and at 8 cm^{-1} and 16 cm^{-1} spectral bandwidths. The NPL measurements were carried out at $f/6.5$ with 5° incidence at 27 °C. The NPL reference standard was calibrated on two different instruments with bandwidths varying from 9.5 cm^{-1} to 5.5 cm^{-1}, and from 17.5 cm^{-1} to 6.5 cm^{-1}, going from high to low wavenumber. Neither laboratory observed significant differences due to bandwidth. The reported uncertainties are given in table 1.

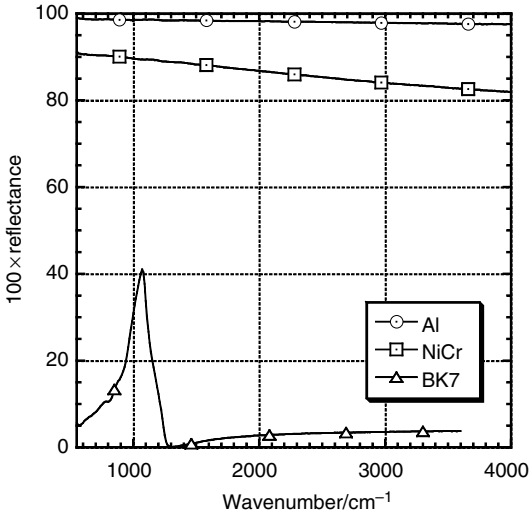

Figure 2. Reflectance curves of the three artefacts (NIST measurements).

The measured values were corrected to a common basis of 0° incidence and 26 °C for randomly polarized incident light. The difference in correction between $f/6$ and $f/6.5$ is negligible. For the NPL measurements, corrections were done from a state of 5° incidence and 29 °C, which were the conditions under which the reference standard (a 1 mm Schott NG11 glass filter NPL no 7) had been calibrated. The polarization bias of the NPL spectrometers was measured, while the NIST measurements were taken to be as for random polarization.

In order to facilitate these corrections NPL made a reassessment of the corrections for tilt, solid angle and polarization that are valid for the Schott NG11 glass transfer standards. These corrections are discussed in [5, 7] and use the same equations as Mielenz and Mavrodineanu [8]. The uncertainties ($k = 1$) due to the temperature correction were 0.008% transmittance for both laboratories, except at 2010 cm^{-1} where it was 0.000%. The uncertainties for the tilt correction (including polarization in the case of NPL) came to 0.005% for both laboratories, except at 2010 cm^{-1} where it was

Table 1. Uncertainties for NIST and NPL measurements.

Wavenumber/ cm^{-1}	100 × Expanded combined uncertainty ($k = 2$)	
	NPL mean	NIST
3990	0.151	0.150
3512	0.055	0.042
3031	0.107	0.072
2739	0.041	0.029
2598	0.070	0.039
2473	0.048	0.029
2010	0.009	0.018

Table 2. Summary of results for transmittance comparison after inclusion of thermochromism and tilt corrections and their uncertainties.

Wavenumber/ cm^{-1}	100 × Transmittance		100 × Expanded combined uncertainty ($k = 2$)		100 × Quadrature sum of uncertainties:	100 × Simple sum of uncertainties:	100 × Difference of values: NPL mean
	NPL mean: 2000, 2001	NIST: 2000	NPL mean	NIST	NPL mean, NIST	NPL mean, NIST	minus NIST
3990	72.925	72.79	0.152	0.151	0.215	0.303	0.135
3512	14.40	14.315	0.058	0.046	0.074	0.104	0.085
3031	35.68	35.57	0.109	0.074	0.132	0.183	0.110
2739	6.35	6.29	0.045	0.035	0.057	0.080	0.060
2598	16.855	16.835	0.072	0.043	0.084	0.116	0.020
2473	9.985	9.94	0.052	0.035	0.062	0.086	0.045
2010	0.0114	0.0160	0.009	0.018	0.020	0.027	−0.004

Table 3. NIST uncertainty budget for NG11 glass measurement at 35% transmittance peak, showing standard uncertainty components and combined expanded ($k = 2$) uncertainty.

Source of uncertainty	$100 \times u_i$
Type B standard uncertainty component	
Interreflections	0.004
Detector non-linearity	0.015
Atmospheric absorption variation	0.007
Inequivalent sample/reference beam geometry	0.018
Retroreflected light lost from entrance port	0.007
Sample port overfill	0.004
Beam geometry, polarization	0.011
Phase errors	0.018
Quadrature sum	**0.033**
Type A standard uncertainty component	0.015
Thermochromism correction to 26 °C	0.008
Correction from 8° angle to 0°	0.005
Expanded uncertainty ($k = 2$)	**0.074**

0.001%. Table 2 summarizes the results of the transmittance comparison after these corrections and their uncertainties have been included.

3.2.2. Uncertainties. Table 3 lists the significant uncertainty components for the NIST transmittance measurement, with values for the 35% transmittance peak given as an example. Other potentially important sources of error in the measurement, such as interreflections, non-source emission, sample non-uniformity and scattering, were not significant for this measurement. The type A component is evaluated from the standard uncertainty in the mean of repeated measurements.

The uncertainties in the NPL measurements arise from two processes: (i) calibration of the reference artefact; (ii) relative measurement of the comparison artefact. Table 4 gives the uncertainty budget for the 35% transmittance level as an example.

In table 2, mean NPL values are used to evaluate the comparison in order to make use of all the measurements. Type B uncertainties dominate, and the overall $k = 2$ uncertainties for the first and second NPL measurements are at most 0.001% transmittance units greater than the uncertainty for the NPL mean.

3.2.3. Analysis. The measurements of all but two of the features lie well within the quadrature combined uncertainties of the two laboratories, while the remaining two measurements, at 3512 cm^{-1} and 2739 cm^{-1}, lie within the simple combined uncertainty. This may be due to a small bias between the laboratories, since the NPL values are generally larger than those of NIST. However, there is no evidence that the uncertainties have been understated by either laboratory.

Table 4. NPL uncertainty budget for 35% transmittance peak of NG11 glass, showing standard uncertainty components and combined expanded ($k = 2$) uncertainty.

Source of uncertainty	Absolute calibration of reference artefact $100 \times u_i$	Relative calibration of comparison artefact $100 \times u_i$
Repeatability (std. dev. of mean) [Type A]	0.010	0.019
Effect of off-axis angle (beam displacement)	0.022	0.005
Uncertainty of angle	0.003	0.001
Non-flatness, non-parallelism	0.007	0.020
Instrument non-linearity	0.035	0.001
Zero offset correction not fully valid	0.003	0.000
Residual ordinate scaling error	0.007	0.010
Uncertainty of temperature	0.007	0.002
Thermochromic correction	0.005	0.001
Residual sample interreflections at 5° angle	0.018	0.012
Residual interreflections through sample position	0.016	0.000
Wavenumber error	0.014	0.002
Combined uncertainty (relative value scaling)		**0.032**
Combined uncertainty (absolute scaling)		0.012
Uncertainty of reference standard (absolute scaling)		0.052
Correction from 5° angle to 0°, including polarization		0.005
Correction to 26 °C		0.008
Combined uncertainty (absolute scaling)	**0.052**	**0.054**
Expanded uncertainty (absolute scaling) ($k = 2$)	**0.104**	**0.109**

3.3. Results for reflectance comparison

3.3.1. Results. The NIST measurements were carried out at $f/6$ with 8° incidence at 23.5 °C. Random polarization was assumed. In order to obtain values at integer wavenumber, cubic-spline fitting was applied to the data in order to calculate

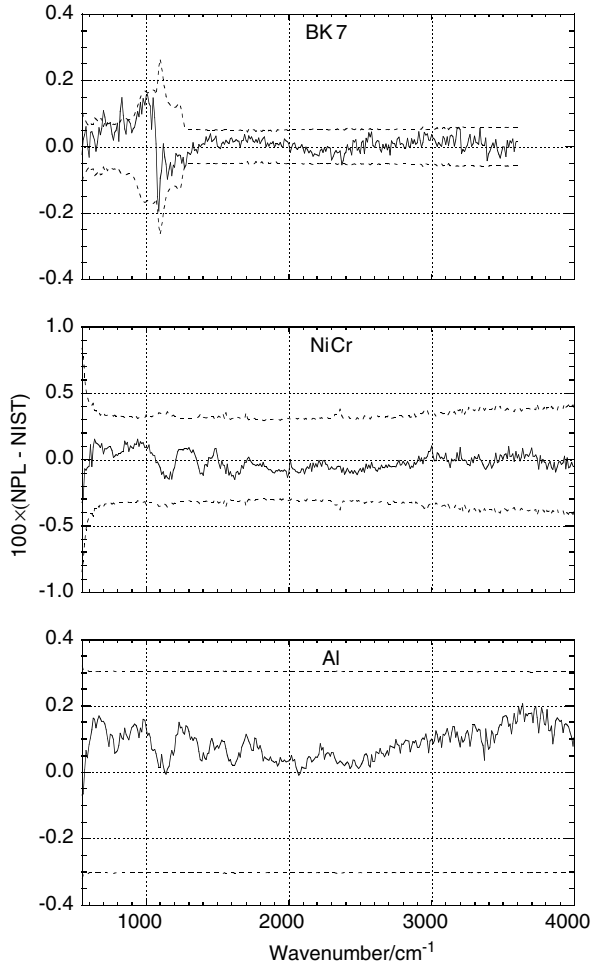

Figure 3. Spectra comparing the results and uncertainties of the reflectance measurements. In each plot, the full curve is the difference between the NPL and NIST results; the dotted curves are the combined uncertainties of the two measurements.

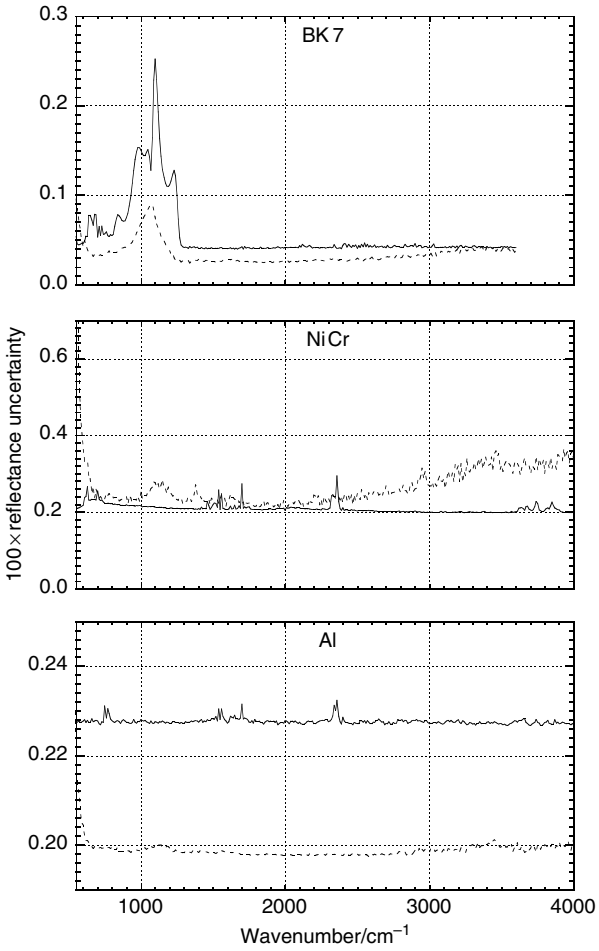

Figure 4. Uncertainties ($k = 2$) for NIST (· · · · · ·) and NPL (——) reflectance measurements.

interpolated values at 10 cm^{-1} intervals from the original data, which had a wavenumber spacing of 7.7 cm^{-1}.

The NPL measurements were carried out at $f/5.9$ with 10° incidence at 27 °C. The reference standard used was reference mirror OG65, which has an approximately uniform spectral reflectance of 98% to 99%. Corrections for polarization bias were derived from supplementary investigations, and the values were corrected to a common basis for randomly polarized incident light, for which the differences in reflectances between 8° and 10° are negligible.

No temperature corrections were applied as there was no evidence of significant thermochromism for these samples, and no thermochromic coefficients were known of.

The results of the reflectance comparison are shown in figure 3. In each figure the full curve shows the difference between the NPL mean and NIST, while the dotted curves denote the range of the quadrature sum of uncertainties. Figure 4 shows the expanded ($k = 2$) uncertainties for NIST and NPL.

3.3.2. Uncertainties. Table 5 lists the uncertainty components for the NIST reflectance measurements, with example values from the 40% reflectance peak in the BK7 spectrum. Two additional potential sources of error not present in the transmittance measurement are beam flip due to the reflection from the sample and entrance port overfill. The relative uncertainty values for the other two samples are similar. The NPL uncertainties have absolute and relative calibration components as for transmittance, and table 6 gives

Table 5. NIST uncertainty budget for BK7 glass measurement at the 40% reflectance peak.

Source of uncertainty	$100 \times u_i$
Type B standard uncertainty component	
Interreflections	0.013
Detector non-linearity	0.011
Atmospheric absorption variation	0.004
Beam flip	0.010
Inequivalent sample/reference beam alignment	0.030
Retroreflected light lost from entrance port	0.012
Entrance port overfill	0.005
Sample port overfill	0.004
Beam geometry, polarization	0.020
Phase errors	0.006
Quadrature sum	**0.044**
Type A standard uncertainty component	0.015
Expanded uncertainty ($k = 2$)	**0.093**

Table 6. NPL uncertainty budget for BK7 glass measurement at the 40% reflectance peak.

Source of uncertainty	Absolute calibration of reference artefact $100 \times u_i$	Relative calibration of comparison artefact $100 \times u_i$
Repeatability	0.013	0.014
Imperfect alignment of VW mirror and sample aperture, and the spectrophotometer with the reflectometer	0.097	0.020
Instrument non-linearity	0.002	0.036
Zero offset correction not fully valid	0.001	0.012
Residual ordinate scaling error	0.019	0.008
Possible residual interreflections across sample position	0.001	0.016
Wavenumber error	0.001	0.000
Combined uncertainty (relative scaling)		**0.049**
Combined uncertainty (absolute scaling)		0.048
Uncertainty of reference standard (absolute scaling)		0.100
Polarization bias correction		0.013
Combined uncertainty (absolute scaling)	**0.100**	**0.112**
Expanded uncertainty (absolute scaling) ($k = 2$)	**0.200**	**0.224**

the uncertainty budget for the 40% reflectance level as an example.

3.3.3. Analysis. For the aluminized mirror and the NiCr coating there are no differences that exceed the quadrature sum of the expanded uncertainties of each laboratory's measurements, and hence there is excellent agreement between the laboratories.

For the uncoated BK7 glass there is also excellent agreement over most of the spectrum. However, there are three short regions of the spectrum, from 1280 cm^{-1} to 1270 cm^{-1}, from 840 cm^{-1} to 800 cm^{-1} and from 750 cm^{-1} to 700 cm^{-1}, where the difference between NIST and NPL exceeds the quadrature sum but not the simple sum of uncertainites. In addition, at 830 cm^{-1} and at 700 cm^{-1} the difference exceeds the simple sum of uncertainties by 0.03 percentage reflectance units.

These discrepancies arise in spectral regions with appreciable spectral gradients of reflectance, and hence wavenumber error, resolution or lineshape may be responsible. Extra tests with additional ammonia absorption lines in these regions have suggested that the problem does not arise from wavenumber scale errors. The NIST measurements were made at 8 cm^{-1} and 16 cm^{-1} bandwidths, and no appreciable differences were found. The bandwidth for the NPL measurements was approximately 3.4 cm^{-1} to 4.2 cm^{-1} in the three spectral regions concerned.

The number of data points where the quadrature sum of uncertainties is exceeded is 13 out of a total of 306, or under 5%, which is consistent with the 95% level of uncertainty used.

4. Conclusions

A comparison of regular transmittance and near-normal reflectance scales in the mid-infrared spectral region has been carried out between NIST and NPL. Three front-surface reflectance artefacts and one transmittance artefact, covering three decades of dynamic range on the ordinate scale, were measured under ambient conditions. No evidence of systematic discrepancies outside the combined uncertainty limits was found in comparing the measurement results from the two laboratories.

Despite the large differences in experimental apparatus and measurement approach between the two laboratories, the good agreement tends to support their stated uncertainties, and to demonstrate the applicability of high-quality standard artefacts for quality assurance checking of mid-infrared spectrophotometers.

Acknowledgments

The NPL work has been funded within the UK DTI's National Measurement Directorate's Programmes on Optical Radiation Metrology.

References

[1] Quinn T J 1999 *Guidelines for Key Comparisons Carried out by Consultative Committees* (Sèvres: BIPM)
[2] Clarke F J J 2002 *Handbook of Vibrational Spectroscopy* ed J M Chalmers and P R Griffiths (Chichester: Wiley) pp 891–8
[3] Kaplan S G and Hanssen L M 1999 *Anal. Chim. Acta* **380** 303–10
[4] Hanssen L M 2001 *Appl. Opt.* **40** 3196–204
[5] Clarke F J J 1999 *Anal. Chim. Acta* **380** 127–41
[6] Clarke F J J 1996 *Proc. SPIE* **2776** 184–95
[7] Chunnilall C J, Clarke F J J and Rowell N L 2003 *Proc. SPIE* **4826** to be published
[8] Mielenz K D and Mavrodineanu R 1973 *J. Res. NBS.* **77A** 699–703

Appendix G.

Comparison of mid-infrared absorptance scales at NMIJ and NIST

J. Ishii
National Metrology Institute of Japan (NMIJ) / AIST, Tsukuba, Japan

L. M. Hanssen
National Institute of Standards and Technology (NIST), Gaithersburg, USA

Abstract. National Institute of Standards and Technology (NIST) realizes scales for infrared absolute absorptance using the integrating-sphere method. National Metrology Institute of Japan (NMIJ) realizes an independent scale for infrared spectral emissivity equivalent to absorptance traceable to the ITS-90. Comparisons of these scales in the mid-infrared part of the spectrum have been performed successfully for the first time and the results are reported here. The results of the comparison show agreement is lying within uncertainty levels for the majority of values measured for opaque materials, and the level of equivalence of the NMIJ and NIST scales.

Introduction

Infrared optical properties such as absorptance are essential in the fields of both radiometry and radiation thermometry. Under the Mutual Recognition Agreement, the metrological equivalence of national measurement standards based on comparisons between the national metrological institutes has increased over time. Recently, the CCT (Consultative Committee for Thermometry) – Working Group 9 is organizing international comparisons of thermophysical properties including emissivity (emittance) of solids. Under such circumstances in this study, a comparison of spectral absorptance scales near room temperature in the mid-infrared portion of the spectrum from 5 μm to 12 μm at NIST and NMIJ based on fundamentally different methods has been performed for the first time. The normal spectral emissivity scale of NMIJ is realized by a direct comparison method between a sample and the reference blackbody cavities traceable to the ITS-90 [1, 2]. On the other hand, NIST realizes the same scale by an integrating sphere based absolute measurements of directional-hemispherical reflectance and transmittance[3].

Measurement techniques and apparatus

Both facilities at NIST and NMIJ employ Fourier transform infrared spectrometers (FTS), however, major differences exist between the techniques used to realize these scales. NMIJ applies the conventional direct technique that consists in measuring the ratio of the spectral radiance of the sample to that of a blackbody radiator at the same temperature and at the same wavelength to derive emissivity values. On the other hand, NIST uses a direct absolute technique with an improved integrating sphere method for measuring spectral reflectance and transmittance of materials. Absolute absorptance is indirectly obtained when the sum of the absolute reflectance and transmittance is subtracted from unity based on Kirchoff's law, which is written in the form for an opaque surfaces which is of primary concern in this study

$$\alpha(\lambda;\theta,\phi) = 1 - \rho(\lambda;\theta,\phi;2\pi) = \varepsilon(\lambda;\theta,\phi), \qquad (1)$$

where α is spectral-directional absorptance, ρ is the spectral-directional-hemispherical reflectance, and ε is spectral-directional emissivity, at wavelength λ, incident angle of radiation θ, ϕ, respectively.

Detailed descriptions of the apparatus of both NMIJ and NIST are found in references[1-3]. Here only brief introductions are presented here.

NMIJ: The spectrometer is a custom designed Michelson interferometer. For calibration of the response of the FTS, two reference blackbody cavities are installed. One is a liquid nitrogen cooled cavity and the other is a variable temperature one operated at 100 °C. The solid sample attached to the holder is heated from the backside by direct contact with the circulating thermostatic fluid. The temperature of the heating fluid is measured with a calibrated PRT sensor placed close to the backside surface of the sample. For minimal uncertainty the samples were measured at 100 °C. To reduce the effects of absorption by air and convective heat exchange, all of the components are assembled and operated in vacuum. The combined standard relative uncertainty for samples with good thermal conductivity is typically around 1 % for high emissivity values and less than 5 % for low emissivity values.

NIST: The spectrometer is a bench-top FTS with external beam output that is interfaced to a custom diffuse gold-coated integrating sphere with an MCT detector. Measurements of absolute reflectance and transmittance are performed at semi-normal incidence (8°) using custom developed methods described in References [3] and [4]. The samples were measured at an ambient temperature of 24 °C, determined by a Pt thermometer. The expanded uncertainty (k=2) for reflectance and transmittance measurements is 3 % of the values for samples of unknown scattering nature, and 0.3 % for specular samples.

We prepared several kinds of solids and coated surfaces as the transfer samples of the comparison. The samples

were 45 mm diameter discs of approximately 1 mm thickness. The samples were measured first at NMIJ and then sent to NIST for measurement.

Results and discussions

Figures 1 to 3 summarize the results measured by NMIJ and NIST for the solids and the coated samples in which transmittance can be disregarded. Figure 1 shows the results for a silicon dioxide sample having a roughened surface. The values measured by the two methods agree to within the combined uncertainty over the entire wavelength range. The discrepancy is at most 0.02 for an absorptance value of 0.6 around 9 μm, which is comparable to the NMIJ uncertainty level of emissivity. Figure 2 illustrates the results obtained for the silicon nitride sample, which is a standard reference material provided by the JFCC (Japan Fine Ceramics Center). It is also seen that the difference between NMIJ and NIST gradually increases as the absorptance values decreases. The discrepancy is about 0.03 when the absorptance value is at its minimum of 0.2 around 10.5 μm. This trend is consistent with an increase in the uncertainty of the radiance measurement for low emissivity materials near room temperatures. Figure 3 shows the results for a black paint, a Heat-resistant black manufactured by Asahi-paint, coated on a copper substrate. It is found that the paint maintains an absorptance value higher than 0.9 and the values observed by NMIJ and NIST are in good agreement over the entire wavelength range. The maximum discrepancy is less than 0.01 and within the combined uncertainty.

Summary

In this study a comparison of spectral absorptance (emissivity) scales in the middle-infrared wavelength region near room temperatures at NIST and NMIJ has been performed for the first time. NIST and NMIJ have established independent scales based on basically different approaches. NIST employs absolute reflectance and transmittance measurement using an improved IR integrating sphere. NMIJ applies a radiance comparison method with reference blackbody radiators traceable to the ITS-90. The results observed by the different approaches almost agree for opaque solid materials within their combined uncertainty levels. The results observed for other materials and details of uncertainty analysis will be also given in the presentation.

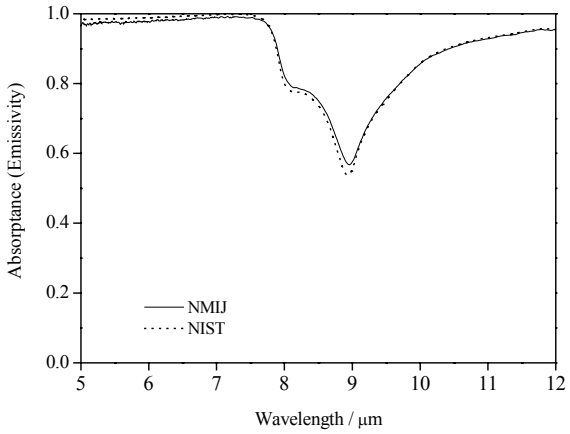

Figure 1. (Semi-) normal spectral absorptance (emissivites) of Silicon dioxide observed by NMIJ and NIST

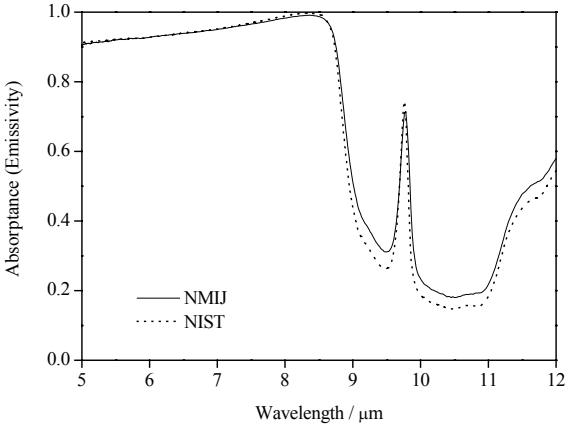

Figure 2. (Semi-) normal spectral absorptance (emissivites) of silicon nitride observed by NMIJ and NIST

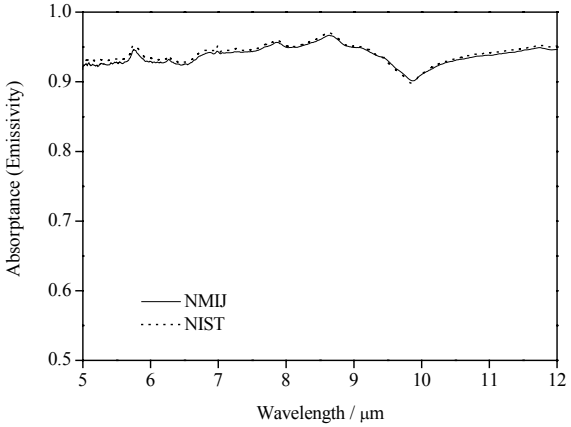

Figure 3. (Semi-) normal spectral absorptance (emissivites) of the black paint (Heat-resistant black, Asahi-paint) on copper substrate observed by NMIJ and NIST

References

1. Ishii J., Ono A., Uncertainty estimation for emissivity measurements near room temperature with a Fourier transform spectrometer, Meas. Sci. Technol. 12, 2103-2112 (2001).
2. Ishii J., Ono A., A Fourier-Transform Spectrometer for Accurate Thermometric Applications at Low Temperatures, Temperature: Its Measurement and Control in Science and Industry, Ripple D. C. (Ed), vol. 7, 705-710, AIP (2003)
3. Hanssen L. M, Integrating-sphere system and method for absolute measurement of transmittance, reflectance and absorptance of specular samples, Applied Optics, 40, 3196-3204 (2001).
4. Hanssen L. M., Snail K. A., Integrating Spheres for Mid- and Near Infrared Reflection Spectroscopy, in *Handbook of Vibrational Spectroscopy*, Chalmers J. M. and Griffiths P. R. (Eds), John Wiley & Sons, Ltd, vol. 2, 1175 - 1192 (2002).

APPENDIX H
Results of a Nationwide Inter-Laboratory Comparison of Infrared Reflectance

L. M. Hanssen, B. Wilthan

NIST
National Institute of Standards and Technology
U.S. Department of Commerce

Outline

I. Background

II. Intercomparision Details

III. Sample & Calibration Description

IV. Calibration & Comparison Results

V. Conclusions

EO-IR Calibration and Characterization Workshop, 7-9 March 2006

Space Dynamics LABORATORY
Utah State University Research Foundation

NIST

SENSIAC
Military Sensing Information Analysis Center

"Presenters from government, industry and academia will discuss the importance and potential of a united effort to improve and standardize measurements and data formats within the EO/IR community. Participants will benefit from presentations on current calibration and characterization activities and lessons learned, while also taking part in focused breakout sessions that will address specific issues of interest to the community. The breakout sessions will foster open discussion and provide participants with the opportunity to share ideas and explore possibilities, as well as contribute to the development of a roadmap based on broad community input."

Outcome of Workshop Discussion Sessions:

Priority of Highest Interest as expressed by the Workshop Participants:

Round Robin of near-normal diffuse & specular reflectance amongst DoD & Contractor Labs/Ranges to be conducted by NIST.

Outline

I. Background

II. Intercomparision Details

III. Sample & Calibration Description

IV. Calibration & Comparison Results

V. Conclusions

Intercomparison Structure

- NIST is Pilot Lab - organizes and coordinates intercomparison
- Process: "Star" Intercomparison approach
  - One sample set for each participant, NIST measures all samples - evaluates uniformity between samples
  - Measurement sequence: NIST-Participant-NIST
  - Advantage:
    - shorter time overall, especially for large group
    - Less risk due to sample accident
  - Disadvantage:
    - sample-sample variability, although characterized
    - more work for Pilot lab
- **Results compiled/analyzed by NIST**
  - Results communicated to all participants
  - Participants information listed, but data not identified (use 1,2,3, …)

Final Participant List

	IR Round Robin Participants		
#	Company/Agency	Contact	State
1	Air Force Research Lab 2	Bill Lynn	Ohio
2	Arnold Engineering Development Center	Dustin Crider	Tennessee
3	Boeing 1	Daniel Northem	Missouri
4	Boeing 2	Myrna Guhit	California
5	Boeing 3	Steve Wicken	Washington
6	CACI MTL Systems, Inc.	David J. Kelch	Ohio
7	General Electric	Joseph Sparks	Ohio
8	Lockheed Martin 1	Mei Graham	Texas
9	Lockheed Martin 2	Sarah Mieding	California
10	MIT Lincoln Labs	Merle Persky	Massachussetts
11	Naitonal Research Council	Nelson Rowell	Ontario, Canada
12	Northrop Grumman 1	Steven Chu	New York
13	NWSC Carderock	Bill Yeager	Maryland
14	Optical Data Associates	Michael Jacobson	Arizona
15	Pratt and Whitney	John Borla	Connecticut
16	Raytheon, El Segundo	Vijay Murgai	California
17	Sandia National Labs	Robert Ellis	New Mexico
18	SRI International	Jeffrey Voss	California
19	Surface Optics Corp.	Martin Szsecznіak	California
20	The Aerospace Corp.	Chung-tse Chu	California
21	USGS	Jim Crowley	Virginia

Participant Survey Results

Survey Responses: 20/25 received

Spectrometer Type: all **FT**, except 1 x broad band; several second instruments, 1 x monochromator, 1 x filter

DHR system: 5 x **integrating sphere**, 6 x **SOC-100**, 16 x unspecified

Spectral Range: **2 µm - 14 µm**; 2 x 2.5 µm, 2 x 12 µm

Spectral Resolution: **8 cm^{-1}**; 5 x 16 cm^{-1}, 6 x 8 cm^{-1}, 5 x 4 cm^{-1}, 2 x ≤ 2 cm^{-1}

Sample Size Acceptable: 18 x **1 inch** dia., 6 x **2 inch** dia., 2 unknown

Geometry: "near normal" incidence angle: **8° - 20°**

Outline

I. Background

II. Intercomparision Details

III. Sample & Calibration Description

IV. Calibration & Comparison Results

V. Conclusions

Intercomparison Transfer Standard Sample Set

5 samples in set:
diffuse - hi, med, low; specular - hi, med
(51 mm dia. set shown)

Intercomparison Transfer Standard Sample Set - Details

- **Specular standards:**
  - High (SA): Electroplated Gold Mirror on polished copper substrate
  - Medium (SD): Polished High Density Silicon Carbide
  - {Low (SC): Z-302 paint on brass substrate: problems with paint thickness and diffuse component in semitransparent region – dropped from comparison}
- **Diffuse standards:**
  - High (DA): Electroplated Gold on Nickel on arc-sprayed aluminum on machined brass substrate
  - Medium (DD): Krylon Silver Paint on arc-sprayed aluminum on machined brass substrate {replaced initial "DB" set due large sample to sample variability}
  - Low (DC): Nextel Black Paint on machined brass substrate

Sample Characterisation

Gold Mirror, Silicon Carbide - Details

Spatial Uniformity:

Gold Mirror

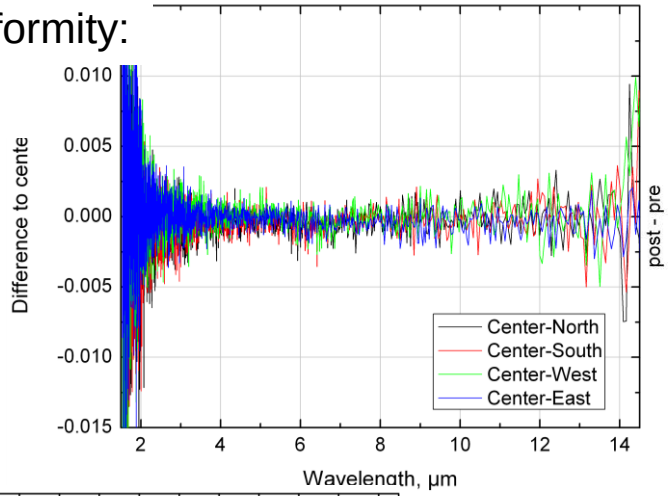

Stability/

Repeatability:

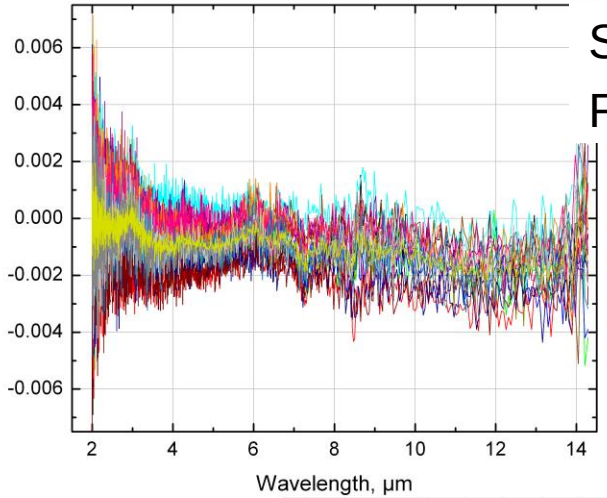

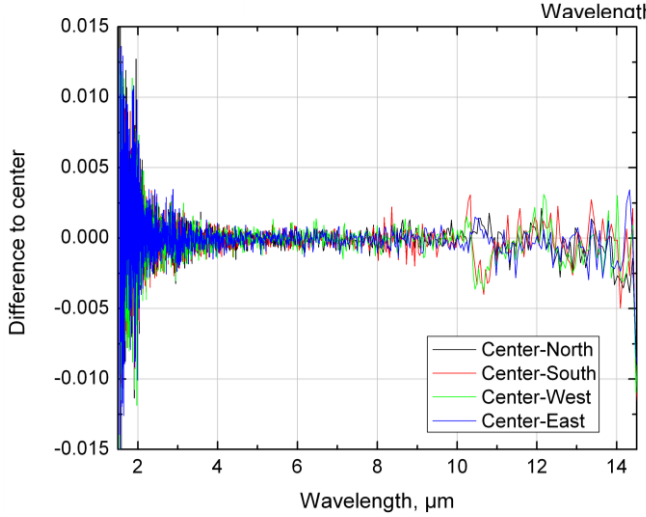

Silicon Carbide

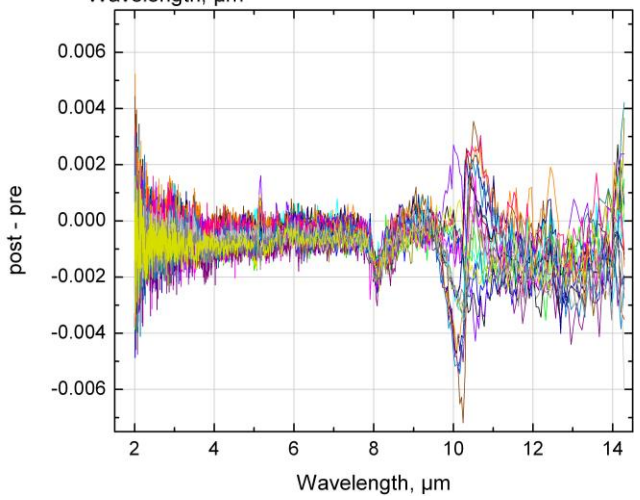

Sample Characterisation

Rough Gold - Details

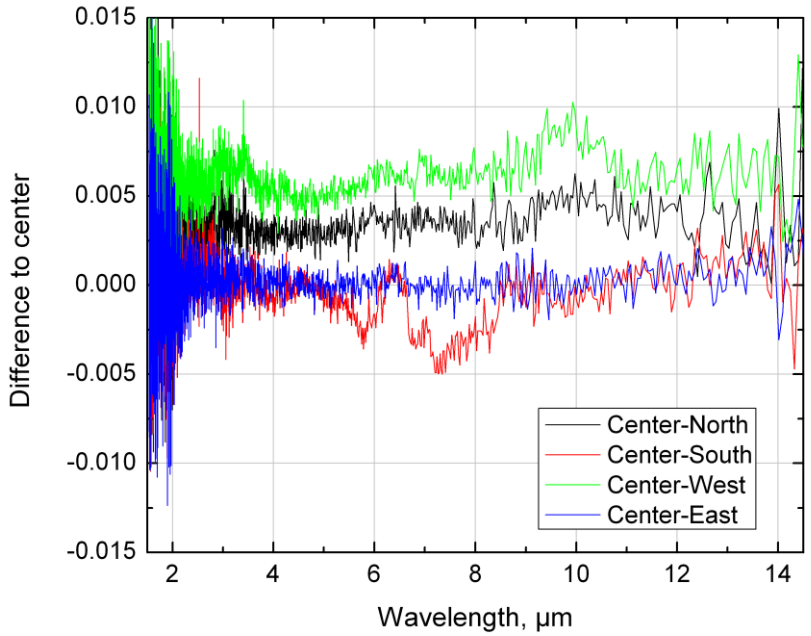

Spatial Uniformity of one sample.

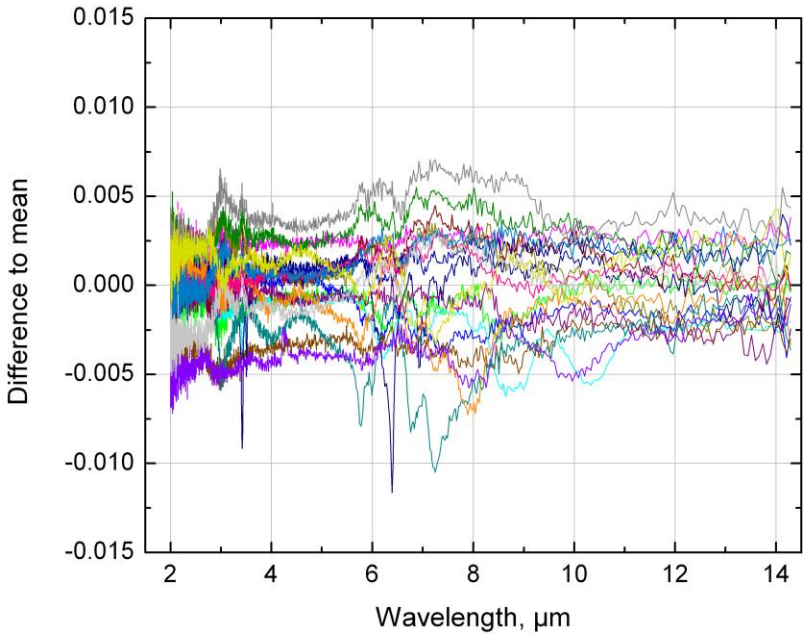

Variability of the sample set.

Sample Characterisation

Krylon Silver Paint - Details

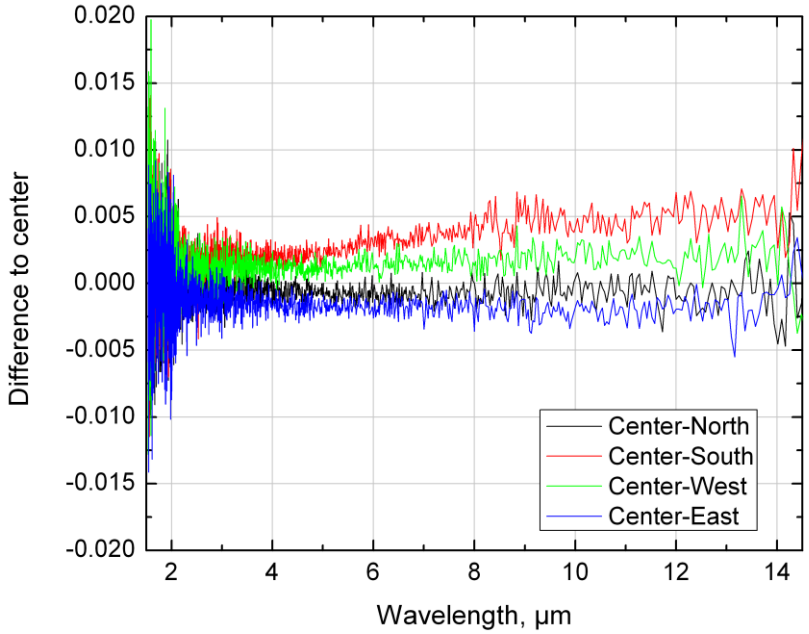

Spatial Uniformity of one sample.

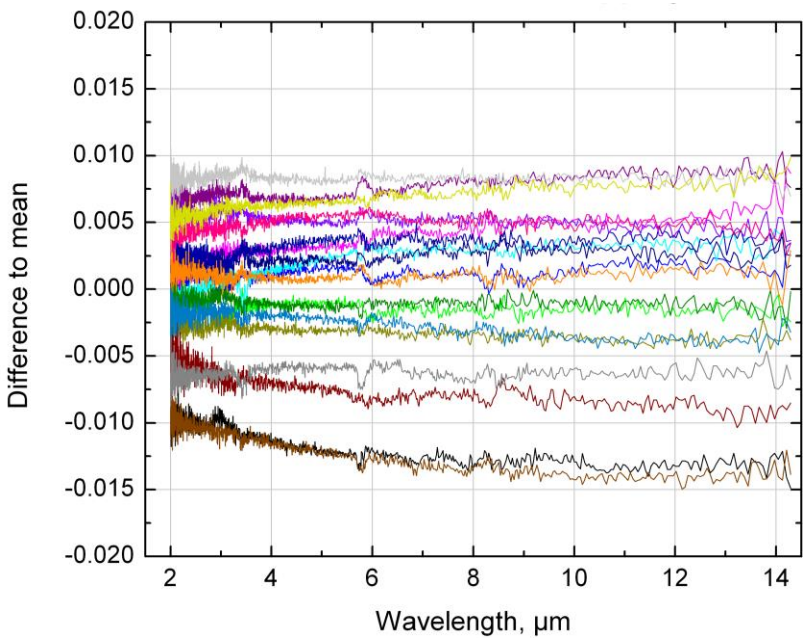

Variability of the sample set.

Intercomparison Specifics

- Quantity: near-normal infrared spectral reflectance of opaque standard samples
- Measurement geometry: for 3 diffuse standards - directional-hemispherical (DHR) or hemispherical-directional (HDRF); for 2 specular standards - collect specular reflection
- Incident angle: $\theta \leq 15^\circ$ (20° for one participant)
- Spectral range: 2 to 14 µm (can vary for some participants)
- Sample set (5): specular: high, medium w/ structure; diffuse high, medium (paint) reflectance, low (paint) reflectance
- Sample size: 1 and 2 inch diameter (3 to 5 mm thick)
- Data submission: preformatted spreadsheet, data at 4 cm^{-1} intervals

Outline

I. Background

II. Intercomparision Details

III. Sample & Calibration Description

IV. Calibration & Comparison Results

V. Conclusions

SxxA – Gold Mirror Samples I

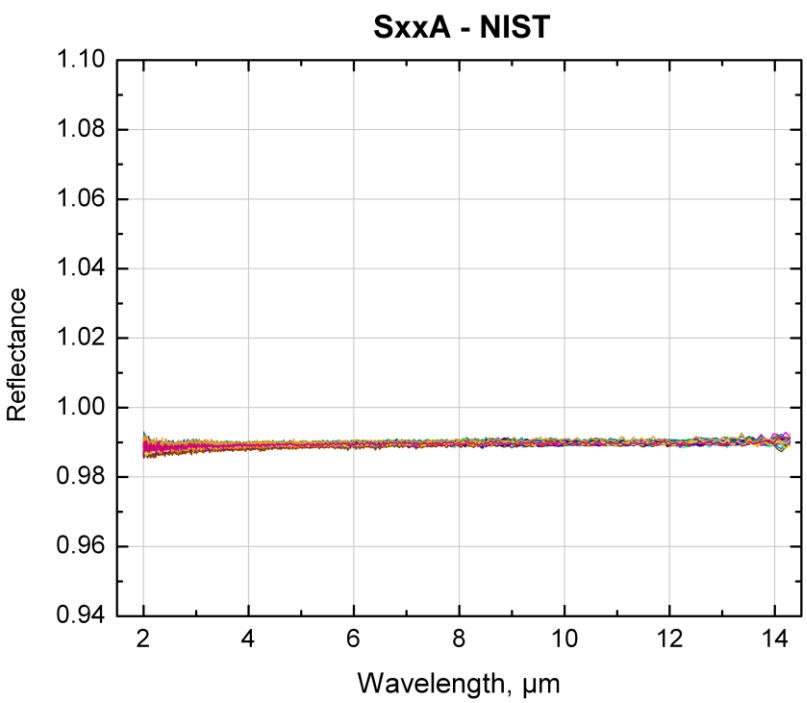

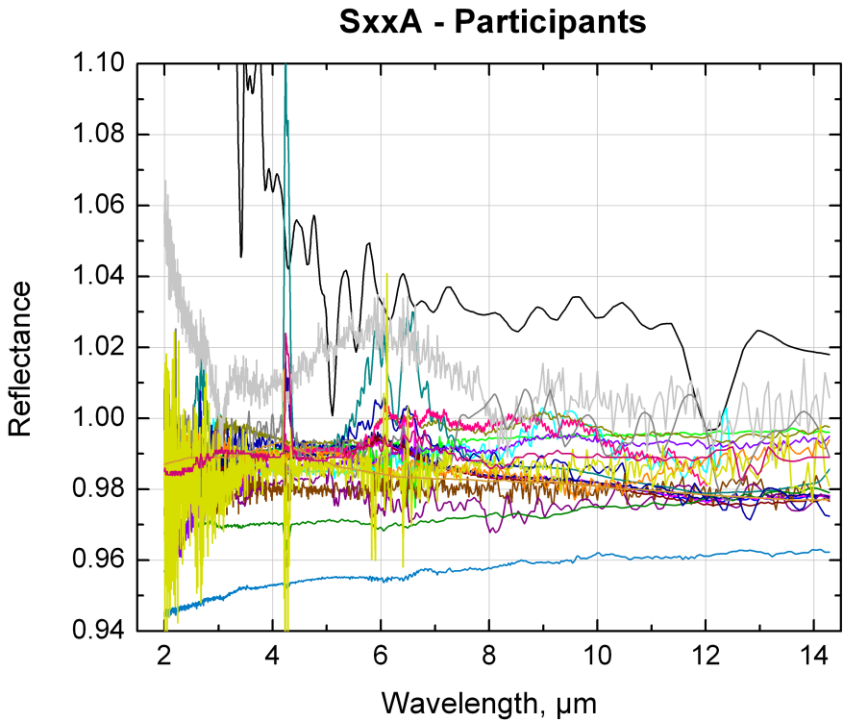

21 Curves overlaid in each plot

NIST data are mean of before and after measurements

SxxA – Gold Mirror Samples II

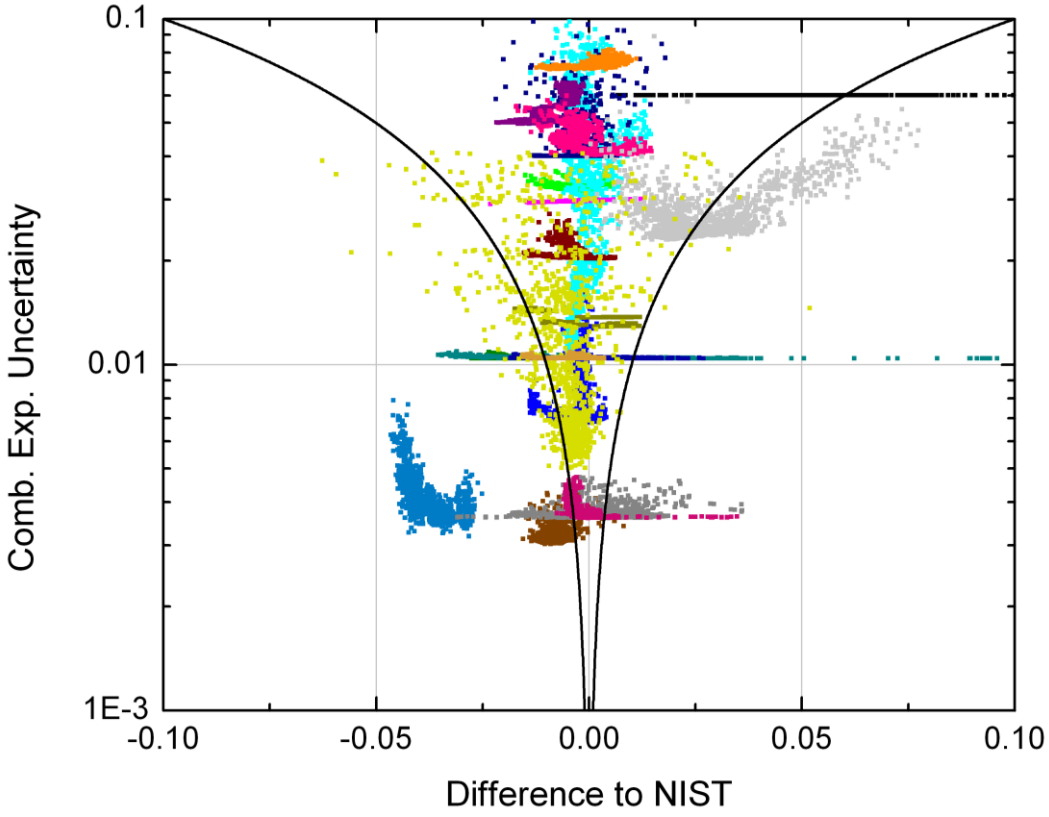

Comparison of Combined Uncertainty with Difference to NIST

Individual results are consistent with claimed uncertainties if points lie within black curves

Combined Expanded Uncertainties = $\sqrt{U(NIST)^2 + U(Sample)^2 + U(Participant)^2}$

Some uncertainties underestimated; some uncertainties overestimated

SxxB – Silicon Carbide Samples I

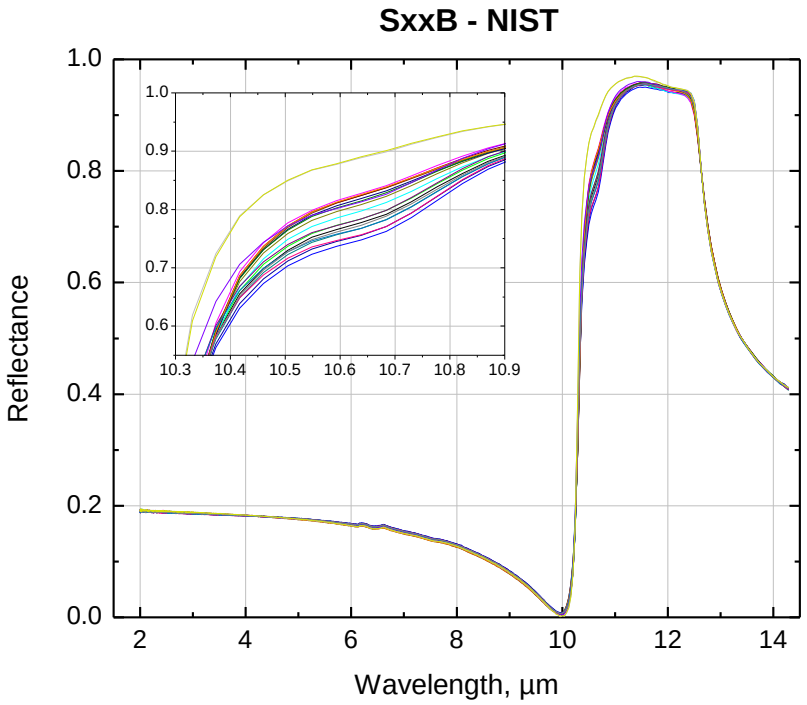

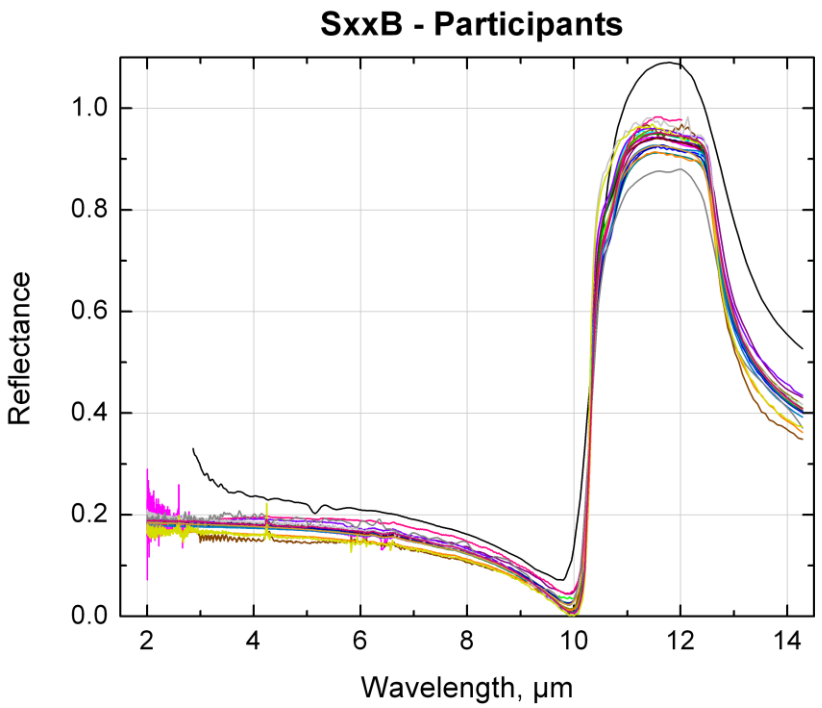

Minor sample to sample variability

Near complete coverage of reflectance range 0 to 1

SxxB – Silicon Carbide Samples II

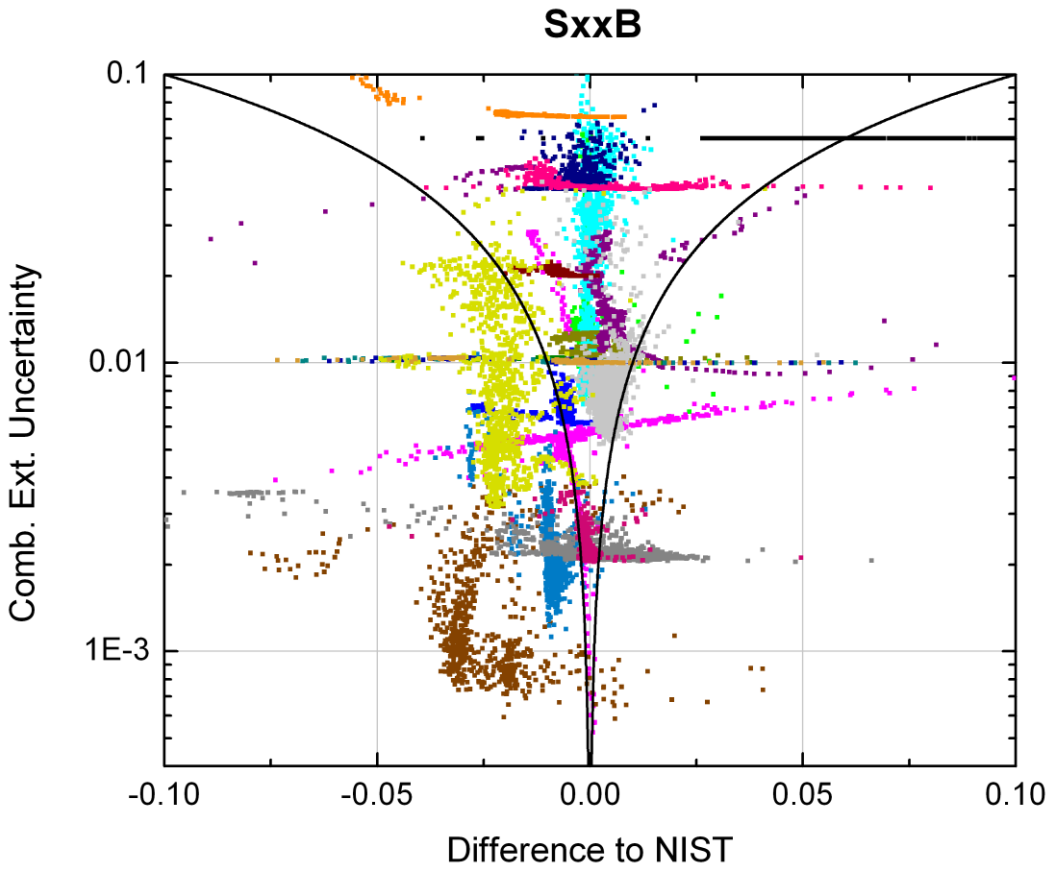

Significant differences seen between NIST & a number of participants results

DxxA – Rough Gold Samples I

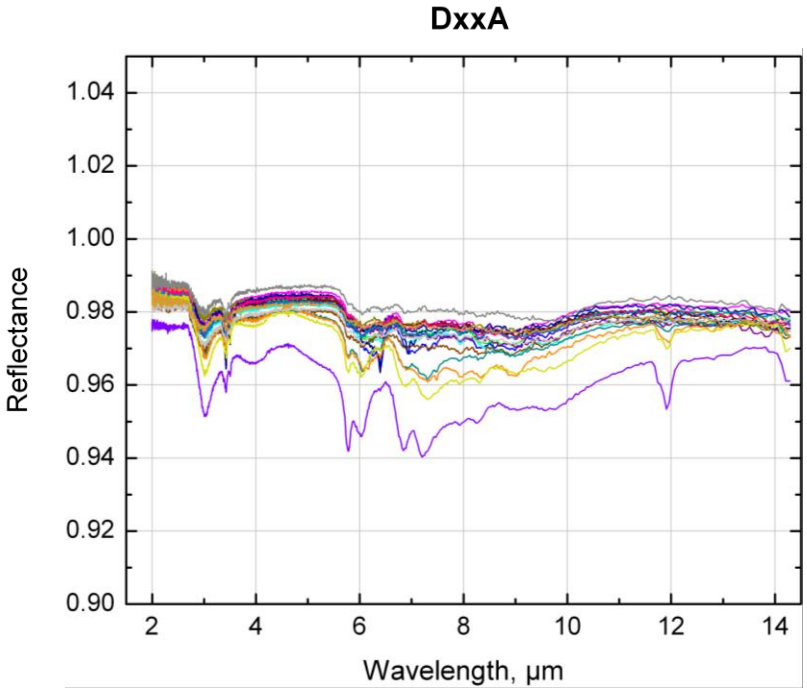

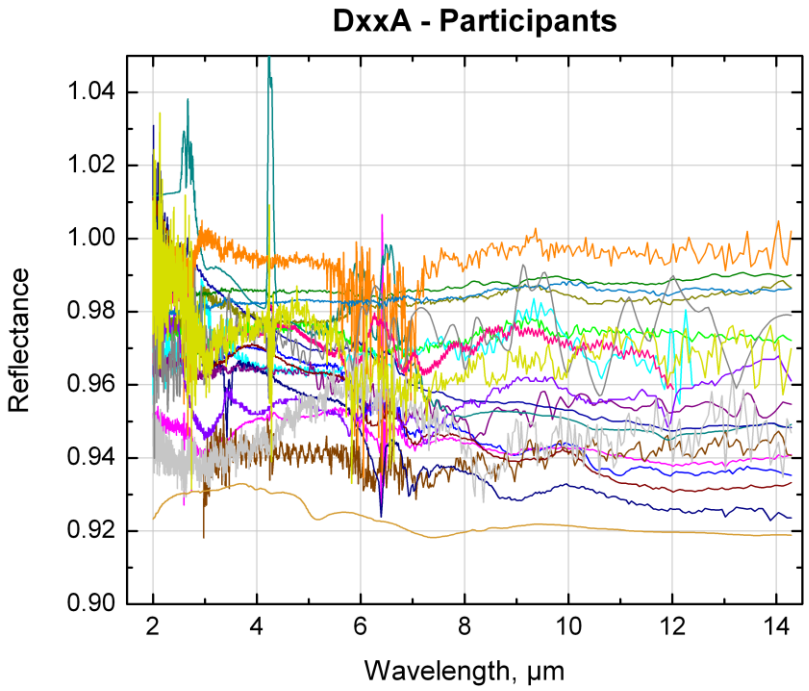

Some change in reflectance seen in a few samples, one poor in particular

Monitoring of samples will continue to examine long term stability

DxxA – Rough Gold Samples II

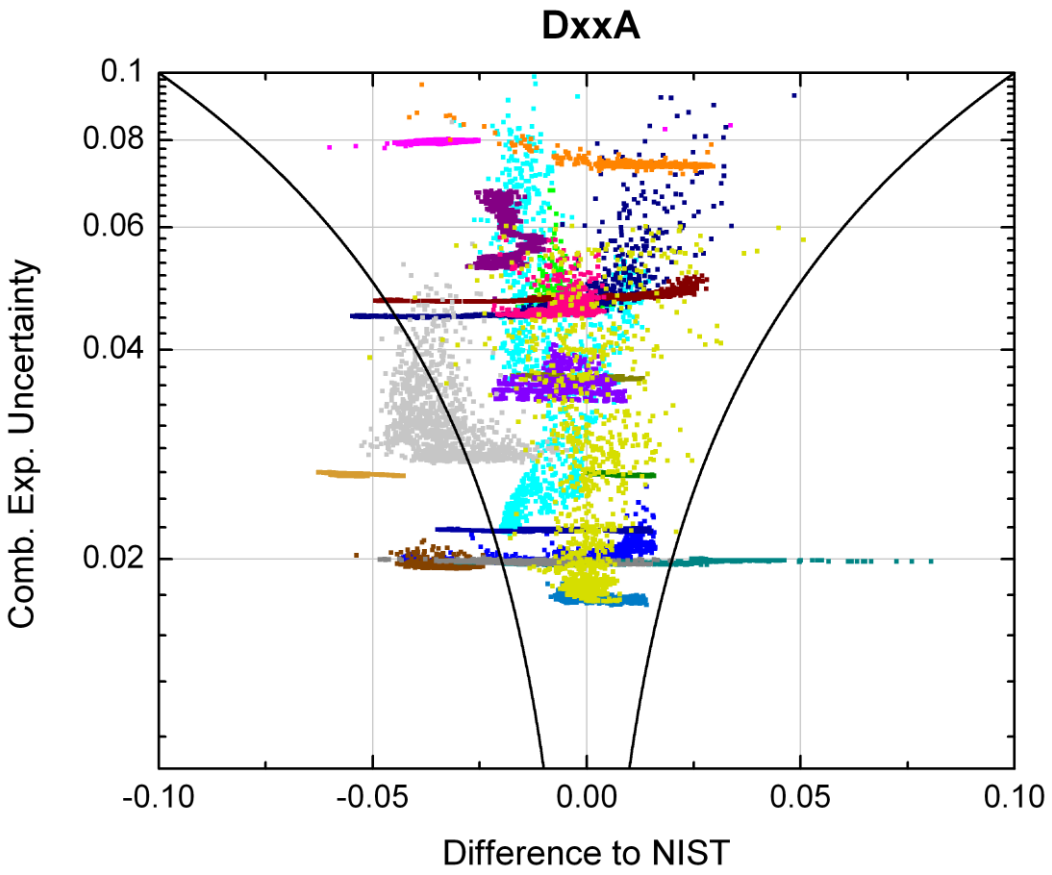

Most (but not all) results within combined uncertainties

DxxC – Nextel Black Paint Samples I

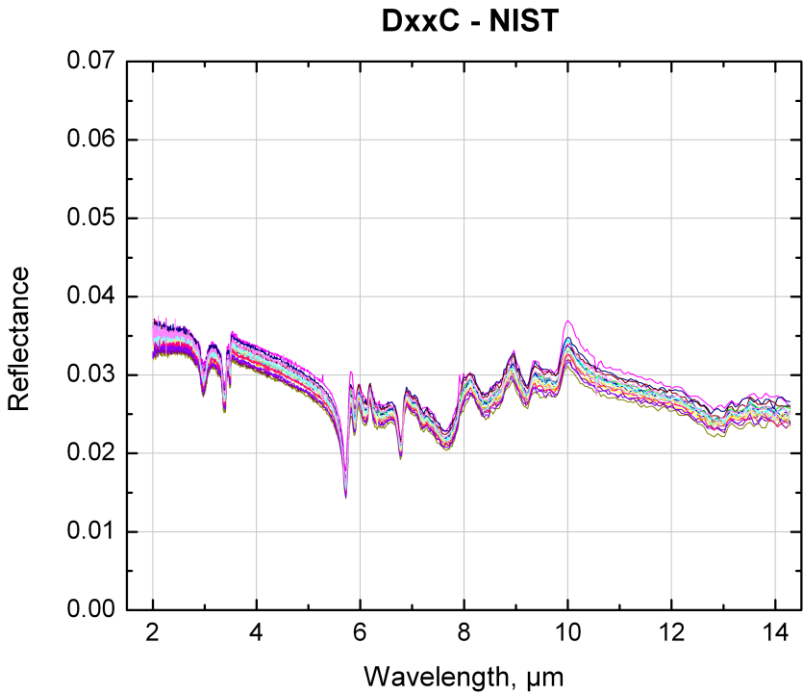

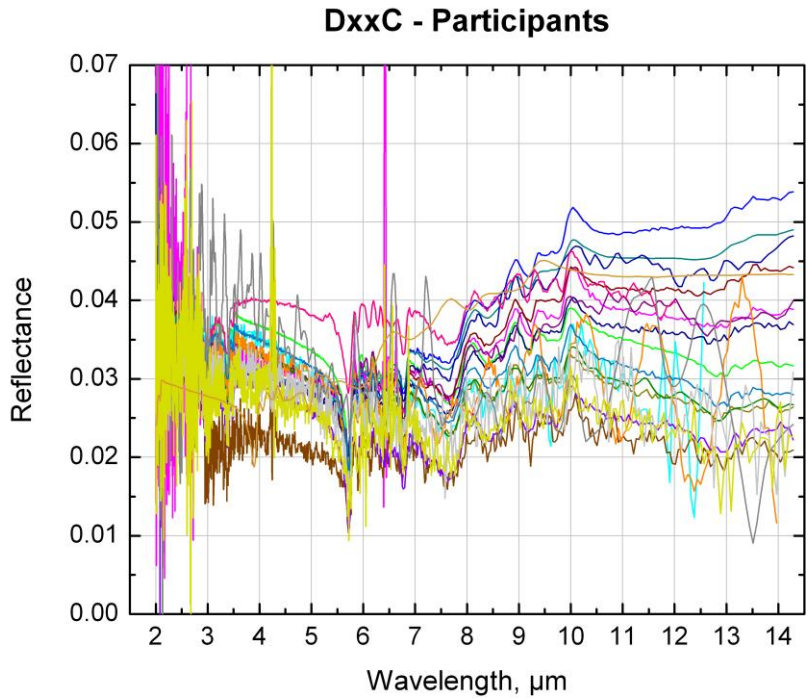

Large relative variability in participants results

DxxC – Nextel Black Paint Samples II

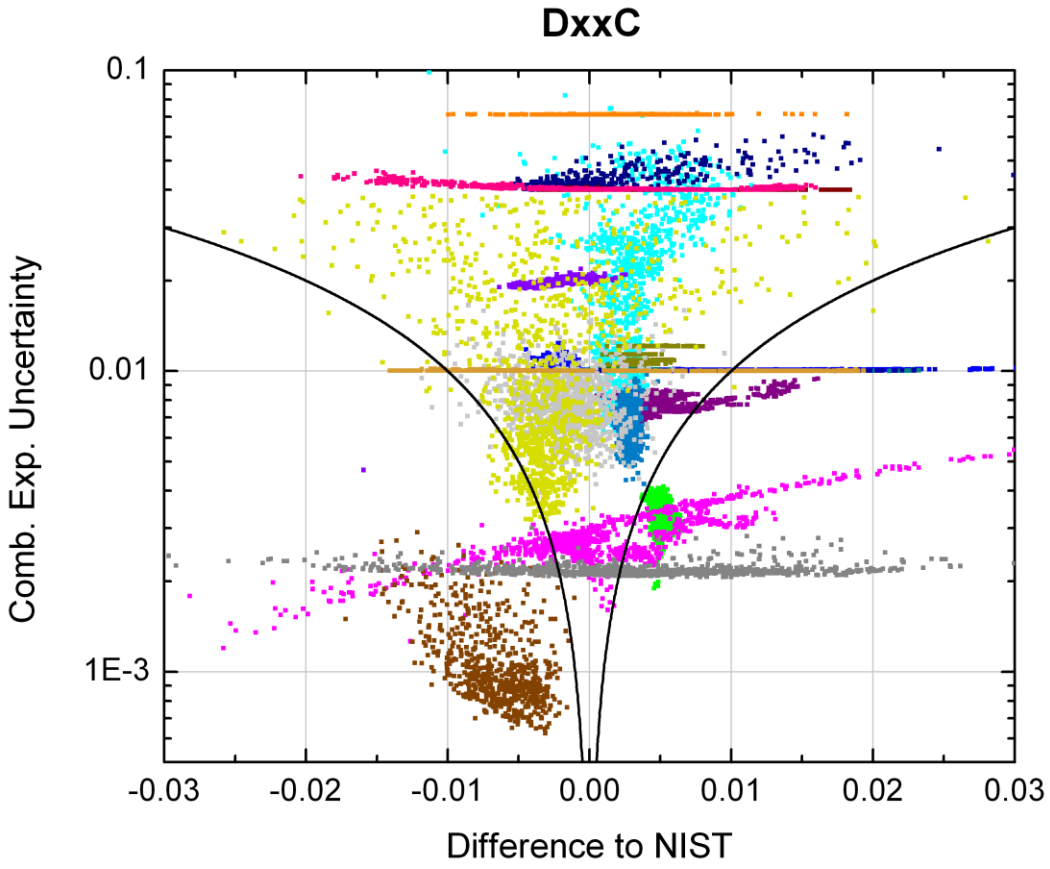

Large range of uncertainties from participants.

Some points outside curves due to failure to include noise component in uncertainty calculation

DxxD – Krylon Silver Paint Samples I

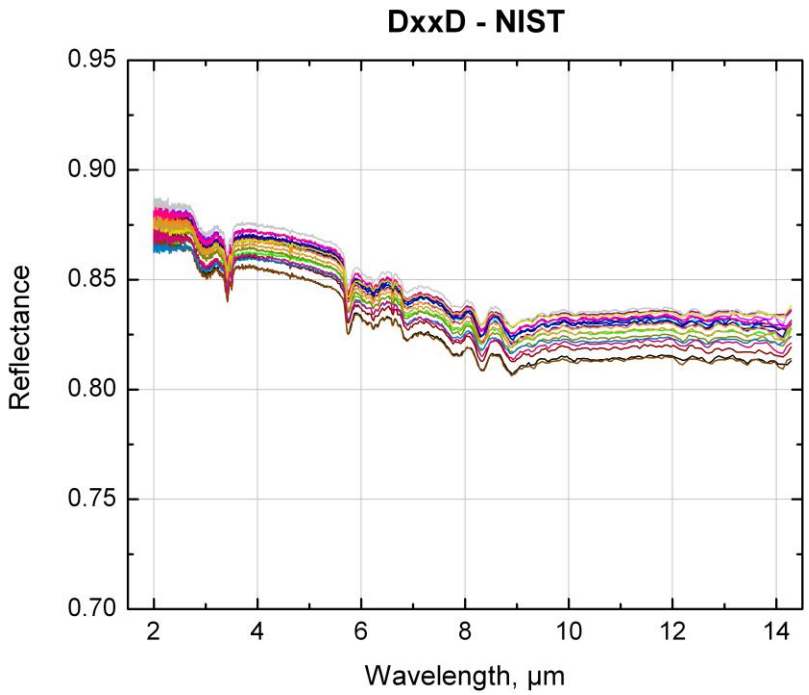

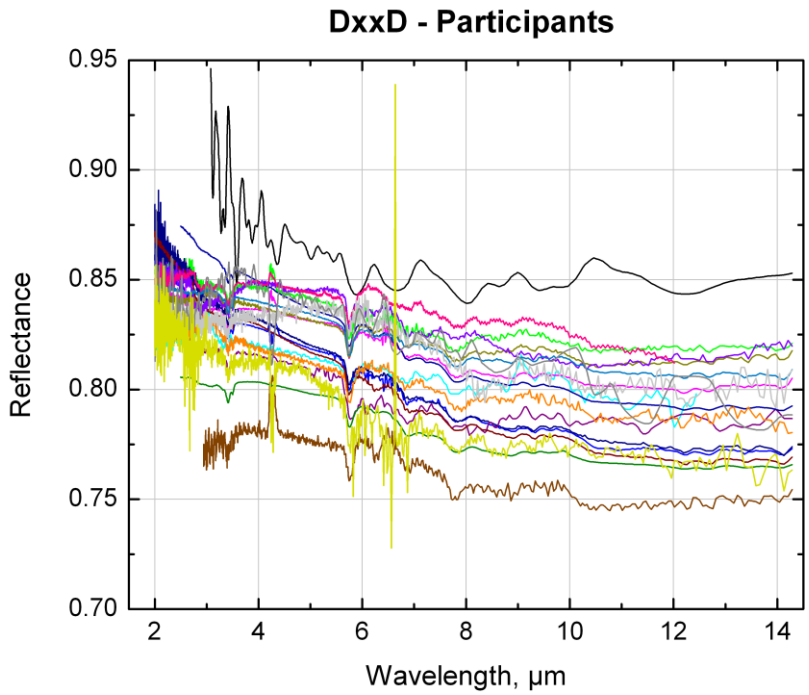

Somewhat larger sample to sample variation

Generally lower values for participants

Not surprising (see followings slides) but clear indication of inherent large(r) uncertainties for diffuse sample measurements

DxxD – Krylon Silver Paint Samples II

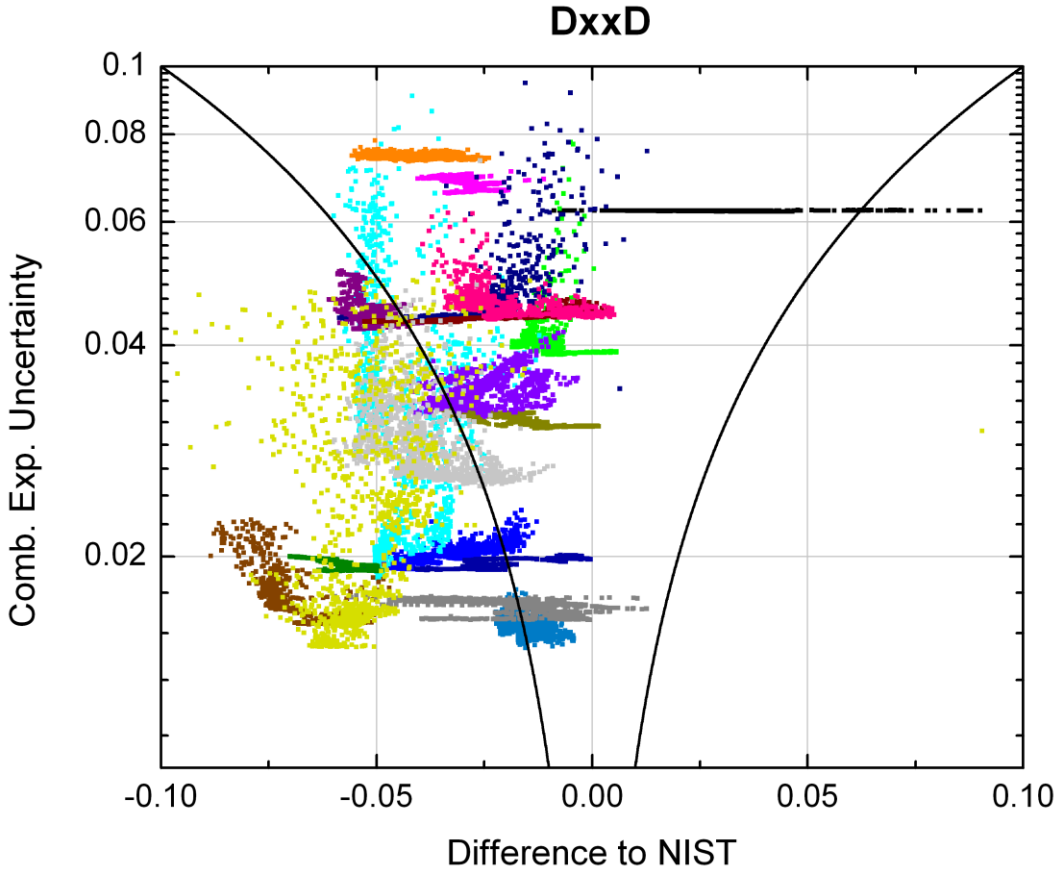

Clear “shift” between most participants and NIST

Not revealed in preliminary comparison plot shown last year

Result of correction applied to NIST data, but unlikely to participant’s data

NIST method for Absolute Diffuse Reflectance

- Basic sample / reference measurement results supplemented with sphere response uniformity (map) characterization and sample BRDF information
- Standard calibration measurements use correction curve determined for Lambertian scattering – uncertainty budget includes possible deviations
- Specialized calibrations (e.g. for IR reflectance intercomparison) include BRDF measurements – and reduced uncertainties
- Specifically, In-plane BRDFs measured at 1.55 µm and 10.6 µm
  - Interactive program used to fit combination of BRDF to measured data
  - 3D BRDF data are generated from fit using Monte Carlo program
  - 3D BRDF data are folded with integrating sphere uniformity map data to generate spectral correction curves for 1.55 µm and 10.6µm
  - Spectral corrections curves are interpolated to obtain final correction curves

DxxD – Krylon Silver Paint BRDF

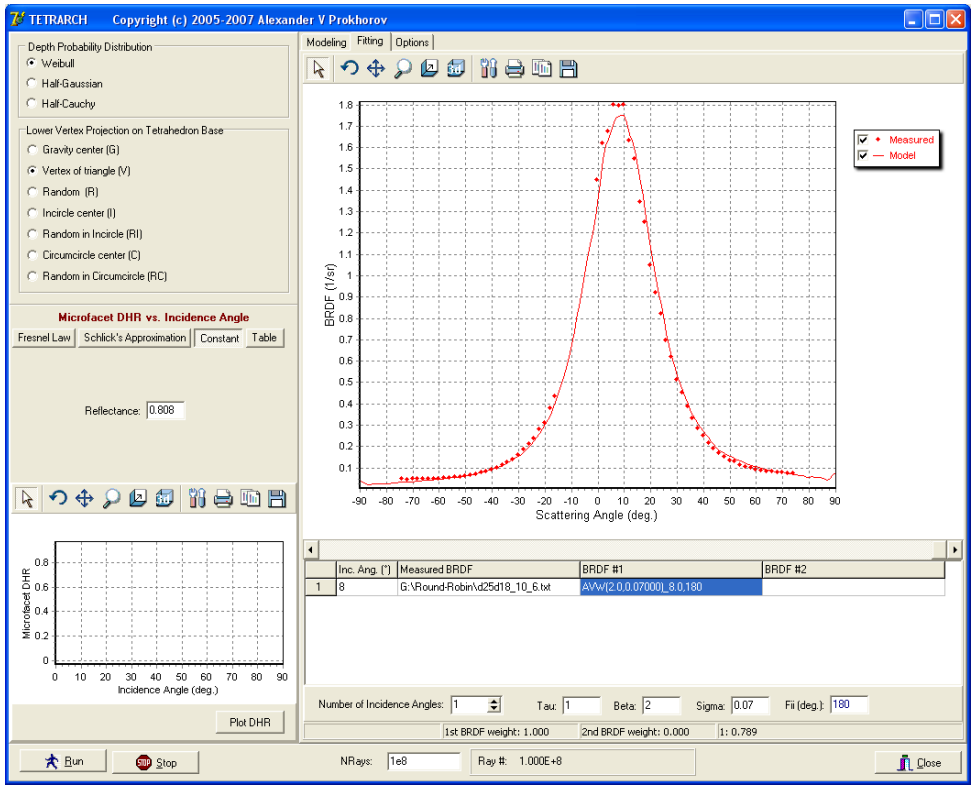

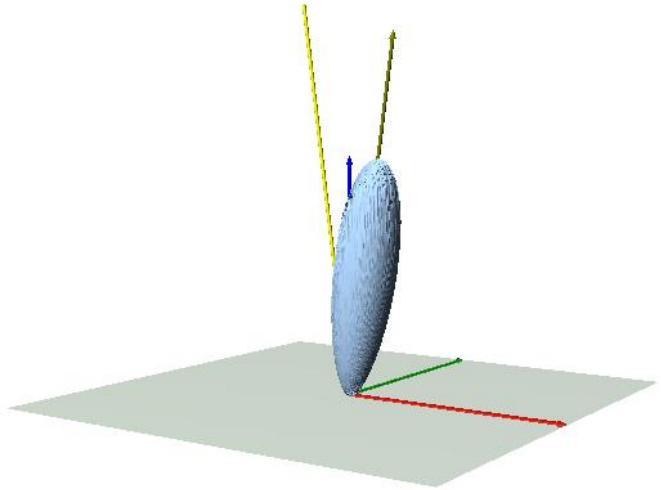

Dependence of Port Loss on BRDF Example

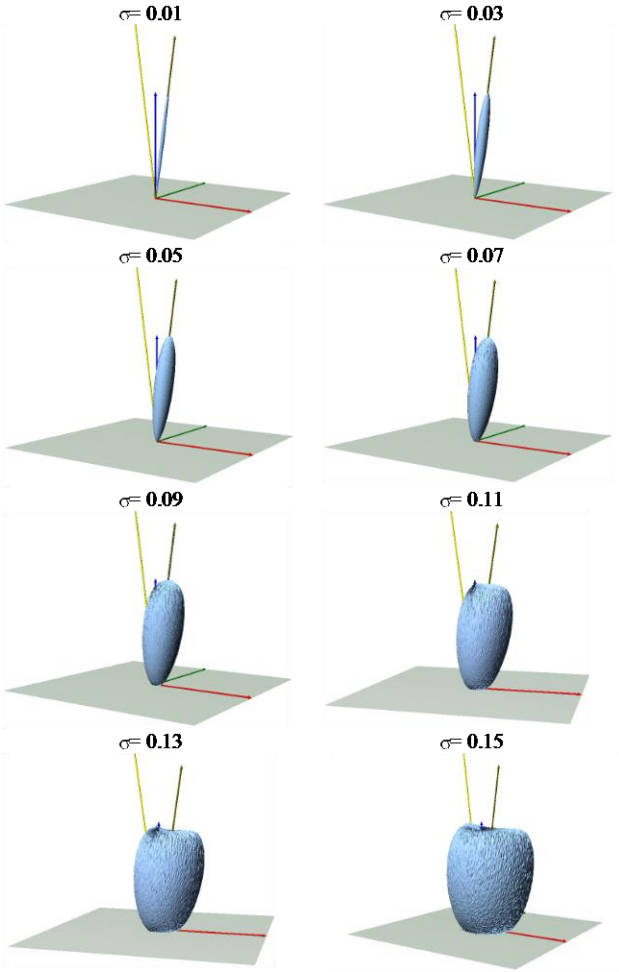

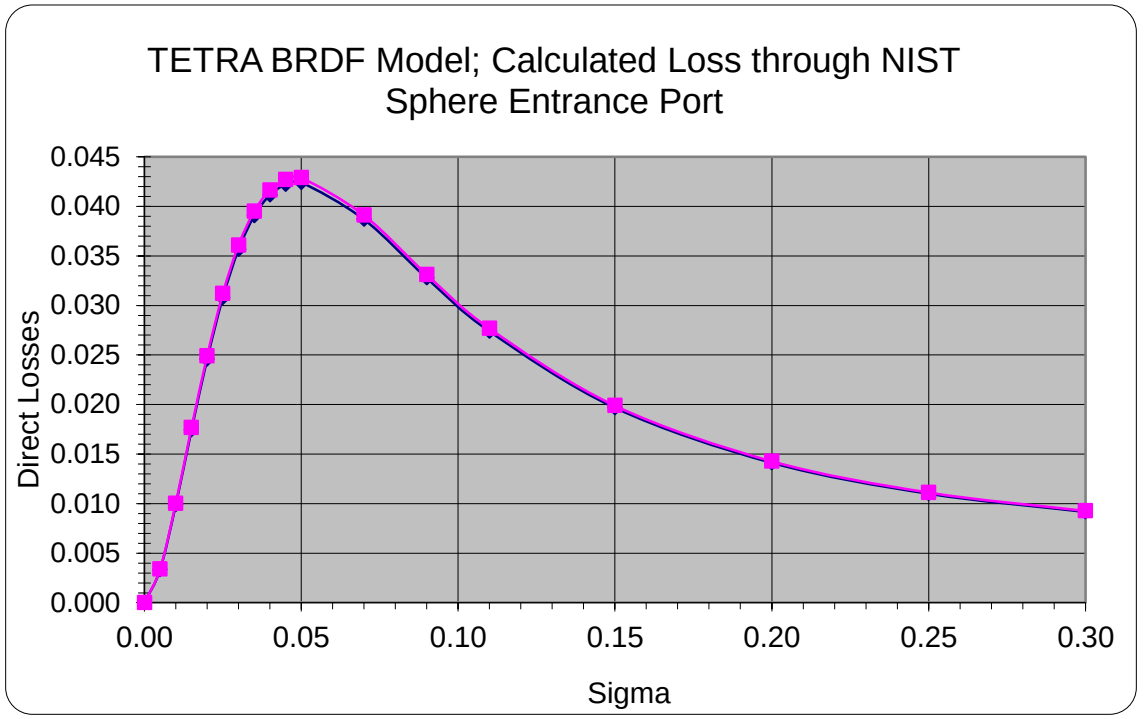

- TETRA procedural model developed to account for multiple surface reflection effects
- Maximum port loss > 4% vs. Lambertian case 1%
- Results used for uncertainty estimate & data correction

Correction Curves for Range of BRDFs

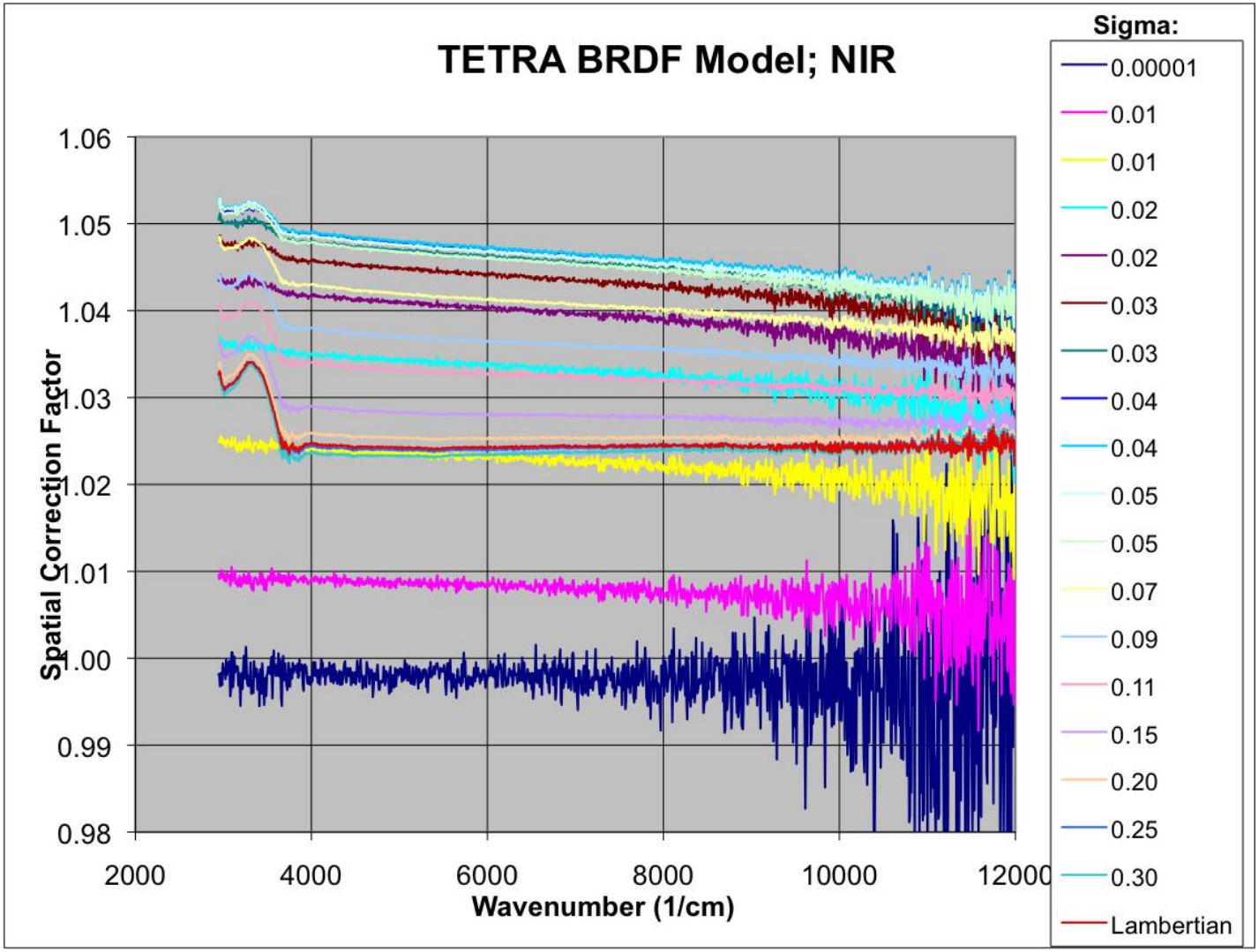

Outline

I. Background

II. Intercomparision Details

III. Sample & Calibration Description

IV. Calibration & Comparison Results

V. Conclusions

Conclusions and Future Directions

- Nationwide IR Reflectance Intercomparison successfully completed
- Results reveal general lack of realistic uncertainty values (both under- and over-estimated)
- Inherent design of measurement instruments (incl. port loss) can limit ultimate accuracy
- Use of calibrated samples/standards can reduce error and uncertainties – standard sets transferred to about 40% of participants (purchase/support)
- NIST capabilities expansion: variable angle & grazing incidence DHR, and extended wavelength range > 50 µm
- Presentation of Results at EO-IR Workshop, CALCON and SPIE San Diego, Publication in progress
- NIST capabilities expansion: variable angle. Potential future Intercomparisons: Variable angle R, BRDF

APPENDIX I

REPORT OF CALIBRATION

38075S Special Tests Infrared Reflectance, Transmittance, and Emittance of Materials

for

Diffuse Gold Sample S/N XXXXXX

Submitted by:

Attn.: Mr. XXXXX
National Institute of XXXX, Optics Division
XXXXXXXXXX
XXXXX
Country
(See your Purchase Order No. CALIBXXX dated Month Date, Year)

1. Description of Calibration Items

One rectangular gold mirror of 20 mm x 30 mm square and 3 mm in thickness.

2. Description of Calibration

Infrared spectral reflectance measurements were performed on a custom Fourier Transform Spectrometer System incorporating an integrating sphere for collecting the sample reflected light. Spectral directional hemispherical reflectance (DHR) was measured from 2.5 microns through 18 microns (4,000 cm^{-1} through 560 cm^{-1}) with the setup of the Fourier Transform Spectrometer in the Mid IR mode with a KBr beamsplitter and a SiC "globar" source. The measurement resolution was 8 cm^{-1}. Measurements were performed with light incident at a central angle of 8 degrees within an f/6 cone. The spot size on the sample is 1 cm in diameter. The collection geometry is hemispherical (i.e. all scattered light is collected and measured). Assuming the diffuse component (scattered light) is less than 0.05%, the DHR is equal to the regular (specular) reflectance. Details of the measurement instrumentation and methodology can be found in References 1 to 4. Each measurement was repeated 40 times over a period of 3 hours.

Sample Environment:
Temperature: 23 °C ± 1 °C.
Relative Humidity: 0.1 % ± 0.1 %

Measurements were performed by Leonard Hanssen, on Month Date, Year.

3. Results of the Calibration

Calibrated directional hemispherical reflectance results obtained are corrected mean values along with estimated expanded uncertainties that include standard deviation of the mean contributions taken from the repeated measurements. These results are shown graphically in Figure 1. The data results are provided in a tab-delimited test file, with 4 cm^{-1} constant spacing in wavenumber. Both wavenumber and wavelength are provided for each data point, along with the reflectance values and their associated expanded uncertainties.

Uncertainty components due to systematic effects are related to the Fourier transform spectrometer and interface optics, the integrating sphere system, and the absolute measurement method. The uncertainties related to the spectrometer and interface optics are wavelength scale error, phase correction error, beam geometry, beam polarization, and system component inter-reflections. The uncertainties related to the integrating sphere system are detector nonlinearity, overfill of the integrating sphere entrance and sample ports, nonequivalence of sample and reference alignment, atmospheric absorption variation, and the local spatial variations of the integrating sphere throughput. The uncertainties related to the absolute measurement method are not significant.

Uncertainty components due to random effects are source stability and detector noise. The uncertainty contributions caused by these effects were evaluated by multiple measurements of the calibration item.

The expanded uncertainties (coverage factor $k = 2$) have a level of confidence of 95 %. Details on the estimation of these uncertainties are given in References 1 and 4. The NIST policy on uncertainty statements is described in Reference 5.

4. General Information

To maintain the highest accuracy, keep the surface of the sample clean and its reflectance recalibrated periodically. Appropriate calibration schedules vary with sample and application and are best determined by the user.

The results of this test apply only to the gold mirror sample referenced in this report. This report shall not be reproduced, except in full, without the written approval of the Optical Properties of Materials Measurements Calibration Service.

Prepared by:

Leonard Hanssen
Optical Technology Division
Physical Measurement Laboratory
(301) 975-2344

Approved by:

Joseph Rice
For the Director,
National Institute of Standards and Technology
(301) 975-2133

References

[1] S. G. Kaplan and L. M. Hanssen, "Infrared regular reflectance instrumentation and standards at NIST," Analytica Chimica Acta **380**, 303-310 (1998).

[2] L. M. Hanssen and K. A. Snail, "Integrating Spheres for Mid- and Near Infrared Reflection Spectroscopy", in *Handbook of Vibrational Spectroscopy*, J.M. Chalmers and P.R. Griffiths (Eds), John Wiley & Sons, Ltd, Volume 2, pp. 1175 - 1192 (2002).

[3] L. M. Hanssen, "Integrating-sphere system and method for absolute measurement of transmittance, reflectance, and absorptance of specular samples," Appl. Opt. **40**, 3196-3204 (2001).

[4] C. J. Chunnilall, F. J. J. Clarke, M. P. Smart, L. M. Hanssen, S. G. Kaplan, "NIST-NPL comparison of mid-infrared regular transmittance and reflectance," Metrologia **40**, S55-S59, (2003).

[5] B. N. Taylor and C. E. Kuyatt, "Guidelines for Evaluating and Expressing the Uncertainty of the NIST Measurement Results," *NIST Technical Note* **1297**, (2nd ed., 1994).

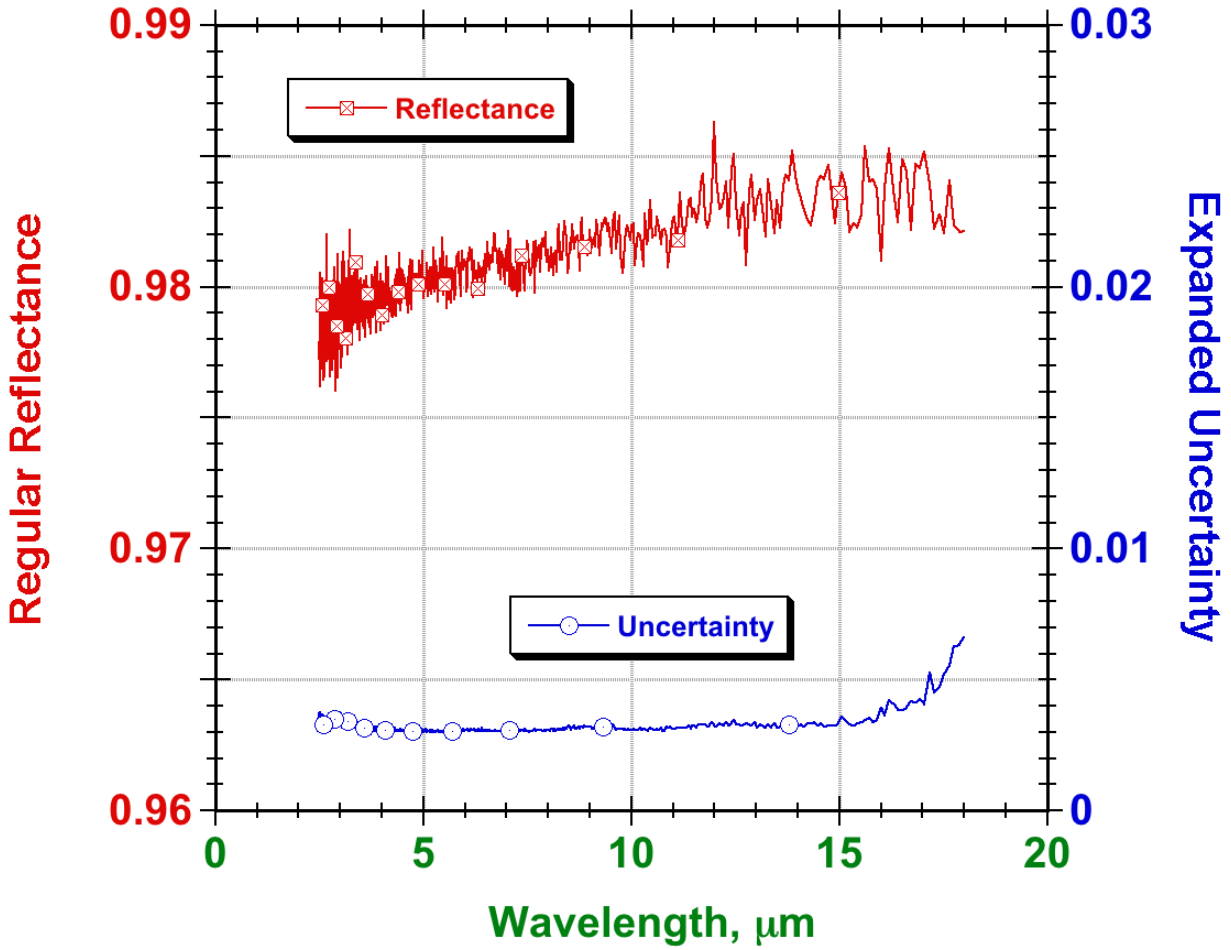

Figure 1. Regular reflectance and expanded uncertainty of gold mirror sample.